Department of Materials Science

PhD program Materials Science and Nanotechnology Cycle XXXVIII

From Green Chemistry to Edible Devices: Synthesising Safer and Functional Materials for Electronic Applications

Surname Fratepietro Name Annapia

Registration number 872597

Tutor: BEVERINA Luca

Co-tutor: CAIRONI Mario

Coordinator: MONTALENTI Francesco

ACADEMIC YEAR 2024/2025

A Mariangela
E alla sua determinazione
che cerco sempre di far mia

Aknowledgments

At the end of this complex chapter of my educational journey, I look back – as I usually do – and, for the first time, I don't try to sum up these past three years: I simply observe them, but above all, I observe myself. I see myself at the beginning, full of enthusiasm and initiative; I see myself in the middle, at the mercy of challenges and emotions; I see myself at the end, tired and dissatisfied, caught in a thousand "what ifs?".

I thought I knew everything about the PhD: its difficulties, frustrations, dissatisfaction, and defeats. Above all, I thought, naively, that I could handle them all on my own, as I always had. I was wrong. And yet, that's exactly what I did for most of these three years: navigating my small boat through the vast ocean of research, struggling, sometimes barely staying afloat, sometimes losing the enthusiasm I had started with.

If I had to reduce these three years solely to the research itself, I doubt I would be satisfied with what this journey has brought me. And yet, if I had the chance to change the mind of the "me" from three years ago, I wouldn't.

Everything that these three years have been has made me into the person I am now – probably as worn out as I am grown. This journey has often taken me far beyond my comfort zone, both academically and personally, confronting me with challenges that I sometimes managed well, and other times simply learned from. In fact, if I had to summarise the PhD in a single word, it would be this: *educational*. For that reason, I begin this manuscript by thanking the one thing that allowed me to keep going despite a thousand doubts: therapy.

Caring for one's mental health in academia is still far too much of a taboo; yet it remains the key to not being devoured by the exhausting pace and countless frustrations that a PhD path often entails. I believe research is wonderful. It nourishes the inner child's curiosity that lives

in every scientist. Nonetheless, it's important to recognise that we are not *only* our research. We don't wake up every day ready to spend hours setting up an experiment that will most likely fail. It's not wrong to be more than just a PhD student. It's not wrong to have "off days." It's not wrong to be tired. It's not wrong to take a break. It's not wrong to stop running and start walking.

To Ivan, who always held my hand – at home, watching me write every day from the same corner of the couch, and from the other side of the world, with his unconditional support. Your warmth was never missing.

To my family, who believe in me even when I stop believing in myself, who have given me, willingly or not, every means to walk the path that brought me here, who rejoice in my small achievements, and who watch me grow from afar.

To my travel companions, who showed me that I was never truly alone on this journey, who opened many doors for me, who reminded me of the lightness of being in our twenties, who proved that it *can* be done despite the falls, who became a family – one that argues, disagrees, sometimes misunderstands, but always cares.

To Deborah and Tory, and little Fiji. You have been "home"; you welcomed me into your world when mine felt too far away. Thank you for being my second family, for never making me feel like a stranger, and for embracing me with open arms in your everyday life.

To Tanya and Sanyukta, for sharing with me your "off days," your moments of exhaustion, but also your small and big achievements. Thank you for your affection, your warmth, and your support. Getting to know you and sharing part of this winding journey with you remains one of the small yet best things these three years have given me.

Table of contents

Chapter 1
A Rational guide for the reader

Considering the structure and content of this dissertation, it is important to provide the reader with some clarifications to help them understand the logical progression of what might otherwise seem like a disparate project, as well as to lay the foundations of the work. I cannot begin without first mentioning the Electronic Food (ELFO) project, of which this dissertation is a part.

Imagine the ability to look inside our bodies using micro-sized cameras. Thanks to advances in research and scientific development, technology once thought to be futuristic has now become accessible. Now, picture taking a further step: detecting physiological parameters inside our bodies without the need for invasive procedures or external devices. This is precisely what ELFO aims to achieve: designing environmentally friendly, biocompatible, cost-effective, and biodegradable electronic devices that are metabolised by the body after completing their task.

Delving into the specifics of Edible Electronics exceeds the scope of this brief introduction, and as such, the full discussion will be presented in the subsequent chapter. However, it was essential to introduce the central theme of the project, as it provides the key terms that

connect all the chapters of this dissertation: green chemistry, green electronics, and green engineering. An edible device should ideally result from a safe production protocol, free from harmful chemicals, from its inception to its disposal.

That said, it is also crucial to acknowledge the intrinsic complexity of the specific task that underlies this research, namely, the synthesis of *fully edible materials* suitable for electronic devices. Developing functional materials that meet the demanding requirements of electronic performance while also being safe for ingestion presents a formidable scientific and technical challenge. It requires balancing chemical functionality with biocompatibility, electronic performance with environmental sustainability, and synthetic feasibility with safety constraints.

With these challenges in mind, the objective of this doctoral work has been to explore and develop some benign strategies to pursue the synthesis of *safer semiconducting materials* that could be integrated into edible electronic devices. The guiding philosophy throughout has been one of minimising ecological impact and toxicological risk, while still striving to achieve meaningful electronic functionality.

In doing so, this dissertation aims to contribute to the broader vision of truly sustainable, transient, and edible electronics, a field that sits at the intersection of materials science, chemistry, and bioengineering.

Chapter 2

Introduction to edible electronics

"Quam multa fieri non posse priusquam sunt facta indicantur?"
Gaius Plinius Secundus /In Pliny: Natural History (1947), Vol. 2, Book 7

The vision of electronic devices that can be safely ingested, operate within the human body, and degrade once their function is completed has always been perceived as "futuristic". In recent years, however, this concept has evolved into a tangible research frontier: "*edible electronics*".[1] This emerging interdisciplinary field aims to integrate electronic functionality with complete biocompatibility, digestibility, and metabolizability, creating devices capable of performing semi-invasive diagnostic, therapeutic, or monitoring tasks while safely degrading into non-toxic metabolites, thereby eliminating the need for retrieval, minimising medical risks and lowering environmental impact.[2]

The origins of *ingestible electronics* date back to the 1950s, when telemetric "Endoradiosondes" were developed to record physiological parameters (pressure, temperature and pH) in the gastrointestinal (GI) tract.[3] Over the subsequent decades, advances in sensor miniaturisation and wireless communication led to the development and

regulatory approval of ingestible cameras, partially dissolvable digital pills and ingestible sensors, able to monitor different GI-related signals, such as local biomarkers that can be linked to inflammation or other diseases when exposed to some specific signals (**Figure 2.1**).[4]

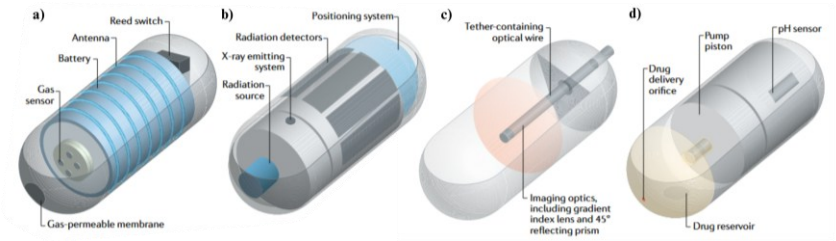

Figure 2. 1 *Available Technologies for ingestible electronics: a) Gas-sensing capsule; b) X-ray scanning capsule; c) Optical coherence tomography; d) IntelliCap for drug delivery.*

Despite these breakthroughs, conventional ingestible devices relied predominantly on rigid, non-degradable materials encapsulated with rigid non-degradable polymers (e.g., polydimethylsiloxane, parylene/epoxy), restricting their application to supervised clinical settings.[5,6] Within this framework, the size of rigid edible devices plays a pivotal role as the risk of device retention is strictly associated with it, and can be mitigated by choosing flexible or biodegradable materials. *Edible Electronics* represents a paradigm shift. It seeks to replace all functional components with materials derived from natural food substances or synthetically produced compounds recognised as safe. It aims to create a new generation of microencapsulated electronic devices that can be dissolved, digested or absorbed after fulfilling the task (diagnosis, monitoring, therapy) they are designed for.[7]

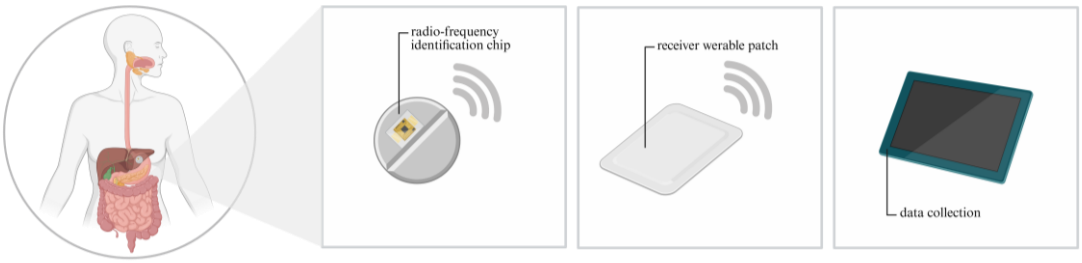

Figure 2. 2 *Schematic representation of the digital compliance monitoring system based on an ingestible RFID chip. The ingestion is detected by a wearable patch, enabling healthcare providers to adjust therapy according to objective, unbiased data.*

This newly born research field opens the possibility of autonomous administration, continuous monitoring, and device integration into food or pharmaceutical products (**Figure 2.2**), supporting the societal trends toward decentralised healthcare and Internet of Things (IoT)-aided health technologies. In this scenario, the pharmaceutical industry can benefit from it in applications involving devices operating outside the human body. "Smart" edible identification (ID) labels integrated into pharmaceutical products offer an effective strategy to prevent counterfeiting and to monitor drug exposure to external factors such as ultraviolet (UV) radiation, temperature, and humidity. Designed to be safely ingested together with the medicine, these labels eliminate the need for removal before administration.[1] Owing to their edible, non-toxic, and environmentally sustainable characteristics, the potential applications of edible electronics extend beyond the pharmaceutical field. In the food industry, ingestible and cost-effective "smart" tags could enable real-time monitoring of product quality and safety throughout the distribution chain. Such systems would enhance traceability and contamination control while contributing to the reduction of food waste and the environmental impact associated with conventional packaging.[8]

2.1 The foundation of Edible Electronics: the green triangle

Beyond the biomedical domain, edible electronics directly comes from green and sustainable technologies (**Figure 2.3**).[9] The principles of green chemistry and engineering have underlined the importance of material design aimed at minimising toxicity, environmental impact, and waste generation.

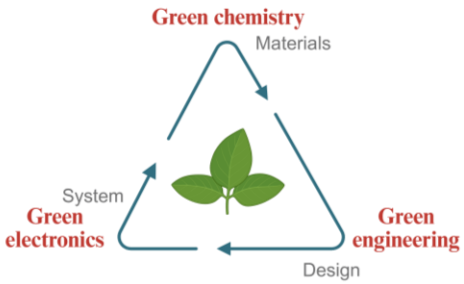

Figure 2. 3 *The "green triangle:" visual representation of the scientific and technical efforts shaping the "green" concept. Stages of the "green" fabrication cycle and disciplines responsible: design - green engineering; material - green chemistry; final system - green electronics.*

The escalating accumulation of electronic waste[10], currently measured in hundreds of millions of tons annually, has prompted the search for biodegradable and renewable alternatives to conventional electronic components.[11,12]

In edible electronics, the notion of a device's "end-of-life" is redefined within a biological context: rather than requiring disposal or recycling, the device is designed to be fully assimilated by the organism. This approach promises a convergence of safety, environmental sustainability, cost-effectiveness, and energy efficiency, establishing a context in which electronics can be both functional and transient. Edible electronic systems retain the essential building blocks of traditional electronics – including conductors, semiconductors, dielectrics, sensors, power sources, and communication modules – while employing materials that are entirely safe for ingestion.

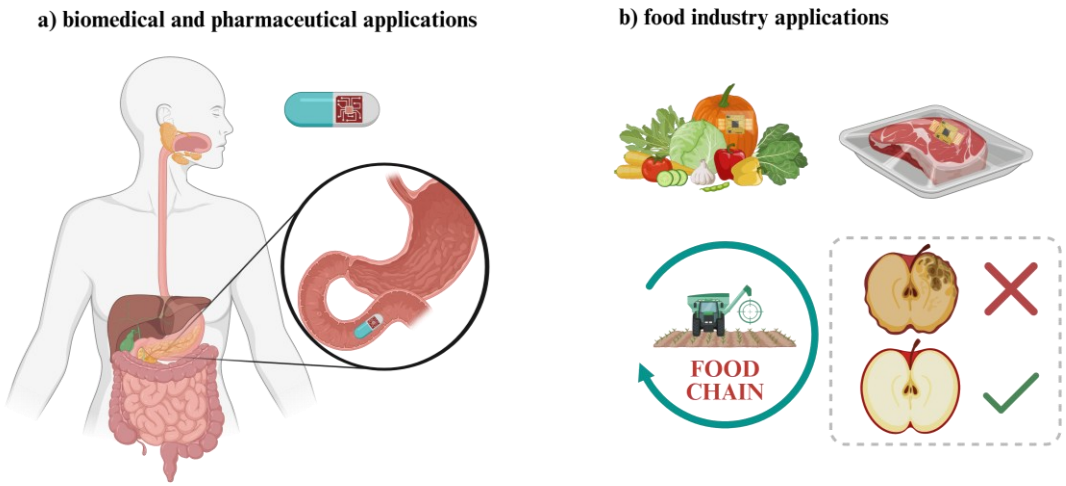

Figure 2. 4 . *Applications of edible electronics. Edible electronic devices, made entirely from food-based or edible synthetic materials derived from sustainable sources, are designed to degrade, be digested, or metabolised after fulfilling their function. a) Biomedical/pharmaceutical applications include diagnostics, therapy, and drug delivery, represented by a smart pill metabolised within the body. b) Food industry applications involve edible "smart" tags for direct labelling and real-time communication with the user, enabling monitoring of food quality, spoilage, and contaminants along the distribution chain.*

As already stated, applications of edible electronics include internal, in-body systems for diagnostic monitoring,[13,14] targeted drug delivery, and medication adherence, as well as external, food-integrated solutions such as ingestible smart labels[8,15] for assessing freshness, detecting contamination, and verifying product authenticity (**Figure 2.4**). The effects of edible electronics could be profound. In healthcare, these technologies promise to revolutionise patient monitoring by providing continuous, real-time physiological data[16]

without invasive procedures or hospitalisation. In the food industry, they offer new strategies for traceability, waste reduction, and safety assurance across complex supply chains. From an ecological perspective, replacing conventional electronic materials with biodegradable, food-derived components can mitigate electronic waste and encourage circular manufacturing models. However, realising these ambitions necessitates overcoming significant interdisciplinary challenges, including the development of edible functional materials,[7] assessment of biocompatibility,[12] establishment of regulatory standards, and design of efficient power and communication strategies. Achieving progress in this field requires coordinated collaboration among materials scientists, food technologists, biomedical engineers, and regulatory experts.

The ultimate aim is to establish a new category of transient, metabolizable electronic devices designed to function safely within the human body and the environment while serving as temporary, active, and potentially nourishing elements. By merging electronics, biology, and sustainability, edible electronics opens new possibilities for technologies that are intelligent, safe, and ecologically responsible, redefining conventional notions of electronic functionality and interaction.[1]

2.2 Edible materials as ingredients for an Edible Electronics platform

At the core of edible electronics lies a unique challenge: identifying materials that combine electronic functionality with safe biochemical and organoleptic properties, making them truly edible. Unlike general biodegradable or ingestible substances, edibility imposes stricter criteria. Materials must be biocompatible, digestible, and metabolically benign. Addressing this challenge requires bridging two historically distinct domains: electronics, which prioritises stability, conductivity, and performance, and food science, which emphasises safety, digestibility, and sensory acceptance.

2.2.1 Semiconductors as "key components" for Edible Electronics

Semiconductors constitute the most scientifically challenging and promising class of edible materials. They require controlled charge transport, a property rarely found in natural compounds. For this reason, this class of materials remains the least explored in terms of edibility. Reports on edible semiconductors are rare, and only a few potential candidates have been identified. This is somewhat surprising, given that many natural chromophores, especially those found in food, owe their colour to π-electron delocalisation, which can also confer semiconducting behaviour in the solid state.

Research in organic semiconductors has shown that efficient charge transport depends critically on molecular packing and intermolecular coupling.[17] Finding naturally occurring materials with comparable structural order is therefore challenging. Moreover, edible semiconductors must achieve a balance between ingestion safety, sufficient electronic stability, and adequate performance within a limited operational timeframe.

Materials of natural origin, such as DNA, proteins, pigments, and dyes, are of particular interest due to their strong hydrogen bonding and π-conjugated networks, which support charge transport and environmental stability. To date, most potentially edible semiconductors derive from naturally occurring pigments and dyes of animal, plant, or mineral origin, as well as from FDA-approved synthetic compounds. Notable examples include: indigo carmine (E132)[18] showing ambipolar charge transport and pH-sensitive optical properties, β-Carotene[19,20] acting as a p-type semiconductor, riboflavin (vitamin B2)[21] and derivatives, employed in bio-organic light-emitting diodes (OLEDs), perylene diimide (PDI),[22] an n-type semiconductor with toxicity lower than table salt, and anthraquinone derivatives, naturally present in plants and approved as food colorants, demonstrating field-effect mobilities on the order of 10^{-3} – 10^{-2} $cm^2V^{-1}s^{-1}$. These examples demonstrate that semiconducting functionality can emerge from compounds already familiar in nutrition and pharmacology. Their practical implementation, however, requires careful optimisation of molecular order, stability in aqueous environments, and strict toxicological validation. In fact, materials synthesised from edible precursors cannot automatically be deemed safe for ingestion and require further toxicological evaluation

While conductors and dielectrics are essential for edible electronic devices, their detailed discussion – including materials, electrical properties, and applications – extends beyond the scope of this thesis. Interested readers are referred to Sharova et al.[1] for comprehensive information on edible conductors and dielectrics.

2.2.2 Toward a database of edible functional materials

Systematic characterisation of edible materials – including electrical, mechanical, and biochemical properties – is crucial for developing a standardised edible electronics platform. A comprehensive database should include parameters such as conductivity, carrier mobility, dielectric constant, degradation rate, and nutritional information (RDI, ADI).[23] Such a resource would accelerate materials discovery, facilitate regulatory approval, and enable the inclusion of "ingredient lists" and nutritional labels for electronic devices, promoting transparency and consumer trust.

Bibliography

1. Sharova, A. S., Melloni, F., Lanzani, G., Bettinger, C. J. & Caironi, M. Edible Electronics: The Vision and the Challenge. *Adv. Mater. Technol.* **6**, 2000757 (2021).
2. Bettinger, C. J. Materials Advances for Next-Generation Ingestible Electronic Medical Devices. *Trends Biotechnol.* **33**, 575–585 (2015).
3. Connell, A. M. & Rowlands, E. N. Wireless Telemetering from the Digestive Tract. *Gut* **1**, 266–272 (1960).
4. Arnott, I. D. R. & Lo, S. K. The Clinical Utility of Wireless Capsule Endoscopy.
5. Rogers, A. M., Kuperman, E., Puleo, F. J. & Shope, T. R. Intestinal Obstruction by Capsule Endoscopy in a Patient With Radiation Enteritis.
6. Xin, L., Liao, Z., Du, Y., Jiang, Y.-P. & Li, Z.-S. Retained capsule endoscopy causing intestinal obstruction—Endoscopic retrieval by retrograde single-balloon enteroscopy. *J. Interv. Gastroenterol.* **2**, 15–18 (2012).
7. Wu, Y. *et al.* Edible and Nutritive Electronics: Materials, Fabrications, Components, and Applications. *Adv. Mater. Technol.* **5**, 2000100 (2020).
8. Wang, Z., Mathiyazhagan, K., Xu, L. & Diabat, A. A decision making trial and evaluation laboratory approach to analyze the barriers to Green Supply Chain Management adoption in a food packaging company. *J. Clean. Prod.* **117**, 19–28 (2016).
9. Anastas, P. & Eghbali, N. Green Chemistry: Principles and Practice. *Chem. Soc. Rev.* **39**, 301–312 (2010).
10. J of Industrial Ecology - 2023 - Fenwick - Recycling plastics from e-waste Implications for effective eco-design.pdf.

11. Irimia-Vladu, M. *et al.* Biocompatible and biodegradable materials for organic field-effect transistors. *Adv. Funct. Mater.* **20**, 4069–4076 (2010).
12. Lei, T. *et al.* Biocompatible and totally disintegrable semiconducting polymer for ultrathin and ultralightweight transient electronics. *Proc. Natl. Acad. Sci. U. S. A.* **114**, 5107–5112 (2017).
13. Becker, D. *et al.* Novel Orally Swallowable IntelliCap® Device to Quantify Regional Drug Absorption in Human GI Tract Using Diltiazem as Model Drug. *AAPS PharmSciTech* **15**, 1490–1497 (2014).
14. Mimee, M. *et al.* An ingestible bacterial-electronic system to monitor gastrointestinal health. *Science* **360**, 915–918 (2018).
15. Stenmarck, Å., Jensen, C., Quested, T. & Moates, G. Estimates of European food waste levels. Preprint at https://doi.org/10.13140/RG.2.1.4658.4721 (2016).
16. Ell, C. *et al.* The First Prospective Controlled Trial Comparing Wireless Capsule Endoscopy with Push Enteroscopy in Chronic Gastrointestinal Bleeding. *Endoscopy* **34**, 685–689 (2002).
17. Matsidik, R. *et al.* Effects of PNDIT2 end groups on aggregation, thin film structure, alignment and electron transport in field-effect transistors. *J. Mater. Chem. C* **4**, 10371–10380 (2016).
18. Yao, M. *et al.* Indigo carmine: An organic crystal as a positive-electrode material for rechargeable sodium batteries. *Sci. Rep.* **4**, 3650 (2014).
19. Llansola-Portoles, M. J., Pascal, A. A. & Robert, B. Electronic and vibrational properties of carotenoids: from *in vitro* to *in vivo*. *J. R. Soc. Interface* **14**, 20170504 (2017).

20. Burch, R. R., Dong, Y.-H., Fincher, C., Goldfinger, M. & Rouviere, P. E. Electrical properties of polyunsaturated natural products: field effect mobility of carotenoid polyenes. *Synth. Met.* **146**, 43–46 (2004).
21. Pietsch, M. *et al.* Biodegradable inkjet-printed electrochromic display for sustainable short-lifecycle electronics. *J. Mater. Chem. C* **8**, 16716–16724 (2020).
22. Kuznetsova, L. I. *et al.* Disubstituted perylene diimides in organic field-effect transistors: Effect of the alkyl side chains and thermal annealing on the device performance. *Org. Electron.* **58**, 257–262 (2018).

Chapter 3

Carotenoids as edible organic semiconductors

"Nature already solved the problem – we are just learning to speak its language."

R.E. Blankenship

In this chapter, the vibrant world of carotenoids steps into electronics. Astaxanthin — a molecule known for giving salmon and flamingos their colour — becomes a bridge between biology and technology. Its natural role as a light harvester becomes the foundation for electronic functionality. By modifying, protecting, and assembling its structure, we turn a biological pigment into an active layer for organic transistors — merging colour, conductivity, and sustainability in one molecular design.

3.1 Introduction

This section of the project is directly linked to the ongoing research carried out at the Istituto Italiano di Tecnologia (iit) as part of the ELFO project, on the use of carotenoids as organic semiconducting materials. Within this context, both *trans*-astaxanthin and β-carotene have been evaluated as active semiconducting layers in organic field-effect transistors (OFETs), where their conjugated π-systems enable charge transport. While these studies confirmed their potential for edible sustainable and bio-derived electronics, they also highlighted key

limitations related to chemical instability and poor solubility, particularly for pristine astaxanthin. The aim of this chapter is to address these challenges by exploiting the chemical reactivity of astaxanthin's functional groups to design and synthesise new astaxanthin derivatives with improved stability, solubility, and processability. This work seeks to enhance the material's robustness at the solid state and its electronic performance, contributing to the broader effort of developing edible semiconductors for organic electronics.

3.1.1 Historical highlights of organic electronics

Conventional electronics is rooted in Lee de Forest's vacuum tube "triode" discovered at the beginning of the last century. However, the transistor forefather only appeared twenty years later, in 1926, when an "*apparatus for controlling the flow of an electric current between two terminals of an electronically conducting solid by establishing a third potential between said terminals*" (**Figure 3.1**) was described for the first time in a J. E. Lilienfeld patent.[24] His early concept was fully demonstrated during the second half of the century with the finalization of silicon-silicon dioxide metal-oxide-semiconductor field-effect transistor (MOSFET) technology that, besides being a well-established commercial technology, gave rise to a fundamental tool to have direct access to the measurement of semiconductor charge-carrier mobility.

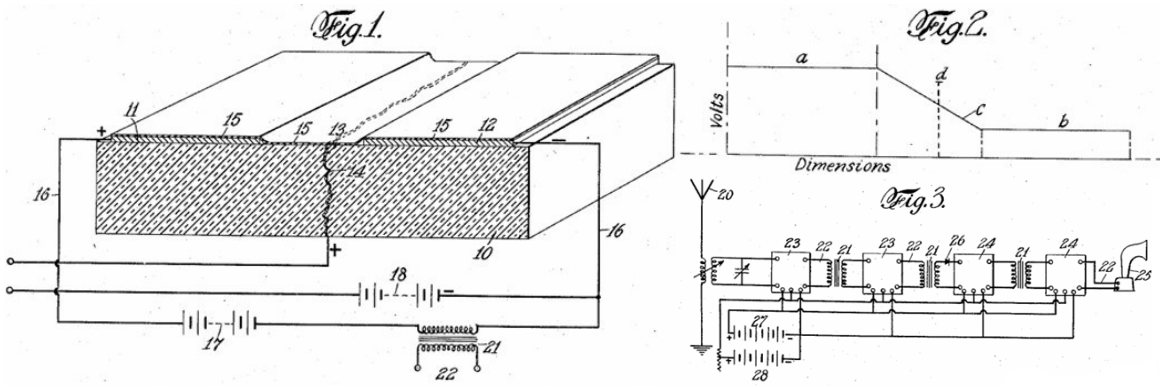

Figure 3. 1 *Structure of the first current flow controlling apparatus patented by J.E. Lilienfeld in 1926, adapted from*[24]

Since their first appearance, field effect transistors (FETs) have been thus perceived not only as a basic unit able to act as an on/off switch in a broad range of electronic and optoelectronic applications but also as a platform for studying charge transport in solid materials, allowing fine control of the charge density in the semiconductor layer.[25,26] Thin-film transistors (TFTs) represent a clear example of such a concept. This architecture was first employed to measure the mobility of hydrogenated amorphous silicon (a-Si:H) and, differently from MOSFET, the conducting channel is induced in the accumulation regime, then employed in applications requiring large areas and where single crystalline silicon cannot be employed. The field of organic electronics arose in the 1960s with the identification of the first organic semiconductors. Initially considered to be materials with low mobility, it was only in the late 1980s that works on organic thin-film transistors (OTFTs) appeared; however, they became the focus of a limited number of academic studies because of their poor performance. The research field extended to industry only ten years later when the mobility of organic semiconductors matched and exceeded that of amorphous silicon. The development of new materials allowed the development of new device designs, processing techniques, and applications ranging from low-cost sensors to radio-frequency identification (RFID) tags and single-use electronics.[27] The rapid advancement of organic electronics in the early 2000s was driven not only by improved charge-carrier mobility but also by the development of novel device architectures and deposition techniques. Solution-processable semiconducting polymers and small molecules enabled low-cost, large-area fabrication methods such as spin coating, inkjet printing, and roll-to-roll processing, which are incompatible with conventional silicon technology. This versatility opened pathways for flexible, lightweight, and even stretchable electronic devices, expanding the potential applications beyond rigid substrates.

Simultaneously, significant progress in understanding the physics of organic semiconductors – such as charge transport mechanisms,[28] interface engineering,[29] and the role of molecular packing[30,31] – allowed researchers to optimise device performance systematically. Organic light-emitting diodes (OLEDs), organic photovoltaics (OPVs), and organic field-effect transistors (OFETs) emerged as key technological pillars, each benefiting from tailored molecular design and thin-film engineering. By the 2010s, some organic devices had achieved performance levels approaching or surpassing that of amorphous silicon in specific metrics, particularly in low-voltage operation and mechanical flexibility.[32]

3.1.2 Organic semiconductors overview and comparison with inorganic ones

A traditional inorganic semiconductive material is described as a "non-metallic solid whose electrical conductivity ranges between a conductor and an insulator" (**Figure 3.2**). It can be either an elementary, binary, or ternary compound having covalent bonds defining its crystal structure (e.g. cubic or lattice). Silicon and Germanium-based materials are the most widespread among inorganic semiconductors. Since their discovery,[25] they have played a fundamental role in modern electronics, enabling many life-shaping technologies, as well as advances in transport, communications, manufacturing, engineering, medicine, energy, and industry. On the other hand – even if they only appeared 40 years later – [33,34] organic semiconductors (OSCs) have also gradually gained the attention of both academic and industrial research groups.

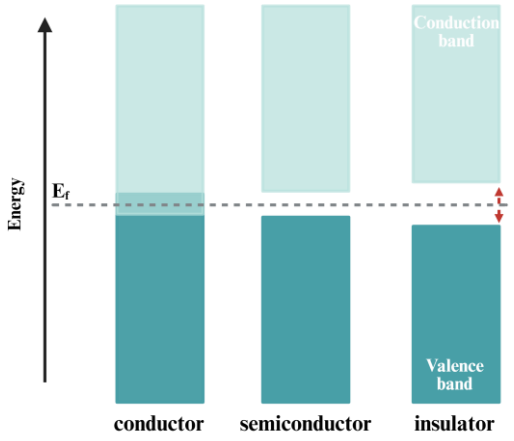

Figure 3. 2 *Schematic representation of conduction and valence band for insulators semiconductors and conductors, showing the different bandgap of the three types of materials. The Fermi level (Ef) is represented as a dotted grey line.*

The differences between these two classes of materials primarily lie in fundamental solid-state properties, such as their molecular structure. OSCs rely on the presence of weak dipole-dipole (Van Der Waals) interactions that bond organic molecules. They usually are amorphous or polycrystalline materials whose molecular arrangement differs from their inorganic counterparts, leading to different material properties, processing, and final application.[35] Inorganic compounds usually require harsh and expensive processing

conditions, such as high temperature and vacuum; milder processing procedures (spin coating, inkjet printing, laser printing, or vacuum deposition) are instead associated with organic materials, allowing material processing at or close to room temperature.[26] Rather than replacing inorganic semiconductors, organic ones are intended to supplement existing technologies and enable the development of new applications where the rigidity makes them inaccessible to silicon-based electronics.

3.1.3 Structure and electronic states of organic semiconductors

Organic semiconductors are carbon-based materials composed of π-conjugated molecules or polymers in which the overlap of delocalized π-electrons forms the foundation of their semiconducting behaviour. The conjugation arises from alternating single and double bonds along the molecular backbone, allowing π-electrons to delocalize across the structure and create an extended electronic system.[36] This delocalisation gives rise to discrete energy levels at the molecular scale, which, when the molecules are assembled in the solid state, broaden slightly to form electronic bands. However, because the molecules interact mainly through weak van der Waals forces rather than strong covalent bonds, the resulting bands are narrow, and charge carriers remain partially localised.[37]

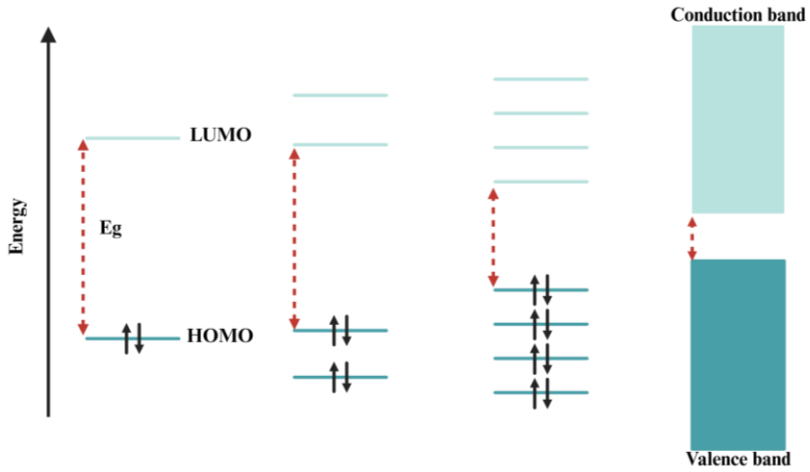

Figure 3. 3 *Distribution of the electronic states of a polymer as a function of its conjugated double bonds, where valence and conduction bands constitute the limit case. The reduction of Eg is represented by red harrows.*

The electronic structure of organic semiconductors (**Figure 3.3**) is defined by two fundamental energy levels known as the frontier molecular orbitals (FOMs): the highest occupied molecular orbital (HOMO) and the lowest unoccupied molecular orbital (LUMO). These levels are the molecular analogues of the valence and conduction bands in inorganic semiconductors.[38] The energy difference between them is denoted as Energy gap (E_g) and described in *Equation (3.1)*

$$E_g = E_{\mathrm{LUMO}} - E_{\mathrm{HOMO}} \quad (3.1)$$

E_g determines the optical absorption threshold and the electrical conductivity of the material. Typically, this band gap lies between 1.5 and 3 eV, depending on the degree of conjugation and the chemical nature of the molecule. The position of the HOMO and LUMO relative to the vacuum level is crucial for charge injection and transport. The HOMO energy defines the ionisation potential (IP), while the LUMO corresponds to the electron affinity (EA). Efficient operation in devices such as OFETs, OPVs, or OLEDs requires proper alignment of these levels with the work functions of the electrodes to minimise energy barriers for carrier injection. By chemical design – such as introducing electron-donating or -withdrawing groups, extending the π-conjugated core, or modifying side chains – the frontier orbitals can be systematically tuned, allowing precise control over the material's electronic properties.[25]

3.1.4 p-Type and n-Type organic semiconductors

Similar to inorganic semiconductors, organic materials are classified as p-type or n-type depending on the predominant charge carrier responsible for conduction. The application of an electric field modulates the electronic state of the material, typically by adding or removing electrons to alter the charge carrier density and enable charge transport. In this context, polymers that transport electrons are referred to as n-type materials, whereas those that transport holes are classified as p-type materials.[39] Their behaviour is primarily determined by the relative positions of the HOMO and LUMO energy levels and their alignment with respect to the electrode work functions and the Fermi Energy level (E_f) (**Figure 3.4**).[40]

p-Type organic semiconductors are characterised by a high-lying HOMO level, typically around –5.0 eV with respect to vacuum, which facilitates hole injection from high-work-function electrodes (e.g., gold or PEDOT:PSS). Charge transport in these materials occurs predominantly through the removal of electrons (i.e., the movement of holes) within the HOMO manifold.[37]

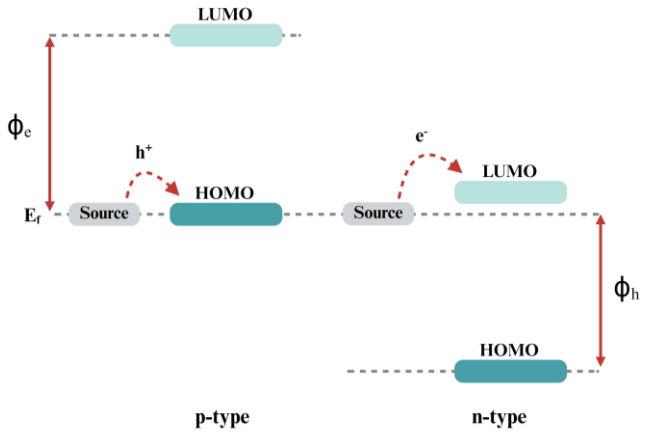

Figure 3. 4 *A schematic representation of the relationships among the Fermi energy (Ef) of the source electrode, the frontier energies of the organic semiconductor, and the polarity of the majority charge carriers, where ϕ_e and ϕ_h denote the electron and hole injection barrier heights, adapted from Quinn et al.[41]© American Chemical Society.*

Conversely, n-type organic semiconductors exhibit a low-lying LUMO level, generally below –3.8 eV, which facilitates electron injection from low-work-function metals (e.g., calcium, aluminium, or barium). Charge transport occurs through the addition of electrons into the LUMO. p-Type semiconductors are often more stable in ambient conditions (since holes are less susceptible to trapping by oxygen or water), on the other hand, n-type materials are often more sensitive to air and moisture due to oxidation of the injected electrons or degradation of the LUMO level alignment. The advancement of n-type polymer semiconductors has traditionally lagged behind that of their p-type counterparts. This disparity arises because p-channel polymers more readily achieve the delicate balance between solubility and strong π–π stacking interactions required for efficient charge transport and high device performance. In contrast, the design of n-type polymers faces additional challenges: to enable low-cost, solution-based processing under ambient conditions, these materials must remain soluble in conventional organic solvents while exhibiting a sufficiently high EA to minimize electron trapping by environmental species such as O_2, H_2O, and OH^-.[42]

Interestingly, some organic semiconductors exhibit ambipolar behaviour, supporting both hole and electron transport under appropriate bias conditions or electrode configurations.

3.1.5 Small molecule versus polymeric organic semiconductors

Organic semiconductors can be broadly divided into two structural classes: small-molecule and polymeric semiconductors. Although both rely on π-conjugation to enable charge transport, their physical structures, processing methods, and electronic behaviours differ markedly. Small-molecule semiconductors are composed of discrete, low-molecular-weight compounds that often crystallise into well-defined molecular lattices (**Figure 3.5**). Their electronic and optical properties are highly reproducible and can be studied with precision because of their structural uniformity.[43] When deposited by thermal evaporation or solution processes followed by controlled crystallisation, these materials can form highly ordered thin films with efficient π–π stacking interactions.[44] As a result, small-molecule semiconductors, exhibit very high charge carrier mobilities, sometimes exceeding 10 $cm^2/V{\cdot}s$ in single-crystal or epitaxial films. However, their brittleness and the tendency to form grain boundaries in polycrystalline films can limit their mechanical flexibility and long-term stability.[45,46]

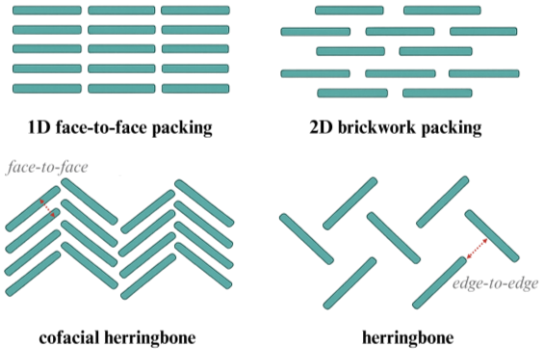

Figure 3. 5 *Typical small-molecule packing motifs and π-electron overlap states. (a) herringbone packing motifs without face-to-face p–p overlap, (b) herringbone packing motifs with slipped face-to-face p–p stacking and (c) lamellar stacking motifs with one-dimensional (1D) charge carrier channel; (d) brickwork arrangements providing two-dimensional percolation paths for charge-carrier transport*

In contrast, because of their long molecular chains and intra and intermolecular interaction, polymeric semiconductors cannot achieve ideal ordered molecular stacking; they instead consist of long π-conjugated chains that can form semi-crystalline or amorphous films

depending on the processing conditions. Typical crystalline packing in semicrystalline conjugated polymers involves ordered lamellae composed of co-facially stacked molecules that exhibit strong π-orbital overlap (**Figure 3.6**).[47]

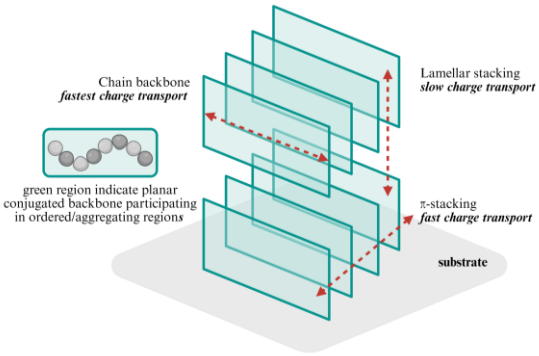

Figure 3. 6 *Typical π-π edge-on packing observed for classic semicrystalline polymers. The three main charge transport directions are shown with red dotted arrow*

Even when optimized for high performance, conjugated polymers inherently retain a considerable degree of lattice and energetic disorder, independent of their specific chemical composition or crystallinity. This disorder leads to electronic localization within π–π stacked molecular aggregates and the formation of trap states that limit carrier mobility. The relationship between local structural order and macroscopic transport properties thus defines a fundamental structure-property correlation in organic semiconductors.(**Figure 3.6**).[48]

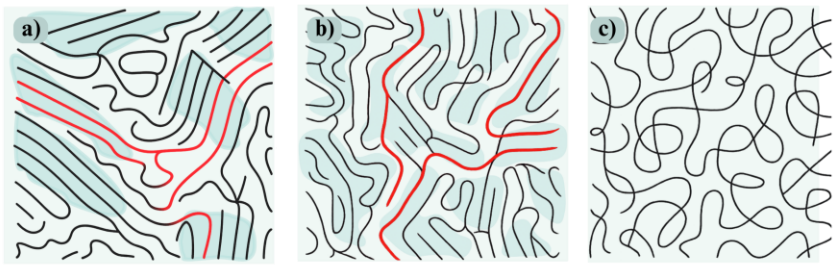

Figure 3. 7 *Graphic representation of the microstructure of a variety of polymeric materials. (a) Semi-crystalline polymer, (b) partial order due to short-range aggregates and (c) an amorphous structure. The darker green shading indicates ordered regions, and long polymer chains, indicated in red, represent clear "paths" for charge transport, significantly improving charge transport; adapted from Noriega et al.*[47] *© American Chemical Society*

In semicrystalline conjugated polymers, charge transport is primarily mediated through ordered π–stacked domains, where efficient intermolecular coupling enables delocalization

of charge carriers. In contrast, amorphous regions, characterized by disrupted conjugation and larger energetic gaps, act as barriers to carrier motion. Effective transport requires the formation of an interconnected network of ordered aggregates, often linked by semiflexible chain segments that preserve partial conjugation and serve as *tie-molecules*. These structural connections facilitate charge percolation across the material, ensuring continuous pathways for transport. As a result, the electronic performance of conjugated polymers is governed predominantly by the degree of π–π stacking, aggregate connectivity, and energetic disorder within the ordered domains, rather than by the amorphous matrix.[47]

3.1.6 Charge Transport in Organic Semiconductor Thin Films

As already mentioned, charge transport in organic semiconductors is a complex phenomenon determined by both the intrinsic electronic properties of the molecules and their spatial arrangement within thin films. Unlike crystalline inorganic semiconductors, where carriers can move freely within wide electronic bands, organic materials exhibit partially localised charge carriers due to weak intermolecular interactions and the discrete nature of molecular orbitals. As a result, the efficiency of charge transport is strongly influenced by the film's microstructure and morphology.[28,47]

Electrical Conductivity and Current Density

The electrical conductivity (σ) and current density (J) are fundamental parameters describing the macroscopic electrical behaviour of organic semiconductors and provide a bridge between microscopic charge transport mechanisms and device performance.[26] σ quantifies how easily charges move through the material under an applied electric field and is defined by *Equation (3.2)*

$$\sigma = qn\mu \quad (3.2)$$

Where q is the elementary charge, n the carrier density, and μ the carrier mobility. J represents instead the current flowing per unit area and is expressed by *Equation (3.3)*

$$J = \sigma E = qn\mu E \quad (3.3)$$

with E being the applied electric field. These relations reveal that both σ and Jdepend critically on the carrier density and mobility, which are governed by the molecular packing, degree of crystallinity, and presence of traps within the film. Highly ordered, π-stacked structures facilitate efficient charge percolation and thus yield higher conductivity and current density, whereas disordered or trap-rich morphologies hinder transport.

Mechanisms of Charge Transport

The movement of charges in organic semiconductors primarily occurs through two complementary mechanisms: (1) hopping and (2) band-like transport (**Figure 3.8**).

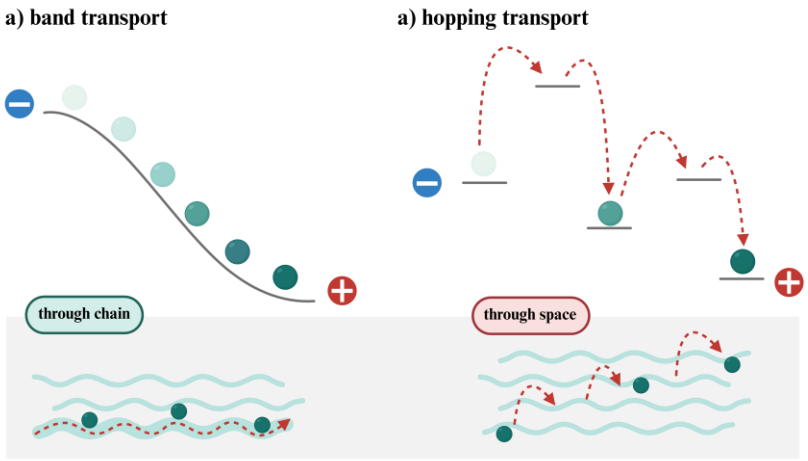

Figure 3. 8 *Cartoon representing the two different mechanisms of charge transport: a) band-like transport and b) hopping transport*

In regions of disorder or amorphous material, transport occurs predominantly through thermally activated hopping between localised molecular sites. The probability of a carrier successfully hopping from one site to another depends on several factors, including the energy difference between donor and acceptor sites, the distance separating them, and the relative orientation of the π-conjugated systems.[49] This process is highly sensitive to energetic disorder and the presence of trap states, which can temporarily immobilise carriers and reduce overall mobility. In contrast, in highly ordered crystalline domains, charges may become delocalized over several molecules, allowing for a more band-like transport (**Figure**

3.9). Although the resulting mobilities are lower than in typical inorganic semiconductors, they are significantly higher than in disordered regions and are critical for achieving high-performance device behaviour.[50]

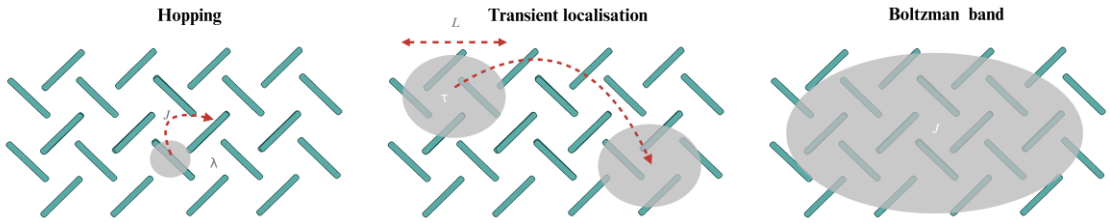

Figure 3. 9 *Schematic representation of the charge transport mechanism taking place in the hopping, transient localisation, and Boltzmann band model. The orange areas represent the charge delocalisation.*

Beyond these basic mechanisms, other factors also modulate charge transport in organic films. Traps arising from structural defects, chemical impurities, or grain boundaries can capture carriers, while local polarisation effects, such as polaron formation, alter site energies and hopping rates. Furthermore, hopping is thermally activated: the probability of a carrier moving from one site to the next increases with temperature, reflecting the energetic barriers inherent to the disordered molecular landscape.

Thin-Film Morphology

The morphology of the thin film is a primary determinant of transport properties. Small-molecule and polymeric semiconductors behave differently due to their distinct molecular architectures and packing tendencies. Deposition methods, including thermal evaporation, spin coating, and printing, as well as post-deposition treatments such as thermal or solvent annealing, significantly influence the resulting microstructure.[31] Highly crystalline domains provide pathways for quasi-delocalized transport, while the connectivity between these domains and the surrounding amorphous regions determines whether charges can traverse the film efficiently. In polymers, the alignment of the polymer backbones relative to the substrate – often described in terms of edge-on or face-on orientation, has a pronounced effect on in-plane mobility.[41] Similarly, in blended or mixed systems, the size and distribution of domains, as well as the degree of phase separation, govern the formation of

continuous pathways for both electrons and holes.[51] Ultimately, the morphology of organic thin films shapes the delicate balance between band-like transport in ordered regions and hopping in disordered domains, and it is this balance that defines the effective mobility and device performance. Optimising film morphology through careful molecular design, controlled processing, and post-deposition treatments is therefore essential for achieving the high performance required in organic electronic devices.

3.1.7 Organic Field Effect Transistors

Organic Field-Effect Transistors (OFETs) represent a fundamental class of devices in organic electronics, enabling the controlled modulation of current through an organic semiconductor channel by means of an external electric field. Their operation relies on the same basic principles as conventional inorganic FETs, but the use of π-conjugated small molecules or polymers introduces distinct electronic and structural considerations that influence device performance (**Figure 3.10**).

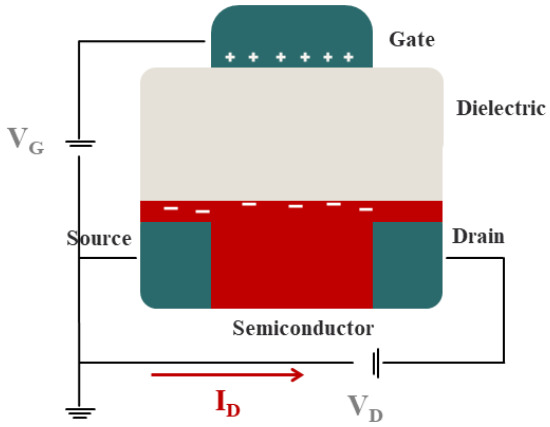

Figure 3. 10 *Schematic representation of an OFET having a top gate – bottom contact configuration*

An OFET is typically composed of four terminals: the source, the drain, the gate, and the gate dielectric. The organic semiconductor forms a thin channel between the source and drain electrodes, while the gate electrode modulates the charge density within this channel via the insulating dielectric layer. By applying a voltage between the gate and source, an electric field is established that induces charge carriers (holes in p-type or electrons in n-type materials) in the semiconductor, thereby enabling current to flow between source and drain.

The magnitude of this current depends on the gate voltage, the mobility of carriers within the channel, and the structural quality of the organic layer.[26]

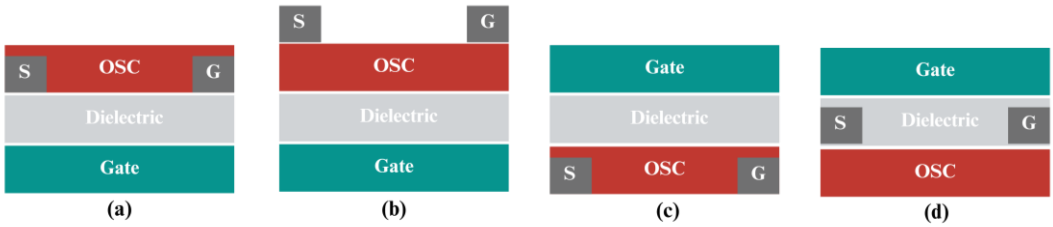

Figure 3. 11 *OFET device structures: (a) bottom gate, bottom contact, (b) bottom gate, top contact, (c) top gate, bottom contact, and (d) top gate, top contact.*

OFETs can adopt several architectural configurations, each with specific advantages and constraints (**Figure 3.11**):

a) Bottom-Gate, Bottom-Contact (**BGBC**): the gate electrode and dielectric lie beneath the organic semiconductor, with source and drain electrodes deposited on top of the dielectric. This architecture is common due to ease of fabrication and compatibility with standard substrates, although the deposition of the organic layer over pre-patterned electrodes can compromise the interface quality and limit contact efficiency.

b) Bottom-Gate, Top-Contact (**BGTC**): the organic semiconductor is deposited first, with source and drain electrodes subsequently evaporated or printed on top. This approach improves the contact interface and often leads to higher charge injection efficiency, but care must be taken to avoid damaging the organic layer during electrode deposition.

c) Top-Gate Configurations (**c**, **d**): the gate electrode and dielectric are deposited on top of the organic semiconductor, while the source and drain contacts reside below. Top-gate devices can offer improved dielectric/semiconductor interfaces and allow for flexible or laminated device structures, although deposition of the gate stack may require low-temperature or solution-processable dielectrics to preserve the organic layer.

The operation of an OFET can be divided into several regimes. At low source-drain voltage, the device behaves in the linear regime, where the current increases proportionally with voltage. As the source-drain voltage exceeds the gate overdrive, the channel near the drain becomes pinched off, entering the saturation regime, where the current reaches a nearly

constant value. The performance metrics of OFETs – most notably the field-effect mobility, threshold voltage, and on/off current ratio – depend sensitively on the intrinsic mobility of the organic semiconductor, the quality of the semiconductor/dielectric interface, and the morphology of the thin film.

3.1.8 Performance Parameters in OFETs

A comprehensive understanding of OFETs performance requires careful evaluation of several interrelated parameters that govern the device's electrical response and its overall functionality. Among these, the field-effect mobility (a), the threshold voltage (b) and the on/off current ratio (c), play a central role. Each of these quantities encapsulates distinct aspects of charge injection, transport, and accumulation within the organic channel.

Field-Effect Mobility (μ) (a)

The field-effect mobility represents the effective charge carrier mobility within the accumulation channel under the influence of the applied gate electric field. It quantifies how efficiently carriers move laterally between the source and drain electrodes and serves as a key figure of merit for comparing materials and device architectures. In ideal crystalline semiconductors, mobility is a material constant determined by band structure and scattering processes. However, in organic semiconductors, it depends strongly on extrinsic factors such as film morphology, trap density, and the dielectric interface. Experimentally, mobility is extracted from the slope of the transfer curve or output characteristics using analytical.

Threshold Voltage (V_t) (b)

The threshold voltage defines the gate bias required to induce a conducting channel at the dielectric/semiconductor interface. It reflects both the intrinsic energy level alignment between the semiconductor and the dielectric and the presence of traps, dipoles, or fixed charges within the gate dielectric or at its interface. In organic transistors, V_t is often shifted from its ideal value due to charge trapping or dipolar disorder in polymeric dielectrics.

On/Off Current Ratio (c)

The on/off ratio – the ratio between the maximum current in the "on" state and the residual leakage current in the "off" state – is a direct indicator of the transistor's ability to switch between conductive and non-conductive states. High on/off ratios (typically 10^4 - 10^7) are desired. However, organic semiconductors often exhibit lower ratios compared to crystalline silicon due to trap-mediated leakage, subthreshold conduction, and thermally activated charge carriers that persist even in the nominally "off" state. The off-state current is particularly sensitive to the quality of the dielectric/semiconductor interface, the presence of pinholes in the semiconductor film, and the degree of molecular ordering. In addition, impurities, unintentional doping, and oxygen or water absorption can introduce shallow trap states that contribute to leakage. Therefore, encapsulation, interface cleaning, and the use of hydrophobic dielectric surfaces are critical to suppress off-state currents and achieve sharp switching characteristics.[26]

3.1.9 Carotenoids as edible organic semiconductor: literature background

Carotenoids represent one of the most promising families of edible organic semiconductors owing to their natural abundance, biocompatibility, and intrinsic π-conjugated electronic structure.[19] These pigments – such as β-carotene, lycopene, bixin, fucoxanthin, and astaxanthin – exhibit extended polyene backbones with alternating single and double bonds, enabling delocalisation of π-electrons and facilitating charge transport along the molecular chain (**Figure 3.12**). They are of notable interest due to their documented high single-molecule conductance, photoinduced charge transfer, and known degradation pathways.

Early studies demonstrated that solid films of carotenoid polyenes display semiconducting behaviour[20], with reported hole mobilities in the range of 10^{-6} – 10^{-4} $cm^2V^{-1}s^{-1}$, thereby confirming their potential as p-type materials. Subsequent experimental and theoretical works have elucidated their optoelectronic characteristics, showing HOMO-LUMO gaps between 1.8 and 2.5 eV and strong photo absorption in the visible range.[52] These attributes make carotenoids suitable candidates for organic OFETs, organic photovoltaics (OPVs), and

dye-sensitised solar cells (DSSCs), where they can serve as light-harvesting or charge-transporting components.[53,54]

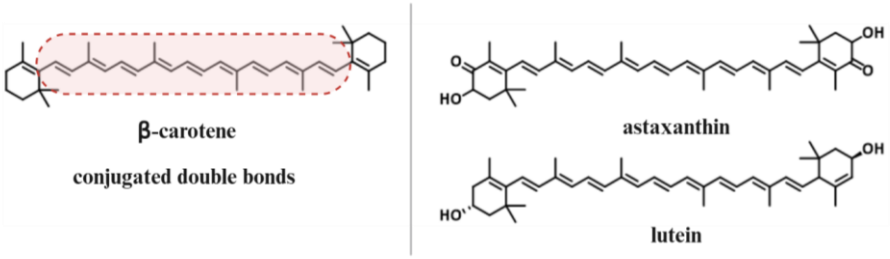

Figure 3. 12 *Chemical structure of three carotenoids: β-carotene, and its derivatives, astaxanthin and lutein; the conjugated double bonds are highlighted in red*

Beyond their electronic properties, carotenoids possess unique advantages for edible and sustainable device architectures. Being naturally occurring food pigments with established nutritional roles and low toxicity, many carotenoids are classified as Generally Recognised As Safe (GRAS), aligning them with the material requirements for edible electronics. Computational investigations further support their environmental and physiological safety, while highlighting the tunability of their electronic levels through molecular length and functionalization. Carotenoids thus embody the intersection of biology and electronics – natural molecules capable of mediating charge transport within systems that are both functional and ingestible, thereby providing a step forward for the next generation of fully edible semiconducting materials.

3.2 Aim of the work

The aim of this work is to explore and advance the use of carotenoids, specifically astaxanthin and its derivatives, as edible organic semiconductors for application in sustainable and bio-derived electronic devices. Within the broader framework of edible electronics, carotenoids offer a unique combination of natural origin, biocompatibility, and intrinsic π-conjugated structures capable of supporting charge transport. However, despite these advantages, their practical implementation in OFETs remains limited by inherent drawbacks such as chemical instability, poor solubility, and morphological disorder in the solid state. To address these challenges, this work builds upon the experimental results obtained within the ELFO project at the *Istituto Italiano di Tecnologia (iit)*, focusing on astaxanthin as a model compound. The research is articulated into three main objectives: (1) Characterisation of pristine astaxanthin to establish its intrinsic structural, thermal, and electronic properties, and to assess its performance as a semiconducting layer in OFETs; (2) Design and synthesis of functional derivatives of astaxanthin through controlled chemical modification, aimed at enhancing its solubility, stability, and processability while preserving its π-conjugated electronic framework. This includes both *temporary functionalisation* (via silyl protection) and *permanent modification* (through hydrazone formation); (3) Development of polymeric architectures incorporating astaxanthin to improve solid-state organisation, suppress degradation pathways, and achieve enhanced mechanical and environmental stability.

3.3 Results and discussion

3.3.1 Operative background

Before proceeding with the chemical modification, it was essential to study the pristine material to gain a comprehensive understanding of its intrinsic properties. Astaxanthin characterisation was therefore performed to evaluate its behaviour and suitability as a semiconductor for OFETs. Establishing the performance of astaxanthin is crucial for assessing how structural modifications may influence its stability, morphology, and electronic performance when used as a semiconducting layer.

Film morphology and annealing influence

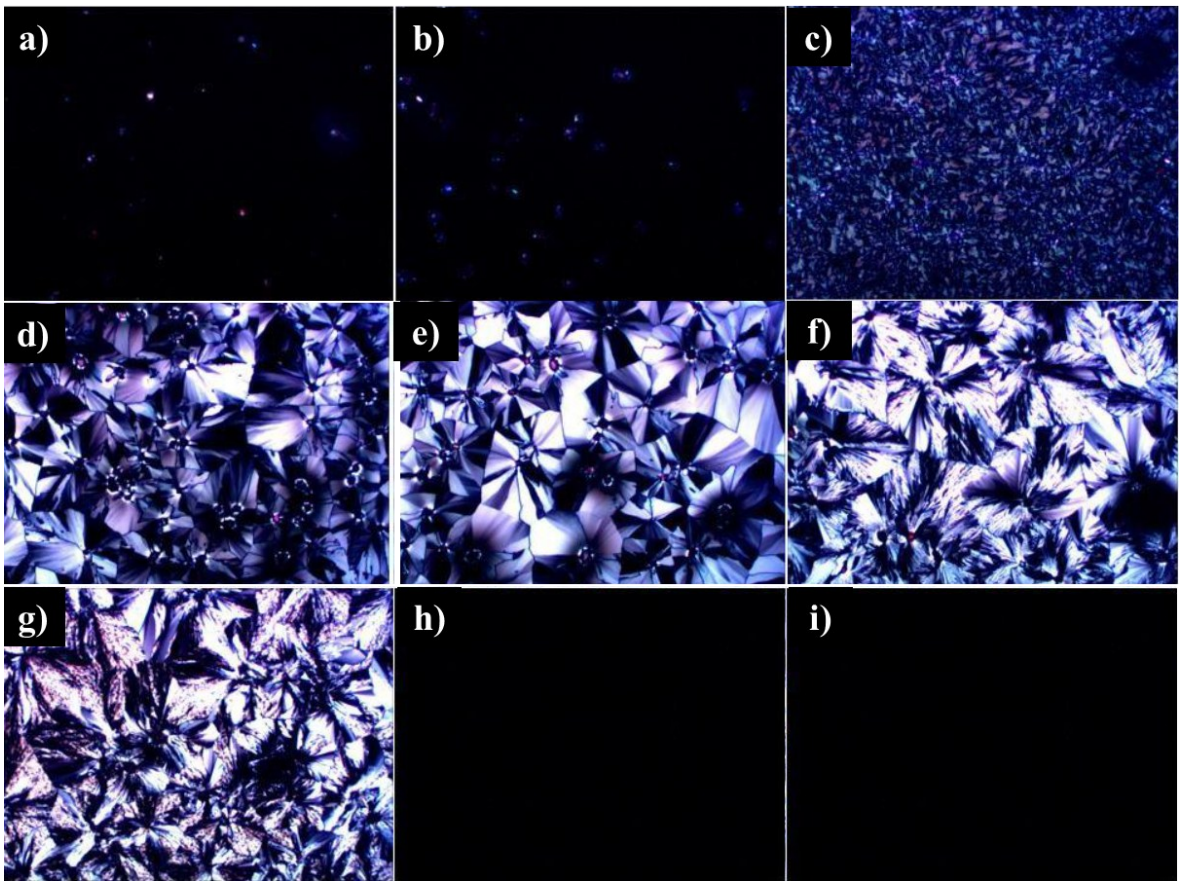

Figure 3. 13 *Astaxanthin micrographs after thermal annealing, under polarised light. (a) as casted, (b) 60 °C, (c) 80 °C, (d) 100 °C, (e) 120 °C, (f) 160 °C, (g) 180 °C, (h) 200°C, (i) 220 °C*

Figure 3.13 reports polarised optical micrographs of astaxanthin thin films spin-coated from THF solutions and subsequently annealed at different temperatures. Polarised light microscopy enables the observation of optical anisotropy associated with birefringence, although it does not directly quantify the degree of crystallinity. As shown in **Figure 3.13**, thermal annealing strongly influenced the morphology and optical response of the films. The as-cast film exhibited no significant polarisation of transmitted light, suggesting a predominantly amorphous morphology. Upon annealing at 120 °C, the highest degree of birefringence was observed, indicating the formation of larger and more ordered crystalline domains. At temperatures above this threshold, however, birefringence decreased, consistent with partial degradation or disruption of the crystal structure. The observed increase in the size and coherence of polarised regions with temperature can be interpreted as evidence of thermally induced crystal growth. These results demonstrate that, despite its known susceptibility to degradation, astaxanthin remains stable up to approximately 120 °C, and under these conditions, improved molecular ordering can be achieved, a crucial factor for efficient charge transport in carotenoid-based OFETs.

Astaxanthin-based OFETs

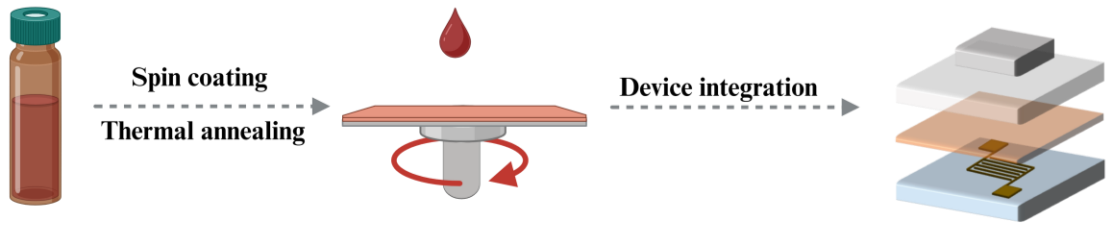

Figure 3. 14 *Workflow for the production of a β-carotene-based OFET*

In the context of developing edible organic electronics, the Istituto Italiano di Tecnologia (iit) provided experimental results concerning the charge carrier mobility of astaxanthin in OFET devices. **Figure 3.14** schematically illustrates the fabrication steps of an OFET based on β-carotene, used here as a structural reference. β-Carotene was first dissolved in tetrahydrofuran (THF) and spin-coated onto a substrate to form a thin semiconducting film. The substrate consisted of glass coated with gold electrodes, which served as the source (S)

and drain (D) contacts for applying the gate potential. On top of the semiconductor layer, a Teflon film was deposited as the insulating dielectric, followed by an aluminium gate (G) contact. These transistors are typically configured in bottom-gate/bottom-contact (BGBC) or bottom-gate/top-contact (BGTC) geometries, which facilitate straightforward deposition of the semiconducting layer for rapid device screening. In contrast, top-gate architectures (TGBC or TGTC) are generally employed in final devices to better protect the active layer and ensure longer operational stability. Following the same fabrication strategy, an astaxanthin-based OFET was prepared and characterised under identical conditions. The as-cast astaxanthin film appeared amorphous, but upon thermal annealing under an inert atmosphere at 100 °C, small crystalline domains became visible. Electrical measurements for both pristine and annealed samples are shown in **Graph 3.15**. The device based on astaxanthin exhibited significant performance improvement after thermal treatment.

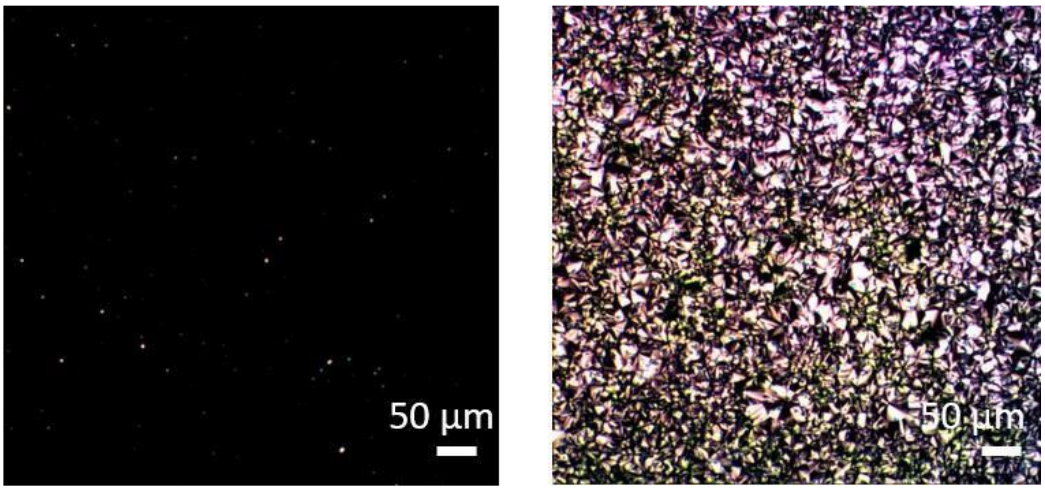

Figure 3. 15 *Optical micrographs under polarised light of astaxanthin spin-coated from THF solution. (left) pristine, (right) after annealing at 100°C.*

Prior to annealing, the amorphous thin film showed low current modulation and poor semiconducting behaviour. As reported in **Graph 3.1**, the I_{DS} vs V_{GS} transfer curves revealed a current on/off ratio of less than 10^3, indicating limited charge carrier transport. After annealing, the on/off ratio increased dramatically to values close to 10^6, consistent with the formation of a more ordered and crystalline semiconducting layer.

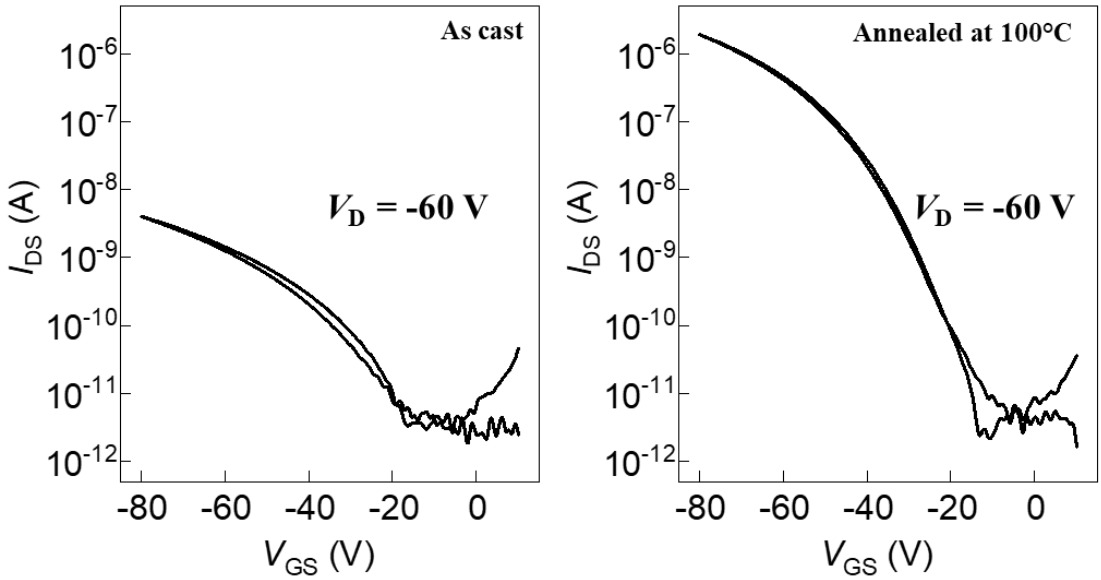

Graph 3. 1 *Drain-source current behaviour varying gate potential, (left) for pristine astaxanthin, (right) after thermal annealing at 100°C*

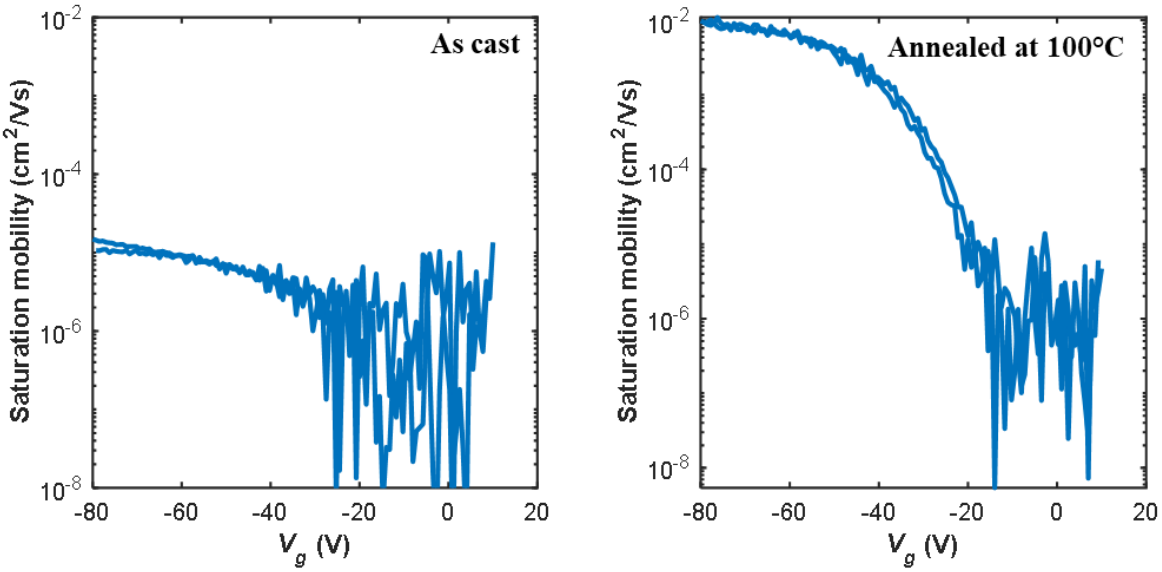

Graph 3. 2 *Saturation mobility measurement as a function of gate potential (left) for pristine astaxanthin, (right) after same thermal annealing.*

Similarly, the field-effect mobility (μ) (**Graph 3.2**) showed a substantial increase after annealing, reaching values around 10^{-2} cm^2 V^{-1} s^{-1}, comparable to those observed for β-carotene under similar conditions. The thermal treatment thus plays a crucial role in enhancing the electrical performance of astaxanthin by promoting crystal growth and improving molecular ordering, both of which facilitate more efficient charge transport within the conjugated π-system.

3.3.2 Protective Functionalization of Astaxanthin for Solution Processing

After establishing the solid-state properties of astaxanthin and its behaviour when incorporated into an OFET, we tried different strategies to overcome the aforementioned limitations. The first one was focused on the reversible derivatisation of astaxanthin through the protection of its hydroxyl groups with trialkyl silyl (SiR_3) moieties. This modification was intended to improve solubility in common organic solvents, thereby facilitating solution-based film deposition techniques such as spin coating. Given the well-known liability of some silyl protecting groups, a processing strategy was envisioned in which film formation is followed by thermal annealing to *in situ* remove the protective group. This approach can not only restore the native carotenoid in the final film but can also provide an opportunity to investigate how the initial presence and subsequent removal of the protective groups affect film crystallisation and morphology. The following sections detail the synthesis of two silyl-protected derivatives and provide a foundation for understanding their solubility, processability, and structural characteristics.

3.3.2.1 Synthetic Strategy and Reaction Optimisation

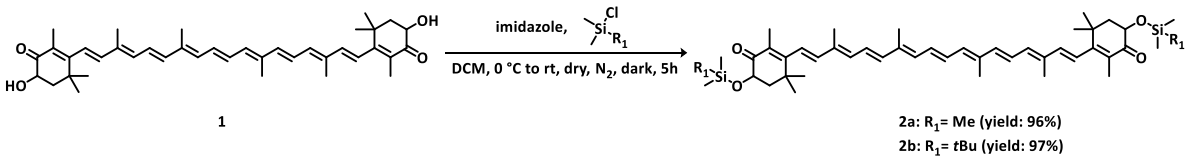

Scheme 3. 1 *Optimised reaction path for the obtainment of the -OSiR₃ derivative of t-astaxanthin, using TMS and TBDMS as silylating agents and imidazole as a mild base*

The synthesis of O-protected derivatives of *t*-astaxanthin (**1**) was first attempted using hexamethyldisilazane (HMDS) as the silylating agent. However, the reaction proceeded with very low conversion, and the desired silylated product could not be isolated in pure form. This observation suggested that the reactivity of HMDS under the employed conditions was insufficient to achieve full derivatisation of the hydroxyl groups, prompting the investigation of alternative silylating agents. Subsequently, trimethylsilyl chloride (TMSCl) and tert-butyldimethylsilyl chloride (TBDMSCl) were selected, both in the presence of imidazole as a base (**Scheme 3.1**). They were found to allow a substantial improvement in terms of

reactivity. Under optimised conditions (anhydrous environment, inert atmosphere and absence of light), both reagents successfully converted trans-astaxanthin into the corresponding O-silylated derivatives with excellent yields, 96% for the TMS-protected (**2a**), and 97% for the TBDMS-protected compound (**2b**).

During the optimisation process, the work-up procedure emerged as a critical factor in obtaining pure products. Initial attempts to remove excess imidazole through flash chromatography or extraction with slightly basic water (pH 7.5) both led to rapid partial deprotection of the silyl groups, confirming the extreme moisture and silica sensitivity of the protected carotenoids. It became evident that any aqueous work-up was incompatible with the integrity of the silyl-protected moieties. To circumvent this issue, non-aqueous purification routes were explored. Reprecipitation from anhydrous isopropanol enabled the removal of imidazole but resulted in significant material loss. Ultimately, precipitation from acetonitrile proved to be the most effective approach, providing clean products in high yield and with excellent reproducibility.

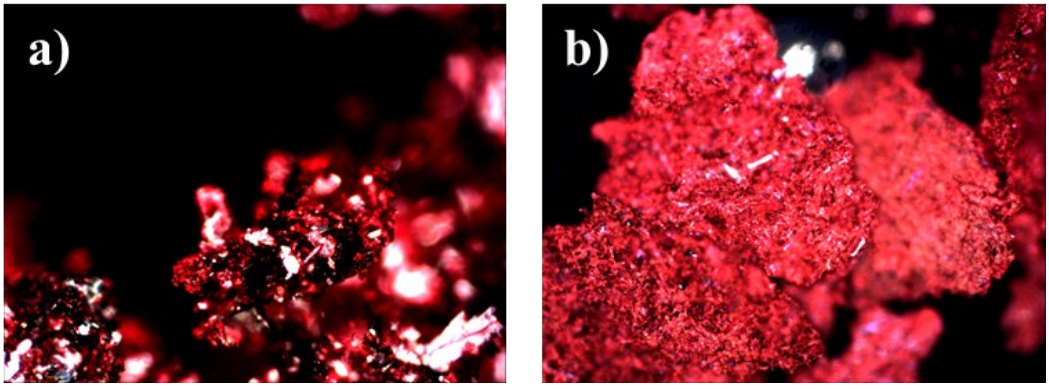

Figure 3. 16 *Optical micrograph under polarised light of the two derivatives a)* ***2a*** *and b)* ***2b*** *in the form of powder showing a highly crystalline morphology*

The degree of anhydricity of the solvent was not surprisingly crucial and dependent on the nature of the protecting group. For the TMS-protected derivative (**2a**), the use of rigorously anhydrous acetonitrile was necessary to prevent hydrolysis during isolation, whereas for the more stable TBDMS analogue (**2b**), non-anhydrous acetonitrile was employed without compromising the integrity of the protection.

Both compounds were obtained as fine crystalline powders (**Figure 3.12**) and exhibited remarkable stability under an inert atmosphere at –32 °C for extended periods. The integrity of the conjugated π-system was preserved by minimising the time the material remained in solution, thereby limiting potential degradation of the polyene backbone. The chemical stability of the conjugated framework after protection and isolation was confirmed by ^{1}H NMR analysis, which showed no evidence of isomerisation (*see experimental section for further information about NMR spectra*). Overall, the optimisation of both reaction and purification protocols enabled the reliable synthesis of two stable, silyl-protected astaxanthin derivatives.

3.3.2.2 Characterisation of Stability and Processing Behaviour

To gain a deeper understanding of the stability and behaviour of the synthesised silyl-protected astaxanthin derivatives, both in solution and in the solid state, a combination of optical and thermal characterisation techniques was employed. Absorption (ABS) spectroscopy in the UV-vis range was first used to investigate the properties of the compounds in solution, to further ensure the preservation of the conjugated π-system after the functionalization. The spectral features, particularly the position and shape of the characteristic carotenoid absorption bands, can be an indicator of the molecular integrity, conjugation length, and possible aggregation[55]. Comparison between the protected and unprotected forms of astaxanthin allows assessment of how the introduction of silyl groups affects the ABS spectra profiles. The UV–Vis absorption spectrum of the silyl-protected astaxanthin derivatives in dichloromethane (DCM) exhibits a sharp and well-defined absorption band having a maximum at 483 nm (**Graph 3.3**). The λ_{max} of unprotected *t*-astaxanthin in the same solvent is 482 nm (**Graph 3.3** dotted red line) in excellent agreement with literature values for *all-trans* astaxanthin in nonpolar media.[56] The minimal redshift observed can be considered an experimental variability. As expected, the silyl protecting groups do not alter the electronic structure of the conjugated π-system.[57] No significant broadening or additional absorption bands are detected. This suggests that the silyl groups enhance the carotenoid solubility without promoting aggregation.

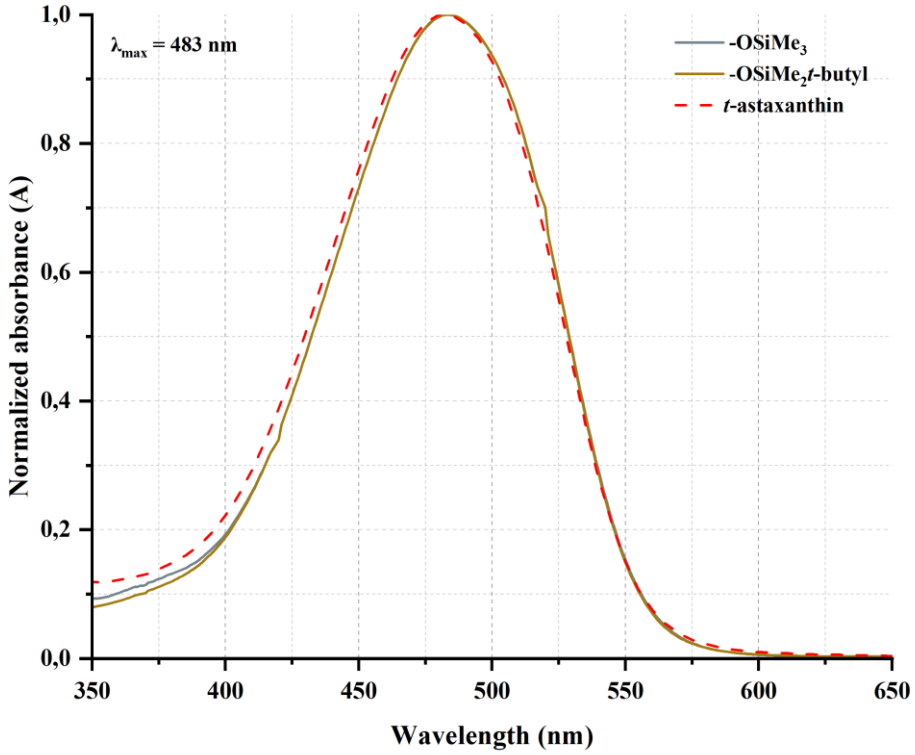

Graph 3. 3 *UV-Vis spectra acquired in the range 350-650 nm using DCM as solvent, showing the derivatives (**2a**) and (**2b**) having the same absorption profile and λ_{max} (483 nm) - $\lambda_{max\ astaxanthin}$ (482 nm)*

As reported by Bruijn et al.[58], cis-trans isomerisation of astaxanthin results in hypsochromic shifts and reduced band intensity due to a decrease in effective π-conjugation. The absence of such spectral features in our derivatives indicates that no significant cis-isomer formation has occurred. This observation is consistent with the synthetic procedure, purification and storage, minimising the exposure to oxygen and light. The preservation of the "all-trans" form is critical for maintaining the electronic structure of astaxanthin.

Thermogravimetric analysis (TGA) was then performed to evaluate the thermal stability of the silyl-protected derivatives and to determine the conditions required for removal of the protecting groups. TGA measurements were carried out both under nitrogen and in air, allowing differentiation between intrinsic thermal decomposition and oxidative processes associated with the presence of oxygen.

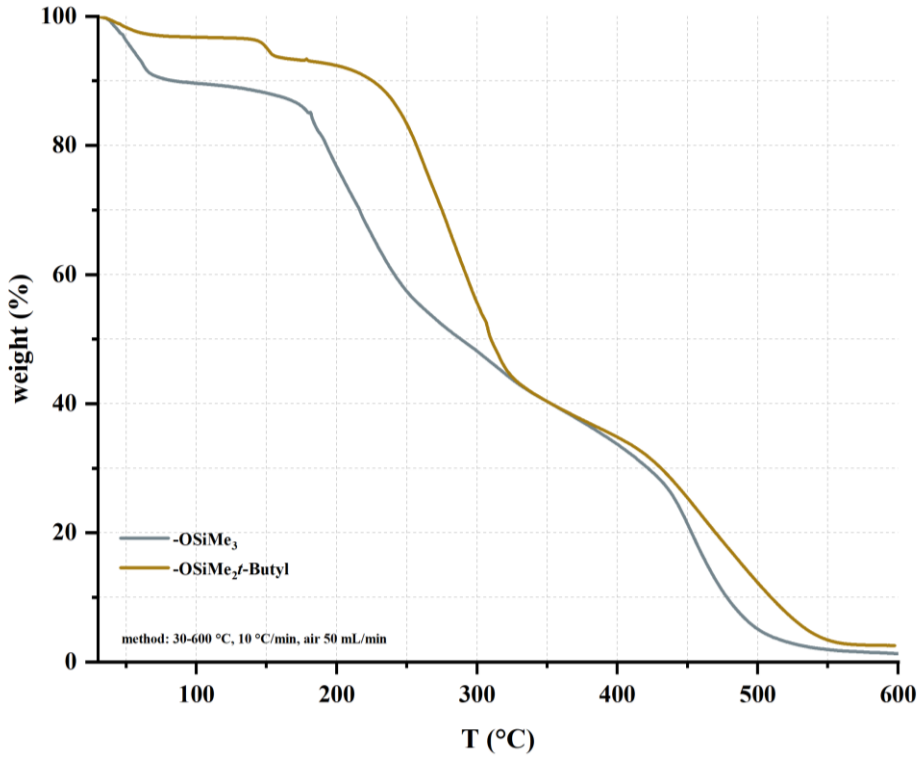

Graph 3. 4 *TGA curve of derivative (**2a**) (grey line) and (**2b**) (brown line) performed under air*

Graph 3.4 shows the TGA of (**2a**) (grey line) and (**2b**) (brown line) performed under air. In both samples, the first weight loss step is associated with the -OH deprotection. Both TMS- and TBDMS-protected derivatives exhibit a mass loss of approximately 10% during corresponding to the removal of the silyl protecting groups. Although the stoichiometric mass of two protecting groups would predict a larger weight loss, the TGA run under air shows an apparent loss smaller than the theoretical value (**Table 3.1**).

Derivative	Theoretical weight loss (%)	Effective weight loss (%)
2a	19,7	12
2b	27,9	9

Table 3. 1 *Comparison in between the theoretical and effective weight loss due to the removal of the protecting groups of derivatives (**2a**) and (**2b**)*

Rather than volatilizing cleanly, silyl fragments, in fact, are prone to oxidation and condensation, yielding Si-O-Si networks or silica-like species that remain in the solid residue.[59] Therefore, the net mass lost as volatile products is lower than the purely stoichiometric estimation.

TGA of the O-silylated derivatives of *t*-astaxanthin under nitrogen (**Graph 3.5**) show a gradual mass loss starting around 150 °C and extending up to 450 °C. Both (**2a**) and (**2b**) derivatives display similar overall profiles, with the TBDMS-protected compound exhibiting a slightly higher onset of degradation, consistent with the major thermal stability generally associated with bulkier silyl groups.

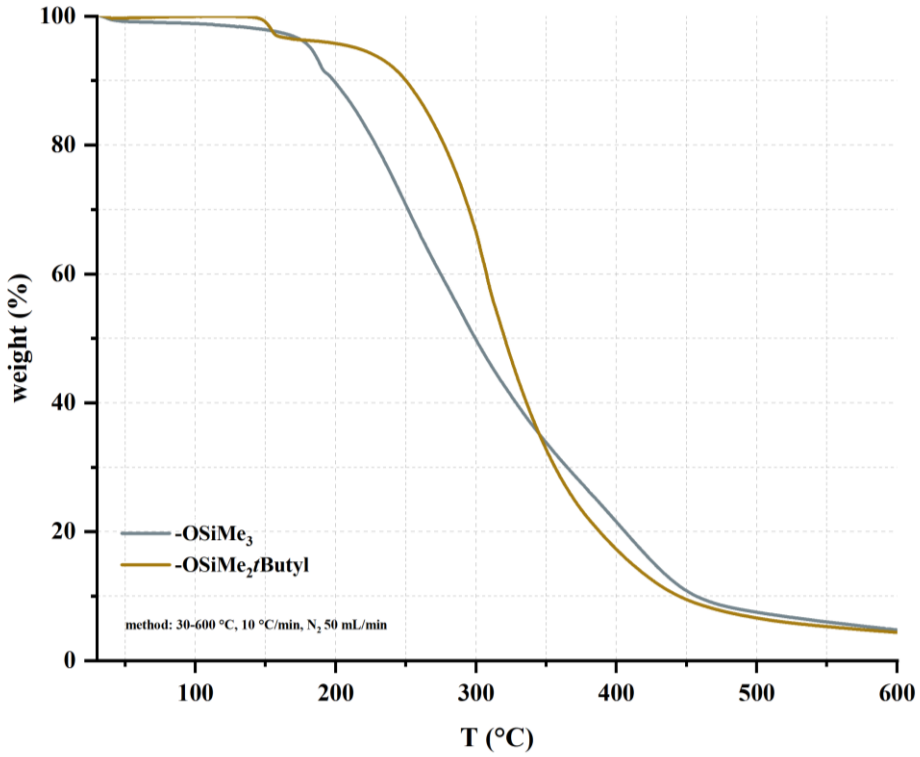

Graph 3. 5 *TGA curve of derivative (**2a**) (grey line) and (**2b**) (brown line) performed under nitrogen*

The total mass loss observed during the first step in both cases is lower than the theoretical value expected for complete volatilisation of the silyl protecting groups, suggesting that the process is not a pure, stepwise desilylation. McGeary et al.[60] study helps in the interpretation of the obtained result: under inert conditions, silyl-containing species evolve as silanols, further condensing to siloxanes.[61] This explains why TGA traces recorded under inert atmosphere show broader, less defined mass loss steps and higher residual mass compared with measurements in air, where oxidative combustion yields lower residual mass.

TGA profiles confirm that the derivatives are stable under the conditions usually required for spin-coating and subsequent thermal annealing (100 °C), and that the silyl groups can be

selectively removed without compromising the integrity of the astaxanthin π-conjugated system.

These results, in combination with the UV-Vis data showing preservation of the all-trans configuration, provide a solid basis for processing the derivatives into thin films with retained optical and electronic properties, suitable for application in OFET and EGOFET devices.

3.3.3 Permanent structural modification of t-astaxanthin for enhanced solubility and solid-state organisation

The synthesis of (3S,3′S)-3,3′-dihydroxy-4,4′-bis(diphenylhydrazono)-β,β-carotene (**3**) was designed to enhance the solubility of astaxanthin in processing solvents commonly used for thin-film fabrication, without introducing removable protecting groups (**Scheme 3.2**). Unlike silyl-protected derivatives, in which deprotection during thermal annealing is required to recover the native π-conjugated framework, the diphenylhydrazono modification represents a permanent structural alteration that remains intact throughout the film processing steps.

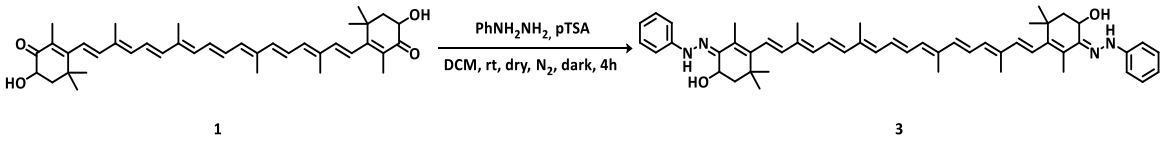

1 3

Scheme 3. 2 *Synthetic protocol for the obtainment of (3)*

The synthetic protocol, based on the condensation of trans-astaxanthin with phenylhydrazine in the presence of catalytic p-toluenesulfonic acid under reflux in anhydrous toluene, afforded the target compound in good yield (79%). The procedure ensures high purity by removing residual hydrazine and pTSA through filtration and brine washing, followed by drying under an inert atmosphere and low-temperature storage. From a processing point of view, the modification significantly improves solubility in organic solvents, which is a critical factor for obtaining homogeneous films via solution-based techniques, like spin-

coating. Moreover, as the structural modification is permanent, thermal treatments, if present, will not aim at removing protecting groups.

It is worth noting that the presence of bulky diphenylhydrazono groups may influence molecular packing in the solid state and, consequently, the morphology of films once fabricated. Although film formation has not yet been experimentally explored, preliminary consideration of the molecular structure suggests that steric effects and altered intermolecular interactions could affect crystallinity and film uniformity. These factors are highly relevant for future studies, as they can impact electronic properties in potential OFET applications. This highlights a complementary approach to removable protecting groups and creates a foundation for subsequent thin-film studies.

3.3.4 Polymerisation strategy to enhance the stability of astaxanthin-based conductive layer

The third strategy for the use of carotenoid-based materials as conductive layers in OFETs addresses the intrinsic instability of this class of molecules. As already stated, (*See chapter 3.1*) carotenoids, including astaxanthin, are highly sensitive to light, oxygen, and thermal stress, which limits their practical application in organic electronics. To enhance their stability, a natural progression of the project has been the exploration of their polymerisation. It is possible to reduce degradation pathways, improve oxidation resistance, and stabilise the π-conjugated backbone by embedding astaxanthin moieties into a polymeric framework. Additionally, polymerisation can enhance material processability and promote uniform film formation, both of which are advantageous for device fabrication. In the following sections, the synthesis and characterisation of two astaxanthin-based copolymers are presented, highlighting their structural design, optical properties, and potential implications for thin-film applications in OFET devices.

3.3.4.1 Preparation of Astaxanthin-Based Polymers

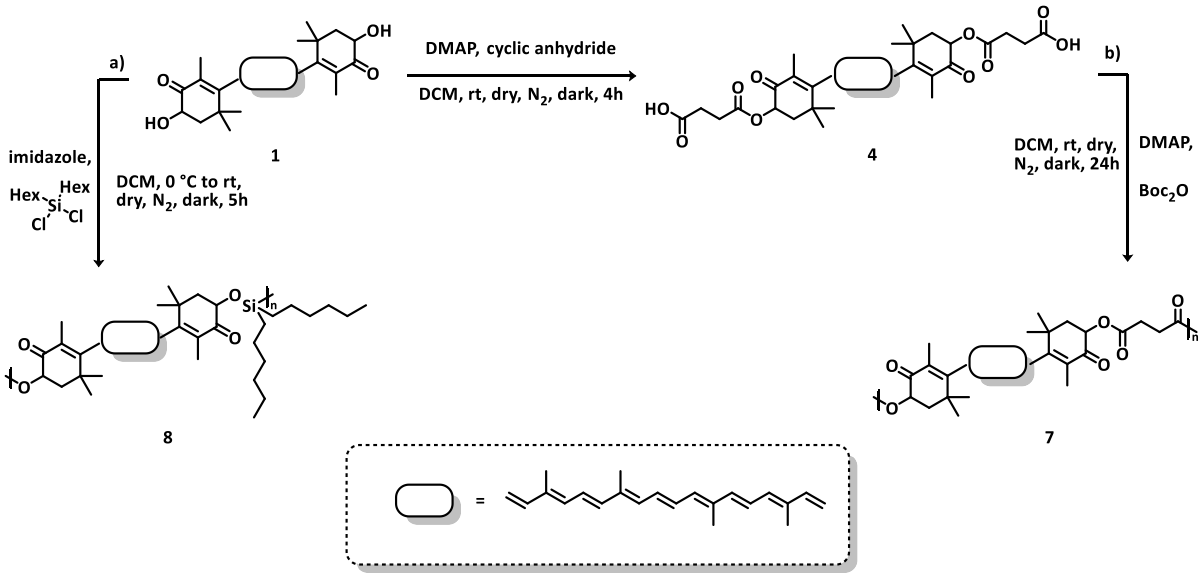

Scheme 3. 3 *Two different synthetic approaches for the obtainment of astaxanthin-containing copolymer; route a) is a straightforward copolymerization with a dialkylsilane, allowing for the introduction of linear chains in the macromolecular structure; route b) involves a two-step process allowing for the carotenoid polycondensation with succinic acid.*

Two complementary synthetic strategies were pursued to obtain astaxanthin-based polymers, addressing stability, functionalization, and potential biocompatibility in distinct ways. The first polymer (**7**) (**Scheme 3.3**, route b) was obtained via a two-step approach. A preliminary astaxanthin (**1**) functionalization with succinate groups (**4**) and subsequent polycondensation of the disuccinate derivative with pristine astaxanthin. The succinylation reaction proceeded efficiently under mild conditions using DMAP as a catalyst, with a quantitative yield (99%). In the second step, the disuccinate was copolymerized with native astaxanthin using di-tert-butyl dicarbonate (Boc_2O) as a coupling agent. Soxhlet purification was employed to remove unreacted monomers and shorter length chains, yielding a red solid. The choice of succinic anhydride as the functionalizing agent was deliberate: in addition to improving solubility and providing reactive functional groups for polymerisation, it allows the polymer to degrade post-use into succinic acid,[62] a naturally occurring and edible compound, and, of course, astaxanthin. This aspect introduces a potential advantage in terms of environmental safety and biocompatibility. Moreover, this polymer does not incorporate alkyl chains, which affects both its solubility profile and the overall microstructure of the

resulting polymer backbone. The second polymer was synthesised via a condensation reaction (**Scheme 3.3**, route a) between astaxanthin (**1**) and dichlorodihexylsilane. This approach introduces silane linkages along the polymer backbone, together with long alkyl chains. These chains are expected to influence solubility and morphology, potentially enhancing processability in organic solvents. The reaction was conducted at low temperature to preserve the carotenoid conjugated core. Importantly, this strategy was chosen to remain in line with the "-O protection" approach, minimising degradation during synthesis while incorporating hydrophobic units that could improve polymer stability in devices. These two synthetic strategies illustrate complementary approaches to designing astaxanthin-based polymers. Polymer (**7**) allows controlled polymer growth, without introducing long alkyl chains, and includes the additional benefit of environmentally benign degradation products. Polymer (**8**), in contrast, introduces hydrophobic alkyl chains via silane linkages, enhancing stability and processability while following a design strategy that preserves the carotenoid chromophore (no high-temperature treatment is involved in both synthesis and purification– *see experimental section for further information about purification*). Overall, these strategies highlight the importance of careful synthetic design to overcome the limitations of carotenoids. By selecting functionalization and polymerisation methods thoughtfully, it is possible to produce materials that enhance astaxanthin stability and processability, with (**7**) providing a rigid, biocompatible framework and (**8**) offering a hydrophobic, alkyl chain-containing structure.

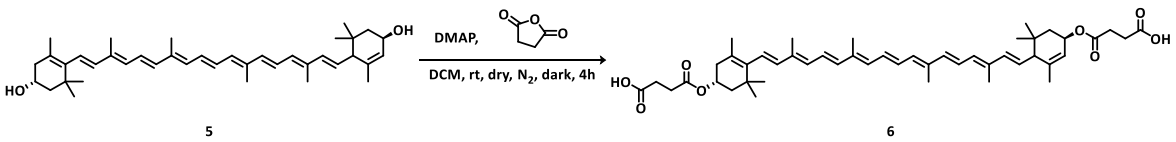

5 6

Scheme 3. 4 *Disuccination protocol performed on lutein (**5**) as starting material to prove the generality of the strategy*

To further assess the general applicability of the succinylation-polymerisation protocol, the disuccination reaction was also performed using lutein (**5**) as a model substrate. This carotenoid was selected because, while maintaining a conjugated backbone similar to that of astaxanthin, it presents slight structural differences, particularly in the terminal hydroxyl functionalities and the absence of keto groups. Evaluating lutein under identical reaction conditions provided valuable insight into whether the same functionalisation strategy can be

extended to other carotenoids with similar molecular architectures. The reaction proceeded efficiently, yielding the lutein disuccinate derivative (**6**) in 75% yield, thereby demonstrating that the methodology is potentially generalisable to other carotenoids and may serve as a versatile platform for future polymerisation studies.

3.3.4.2 Optical and thermal characterisation of astaxanthin-based copolymers

A detailed characterisation of the synthesised astaxanthin-based polymers was performed to evaluate the structural integrity of the chromophore and the impact of the two different synthetic strategies on the resulting materials. A combination of complementary analytical techniques was employed. UV-vis spectroscopy was used to investigate the optical absorption features of the polymers and to monitor possible alterations in the electronic conjugation of the astaxanthin backbone.

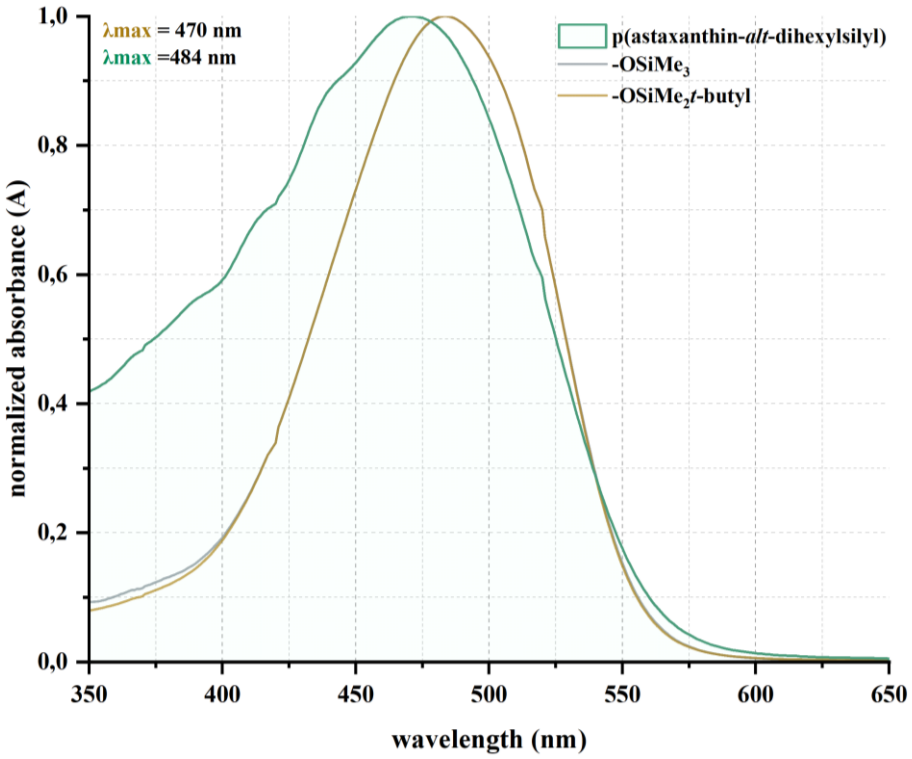

Graph 3. 6 *Normalised ABS spectra in the spectral range 350-700 nm of the two-$OSiR_3$ protected derivative of astaxanthin (**2a**) (grey line) and (**2b**) (grey line) in comparison with polymer (**8**) (green line) using DCM as solvent.*

The normalised UV–Vis absorption spectra of O-silyl protected derivatives **2a** and **2b**, and the corresponding polymer (**8**) are shown in **Graph 3.6**. As already reported in the chapter, both O-protected derivatives display the same absorption maxima of the pristine carotenoid ($\lambda_{max} \approx 484$ nm).[56] The absence of appreciable spectral shifts confirms that the introduction of silyl protecting groups does not perturb the π-conjugated system[57] or induce aggregation in solution. Upon polymerisation, the material exhibits a modest hypsochromic shift of the main absorption band ($\lambda_{max} \approx 470$ nm) accompanied by a slight broadening of the band. These changes can be attributed to different aggregations of the polymer, rather than to any disruption of the π-conjugation. The polymerisation presumably alters intermolecular interactions and packing without affecting the characteristic optical transition of the chromophore, preserving the electronic structure that is crucial for charge-transport in OFET devices.

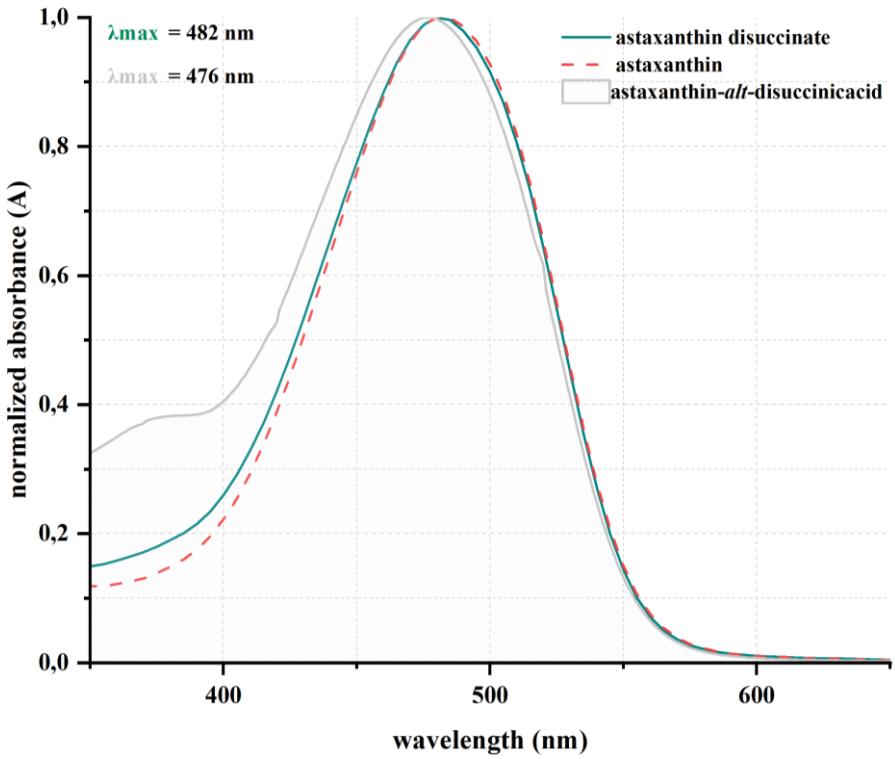

Graph 3. *7 Normalised ABS spectra in the spectral range 350-700 nm of pristine astaxanthin (**1**) (dotted red line), astaxanthin disuccinate (**4**) (blue line) and polymer (**7**) using tetrahydrofuran (THF) as solvent.*

Graph 3.7 shows the ABS spectra of pristine *t*-astaxanthin, its di-succinate derivative (**4**), and the corresponding polymer (**7**). The spectrum of the native carotenoid and the di-

succinyl derivative features the characteristic maximum at 482 nm, typical of the *all-trans* configuration, confirming that also the esterification at the terminal hydroxyl positions does not perturb the conjugated π-system. As in the previous case, the polymeric sample exhibits a slight blue shift (λ_{max} = 476 nm), indicating a small decrease in planarity due to the incorporation of the ester linkages. The small shoulder observed in the 340–370 nm region is likely due to the formation of cis-isomers,[58] presumably resulting from the Soxhlet extraction process, which exposes the polymer to elevated temperatures in solution.

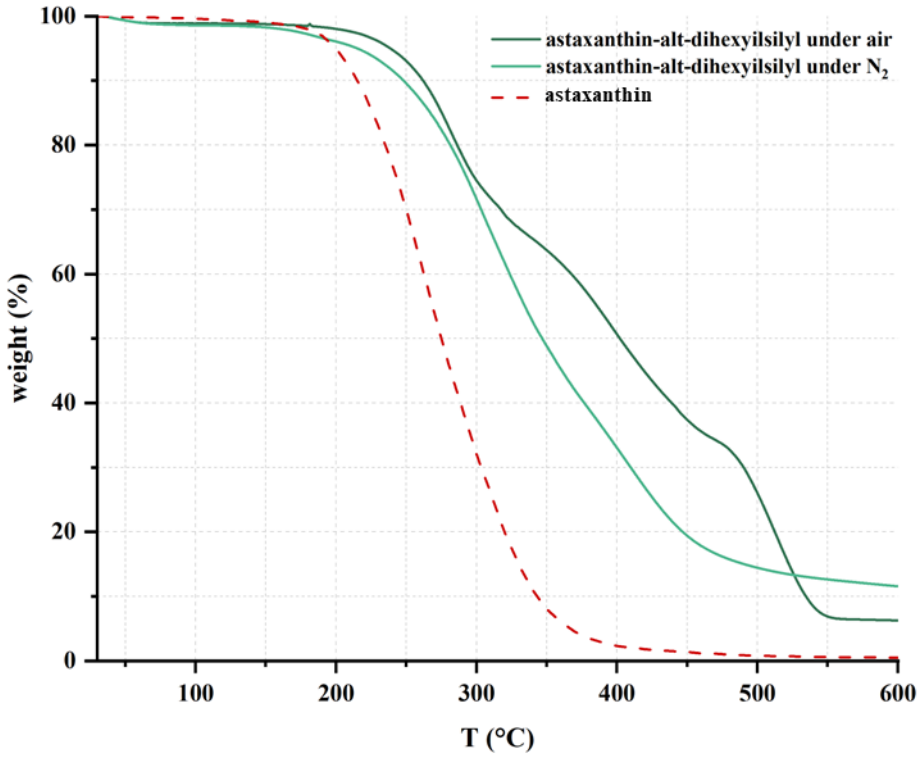

Graph 3. 8 *TGA curve of polymer (8) performed under air (dark green line) and under nitrogen (light green line) compared with the TGA curve of astaxanthin (red dotted line) performed under nitrogen*

TGA was used to assess the thermal stability of the materials and to compare the influence of the polymerisation on the degradation behaviour. The TGA profile reveals clear differences between the polymer (**8**) (**Graph 3.8,** green lines) and the pristine astaxanthin (dotted red line), highlighting the stabilising role of polymerisation and the introduction of alkyl–silane linkages. In both oxidative (air) and inert (N_2) atmospheres, polymer (**8**) displayed a significant improvement in thermal stability compared to pristine astaxanthin. The onset of weight loss shifted from approximately 175 °C for the molecular compound to

about 200 °C for the polymer, confirming that polymerisation and silane incorporation effectively delay the initial decomposition processes. In addition to the higher onset temperature, a residual mass is clearly observed at the end of the TGA run for the polymer, whereas pristine astaxanthin is almost completely volatilised. This behaviour indicates the formation of thermally stable inorganic fragments, plausibly related to silicon-containing residues that do not decompose within the temperature range explored. Notably, the residual fraction is larger under nitrogen than under air, suggesting that, in inert conditions, the silicon-based moieties tend to condense into non-volatile silicate-like structures rather than being oxidised into gaseous products such as SiO_2 This trend is consistent with the behaviour previously observed for similar silane-containing systems (compounds **2a** and **2b**), where the TGA curves also displayed a more pronounced residue when analysed under nitrogen. Under oxidative atmosphere, instead, partial oxidation of the alkyl substituents and of the silicon framework leads to a more complex, multi-step degradation pathway and a reduced residual fraction.

3.3.4.3 Potential degradation pathway of an astaxanthin-succinic acid copolymer in the human gastrointestinal system

The proposed copolymer comprising astaxanthin and succinic acid is hypothesised to undergo enzymatic hydrolysis and metabolic conversion upon oral ingestion, based on existing literature on carotenoid esters and dicarboxylic acid derivatives. However, it is important to note that no specific studies have been conducted on this particular copolymer. The following discussion outlines a plausible degradation pathway, referencing relevant studies on the metabolism of astaxanthin and succinic acid derivatives (**Figure 3.17**). Upon ingestion, the copolymer reaches the stomach, where it may undergo partial disaggregation due to acidic conditions and mechanical action. In the small intestine, bile salts facilitate the emulsification of lipophilic components like astaxanthin, forming micelles that enhance their enterocyte absorption.[63] Simultaneously, esterases and lipases can hydrolyse ester bonds, releasing free astaxanthin[64] and succinic acid.[65] Astaxanthin is subsequently transported via the lymphatic system as part of chylomicrons, reaching the liver and entering systemic circulation, often associated with lipoproteins such as VLDL, LDL, or HDL[63,66] Succinic

acid, upon hydrolysis, is absorbed into the portal circulation and transported to the liver. There, it is converted to succinyl-CoA, entering the citric acid cycle as an intermediate metabolite.[65] Once it reached the liver, astaxanthin can be converted into various metabolites, including 3-hydroxy-4-oxo-β-ionone,[67] then primarily excreted via the bile. As a matter of fact, the degradation of the copolymer within the GI tract is likely influenced by factors such as the polymer's molecular weight, crystallinity, and solubility.

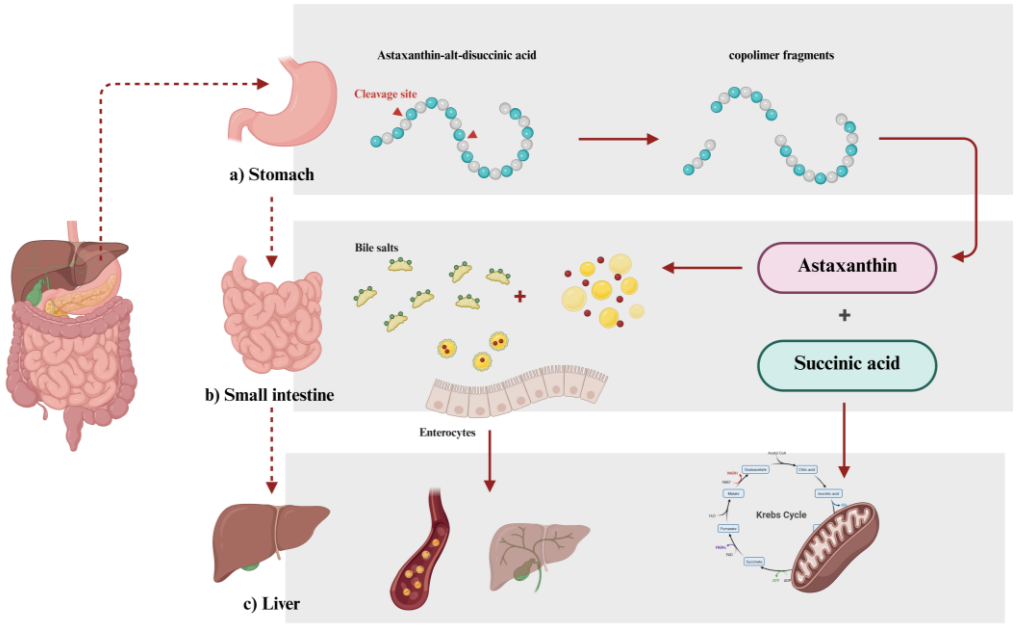

Figure 3. 17 *Hypothetical degradation pathway of astaxanthin copolymer (7) based on the metabolic pathway of its single components*

Polymers with high molecular weight and low solubility may have incomplete digestion and absorption. While direct studies on the metabolism of an astaxanthin-succinic acid copolymer are lacking, existing literature on the individual components suggests that such a copolymer could be metabolised through pathways involving enzymatic hydrolysis and absorption. However, the efficiency of these processes would be contingent upon the copolymer's physicochemical properties.

3.4 Conclusions

This work demonstrates the feasibility of employing carotenoids, and particularly astaxanthin, as functional materials for edible organic electronics, while addressing their inherent chemical and physical limitations through targeted molecular design. The investigation of pristine astaxanthin revealed that, despite its limited solubility and susceptibility to degradation, the molecule can form semi-crystalline films upon moderate thermal annealing (~120 °C), resulting in a marked improvement in field-effect mobility. These results confirm that carotenoids can indeed support charge transport when appropriately ordered in the solid state. Building upon this foundation, the chemical modification strategies explored, namely silyl protection and hydrazone derivatisation, successfully enhanced astaxanthin's solubility and stability without disrupting the π-conjugated backbone. The reversible sylilation approach enabled solution processing under mild conditions, with the protecting groups removable upon gentle heating, thereby restoring the pristine chromophore. Conversely, the hydrazone derivative introduced permanent solubility improvements, suggesting an alternative route toward stable carotenoid-based semiconductors. Furthermore, the polymerisation of astaxanthin into copolymers with succinic acid and dialkylsilane demonstrated a significant enhancement in thermal stability and structural robustness. These polymeric systems combine improved processability with potential biodegradability, aligning with the principles of green and edible electronics. Preliminary analyses also indicate that the succinic acid copolymer could undergo enzymatic degradation into naturally metabolizable products, further supporting its suitability for ingestible applications.

In conclusion, this study provides a comprehensive framework for transforming carotenoids from nutritional pigments into functional, processable, and edible semiconductors. By integrating molecular engineering, solid-state characterisation, and materials design, it advances the broader vision of sustainable, bio-integrated electronic systems capable of safely interacting with living organisms and the environment. The strategies developed here open the path toward a new generation of transient, metabolizable devices that merge functionality with biocompatibility, bridging the gap between materials science, electronics, and life sciences.

3.5 Experimental

3.5.1 Materials and methods

All reagents are purchased from VWR, Sigma-Aldrich, Fluorochem, BLD Pharm, TCI, Ambeed, Fisher Scientific, and ThermoFisher. Solvents – including anhydrous and NMR solvents – are purchased from Carlo-Erba, Fisher Scientific, and Acros and used as received unless otherwise stated. Extra dry solvents packed under Ar and stored over molecular sieves having a >99,5% purity are always employed if a reaction requires inert and anhydrous conditions. Glassware is dried for 24 hours at 130 °C before being used when the synthetic protocol requires an anhydrous environment. All the synthetic protocols and workups of this chapter are performed in the dark to prevent the degradation of the carotenoids. For the same reason, all the obtained products are always stored in dark places. If the synthetic protocol requires an inert atmosphere, solid reagents are always degassed using high vacuum (~0,02 mbar) and then refilling the reaction vessel with nitrogen (the procedure is repeated three times). Liquid or low-melting-point solids are degassed through a freeze-pump-thaw procedure using liquid nitrogen as a cooling agent. Reactions are monitored using Xtra SIL G UV254 silica gel plates (pore size: 60 Å, thickness 200 μm) and a double-wave UV lamp (λ: 254 and 365 nm). When cited, the composition of solvent mixtures is always indicated as a volume/volume ratio. Melting points are measured employing a Büchi M-560 apparatus. Solution Nuclear Magnetic Resonance (NMR) spectra are acquired with a Bruker Avance 400 NEO spectrometer. ^{1}H NMR of known compounds are included after each synthetic procedure to provide the reader with the chemical shifts of the compound. ^{1}H NMR spectra of new molecules are also included in *Chapter 3.5.3*.

3.5.2 Synthetic procedures

*Synthesis of (all-E)-3,3'-bis[(trimethylsilyl)oxy]-β,β-carotene-4,4'-dione (**2a**) and (all-E)-3,3'-bis[(tert-butyldimethylsilyl)oxy]-β,β-carotene-4,4'-dione (**2b**)*

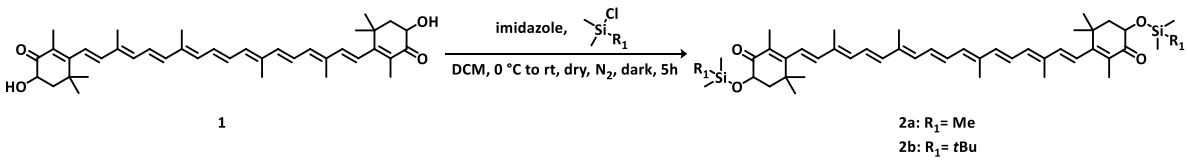

Scheme 3. 5 *Synthetic protocol for the obtainment of (**2a**) and (**2b**)*

The two O-protected derivatives of trans-astaxanthin are synthesized following the same procedure and purified accordingly. TMSCl is distilled from CaH prior to the reaction; TBDMSCl is used as received without further purification. It is degassed through freeze-pump thaw in an oven-dried 2-neck 25 mL round-bottom flask, dissolved in anhydrous DCM, and added to the reaction mixture as a 1,02 M solution.

200 mg of trans-astaxanthin (**1**) (0,34 mmol, 1 eq) and 138,7 mg of imidazole (2,04 mmol, 6 eq) are added to an oven-dried 2-neck 25 mL round-bottom flask. The reagents are degassed, then dissolved in 4 mL of anhydrous DCM. The mixture is stirred at room temperature for 10 minutes, then 0,13 mL (1,02 mmol, 3 eq) of the corresponding R_3SiCl (TMSCl or TBDMSCl solution) are dropwise added to the reaction flask. After 5 hours, the products are precipitated by adding 20 mL of anhydrous acetonitrile (ACN) to the reaction flask. The powders are filtered and washed with cold ACN, then dried for 1 hour using the Schlenk line. The products are stored under Ar at -32 °C. (***2a*** yield: 96%; ***2b*** yield: 97%)

2a: **^{1}H NMR** (400 MHz, C_6D_6) δ(ppm) 6.73-6.61 (4H, m), 6.49 (2H, d, J=14.8), 6.39-6.31 (4H, m), 6.27 (2H, d, J=11.4), 6.08 (2H, d, J=16.2), 4.46 (2H, q, J=5.6), 2.09 (6H, s), 1.85 (6H, s), 1.79 (6H, s), 1.00 (12H, d, J=33.4), 0.41 (18H, s), 0.28 (4H, s)

2b: **^{1}H NMR** (400 MHz, C_6D_6) δ(ppm) 6.73-6.61 (4H, m), 6.49 (2H, d, J=14.8), 6.39-6.31 (4H, m), 6.27 (2H, d, J=11.4), 6.08 (2H, d, J=16.2), 4.46 (2H, q, J=5.6), 2.09 (6H, s), 1.85 (6H, s), 1.79 (6H, s), 1.12 (18H, s), 1.02 (12H, d, J=33.4), 0.45 (6H, s) 0.39 (4H, s), 0.28 (6H, s)

*Synthesis of (3S,3'S)-3,3'-dihydroxy-4,4'-bis(diphenylhydrazono)-β,β-carotene (**3**)*

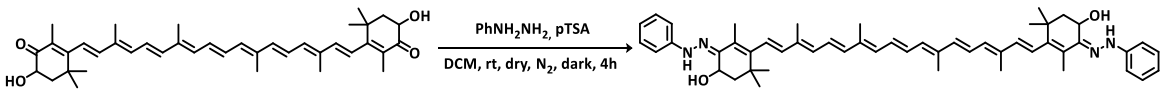

1 3

Scheme 3. 6 *Synthetic protocol for the obtainment of (3)*

300 mg of trans astaxanthin (**1)** (0,5 mmol, 1 eq) and 9,51 mg of p-toluenesulfonic acid (*p*TSA) (0,05 mmol, 0,1 eq) are added to an oven-dried 2-neck 25 mL round-bottom flask. The reagents are degassed, then dissolved in 2 mL of anhydrous toluene. 54,2 mg of phenyl

hydrazine are dropwise added to the reaction mixture, then the solution is stirred at reflux temperature for 4 hours. The reaction mixture is brought back to room temperature and 10 mL of toluene are added. The formed precipitate is filtered, then washed with brine to remove residual hydrazine and PTSA. The solid is dried for 3 hours using the Schlenk line, then stored under Ar at -35 °C. (yield: 79%)

^{1}H NMR (400 MHz, C_6D_6) δ(ppm) 7.27 (4H, t, J=7,9), 7.13 (4H, d, J=7,9), 6.85 (2H, t, J=7,1), 6.80-6.65 (4H, m), 6.50-6.14 (10H, m), 4.87 (2H, q, J=6.3), 2.17-1.98 (22H, m), 1.23 (6H, s), 1.17 (6H, s)

*Synthesis of (all-E)-3,3'-bis(succinoyloxy)-β,β-carotene-4,4'-dione (**4**)*

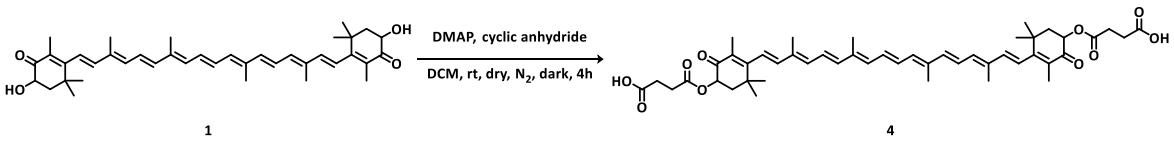

***Scheme 3.** 7 Synthetic protocol for the obtainment of (**4**)*

300 mg of trans-astaxanthin (**1**) (0,5 mmol, 1 eq), 400,2 mg of succinic anhydride (4,0 mmol, 8 eq), and 614,1 mg of 4-dimethylaminopyridine (DMAP, 5,02 mmol, 10 eq) are added to an oven-dried 2-neck 25 mL round-bottom flask. The reagents are degassed, then dissolved in 2,5 mL of anhydrous DCM. After 4 hours, the mixture is quenched by adding 3 mL of aqueous 5% citric acid. The product is then extracted with 3x15 mL of DCM and washed with brine. The organic layer is dried with Na_2SO_4 and filtered. The solvent is evaporated to afford a green solid. The product is dried overnight using the Schlenk line (yield: 99%).

^{1}H NMR (400 MHz, $CDCl_3$) δ(ppm) 6.70-6.60 (4H, m), 6.43 (4H, t, J=14.2), 6.33-6.25 (4H m), 6.20 (2H, d, J=16.1), 6.54 (2H, q, J=6.3), 2.83-2.72 (8H, m), 2.09-2.02 (4H, m), 1.99 (12H, s), 1.90 (6H, s), 1.35 (6H, s), 1.22 (6H, s)

*Synthesis of (3R,3'R,6'R)-3,3'-bis(succinoyloxy)-β,ε-carotene (**6**)*

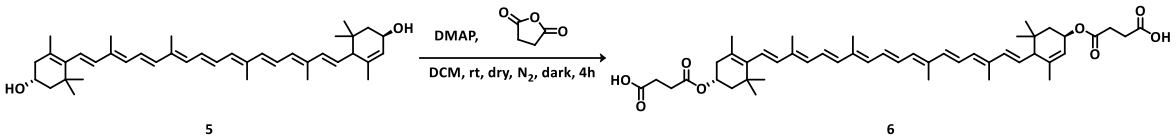

Scheme 3. 8 *Synthetic protocol for the obtainment of (**6**)*

300 mg of lutein (**5**) (0,5 mmol, 1 eq), 400,2 mg of succinic anhydride (4,0 mmol, 8 eq), and 614,1 mg of 4-dimethylaminopyridine (DMAP, 5,02 mmol, 10 eq) are added to an oven-dried 2-neck 25 mL round-bottom flask. The reagents are degassed, then dissolved in 2,5 mL of anhydrous DCM. After 4 hours, the mixture is quenched by adding 3 mL of aqueous 5% citric acid. The product is then extracted with 3x15 mL of DCM and washed with brine. The organic layer is dried with Na_2SO_4 and filtered. The solvent is evaporated to afford a green solid. The product is dried overnight using the Schlenk line (yield: 75%).

^{1}H NMR (400 MHz, $CDCl_3$) δ(ppm) 6.76-6.73 (4H, m), 6.41 (2H, dd, J1=13.8, J2=3.3), 6.34-6.27 (2H, m), 6.26-6.06 (6H, m), 5.57-5.46 (2H, m), 5.16-5.06 (1H, m), 2.70-2.60 (8H, m), 2.54-2.41 (2H, m), 2.19 (1H, m), 2.00 (9H, s), 1.94 (3H, s), 1,13 (1H, d, J1=6.6), 1.86 (1H, d, J=5.6), 1.77 (3H, s), 1.69 (3H, s), 1.62 (1H, t, J=11.8), 1.49 (1H, dd, J1= 13.7, J2=4.8), 1.15 (3H,s), 1.12 (3H, s), 1.04 (3H, s), 0.92 (3H, s)

Synthesis of poly[(all-trans-(3S,3'S)-3,3'-dihydroxy-β,β-carotene-4,4'-dione) succinate] (7)

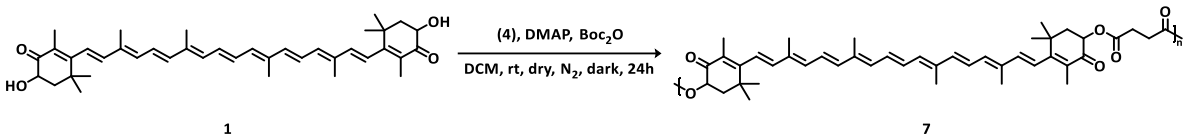

Scheme 3. 9 *Synthetic protocol for the obtainment of (7)*

223 mg of astaxanthin disuccinate (**4**) (0,28 mmol, 1 eq), 200 mg of astaxanthin (**1**) (0,28 mmol, 1 eq), 23 mg of DMAP (0,14 mmol, 0,5 eq), and 185 mg of di-*tert*-butyl dicarbonate (Boc_2O) (0,84 mmol, 3 eq) are added to an oven-dried 2-neck 25 mL round-bottom flask. The reagents are degassed, then dissolved in 2,5 mL of anhydrous DCM and stirred in an ice bath for 24 hours. The solvent is then evaporated, and the obtained polymer is purified by

Soxhlet extraction using MeOH, Acetone, PE, and THF as extracting solvents. The polymer 7is recovered with THF, then the solvent is evaporated to afford 118 mg of a red powder.

^{1}H NMR (400 MHz, $CDCl_3$) δ(ppm) 6.88-5.95 (14H, m), 5.63-5.43 (2H, br), 2.96-2.69 (4H, m), 2.13-1.77 (22H, m), 1.38-1.11 (12H, m)

*Synthesis of poly[(3,3'-dihydroxy-β,β-carotene-4,4'-dion-3,3'-yl)alt(dihexhylsilylene)] (**8**)*

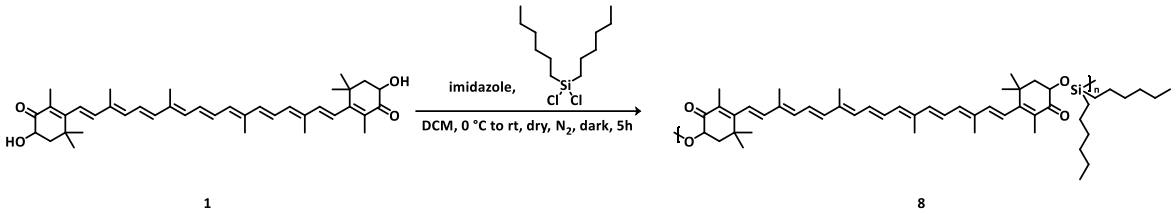

1 8

***Scheme 3. 10** Synthetic protocol for the obtainment of (**8**)*

200 mg of trans-astaxanthin (**1**) (0,34 mmol, 1 eq) and 163,2 mg of imidazole (2,04 mmol, 6 eq) are added to an oven-dried 2-neck 25 mL round-bottom flask. The reagents are degassed, then dissolved in 4 mL of anhydrous DCM. The mixture is stirred at 0 °C for 30minutes, then 0,1 mL of dihexyildichlorosilane (0,34 mmol, 1 eq)) are dropwise added to the reaction flask. After 5 hours, the solvent is removed under vacuum, and the crude product is taken up with MeOH. The precipitate is filtered and washed with cold MeOH, then dried for 3 hours using the Schlenk line to afford 382 mg of a red powder. The product is stored under Ar at -32 °C.

^{1}H NMR (400 MHz, CD_2Cl_2) δ(ppm) 6.88-6.10 (14H, m), 4.90-4.39 (2H, br), 2,25-1.68 (20H, m) 1.55-1.03 (36H, m), 1.01-0.85 (9H, br), 0.76-0.49 (6H, br)

3.5.3 Materials characterizations

3.5.3.1 Optical characterizations

ABS analysis in the UV-vis range are performed to characterize the optical properties of the samples and to monitor possible variations induced by chemical treatments. Spectra are collected using a Jasco V-750 UV/Vis/NIR spectrophotometer equipped with a PbS detector and a dual-beam optical system. The instrument covers a spectral range from 190 to 2500

nm, using a deuterium lamp for the UV region (190–350 nm), a tungsten–halogen lamp for the visible region (350–800 nm), and a PbS photoconductive detector for the near-infrared region. The spectral resolution is set to $\Delta\lambda = 1$ nm and the scanning speed to 400 $nm \cdot min^{-1}$. All measurements are performed in two-face 1 cm path length quartz cuvettes. Background correction is performed using the spectrum of pure DCM or THF as a reference. Baseline and absorbance of the samples are recorded in the range 200–800 nm. All samples were prepared by dissolving the analytes in DCM or THF at concentrations in the range of 0,3–0,1 $mg \cdot mL^{-1}$ ($\approx 10^{-5}$ $mmol \cdot mL^{-1}$), ensuring absorbance values within the linear range of the Beer–Lambert law ($A < 1$)

$$A = \varepsilon \cdot l \cdot c$$

where A is the absorbance, ε ($M^{-1} \cdot cm^{-1}$) is the molar absorption coefficient, l (cm) is the optical path, and c is the concentration ($mol \cdot L^{-1}$). Data acquisition and preliminary processing were performed with Jasco Spectra Manager, while further analysis (λ_{max} determination, normalisation) was carried out using OriginPro software.

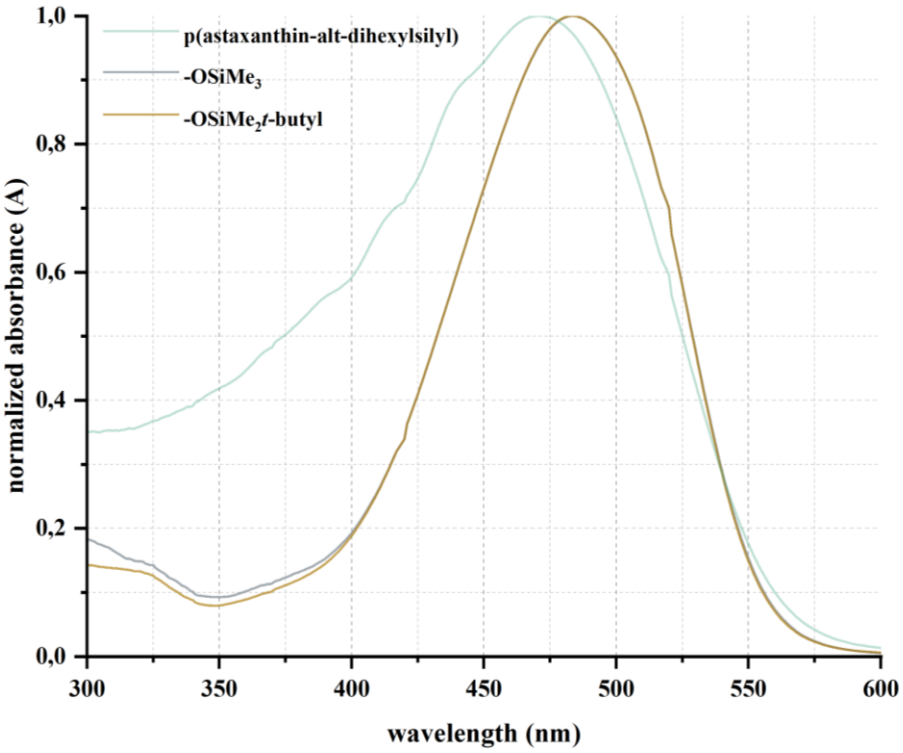

Graph 3. 9 *Normalised ABS spectra of derivatives (**2a**) (grey line), (**2b**) (brown line), and polymer (**8**) (green line) using DCM as solvent*

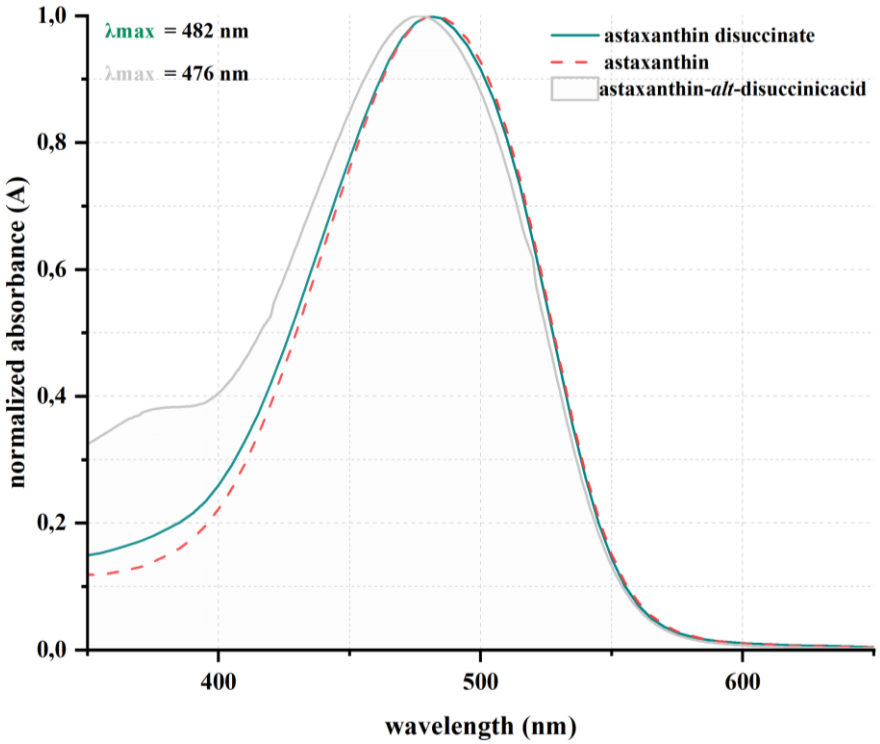

Graph 3. 10 *Normalised ABS spectra in the spectral range 350-700 nm of pristine astaxanthin, (4) (blue line) and (7) using THF as solvent.*

3.5.3.2 Thermogravimetric analysis

TGA are carried out using a TGA/DSC 1 STARe System (Mettler Toledo) equipped with alumina crucibles. Approximately 5–10 mg of each sample are heated from 30 °C to 600 °C at a constant heating rate of 10 °C·min^{-1}, under a continuous gas flow of 50 mL·min^{-1}. Measurements are performed both under a nitrogen atmosphere (to evaluate intrinsic thermal stability) and under an air atmosphere (to assess oxidative degradation). Further analysis, e.g., thermogravimetric derivative (TGD) calculation and weight loss steps determination, are performed using OriginPro software.

Herein are reported the TGA curves (continuous lines) and the TGD (dotted curves) of compounds **2a**, **2b**, **4** and **7**

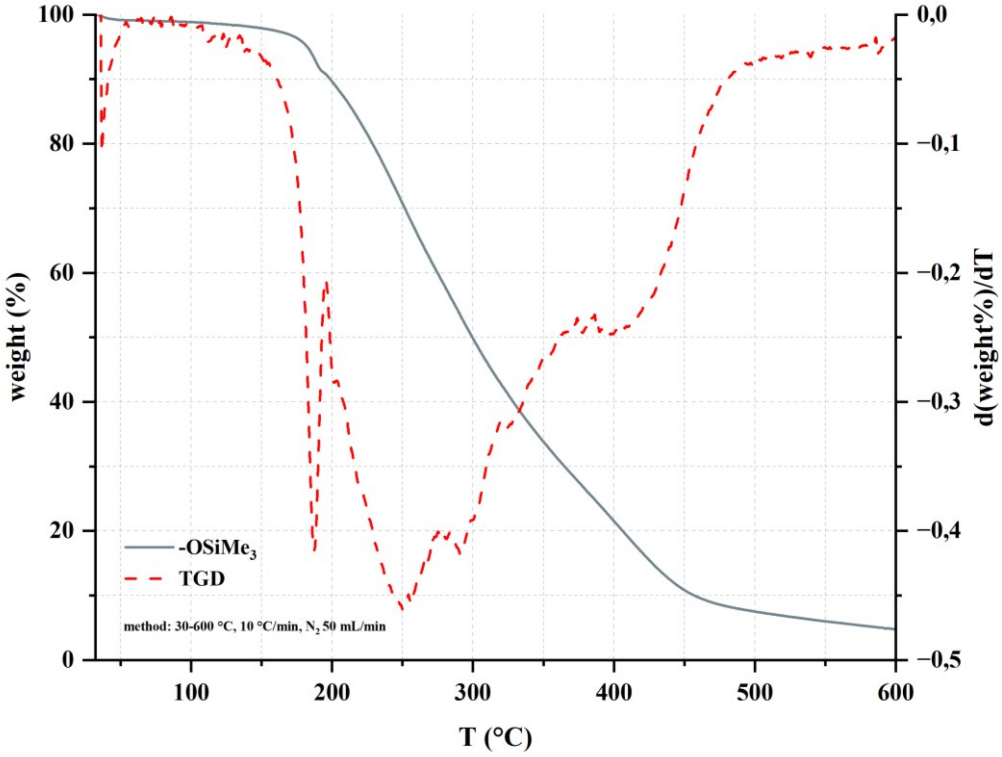

Graph 3. 11 *TGA and TGD of derivative (**2a**) performed under nitrogen*

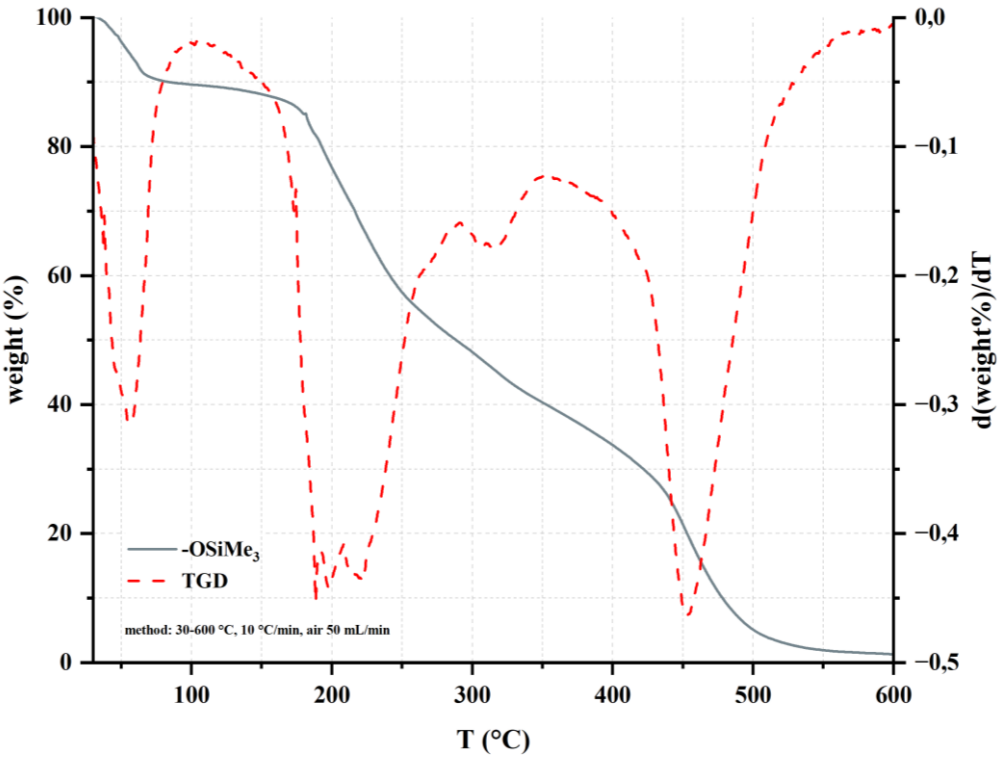

Graph 3. 12 *TGA and TGD of derivative (**2a**) performed under air*

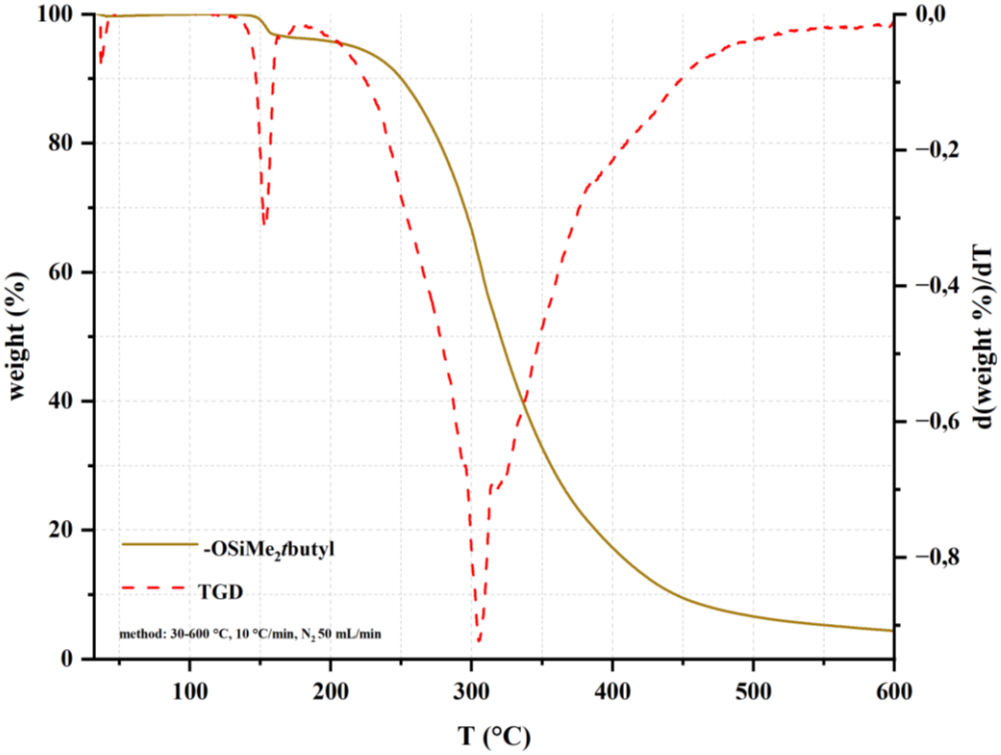

Graph 3. 13 *TGA and TGD of derivative (**2b**) performed under nitrogen*

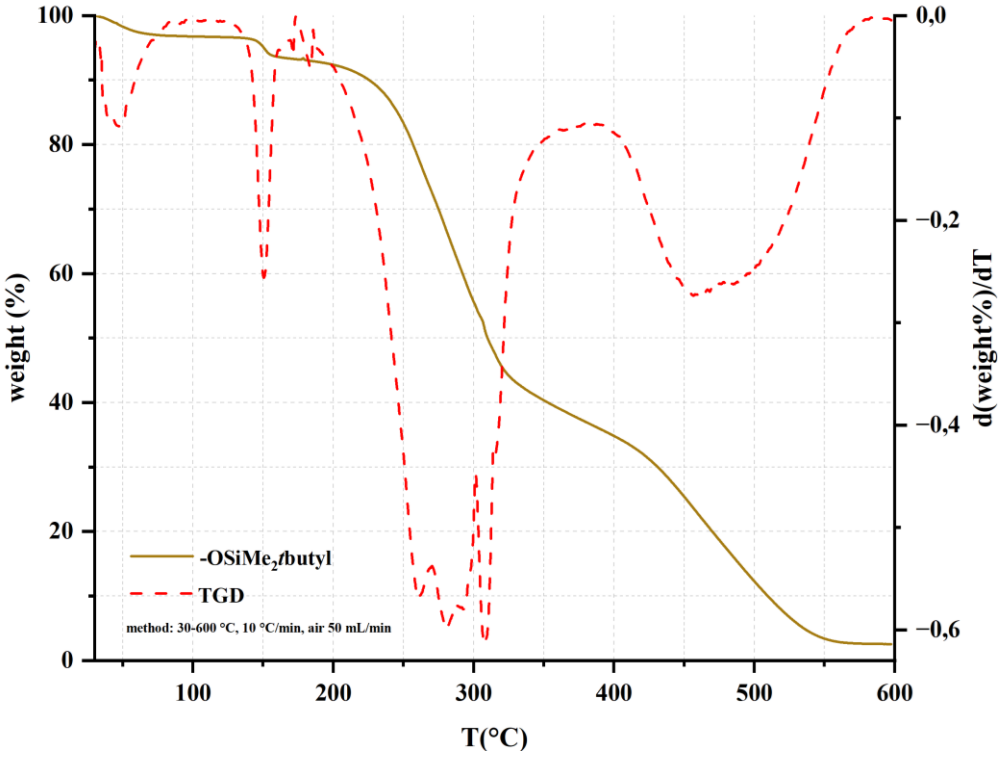

Graph 3. 14 *TGA and TGD of derivative (**2b**) performed under air*

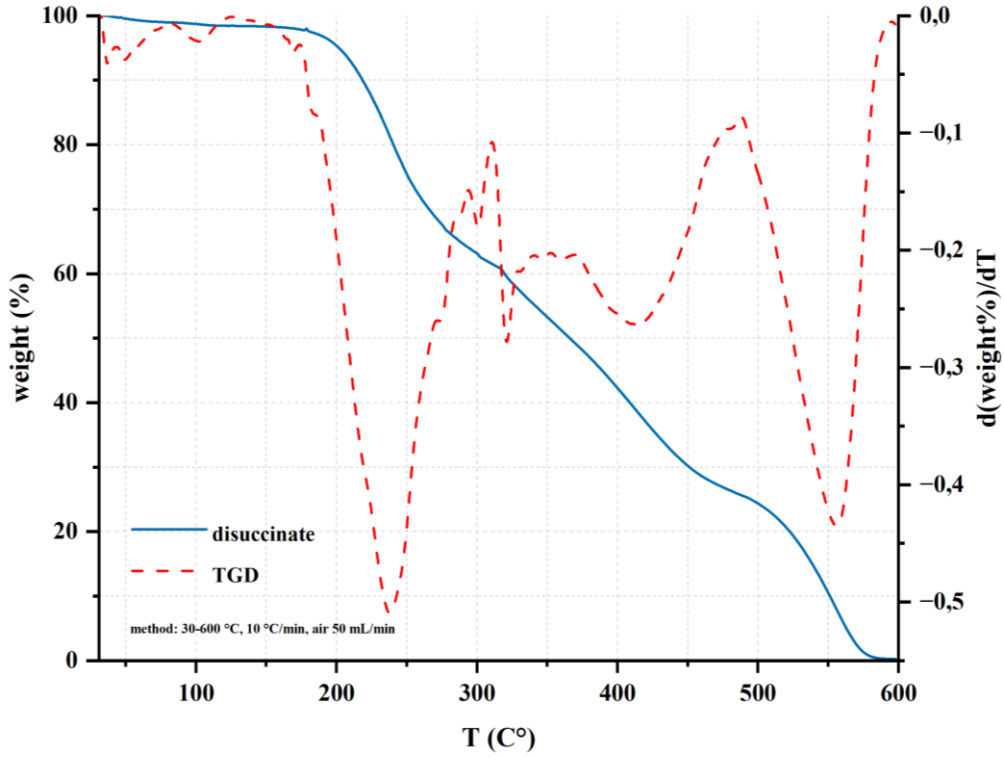

Graph 3. 15 *TGA and TGD of derivative (4) performed under air*

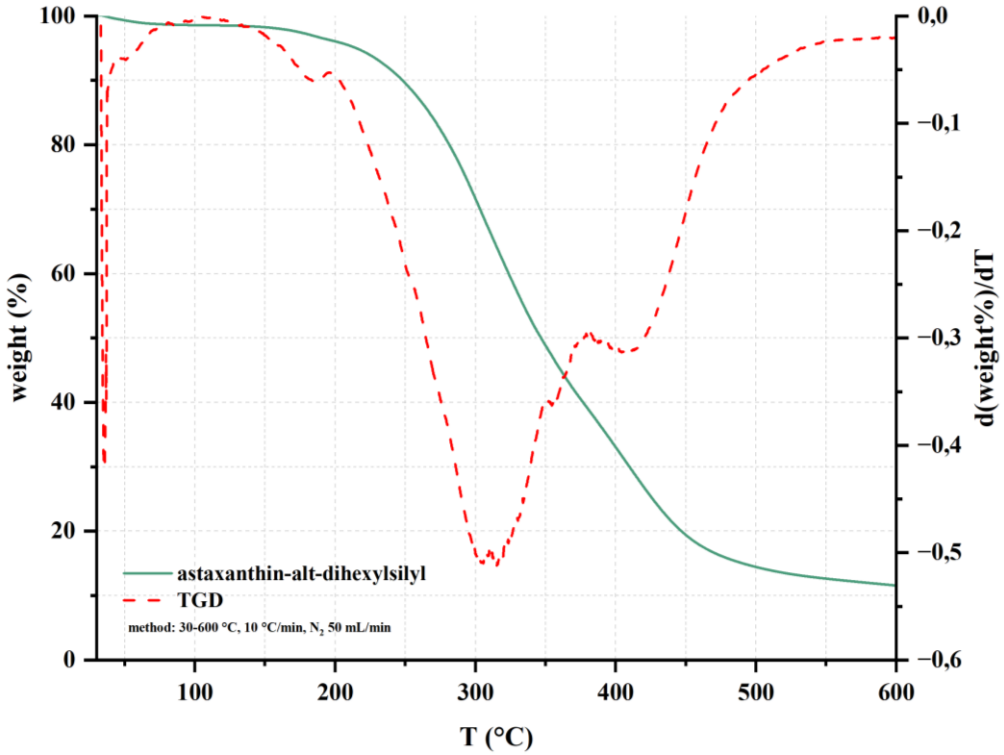

Graph 3. 16 *TGA and TGD of derivative (8) performed under nitrogen*

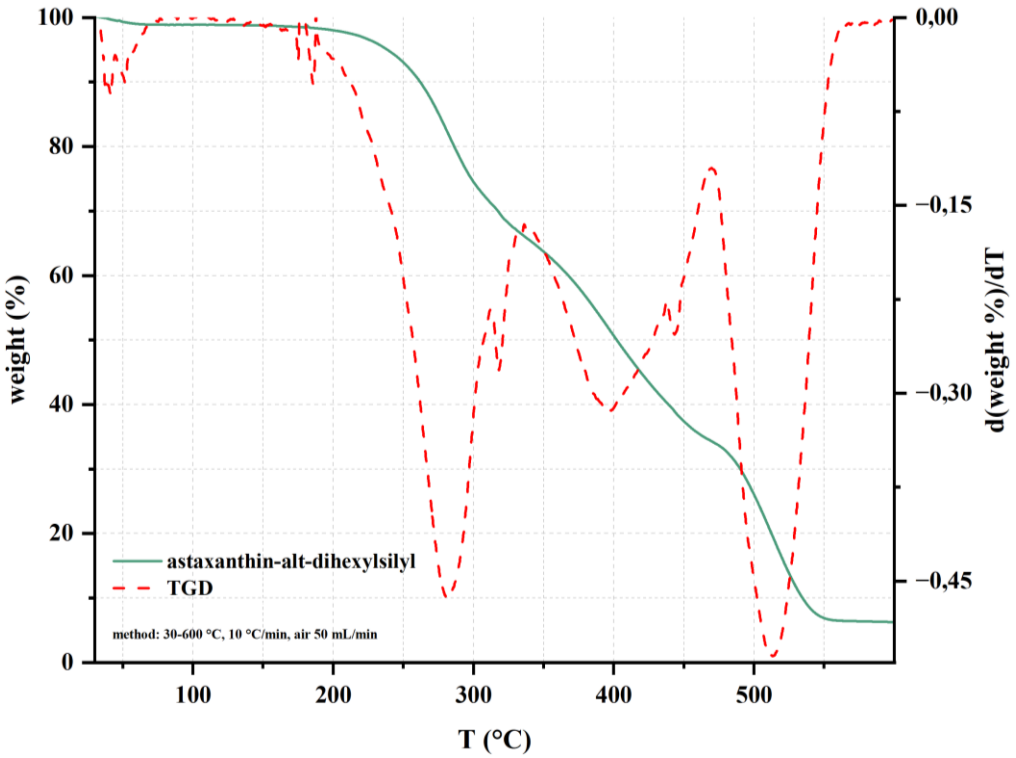

Graph 3. 17 *TGA and TGD of derivative (8) performed under air*

3.5.3.3 Spectroscopic characterizations

^{1}H NMR spectra

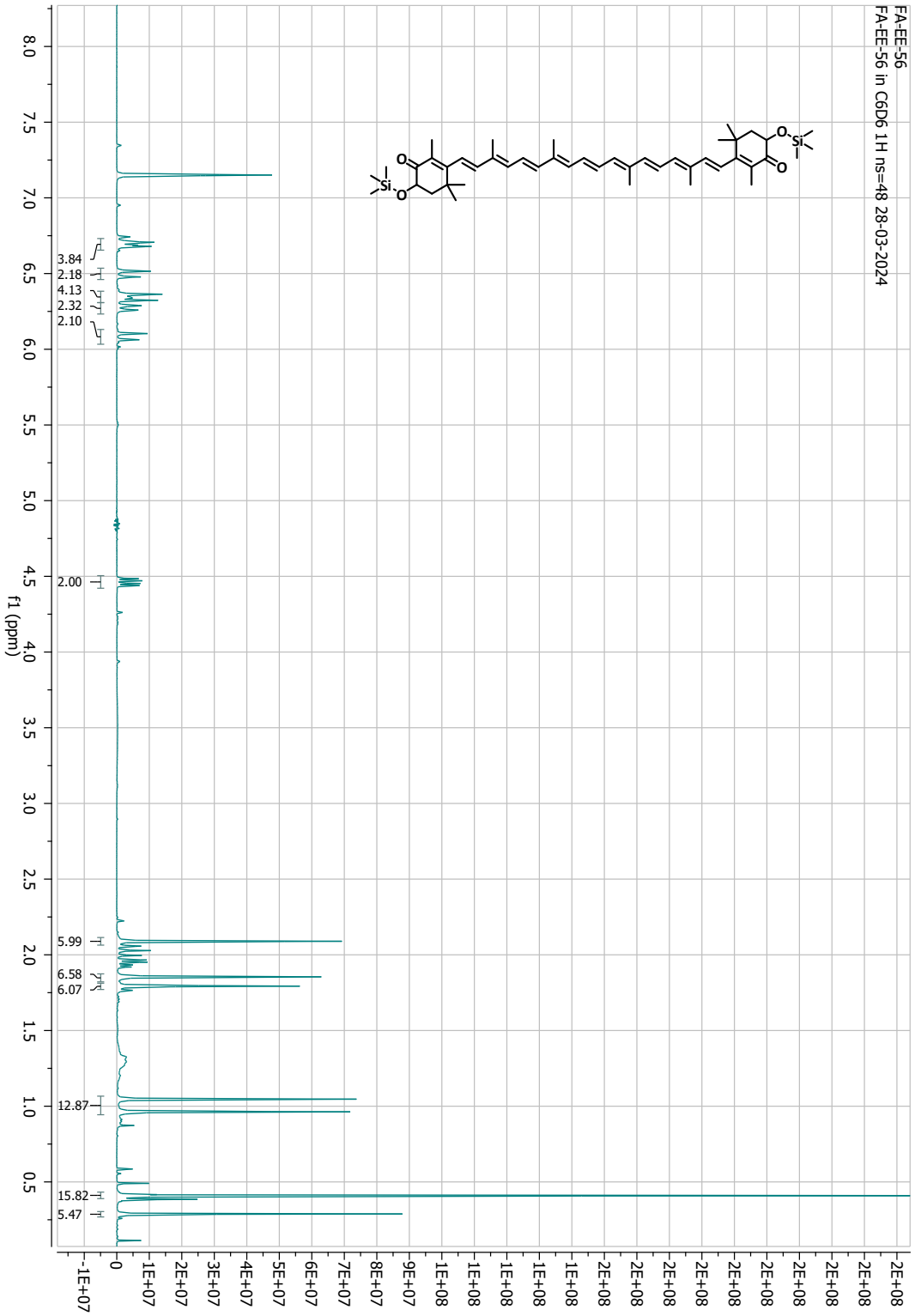

Figure 3. 18 *^{1}H NMR in C_6D_6 spectrum of compound (**2a**)*

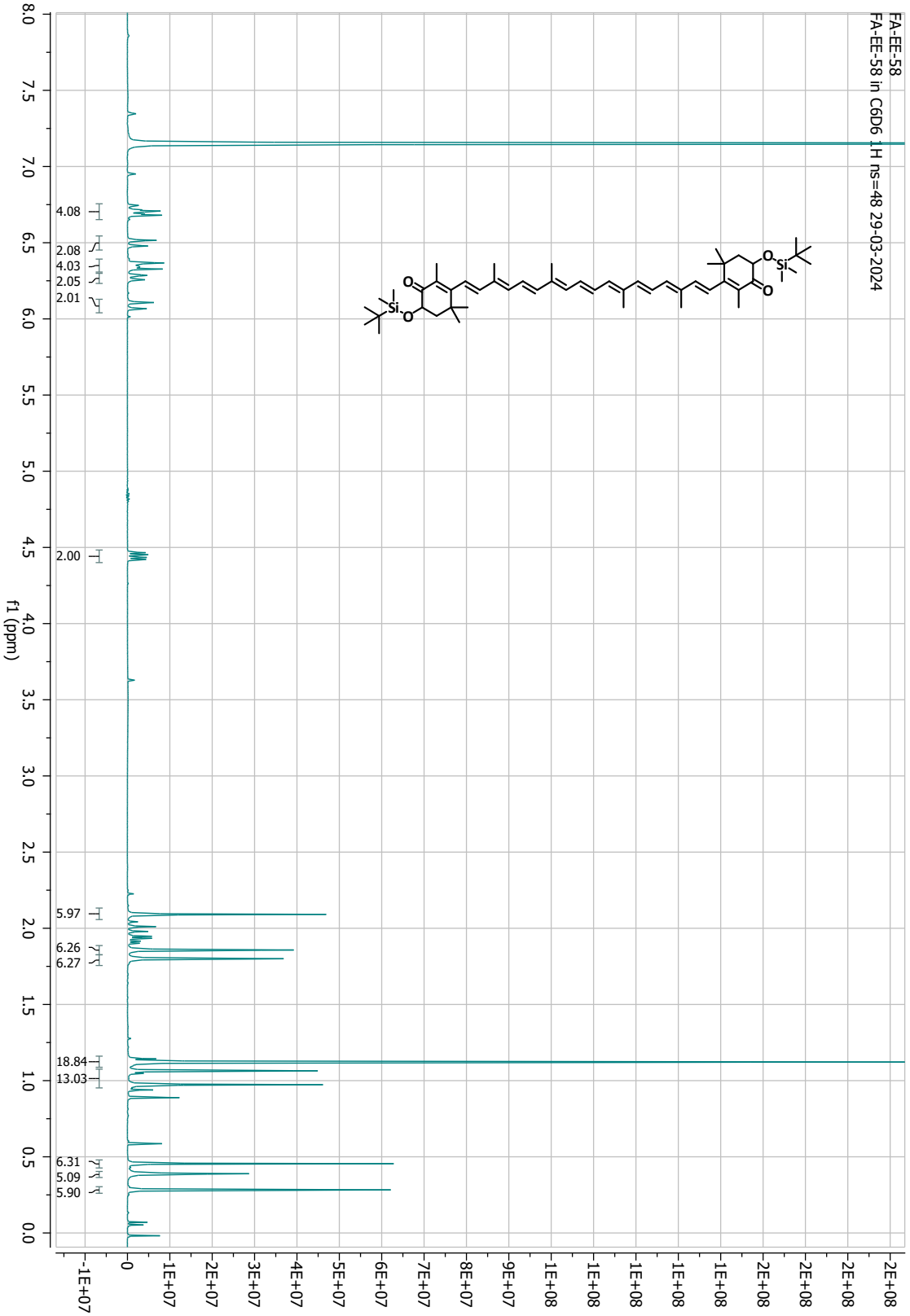

Figure 3. 19 *^{1}H NMR in C_6D_6 spectrum of compound (**2b**)*

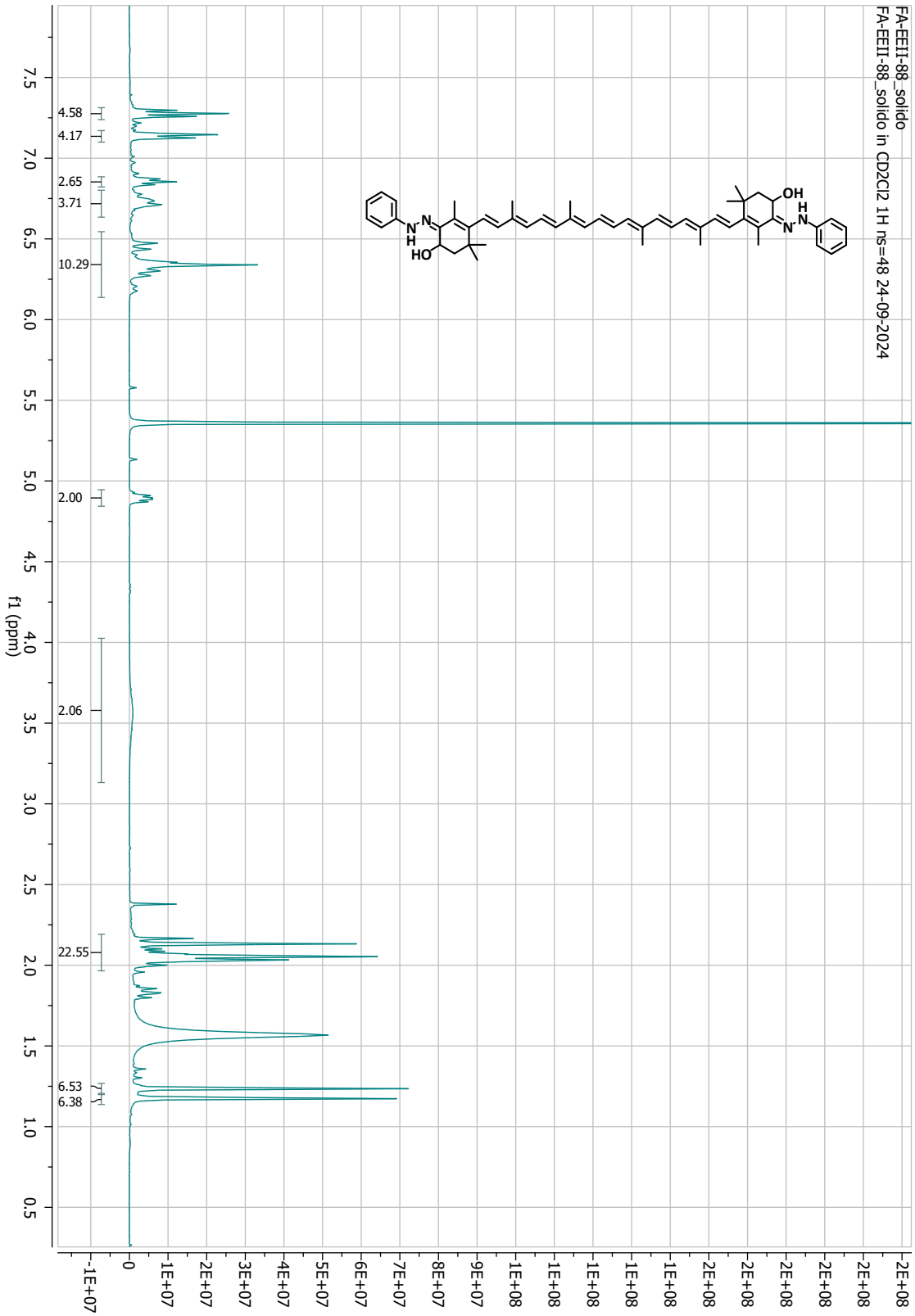

Figure 3. 20 *^{1}H NMR in CD_2Cl_2 spectrum of compound (**3**)*

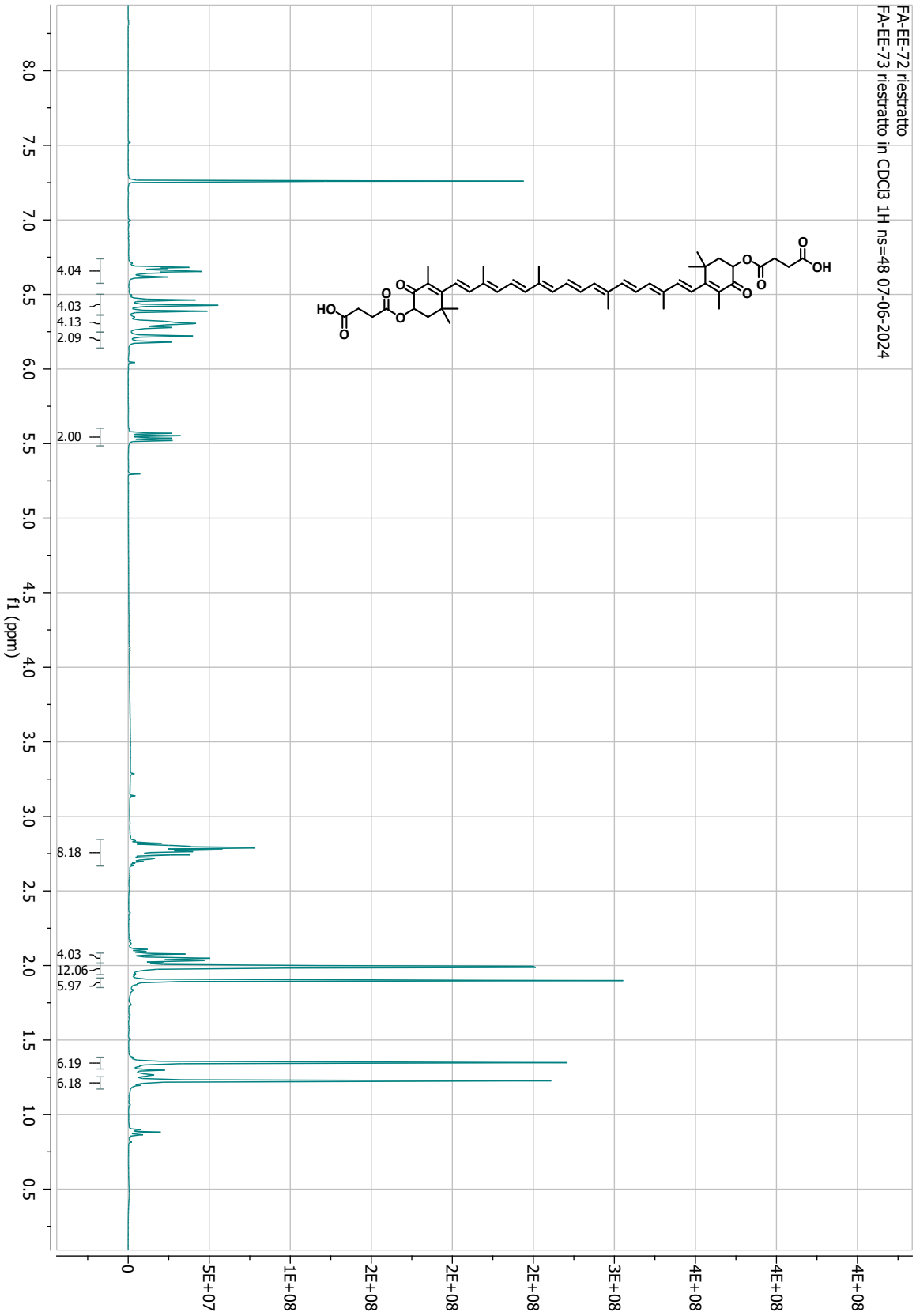

Figure 3. 21 *^{1}H NMR in $CDCl_3$ spectrum of compound (4)*

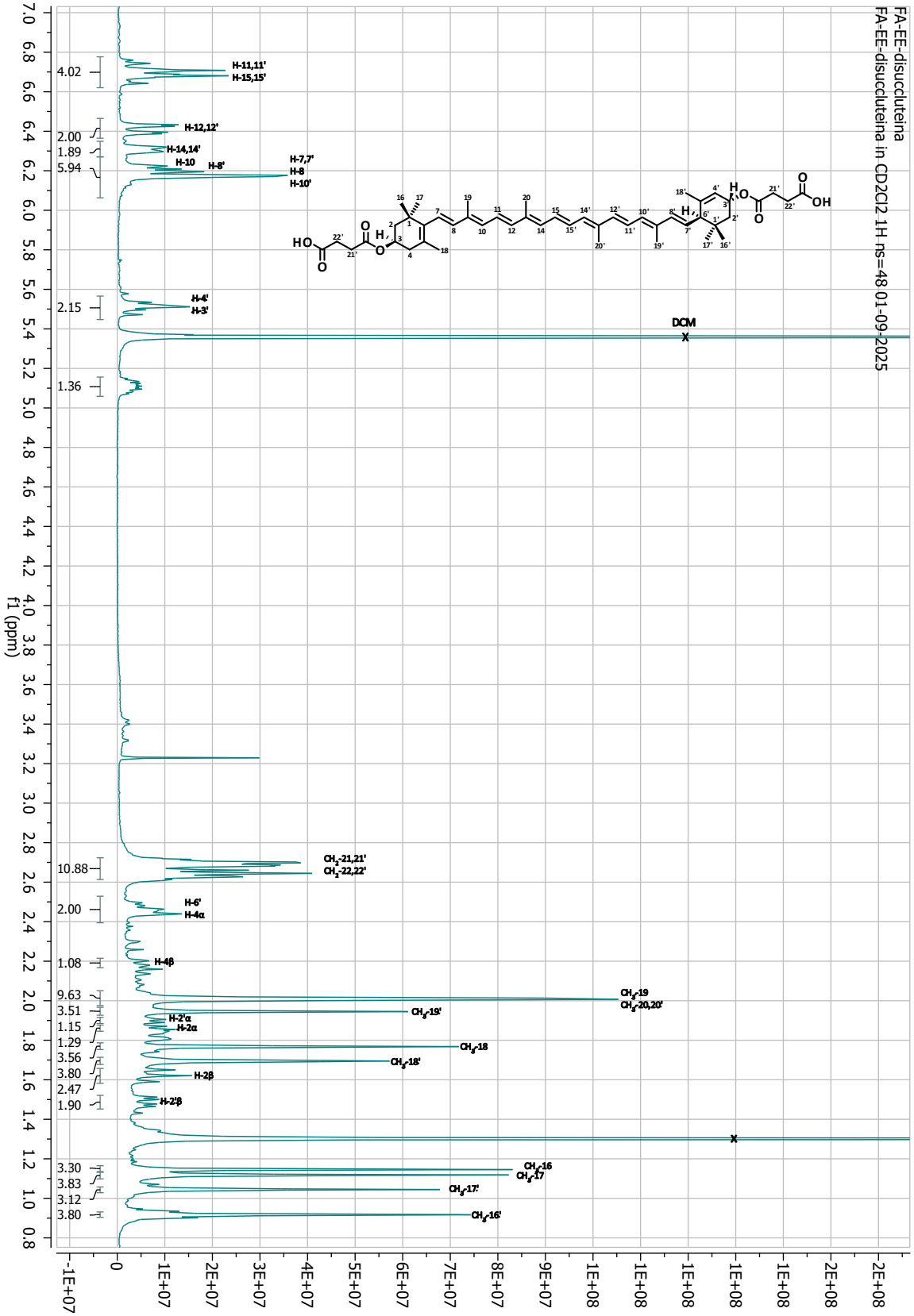

Figure 3. 22 *[1]H NMR in CD_2Cl_2 spectrum of compound (**6**) with peak identification*

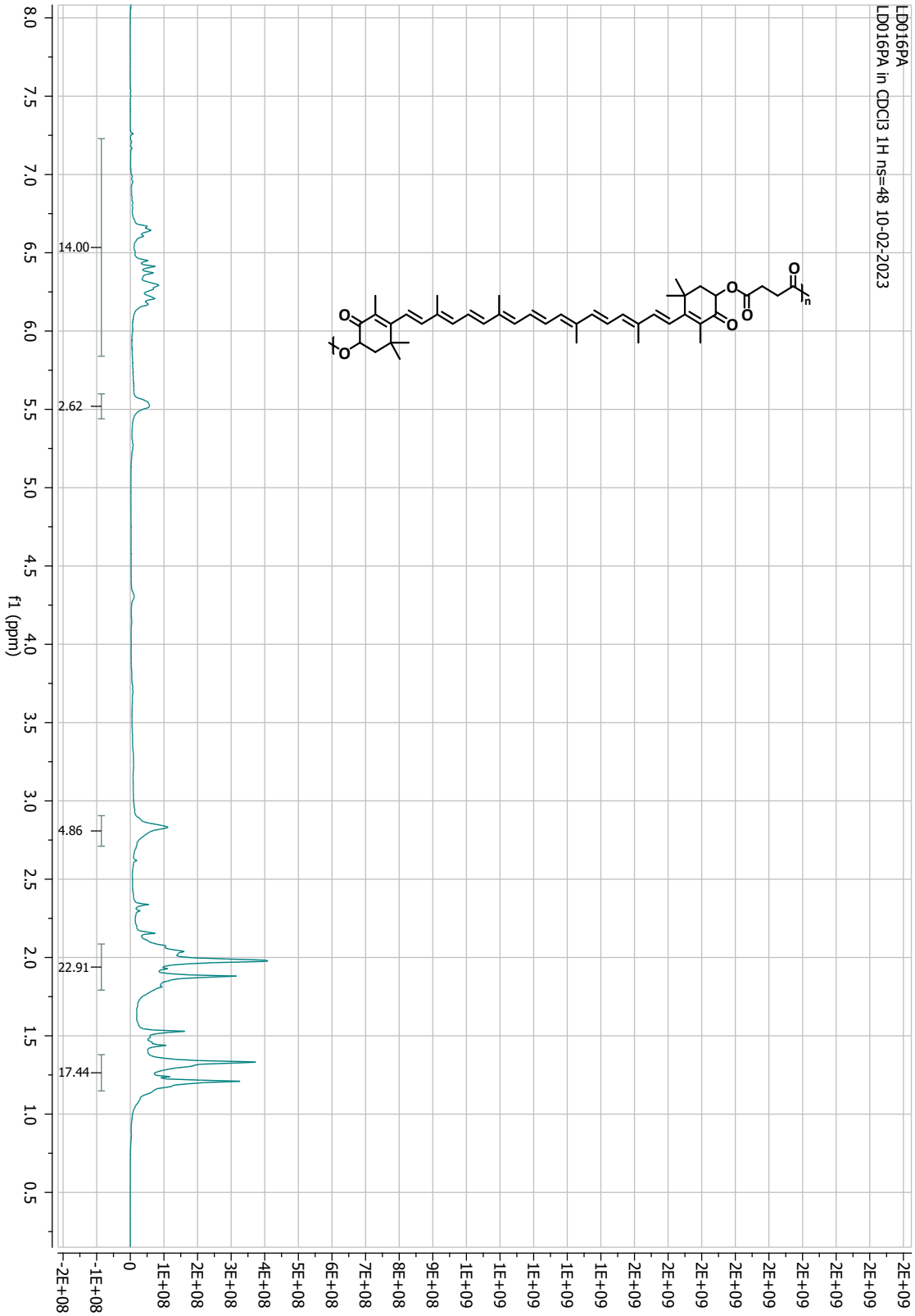

Figure 3. 23 *^{1}H NMR in $CDCl_3$ spectrum of compound (7)*

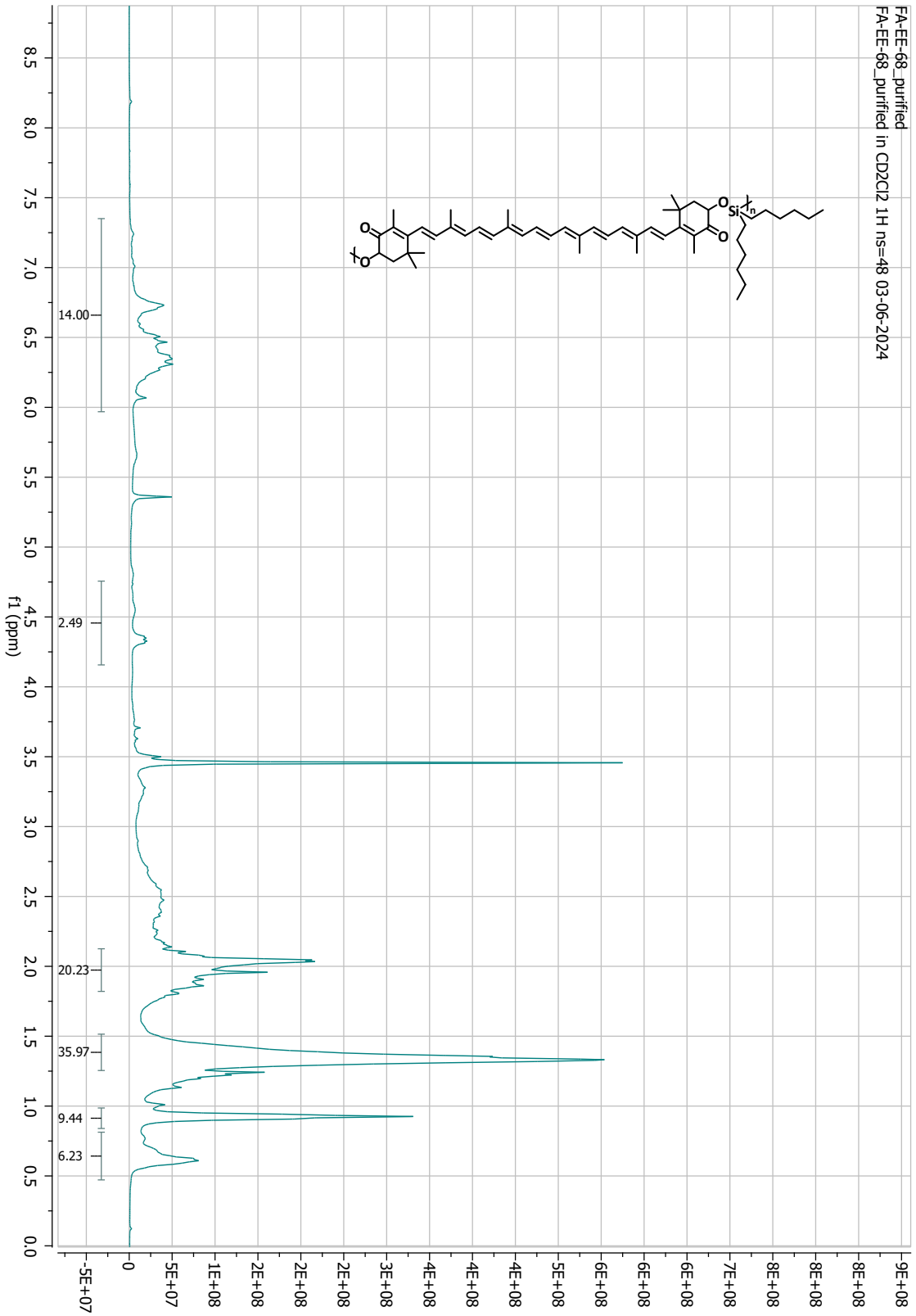

Figure 3. 24 *^{1}H NMR in CD_2Cl_2 spectrum of compound (**8**)*

Bibliography

24. Lilienfeld, J. E. Method and apparatus for controlling electric currents. 4 (1930).
25. Horowitz, G. Organic Transistors. in *Organic Electronics* (ed. Klauk, H.) 1–32 (Wiley, 2006). doi:10.1002/3527608753.ch1.
26. Lamport, Z. A., Haneef, H. F., Anand, S., Waldrip, M. & Jurchescu, O. D. Tutorial: Organic field-effect transistors: Materials, structure and operation. *J. Appl. Phys.* **124**, 071101 (2018).
27. Horowitz, G. Organic thin film transistors: From theory to real devices. *J. Mater. Res.* **19**, 1946–1962 (2004).
28. Chen, X. *et al.* Charge transport in organic field-effect transistors. *Mater. Today Electron.* **6**, 100077 (2023).
29. Chen, H., Zhang, W., Li, M., He, G. & Guo, X. Interface Engineering in Organic Field-Effect Transistors: Principles, Applications, and Perspectives. *Chem. Rev.* **120**, 2879–2949 (2020).
30. Maslennikov, D. R. *et al.* Tuning Molecular Packing, Charge Transport, and Luminescence in Thiophene–Phenylene Co-Oligomer Crystals via Terminal Substituents. *J. Phys. Chem. C* **128**, 9364–9375 (2024).
31. Li, H., Giri, G., Tok, J. B.-H. & Bao, Z. Toward high-mobility organic field-effect transistors: Control of molecular packing and large-area fabrication of single-crystal-based devices. *MRS Bull.* **38**, 34–42 (2013).
32. Klauk, H. Organic thin-film transistors. *Chem. Soc. Rev.* **39**, 2643 (2010).
33. LeBlanc, O. H. Hole and Electron Drift Mobilities in Anthracene. *J. Chem. Phys.* **33**, 626–626 (1960).

34. Kepler, R. G. Charge Carrier Production and Mobility in Anthracene Crystals. *Phys. Rev.* **119**, 1226–1229 (1960).
35. Riede, M., Lüssem, B. & Leo, K. *Comprehensive Semiconductor Science and Technology*. vol. 4 (Elsevier, 2011).
36. Kunkel, C., Margraf, J. T., Chen, K., Oberhofer, H. & Reuter, K. Active discovery of organic semiconductors. *Nat. Commun.* **12**, 2422 (2021).
37. Grundmann, M. *The Physics of Semiconductors: An Introduction Including Nanophysics and Applications*. (Springer International Publishing, Cham, 2021). doi:10.1007/978-3-030-51569-0.
38. Tsidilkovski, I. M. Introduction. in *Band Structure of Semiconductors* 1–10 (Elsevier, 1982). doi:10.1016/B978-0-08-021657-7.50006-6.
39. Griggs, S., Marks, A., Bristow, H. & McCulloch, I. n-Type organic semiconducting polymers: stability limitations, design considerations and applications. *J. Mater. Chem. C* **9**, 8099–8128 (2021).
40. Anthony, J. E., Facchetti, A., Heeney, M., Marder, S. R. & Zhan, X. n-Type Organic Semiconductors in Organic Electronics. *Adv. Mater.* **22**, 3876–3892 (2010).
41. Quinn, J. T. E., Zhu, J., Li, X., Wang, J. & Li, Y. Recent progress in the development of n-type organic semiconductors for organic field effect transistors. *J. Mater. Chem. C* **5**, 8654–8681 (2017).
42. Qu, D., Qi, T. & Huang, H. Acceptor–acceptor-type conjugated polymer semiconductors. *J. Energy Chem.* **59**, 364–387 (2021).
43. Chen, J., Zhang, W., Wang, L. & Yu, G. Recent Research Progress of Organic Small-Molecule Semiconductors with High Electron Mobilities. *Adv. Mater.* **35**, 2210772 (2023).

44. Dong, H., Wang, C. & Hu, W. High performance organic semiconductors for field-effect transistors. *Chem. Commun.* **46**, 5211 (2010).

45. Kang, J., Shin, N., Jang, D. Y., Prabhu, V. M. & Yoon, D. Y. Structure and Properties of Small Molecule−Polymer Blend Semiconductors for Organic Thin Film Transistors. *J. Am. Chem. Soc.* **130**, 12273–12275 (2008).

46. Sawatzki-Park, M., Wang, S.-J., Kleemann, H. & Leo, K. Highly Ordered Small Molecule Organic Semiconductor Thin-Films Enabling Complex, High-Performance Multi-Junction Devices. *Chem. Rev.* **123**, 8232–8250 (2023).

47. Noriega, R. *et al.* A general relationship between disorder, aggregation and charge transport in conjugated polymers. *Nat. Mater.* **12**, 1038–1044 (2013).

48. Seifrid, M., Reddy, G. N. M., Chmelka, B. F. & Bazan, G. C. Insight into the structures and dynamics of organic semiconductors through solid-state NMR spectroscopy. *Nat. Rev. Mater.* **5**, 910–930 (2020).

49. Giannini, S., Carof, A. & Blumberger, J. Crossover from Hopping to Band-Like Charge Transport in an Organic Semiconductor Model: Atomistic Nonadiabatic Molecular Dynamics Simulation. *J. Phys. Chem. Lett.* **9**, 3116–3123 (2018).

50. Zahabi, N. & Zozoulenko, I. Band Versus Hopping Transport in Conducting Polymers by Ab Initio Molecular Dynamics: Exploring the Effect of Electric Field, Trapping and Temperature. *Adv. Electron. Mater.* **11**, 2400239 (2025).

51. Kang, J., Shin, N., Jang, D. Y., Prabhu, V. M. & Yoon, D. Y. Structure and Properties of Small Molecule−Polymer Blend Semiconductors for Organic Thin Film Transistors. *J. Am. Chem. Soc.* **130**, 12273–12275 (2008).

52. Ruiz-Anchondo, T., Flores-Holguín, N. & Glossman-Mitnik, D. Natural Carotenoids as Nanomaterial Precursors for Molecular Photovoltaics: A Computational DFT Study. *Molecules* **15**, 4490–4510 (2010).

53. Hug, H., Bader, M., Mair, P. & Glatzel, T. Biophotovoltaics: Natural pigments in dye-sensitized solar cells. *Appl. Energy* **115**, 216–225 (2014).

54. Singh, A. & Mukherjee, T. Application of carotenoids in sustainable energy and green electronics. *Mater. Adv.* **3**, 1341–1358 (2022).

55. Olsina, J., Durchan, M., Minofar, B., Polivka, T. & Mancal, T. Absorption Spectra of Astaxanthin Aggregates. Preprint at https://doi.org/10.48550/arXiv.1208.4958 (2012).

56. Middleton, H., Tempelaar, S., Haddleton, D. M. & Dove, A. P. Organocatalytic synthesis of astaxanthin-containing poly(lactide)s. *Polym Chem* **2**, 595–600 (2011).

57. Virchenko, O. & Stefánsson, T. Light Increases Astaxanthin Absorbance in Acetone Solution through Isomerization Reactions. *Molecules* **28**, 847 (2023).

58. De Bruijn, W. J. C., Weesepoel, Y., Vincken, J.-P. & Gruppen, H. Fatty acids attached to all-trans-astaxanthin alter its cis–trans equilibrium, and consequently its stability, upon light-accelerated autoxidation. *Food Chem.* **194**, 1108–1115 (2016).

59. Camino, G., Lomakin, S. M. & Lageard, M. Thermal polydimethylsiloxane degradation. Part 2. The degradation mechanisms. *Polymer* **43**, 2011–2015 (2002).

60. McGeary, M. J., Wedlich, R. C., Coan, P. S., Folting, K. & Caulton, K. G. Synthesis and thermal decomposition of copper(I) silyloxide complexes. X-ray crystal structures of [Cu(OSiPh3)]4 and [Cu(OSiPh3)(PMe2Ph)]2. *Polyhedron* **11**, 2459–2473 (1992).

61. Xiao, S., Cui, X. & Iroh, J. O. A Study of the Degradation Mechanism of Ladder-like Polyhedral Oligomeric Silsesquioxane via Fourier Transform Infrared Spectroscopy. *Fire* **6**, 429 (2023).

62. Zhang, W. & Lang, R. Succinate metabolism: a promising therapeutic target for inflammation, ischemia/reperfusion injury and cancer. *Front. Cell Dev. Biol.* **11**, 1266973 (2023).
63. Molteni, C., La Motta, C. & Valoppi, F. Improving the Bioaccessibility and Bioavailability of Carotenoids by Means of Nanostructured Delivery Systems: A Comprehensive Review. *Antioxidants* **11**, 1931 (2022).
64. Petry, F. C. & Mercadante, A. Z. Bile amount affects both the degree of micellarization and the hydrolysis extent of carotenoid esters during *in vitro* digestion. *Food Funct.* **10**, 8250–8262 (2019).
65. Zhang, W. & Lang, R. Succinate metabolism: a promising therapeutic target for inflammation, ischemia/reperfusion injury and cancer. *Front. Cell Dev. Biol.* **11**, 1266973 (2023).
66. Yang, C. *et al.* Bioaccessibility, Cellular Uptake, and Transport of Astaxanthin Isomers and their Antioxidative Effects in Human Intestinal Epithelial Caco-2 Cells. *J. Agric. Food Chem.* **65**, 10223–10232 (2017).
67. Kistler, A. *et al.* Metabolism and CYP-inducer properties of astaxanthin in man and primary human hepatocytes. *Arch. Toxicol.* **75**, 665–675 (2002).

Chapter 4
Introducing RAFT pendants on isoindigo core

"The best way to have a good idea is to have lots of ideas and share them."

Linus Pauling

The isoindigo core, long valued for its electronic stability, is reimagined as a platform for controlled growth. Through RAFT chemistry, short oligomers of PDMA and polystyrene are grafted onto its backbone, transforming ordinary side chains into functional extensions that guide structure and performance. Two chemistries, one hydrophilic and flexible, the other hydrophobic and rigid, are connected, defining how the material organises, interacts, and conducts. This gives rise to isoindigo-based materials designed for both OECTs and OFETs, where control at the molecular level becomes the key to multifunctional behaviour.

4.1 Introduction

This part of the project represents a transversal research effort aimed at developing alternative side-chain architectures for isoindigo-based semiconducting polymers intended for use as active materials in OFET and OECTs. It was carried out within the research group where I conducted my doctoral studies, in close collaboration with a postdoctoral researcher.

The project originated from the convergence of our respective areas of expertise: the chemistry of organic semiconductors and the controlled synthesis of polymeric side chains via Reversible Addition–Fragmentation Chain Transfer (RAFT) polymerization. By combining these two domains, the primary motivation is to identify new polar side chains capable of supporting mixed ionic-electronic conduction while avoiding the extensive reliance on PEG substituents[68]: they currently are the most common strategy to enhance ionic transport and water compatibility in conjugated polymers operating in accumulation mode, yet they also impose certain limitations in terms of synthetic flexibility, long-term stability, and control over interfacial interactions.[69] To address these aspects, this work combines the classical synthetic approaches of conjugated polymer chemistry with RAFT,[70] a living radical polymerisation technique. In contrast to its conventional application in preparing high-molecular-weight polymers, RAFT polymerisation is here exploited (although with its limitations) to synthesise short, oligomeric segments[71] that can be covalently attached as side chains to the conjugated backbone. This approach enables a systematic fine-tuning of side-chain polarity, length, and composition.

4.1.1 An introduction to Organic Electrochemical Transistors (OECTs)

During the last decade, the rapid development of the field of bioelectronics has accelerated the emergence of new platforms capable of acting as interfaces between biological and electronic systems. Since biological systems rely on ions and neutral molecules for communication, signalling, and the regulation of physiological states,[72,73] hybrid devices able to translate biological signals into electronic ones — or vice versa — through ionic signalling have become crucial. Such technologies enable more effective sensing, recording, and monitoring of biological activity.[74] Organic electronic devices have thus gained significant attention as effective translators between the signals and functions of biological systems and those required by human-made electronic technologies. Their capability to conduct and process both electronic and ionic signals is enabled by the intimate coupling between ionic motion and electronic charge compensation. Furthermore, the chemical versatility of organic molecules and polymers allows for precise control over their physical, mechanical, and interfacial properties. Through molecular design and synthesis, materials can be engineered to exhibit tailored morphology, flexibility, and elasticity, along with

surface chemistries that ensure biocompatibility and long-term operational stability.[75] The ability of a material to conduct electrons and ions simultaneously is known as *mixed conductance*, and organic compounds capable of absorbing and transporting both types of charge carriers are classified as organic mixed ionic and electronic conductors (OMIECs).[76] Conjugated polymers constitute an ideal platform for such behaviour: their π-conjugated backbone supports efficient electronic transport, while their bulk structure can accommodate the motion of ions.[77] This dual transport capability has enabled the development of a wide range of innovative electronic devices, among which the organic electrochemical transistor (OECT) stands out as a particularly versatile example. OECTs effectively translate ionic biological signals into electronic outputs and provide substantial signal amplification, a feature that arises directly from the interaction between electrolyte ions and the active OMIEC material throughout its volume.[78] An OECT consists of an organic semiconductor film in direct contact with an electrolyte, within which a gate electrode is immersed.[79,80] The conductive channel, formed by the organic material, is connected to two metallic electrodes, termed the source (S) and drain (D) , which allow the flow of charge carriers (electrons or holes) across the channel (Figure 4.1).

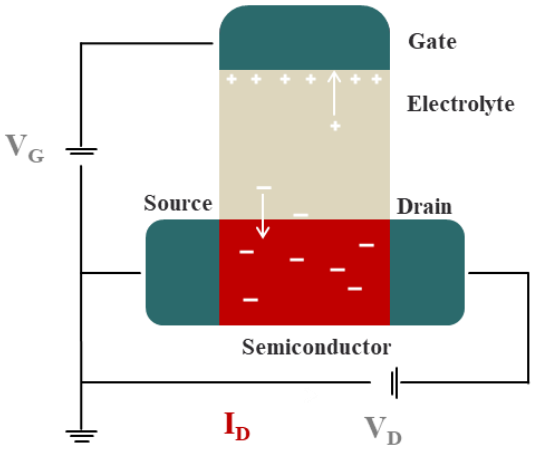

Figure 4. 1 *Schematic representation of the typical structure of an organic electrochemical transistor (OECT), showing the source (S), drain (D), electrolyte, OMIEC and gate (G)*

A defining feature of OECTs, in contrast to conventional OFETs or inorganic semiconductors, is that, thanks to OMIEC capability of ion infiltration,[81] conductivity modulation occurs through the injection of ions from the electrolyte into the bulk of the channel, thereby altering its oxidation state and overall conductivity.[82] Device operation is

governed by the voltages applied to the gate (V_G) and the drain (V_D), measured relative to the source; the gate voltage controls ionic injection, while the drain voltage induces a current (I_D) proportional to the number of mobile charge carriers in the channel.

4.1.1.1 Charge Transport and Operational Principles of OECTs

Depletion and accumulation mode

OECTs can operate in either depletion or accumulation mode, depending on the intrinsic doping of the channel material and the polarity of the applied gate voltage.[79,82]

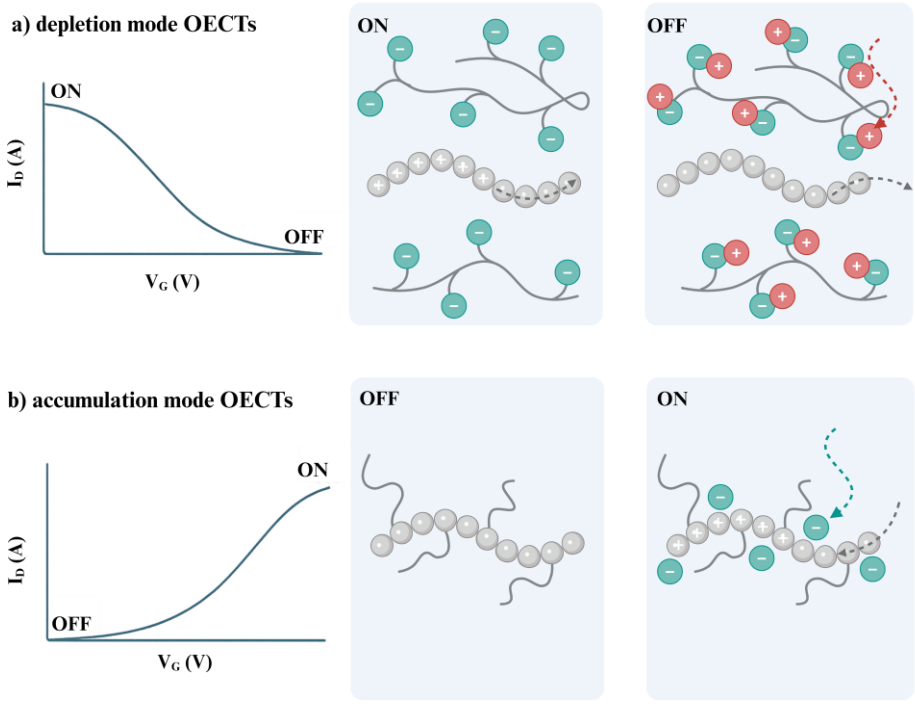

Figure 4. 2 *a) Transfer curve showing depletion-mode operation of an OECT with a conducting polymer channel. At zero gate voltage, holes on the conducting polymer contribute to a high drain current, and the transistor is ON. When a gate voltage is applied, the holes are replaced by cations, and the transistor is OFF; b) Transfer curve showing accumulation-mode operation of an OECT with a semiconducting polymer channel. At zero gate voltage, the channel has few mobile holes and the transistor is OFF. When a gate voltage is applied, holes accumulate and compensate for the injected anions, and the transistor is ON.*

In depletion-mode devices, the channel is initially highly conductive due to the presence of mobile carriers (e.g., holes in PEDOT:PSS), and application of a gate voltage induces the injection of counter-ions from the electrolyte, which compensate the existing carriers and reduce the channel conductivity, switching the transistor from ON to OFF. Conversely,

accumulation-mode OECTs feature a channel with a low initial carrier density; in this case, gating injects ions that electrochemically dope the channel, increasing carrier concentration and turning the device ON (Figure 4.2).[83] The dynamics of ion injection and redistribution govern the temporal response of the transistor: ions migrate from the electrolyte into the channel under the influence of the gate potential, modulating the bulk conductivity.

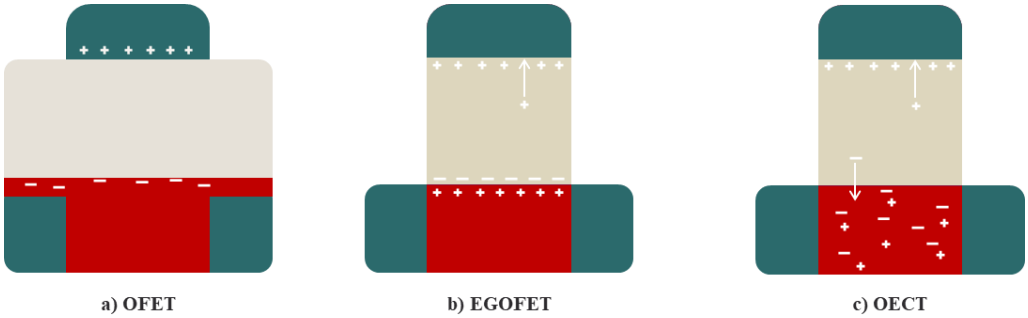

Figure 4. 3 *Schematic of the three device types. A) In OFETs, the gate voltage induces carriers at the semiconductor–dielectric interface; b) In EGOFETs, a liquid electrolyte forms an electric double layer at the interface, enhancing interfacial charge accumulation; c) In OECTs, ions penetrate the bulk of the semiconductor, modulating the volumetric doping and enabling large drain current changes at low gate voltages.*

The spatial distribution of these ions throughout the channel thickness gives rise to the volumetric gating characteristic of OECTs, in contrast to conventional FETs or electrolyte gated field effect transistors (EGOFET), where charge modulation occurs primarily at the interface (**Figure 4.3**).[84]

Device Physics of OECTs

The operation of OECTs is based on their ability to transduce small variations in gate voltage into large modulations of the drain current. This relationship is described by the transfer curve, which represents the dependence of the drain current (I_D) on the gate voltage (V_G). The slope of this curve defines the transconductance (*Equation 4.1*)

$$(4.1) \quad g_m = \partial I_D / \partial V_G$$

a key parameter quantifying the amplification efficiency of the device. OECTs exhibit remarkably high transconductance values, due to their *volumetric gating mechanism*,[78] in

which ions penetrate and modulate the entire semiconductor bulk rather than only an interfacial region, as in conventional FETs. A quantitative basis for OECT operation is provided by the Bernards model, which describes the device as two coupled circuits: an electronic circuit (**Figure 4.4a**), corresponding to the source – channel – drain pathway (modelled as a variable resistor following Ohm's law), and an ionic circuit (**Figure 4.4b**), representing the gate – electrolyte – channel configuration.

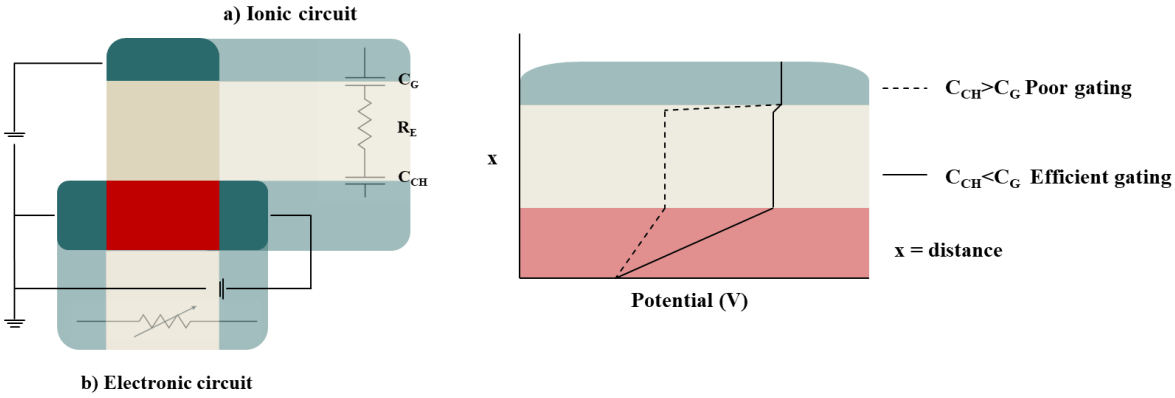

Figure 4. 4 *Schematic representation of a) ionic and b) electronic circuits used to model OECTs. The ionic circuit (a) consists of capacitors corresponding to the channel (C_{CH}), and gate, (C_G), respectively, and a resistor corresponding to the electrolyte (R_E). The electronic circuit (b) is modelled as a resistor with a resistance that varies upon gating. The panel on the right shows the distribution of potential in the ionic circuit. The solid line corresponds to the case of efficient gating, in which most of the applied gate voltage drops at the electrolyte-channel interface, driving ions inside the channel. The dashed line corresponds to the case of poor gating, where most of the applied gate voltage drops at the gate–electrolyte interface.*

The ionic circuit comprises a resistor associated with ion transport through the electrolyte and a capacitor describing ionic accumulation in the channel. In this model, the gate voltage drives ions from the electrolyte into the channel, where they balance the existing electronic charges without undergoing any chemical reactions with the semiconductor. Once the ions are fully distributed and the channel is stabilised, the gate current drops to nearly zero, and the drain current reflects the new equilibrium doping of the channel.[79] The Bernards model provides a reliable description of OECT output characteristics and allows quantitative prediction of the transconductance (g_m). For depletion-mode devices operating in saturation, it is expressed through *Equation 4.2*

$$(4.2) \quad g_m = \frac{W}{L} d\,\mu\,C^*\,(V_{\mathrm{Th}} - V_G),$$

where W, L, and d respectively are the channel width, length, and thickness; μ is the charge-carrier mobility; $C^*$is the volumetric capacitance of the channel; and $V_{\mathrm{Th}}$is the threshold voltage. For accumulation-mode devices, the voltage terms are reversed. This equation is analogous to that of a conventional FET, with the key difference that the product $d \cdot C^*$ replaces the areal capacitance (C').[85] The volumetric gating mechanism thus enables OECTs to achieve superior amplification compared with other transistor technologies.

However, high transconductance comes at the cost of slower operation. According to the Bernards model, the response time is limited by either the electronic or ionic circuits, with most devices being dominated by the ionic pathway. In this case, the response time is determined by the product of the electrolyte resistance and the channel capacitance, the latter being proportional to the channel thickness. Consequently, thicker channels reduce the device speed. Therefore, channel thickness can be strategically adjusted to balance the trade-off between gain and bandwidth, optimising OECT performance for specific applications.[86]

4.1.1.2 Organic Mixed Ionic - Electronic Conductors as active layer for OECTs

As already stated (*see chapter 4.1.1*), OMIECs are a class of soft organic materials that simultaneously conduct electronic and ionic charges, enabling volumetric modulation of electronic conductivity when ions from an electrolyte penetrate the material. Unlike conventional organic semiconductors or field-effect transistors, where charge accumulation occurs primarily at the interface, OMIECs allow ions to permeate the bulk of the polymer, modulating the charge density throughout the volume. This unique property underlies the high transconductance, large volumetric capacitance, and efficient signal amplification observed in devices such as OECTs, bioelectronic sensors, and neuromorphic circuits. The design of OMIECs requires careful balance between electronic transport, ionic accessibility, and morphological stability under repeated ion injection, swelling, or hydration, which can otherwise degrade device performance.[80,87]

Material Classes of OMIECs

OMIECs are typically categorized along two dimensions: whether the material intrinsically contains fixed ionic groups, and whether ionic and electronic transport pathways are spatially segregated (heterogeneous) or co-localized within a single mixed-conducting phase (homogeneous) (**Figure 4.5**).

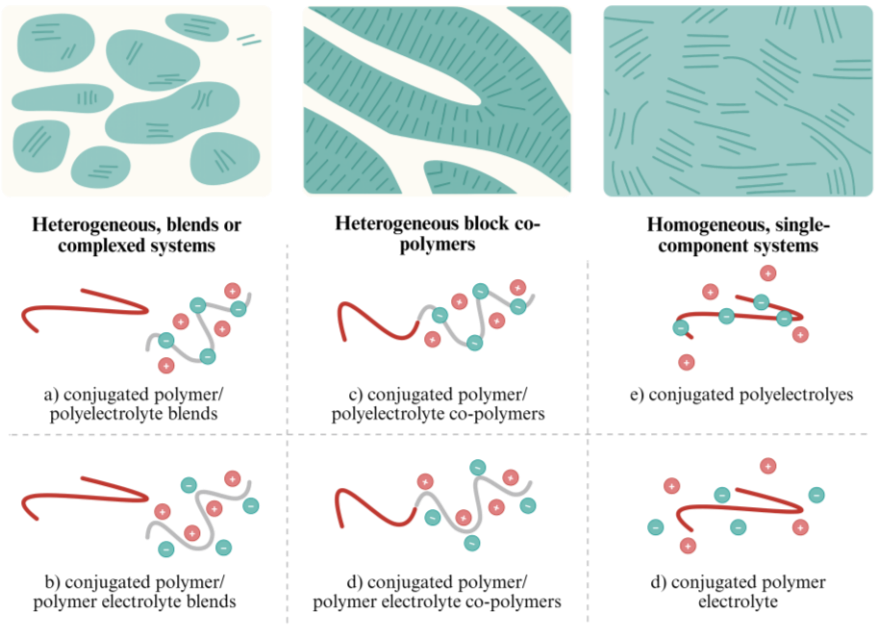

Figure 4. 5 *Heterogeneous blends of a conjugated polymer with (a) a polyelectrolyte or (b) an ion-solvating polymer electrolyte, forming largely disordered phase-separated morphologies; block copolymers combining a conjugated segment with (c) a polyelectrolyte or (d) an ion-solvating segment, yielding more ordered, tuneable microphase-separated structures; homogeneous OMIECs based on fully conjugated (e) polyelectrolytes or (f) ion-solvating polymers, forming a single mixed-conducting phase. Sketches illustrate ionic components (grey), electronic components (red), cations (pale red), and anions (cyan).*

The intersection of these criteria yields six widely recognized OMIEC types. Heterogeneous OMIECs include blends of conjugated polymers with polyelectrolytes (a),[88,89] blends with solid polymer electrolytes (b), and block OMIECs (types c, d), in which electronically conducting and ion-conducting segments are covalently linked and self-assemble into phase-separated morphologies. Homogeneous OMIECs (e, f) incorporate ionic or polar functionalities directly along the molecular backbone or side chains, thereby forming a single, continuous mixed-conducting phase. This classification provides a useful basis for understanding how chemical structure and morphology influence ionic uptake, electronic charge transport, and volumetric doping in OMIEC-based devices.

Coupled Processes in OMIECs

In OMIECs, ionic and electronic transport may occur homogeneously within a single mixed-conducting phase or be spatially segregated between microphase-separated regions enriched in solid electrolyte or conjugated polymer, respectively (**Figure 4.6**). Consequently, ionic-electronic coupling can also manifest uniformly throughout the material, be confined to the interfaces between these domains, or follow more complex hierarchical pathways. Importantly, these interactions take place throughout the bulk of the material, giving rise to intrinsically volumetric behaviour at the device level. Unlike classical electrochemical or semiconductor systems, where functionality is dominated by two-dimensional interfaces, OMIECs operate through three-dimensional, volumetric interfaces in which electronic carriers and ions interact.[90]

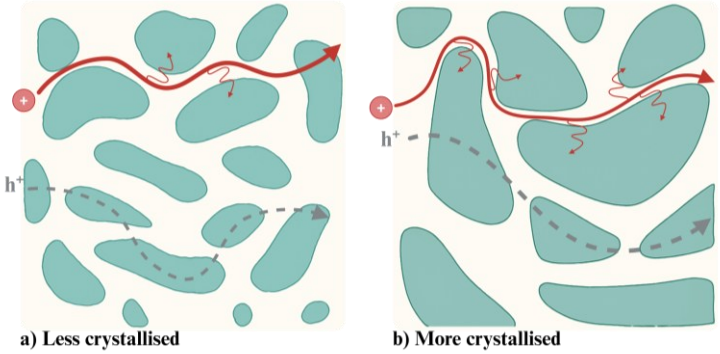

Figure 4. 6 *Schematic representing film microstructure of PEDOT:PSS. Electron transport takes place in (semi)crystalline regions of the polymer, featuring π-π stacking, while ionic transport occurs in the amorphous regions subject to swelling upon hydration.*

The description of ionic-electronic coupling in OMIECs remains a topic of ongoing discussion, yet one fundamental principle is universally accepted: electroneutrality must always be maintained. The presence of electronic charge within an OMIEC requires stabilization by an oppositely charged excess ionic species (net ionic charge). This mutual compensation, commonly referred to as doping, increases the electronic conductivity of the material. OMIECs containing fixed ionic groups are on the other hand intrinsically doped. These materials can only be de-doped through the incorporation of mobile counter-ions that neutralize the fixed charges (**Figure 4.7**).

In some systems, ionic-electronic coupling occurs through direct charge-transfer reactions, (e.g., the protonation of polyaniline) which stabilizes electronic charge. At equilibrium and in the absence of an applied potential, the concentration of electronic charge and its counterbalancing ionic charge is governed by the energetic positions of the molecular orbitals. A sufficiently shallow HOMO favours stabilization of holes by excess anions, giving rise to p-type doping. Conversely, a deep LUMO favours the stabilization of electrons by excess cations, resulting in n-type doping.[80,87]

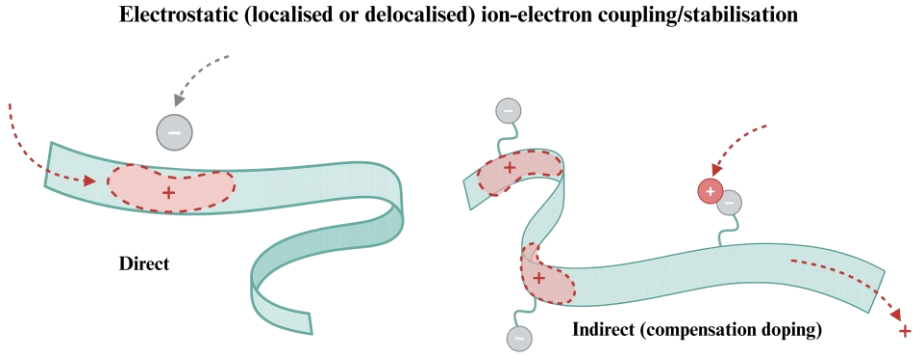

***Figure 4.** 7 Schematic representation of ionic-electronic interactions: charge coupling/stabilization through electrostatic interactions*

OMIECs, like many π-conjugated organic semiconductors, are held together by van der Waals interactions and typically exhibit considerable structural disorder. Their conjugated backbones support delocalized π-electrons, but disorder restricts delocalization and intermolecular coupling, so charge transport usually occurs through thermally activated hopping between localized states.[91] In the undoped state, the low density of carriers and accessible hopping sites results in low mobility and poor conductivity. Because OMIECs inherently couple ionic and electronic charges, doping is often substantial and can span several orders of magnitude under device operation.[92] Carrier mobility depends non-monotonically on doping level: at low concentrations, dopant ions act as Coulombic traps; with increasing doping, hopping barriers decrease and mobility rises, approaching diffuse band-like transport in some systems; at very high doping, additional disorder re-localizes carriers and mobility plateaus or declines.[93]

Ionic transport is more complex than electronic transport as multiple ionic species may coexist; ions can be multivalent or form clusters, and their mobility is strongly influenced by solvation. The total ionic conductivity reflects the combined contributions of all mobile

ions, whose mobilities relate to their diffusivities through the Einstein relation (*Equation 4.3*)

$$D = \frac{\mu k_B T}{e} \quad (4.3)$$

Where D is the ion diffusivity, μ is the ion mobility, k_B is the Boltzmann's constant, T is the temperature and e is the elementary charge. In dry OMIECs, ionic motion typically occurs through thermally activated hopping coupled to the segmental dynamics of the polymer backbone or side chains. Depending on the OMIEC class, either one or both ionic species may be mobile. Hydration dramatically enhances ion mobility: even small amounts of water can increase mobility by several orders of magnitude by facilitating segmental motion and solvation.[94] When swollen by liquid electrolyte, ion transport becomes much faster and is dominated by the vehicle mechanism of solvated ions; in aqueous environments, proton transport can be even more rapid via the Grotthuss mechanism (**Figure 4.8**).[77]

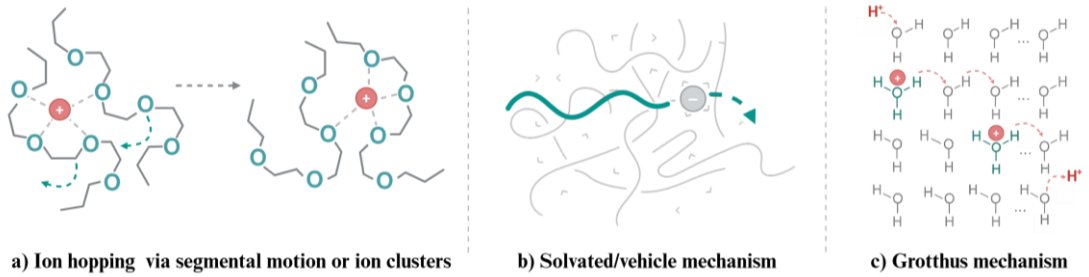

Figure 4. 8 *Ionic charge transport mechanism: segmental motion-assisted ion hopping (a), solvated ion vehicle transport (b) and Grotthuss mechanism of proton hopping (b). Ionic species are shown in red (positive) or grey (negative).*

Beyond the general considerations on ionic transport described above, additional factors further shape ion motion in OMIECs. The chemical structure of the polymer backbone and side chains can strongly influence ion dissociation and mobility. In particular, incorporating coordinating heteroatoms (e.g., oxygen or nitrogen) within the conductive pathway enhances ion dissociation by stabilizing the charge of the free ion. Nonconjugated polymers such as poly(ethylene oxide) (PEO) exemplify this effect: their high chain flexibility enables coordination with a variety of cations (Na^+, Li^+, Mg^{2+}, K^+), resulting in relatively high ionic conductivities, although crystallization significantly suppresses transport below the melting

temperature. Ionic motion in such systems has been described as reptation-assisted hopping along the polymer backbone. Analogous behaviour has been proposed for conjugated OMIECs, where ions move through hopping processes coupled to segmental motions of the polymer matrix, particularly in dry or minimally hydrated films. Introducing ion-coordinating moieties within the OMIEC can enhance this segmental-motion–assisted transport by promoting ion dissociation and increasing the density of accessible hopping sites.[68,95]

4.1.1.3 Side-chin engineering in OMIECs: OEG and other ionic side chains

As already stated, the mixed conduction performance of conjugated polymers is dictated not only by the electronic structure of the π-conjugated backbone but also by the chemistry and architecture of the sidechains.[96] The role of sidechains in shaping OMIEC behaviour has received little attention, even though structural modifications, such as the incorporation of ethylene glycol (EG) units or ionic functionalities, strongly influence swelling, ion uptake, and overall mixed conduction. Indeed, sidechains directly affect ion mobility, electronic conductivity, and long-term device stability.

Oligo ethylene glycol side chains

Among sidechains, EG-based sidechains (with or without intervening alkyl spacers) have become particularly prevalent. Their popularity arises from several advantages. The ether oxygen atoms within glycolated side chains efficiently coordinate and solvate a broad range of ionic species, thereby boosting ion mobility within the polymer matrix. This coordination capability enables rapid ion insertion and migration, yielding significantly faster doping kinetics than those observed in polythiophenes bearing purely alkyl sidechains. Moreover, doping dynamics can be further accelerated by increasing the number of oxygen atoms in the sidechain or by positioning these oxygen sites farther from the conjugated backbone, which enhances solvation volume and ion accessibility.[97]

Second, the hydrophilic nature of ethylene-glycol-containing sidechains promotes water and ion uptake, which can significantly influence mixed conduction. However, excessive hydrophilicity leads to substantial water uptake, which can compromise efficient ion

insertion and ultimately reduce C*. Moreover, uncontrolled swelling may disrupt the interconnectivity between crystalline domains, thereby limiting electronic mobility. The incorporation of hydrophilic glycolated sidechains not only enhances ion transport but may also alter the fundamental doping mechanism. In p-type OMIECs, doping is classically considered to occur through anion uptake accompanied by solvent penetration. However, passive swelling can enable cation uptake as well.[98] Overall, while ethylene glycol sidechains can significantly enhance doping kinetics, ion uptake, and C*, they also introduce a critical trade-off: excessive swelling, water uptake, and morphological disruption can diminish electronic mobility and undermine device stability.

Alkyl spacers

A widely adopted strategy for balancing the trade-off between μ and C* is the careful tuning of alkyl spacer length within the sidechain architecture. Increasing the distance between the conjugated backbone and the coordinating moieties reduces excessive hydration and suppresses disruptive swelling, thereby helping to preserve thin-film morphology and stabilize mixed conduction.

Ionic and hybrid side chains

While EG sidechains have become widespread due to their favourable effects on ion transport and doping kinetics, their dominance may have limited exploration of alternative sidechain chemistries.[99] Incorporating ionic sidechains offers a complementary strategy to modulate ion uptake, swelling, and mixed conduction in OMIECs. (e.g., carboxylic-acid and ester-functionalized sidechains).
Another strategy consist in combining spacer units (alkyl or glycol) with ionic moieties or incorporating zwitterionic groups enables controlled swelling, preserves structural integrity, and enhances electronic transport. Zwitterionic sidechains on the other hand offer intrinsic charge neutrality, enabling ionic conduction without substantial volumetric changes, thereby preserving electrochemical reversibility, increasing redox stability, and enhancing mixed conduction in physiological electrolytes.[100]

4.2 Aim of the work

The primary aim of this work was to explore novel side-chain engineering strategies for isoindigo-based semiconducting polymers, targeting applications in OFETs and OECTs. Specifically, the project sought to introduce RAFT-active oligomeric pendants, hydrophilic OligoDMA and hydrophobic OligoSty, onto the isoindigo core, in order to systematically investigate how side-chain chemistry and architecture influence ionic and electronic transport, film morphology, and interfacial properties.

Two complementary synthetic strategies were evaluated: (1) Grafting-from approach: esterification of the RAFT chain transfer agent (BTPA) directly onto the hydroxyl-functionalized isoindigo to create a bis-macroCTA, followed by attempted polymerisation of monomers directly from the core; (2) Grafting-to approach: independent synthesis of oligomeric chains via RAFT polymerisation, followed by their attachment to the isoindigo core through acid-catalysed esterification.

Through these strategies, the work aimed to establish a versatile platform for precision functionalization of conjugated cores and to provide fundamental insights into the challenges and limitations of grafting oligomeric side chains onto sterically hindered conjugated monomers. This effort is particularly innovative with respect to the introduction of OligoDMA, which, to the best of our knowledge, has not been previously explored as a side chain for OECT-active conjugated polymers.

4.3 Results and discussion

4.3.1 Literature background

4.3.1.1 Isoindigo as acceptor unit for semiconductive polymers

Isoindigo is a structural isomer of the industrial dye *indigo* and can be directly isolated from natural sources.[101] The two molecules differ in the relative positions of the nitrogen and carbonyl groups: whereas indigo features nitrogen atoms that are not directly connected to the carbonyl groups, isoindigo is characterized by each nitrogen being directly bonded to a carbonyl. Indigo was first reported as an active layer material for organic field-effect transistors (OFETs) in 2012, showing well-balanced ambipolar transport.[102]

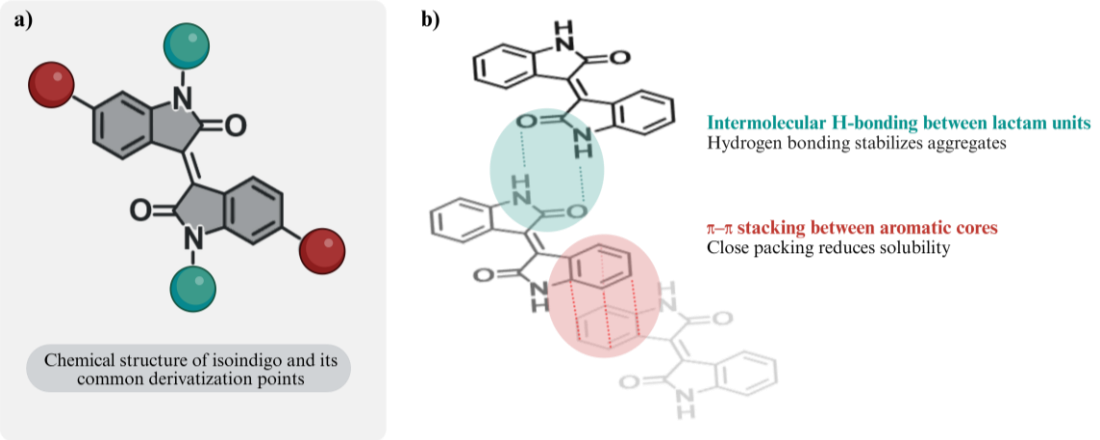

Figure 4. 9 *a) Chemical structure of isoindigo and key points of functionalization; b) molecular arrangement showing its two main interactions: intermolecular hydrogen bonding (cyan dotted lines and area) between the lactam units, which stabilizes molecular aggregates, and π–π stacking interactions (red dotted lines and area) between aromatic cores, promoting further aggregation and crystalline order. This illustration highlights how isoindigo self-organizes through hydrogen bonding and π–π interactions, which are crucial for its optical and electronic properties.*

However, the strong intermolecular hydrogen bonding present in indigo results in very low solubility. Introducing solubilizing side chains onto the nitrogen atoms can improve processability but, at the same time can disrupt the intermolecular hydrogen-bond network responsible for its structural order, which negatively affects conjugation and charge transport. In isoindigo, however, N-alkylation does not interfere with the key structural interactions that preserve its planar, conjugated backbone. The unique structure of isoindigo imparts a strong electron withdrawing character owing to conjugation of the lactam rings in conjunction with an extended delocalized π -system throughout the bis-oxindole

framework.[103] As a result, isoindigo can be functionalized for solubility without sacrificing its electronic properties, making it a superior building block for organic electronics (**Figure 4.9**).[104] It has attracted attention, particularly in donor–acceptor (D-A) type polymers, due to its straightforward synthesis and good stability under ambient conditions. However, isoindigo is one of the less explored building blocks in OMIECs and it has only recently gained interest in this research area.[105,106] Its highly planar structure promotes strong π–π stacking and backbone planarity, which is beneficial for electronic conduction but can hinder ion insertion. Such strong aggregation has often limited the use of isoindigo in OMIEC design, as an ideal mixed conductor must efficiently accommodate both ionic species and electronic charge carriers.[107] Consequently, isoindigo remains less studied compared to other, less crystalline cores such as ethylenedioxythiophene (EDOT) and diketopyrrolopyrrole (DPP). In these D-A polymers, copolymerization provides a strategy to combine monomers with different side chains, enabling polymer structures that support mixed conduction. A combination of hydrophobic long alkyl chains and hydrophilic side chains, such as ethylene glycol, is commonly used to improve solubility for solution processing while enhancing electrolyte uptake and ionic transport.[108] In the case of isoindigo, copolymerization often increases the extent of π-π stacking, which poses additional challenges for its incorporation into OMIECs. Successful examples of isoindigo-based mixed conductors have therefore relied on copolymerizing with monomers designed to disrupt chain planarity and aggregation, thereby maximizing electrolyte penetration and redox activity.[109]

4.3.1.2 Rationale for the introduction of OligoDMA and polystyrene side chains on IIG core

Poly(N,N-dimethylacrylamide) (PDMA) is a hydrophilic, non-ionic polymer whose amide functionality enables extensive hydrogen bonding and strong affinity for aqueous and polar environments. While PDMA has been primarily explored in biomedical and hydrogel systems, where it provides high water uptake, ion mobility, and biocompatibility, its physicochemical properties can also be highly relevant for mixed ionic-electronic conductors. In particular, PDMA networks have been shown to support efficient ion

transport through reversible ion–dipole interactions and water-mediated pathways, while maintaining mechanical integrity and environmental stability.[110]

Recent literature highlights the primary role of side-chain engineering in optimising the performance of OECTs, emphasising how the incorporation of hydrophilic, non-ionic side chains can enhance ionic transport and device stability.[77,111] When incorporated as short oligomeric side chains in a conjugated polymer matrix, Oligo(N,N-dimethylacrylamide) (OligoDMA) could introduce localised hydrophilic domains resulting in ionic penetration in the semiconducting layer when in contact with an electrolyte medium. Such a strategy is aligned with the requirements of OMIEC for OECTs (**Figure 4.10**), where efficient coupling between ionic and electronic transport is essential for device performance.

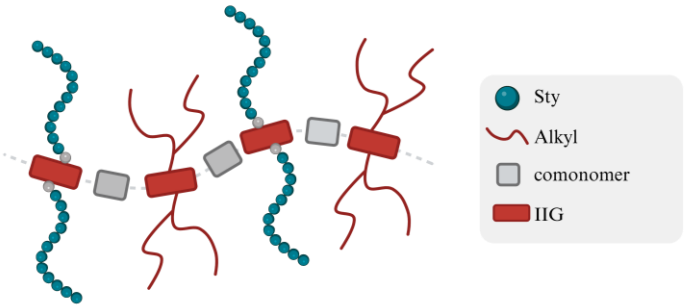

Figure 4. 10 *Schematic representation of an OligoDMA-containing IIG-based semiconductive polymer as a conductive layer of an OECT*

Therefore, OligoDMA-based side chains offer a promising alternative to the commonly used PEG units, potentially improving ionic accessibility while avoiding issues related to oxidative instability and uncontrolled swelling.[69]

Oligostyrene (OligoSty) grafts have been explored as side-chain motifs on isoindigo-containing conjugated polymers and provide a useful experimental precedent for hydrophobic, rigid side-chain engineering. Introducing polystyrene grafts onto isoindigo-based backbones yields soluble, processable materials with markedly altered nanomorphology, showing that OligoStyr can be used to tune phase behaviour and film microstructure (**Figure 4.11**).[112] Although direct studies of polystyrene-grafted isoindigo copolymers in OFETs and OECTs are scarce, general side-chain engineering on isoindigo systems indicates that hydrophobic, bulky side chains tend to promote tighter π–π stacking and lamellar order of the conjugated backbone, reduce solvent uptake/swelling in OECTs

and thus limit ion penetration, all factors that strongly influence device behaviour.[68,113] From a microstructural point of view, OligoSty pendants are expected to encourage formation of crystalline or ordered domains of the conjugated backbone (smaller π–π distances, stronger interchain coupling), which typically translates into higher charge-carrier mobility in OFET-type measurements.[113] Differently from OligoDMA, the hydrophobic character and limited ion uptake associated with OligoSty side chains imply that polymers bearing OligoSty side chains will be poor candidates for OECTs, where volumetric ionic capacitance and facile ion penetration are required, but promising for OFETs where it's crucial the preservation of the backbone order and maximisation of electronic mobility.

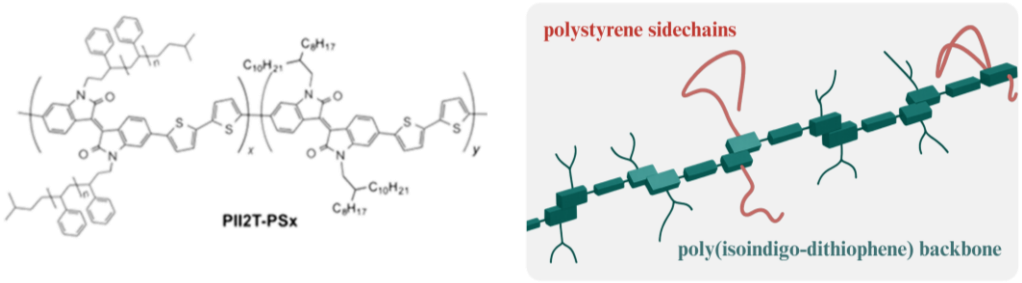

Figure 4. 11 *Molecular structure (left) and schematic representation (right) of backbone packing and phase separation in polystyrene-grafted isoindigo polymers. Adapted from Fang et al.[112] Copyright © 2013 American Chemical Society.*

These two distinct types of side chains were selected to modulate the polarity and microstructural organisation of isoindigo-based semiconductors: hydrophilic OligoDMA and hydrophobic OligoSty. While ODMA introduces polar, ion-permeable domains that could promote mixed ionic–electronic conduction in OECTs, polystyrene is expected to enhance backbone packing due to its rigid aromatic structure and favourable π–π interactions. They allow the investigation of how different side-chain features influence film morphology, charge transport, and interfacial properties.

To the best of my knowledge, no examples where PDMA has been employed as a side-chain substituent in conjugated polymers designed for OECTs have been reported in the literature. This work, therefore, represents an innovative attempt to explore PDMA-functionalized isoindigo systems, motivated by its well-established hydrophilicity, ion affinity, and biocompatibility in aqueous media. Conversely, polystyrene-based side chains have been occasionally used to improve film-forming ability and microstructural stability in conjugated systems, though their application remains relatively limited compared to alkyl substituents.

4.3.1.3 A quick overview on reverse addition-fragmentation chain-transfer (RAFT) polymerization

Since its first report in 1998, the reversible addition–fragmentation chain transfer (RAFT) process has become one of the most versatile techniques for synthesizing well-defined polymer architectures. RAFT is part of the wider class of reversible deactivation radical polymerizations (RDRP), which reproduce the key features of living polymerization while preserving the flexibility of radical chemistry. These systems allow precise control over molecular weight, molar mass dispersity, end-group retention, and chain extension capabilities. RDRP strategies operate through an equilibrium between active and dormant chains and are implemented either by reversible deactivation (e.g., nitroxide-mediated polymerization (NMP) and atom transfer radical polymerization (ATRP)) or through degenerative chain transfer, as in RAFT.[70]

RAFT mechanism

RAFT polymerization mechanism is described in **Figure 4.12**. The propagating radicals (step 1 and 2) react with a chain transfer agent (CTA), forming a radical intermediate that undergoes fragmentation to re-establish equilibrium between active and dormant species.

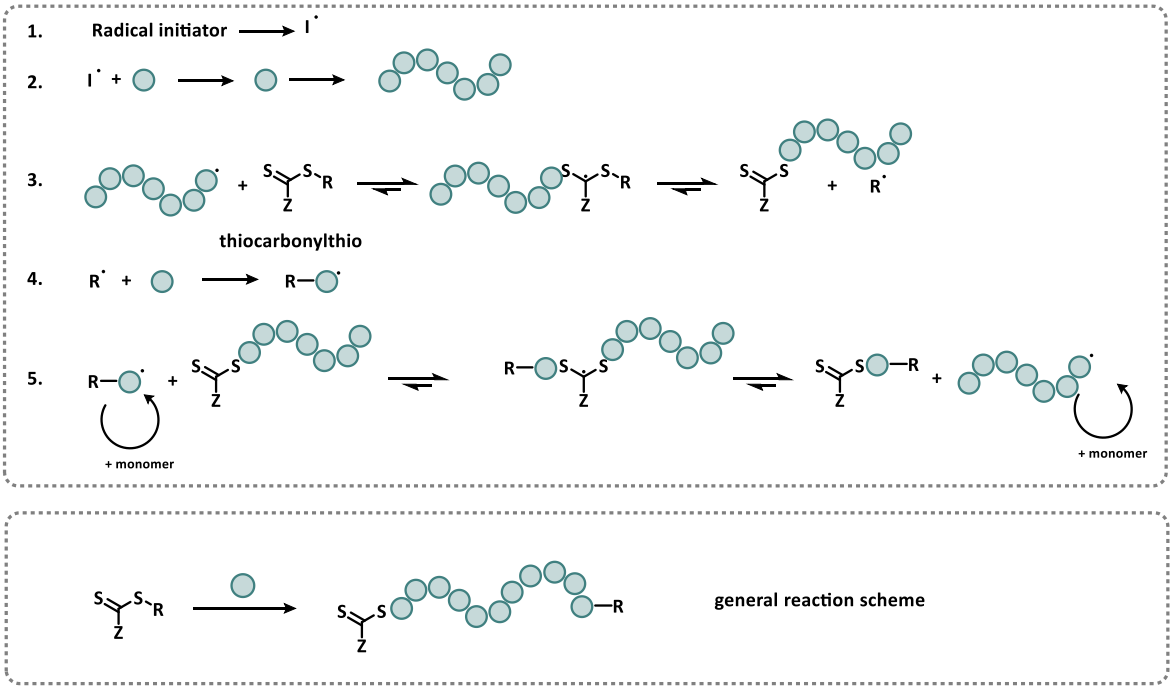

Figure 4. 12 *Proposed Mechanism of Reversible Addition−Fragmentation Chain Transfer Polymerization*

The chain-transfer steps (step 3 and 5) are degenerate and involve the reversible exchange of the thiocarbonylthio end-group, Z–C(=S)–S–R, between propagating radicals and dormant chains (macro-CTA). Effective control is achieved when the addition-fragmentation equilibrium rate exceeds the propagation rate so that, on average, fewer than one monomer unit is inserted per activation event. Most chains therefore retain α- and ω-end groups derived from the R-group and Z–C(=S)–S– moieties of the RAFT agent.[114]

A defining feature of RAFT is that the number of dead chains is determined solely by the number of radicals generated from the initiator. Termination does not remove the thiocarbonylthio ω-end group from surviving chains, unlike in reversible-deactivation systems. The populations of the chain families formed, living chains initiated by the RAFT R-group, living chains initiated by the initiator fragment, and their terminated counterparts, are governed by the initial concentrations of RAFT agent and initiator.[71]

Polymerization kinetics

The polymerization rate in RAFT follows the kinetics of conventional radical polymerization and can be expressed by *Equation 4.4*:

$$R_p = k_p\,[\mathrm{M}]\left(\frac{f k_d [\mathrm{I}]_0 e^{-k_d t}}{k_t}\right)^{1/2} \tag{4.4}$$

where k_p is the propagation rate coefficient, $[M]$ the monomer concentration, f the initiator efficiency, k_d the initiator decomposition rate coefficient, $[\mathrm{I}]_0$ the initial initiator concentration, and $k_t$the termination rate coefficient. Monomers with high $k_p$values and initiators with rapid decomposition kinetics (high k_d) allow fast polymerization while maintaining low initiator concentrations. The fraction of living chains, L, is on the other hand expressed by *Equation 4.5*:

$$L = \frac{[\mathrm{CTA}]_0}{[\mathrm{CTA}]_0 + 2[\mathrm{I}]_0(1 - e^{-k_d t})(1 - f_c/2)} \tag{4.5}$$

where $[CTA]_0$and $[I]_0$are the initial concentrations of chain transfer agent and initiator, and $f_c$is the coupling factor (with $f_c = 1$ for 100% combination and $f_c = 0$ for 100% disproportionation).[115]

Living character

RAFT polymerization differs significantly from reversible-deactivation systems such as ATRP and NMP with respect to chain extension behaviour. Because the number of living chains is dictated exclusively by the number of radicals generated from the initiator, high monomer conversion does not compromise livingness. As a result, block copolymers can be synthesized even at 100% conversion.[116] During subsequent chain-extension steps, new initiator-derived radicals generate additional short chains, but their number can be predicted directly from the initiator concentration. This feature enables the preparation of multiblock copolymers with high structural fidelity and controlled end-group retention.

4.3.2 Synthetic pathway for the synthesis of OligoDMA-dibromoisoindigo (ODMA-IIG-Br$_2$) and OligoSty-dibromoisoindigo (OStyIIG-Br$_2$)

4.3.2.1 Isoindigo core synthesis

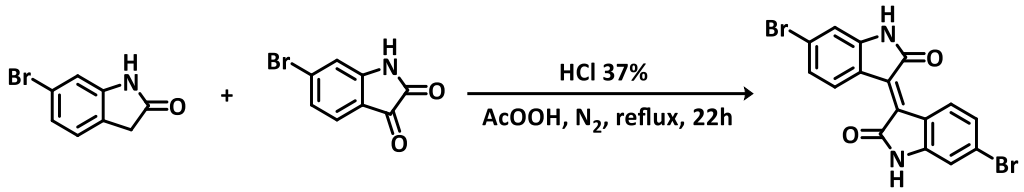

9 **10** **11**

Scheme 4. 1 *Synthetic protocol for the obtainment of (11)*

The synthetic approach employed in this study begins with the condensation of 6-bromo-2-oxindole (**9**) and 6-bromoisatin (**10**) to yield 6,6′-dibromoisoindigo (Br$_2$IIG, **11**). This reaction (**Scheme 4.1**) is typically carried out under acidic conditions, such as in glacial acetic acid, at elevated temperatures, and is catalysed by hydrochloric acid. This method has been extensively documented in the literature as a reliable and efficient route to isoindigo derivatives.[117]

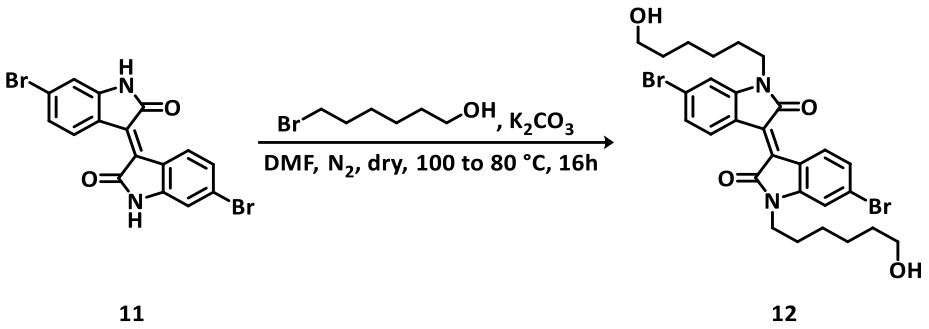

Scheme 4. 2 Synthetic pathway for the obtainment of (12)

Subsequently, the isoindigo core undergoes alkylation with 6-bromo-1-hexanol, a six-carbon chain terminated with a hydroxyl group (**Scheme 4.2**). This functionalization is achieved by treating Br_2IIG (**11**) with 6-bromo-1-hexanol in the presence of potassium carbonate (K_2CO_3) in anhydrous dimethylformamide (DMF). The reaction is deliberately conducted at temperatures below 120 °C to avoid potential interference from DMF decomposition products, which could affect the efficiency and selectivity of the alkylation. Under these controlled conditions, the reaction proceeds smoothly, affording the desired alkylated isoindigo (**12**) in high yield (97%). [118]

The introduction of the hydroxyl-terminated alkyl chain is a strategic design choice, as it provides a functional handle for the subsequent attachment of oligomeric side chains, such as OligoDMA.

4.3.2.2 Synthesis and characterisation of the RAFT pendants

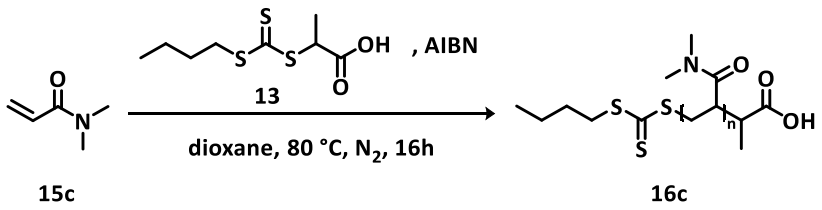

Scheme 4. 3 Synthetic route for the obtainment of OligoDMA (16c)

The controlled synthesis of OligoDMA was carried out via RAFT polymerisation using BTPA as the chain transfer agent and AIBN as the radical initiator (**Scheme 4.3**). Prior to polymerisation, the DMA monomer was purified over basic alumina to remove monomethyl ether hydroquinone and stored at low temperature to prevent uncontrolled polymerisation.

The reaction was performed in dioxane at 80 °C for 16 hours under an inert atmosphere, with a monomer-to-initiator ratio of 12:1, deliberately chosen to target low-molecular-weight oligomers, and yielded an oligomer with Mn = 566 Da and dispersity Đ = 1.12, isolated as a glassy yellow solid (**16a**) after solvent removal and sublimation of unreacted monomer under high vacuum. At the end of the reaction, the resulting oligomer was found to contain an average of only four repeating units, highlighting the known limitation of RAFT polymerisation at very low molecular weights, where some "livingness" can be lost.[70,114] Despite this constraint, the method produces oligomers with sufficiently narrow dispersity for the intended functionalization.

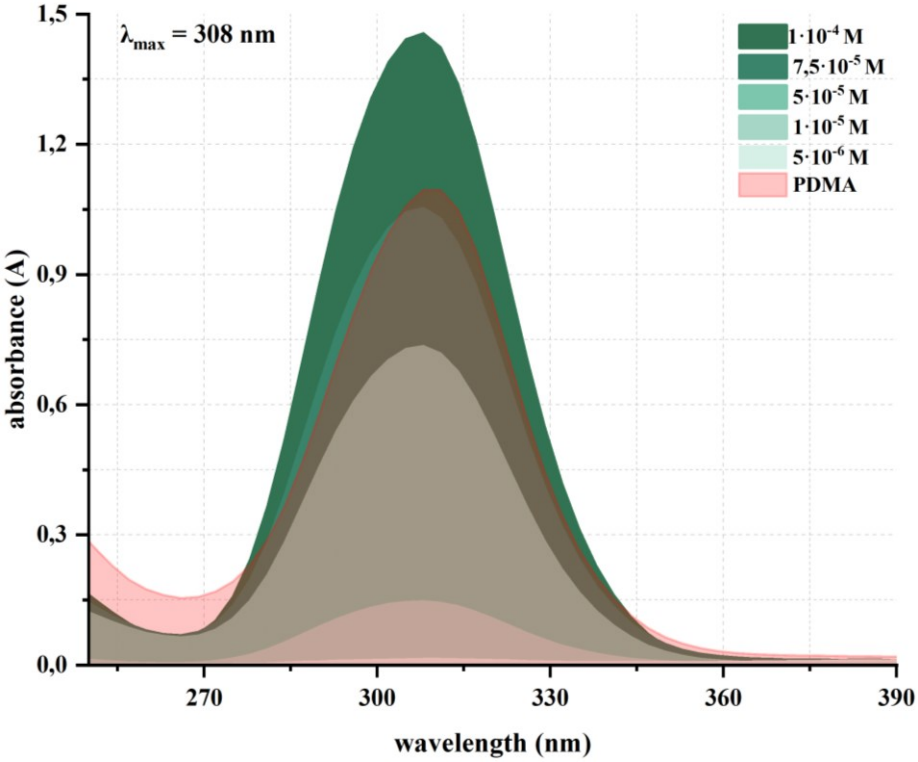

Graph 4. 1 *Absorption spectra in DCM of the five BTPA calibration standards and a PDMA solution for the quantification of the thiocarbonyl groups present in the product through its peculiar 308 nm absorption due to the p–p* allowed transition*

The same RAFT-based strategy was successfully applied to the synthesis of oligostyrene and other oligoacrylamides, affording materials with comparable molecular weights and low dispersities (*see Experimental Section for further details*). This demonstrates the overall versatility and robustness of the approach for generating oligomeric side chains.

To accurately determine the number of carboxylic functionalities on the oligomeric samples, a combination of ^{1}H NMR, GPC, and UV–Vis spectroscopy was employed (**Graph 4.1**), following the approach reported by Laschewsky et al.[119] The UV–Vis absorption of the thiocarbonyl end groups introduced via the RAFT agent serves as a quantitative probe. The characteristic absorption arises from the strong absorption in the near UV range (allowed $\pi \rightarrow \pi^*$ transition) and weak absorption in the visible range (forbidden $n \rightarrow \pi^*$ transition) due to the electronic transitions of the thiocarbonyl moiety, allowing direct estimation of the number of functional chain ends in solution. By calibrating the UV–Vis signal using known BTPA standards (*see Experimental Part for further information on the obtainment of the calibration curve*), the average number of functional end groups per oligomer can be determined. This technique provides a reliable measure of end-group fidelity and the number of functional handles suitable for subsequent post-functionalization reactions, such as grafting onto hydroxyl-terminated isoindigo. Complementary information was obtained from ^{1}H NMR and GPC (*see Experimental Session for further information*).

4.3.2.3 Introduction of the RAFT pendant on the IIG core: grafting from VS grafting to approach

To covalently anchor the oligomeric side chains onto the isoindigo-based conjugated system, two distinct synthetic strategies were explored, differing in the sequence of the functionalization and polymerisation steps. These two approaches – referred to as route A (grafting-from) and route B (grafting-to) (**Figure 4.13**) – ideally represent two complementary strategies for the creation of a scaffold containing a conjugated core and oligomeric side chains.

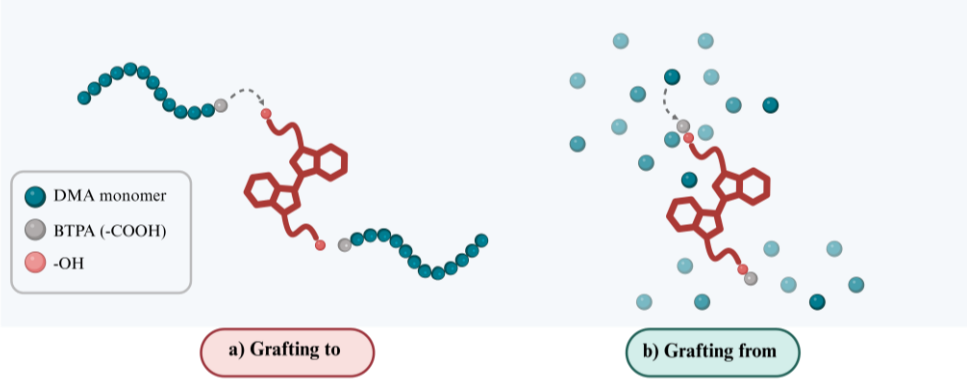

Figure 4. 13 *Cartoon representation of the two possible strategies to introduce RAFT-polar pendant on the IIGBr$_2$ core; a) grafting to and b) grafting from protocol*

In route A (**Scheme 4.4**), the CTA (BTPA) was first esterified onto the isoindigo core, which bears two terminal hydroxyl groups on its C6 side chains. This reaction yields a bis-macroCTA (**14**), where each thiocarbonylthio moiety serves as an initiation site for subsequent RAFT polymerisation. The oligomeric chains can thus grow directly on the conjugated monomer under controlled radical polymerisation conditions, following a "grafting-from" strategy. This approach ideally offers the main advantage of achieving the polymerisation directly on the $IIGBr_2$ monomer. However, the method also presents significant challenges: the polymerisation must be carefully optimised to avoid eventual side reactions between the radical intermediates and the conjugated core, and controlling the chain length distribution of the growing oligomers can be more difficult compared to reactions performed in standard conditions.

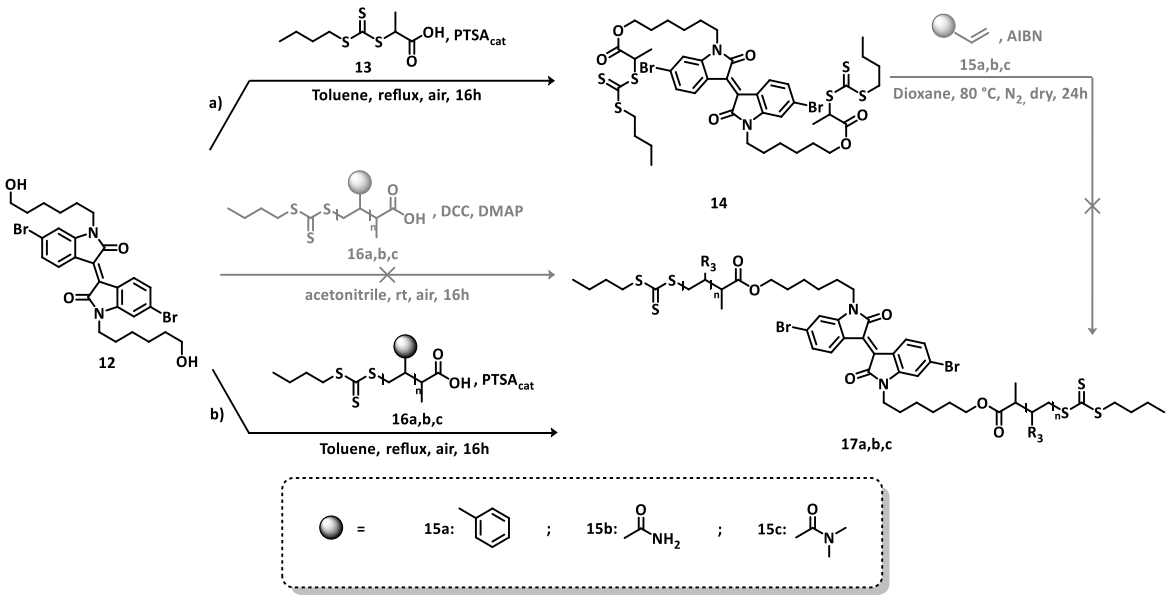

Scheme 4. 4 *Two different pathways for the synthesis of target molecule **17a,b,c**: pathway a) grafting from protocol via the formation of a double macro-cta (**14**); pathway b) grafting to protocol*

In route B (**Scheme 4.4**), by contrast, the oligomeric side chains are first synthesised independently through RAFT polymerisation (**16 a, b, c**), as described in the previous section, and subsequently coupled to the hydroxyl-functionalized isoindigo via esterification. This "grafting-to" strategy allows precise control over the molecular weight and dispersity of the oligomers prior to attachment. Additionally, the use of pre-formed oligomers enables systematic tuning of chain length before their integration into the conjugated framework. The main limitation of this approach lies in reduced coupling

efficiency: as the molecular weight of the oligomers increases, steric hindrance can limit the extent of grafting, leading to incomplete functionalization.

Route a: "grafting from" strategy

The first stage of Route A involved, as already mentioned, the preparation of a bis-macroCTA (**14**), which serves as the initiation platform for the subsequent growth of oligomeric side chains directly on the IIG core. This strategy (**Scheme 4.5**) relies on the introduction of two RAFT-active thiocarbonylthio groups (**13**) onto the hydroxyl-functionalized isoindigo, effectively converting each terminal hydroxyl into a site capable of initiating controlled radical polymerisation.

The Fischer esterification was carried out under acid-catalysed conditions in toluene with continuous removal of the water generated during the reaction using a Dean-Stark apparatus. This setup ensures that the reaction equilibrium favours the complete functionalization of the hydroxyl groups. The reaction provides the bis-macroCTA in high yield (78%) as a red, viscous liquid.

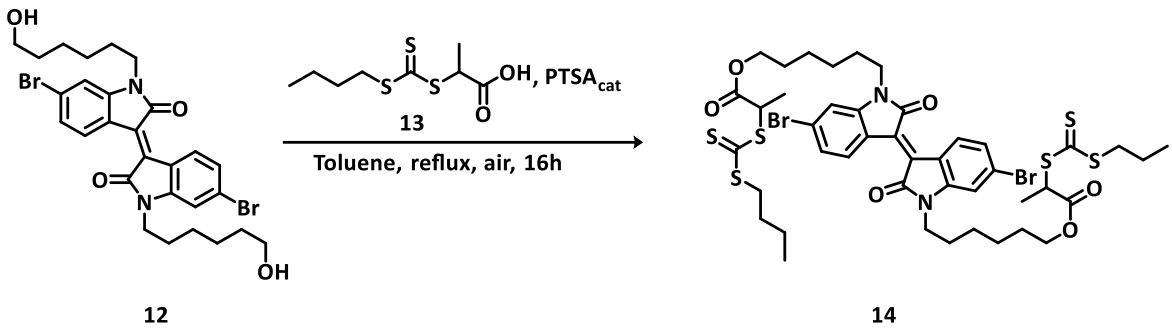

Scheme 4. 5 *Synthetic protocol for the obtainment of the macroCTA (**14**)*

Following the synthesis of the bis-macroCTA, the initiation of the RAFT polymerisation directly from the IIG core using styrene (**15a**), acrylamide (**15b**) and DMA (**15c**) as monomers was attempted. The procedure mirrored standard RAFT conditions previously optimised for these monomers, with the macroCTA (**14**) replacing BTPA (**13**) as the chain transfer agent, and AIBN serving as radical initiator in dioxane at 80 °C under degassed conditions. Despite the application of these conditions, no polymerisation was observed, as evidenced by ^{1}H NMR analysis, likely due to steric hindrance around the macroCTA, and

potential reactivity mismatches between the macroCTA and the monomers. These factors probably prevent effective radical addition and propagation, highlighting intrinsic limitations of the grafting-from approach in this context.

Route b: "grafting to" strategy

In the "grafting to" strategy, pre-formed oligomeric chains are covalently attached to the hydroxyl-functionalized IIG core via esterification. Two different reaction conditions were explored. The first approach employed basic conditions using DMAP and DCC in acetonitrile at room temperature under ambient atmosphere. Under these conditions, no formation of the desired esterified product was observed.

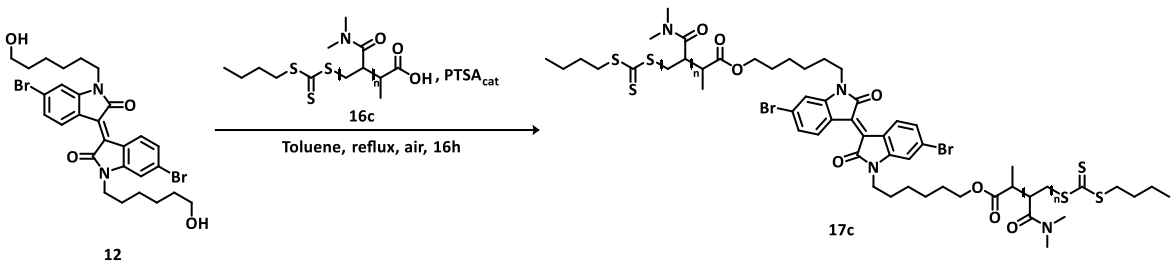

Scheme 4. 6 *Synthetic strategy for the obtainment of (**17c**) through the "grafting to" route*

The second strategy was again an acid-catalysed esterification in toluene under reflux (**Scheme 4.6**). This approach proved once again successful with OligoSty and OligoDMA, efficiently producing the esterified isoindigo derivatives in high yield. For example, the reaction of the hydroxyl-functionalized IIG with pre-formed OligoDMA under these conditions afforded a red glassy solid in 99% yield. In contrast, attempts to couple oligoacrylamide (OligoAA) chains failed due to the insolubility of OligoAA in toluene, which prevented effective reaction with the IIG hydroxyl groups. These results illustrate that the grafting-to approach is strongly influenced by oligomer solubility and reaction conditions. It allows pre-determined control over chain length and functionality; however, successful esterification requires compatibility of both the oligomer and the IIG core with the chosen reaction medium.

4.4 Conclusion

This chapter demonstrates the development of RAFT-based strategies for the functionalization of isoindigo cores with oligomeric side chains, highlighting both the opportunities and limitations inherent to such approaches. The grafting-from strategy, although conceptually attractive for direct polymer growth on the conjugated monomer, was hindered by steric constraints and reactivity mismatches, preventing effective polymerisation under standard RAFT conditions. In contrast, the grafting-to approach successfully yielded isoindigo derivatives functionalized with OligoDMA and OligoSty, illustrating the importance of oligomer solubility and reaction medium compatibility in achieving efficient esterification.

The introduction of hydrophilic OligoDMA offers a pioneering route toward enhancing ionic transport within conjugated polymer films, potentially supporting mixed ionic-electronic conduction for OECT applications. Meanwhile, OligoSty pendants provide a complementary tool for tuning film microstructure, backbone packing, and electronic mobility, relevant for OFET performance. Overall, the work establishes a modular and controllable platform for side-chain engineering on isoindigo-based semiconductors, combining the precision of RAFT polymerisation with strategic chemical design. These findings are the basis for future studies exploring structure-property relationships in conjugated polymers with tailor-made oligomeric side chains, bridging the gap between molecular design and device functionality.

4.5 Experimental

4.5.1 Materials and methods

All reagents are purchased from VWR, Sigma-Aldrich, Fluorochem, BLD pharm, TCI, Ambeed, Fisher Scientific, and ThermoFisher. Solvents – including anhydrous and NMR solvents – are purchased from Carlo-Erba, Fisher Scientific, and Acros and used as received unless otherwise stated. Extra dry solvents packed under Ar and stored over molecular sieves having a >99,5% purity are always employed if a reaction requires inert and anhydrous conditions. Glassware is dried for 24 hours at 130 °C before being used when the synthetic protocol requires an anhydrous environment. If the synthetic protocol requires an inert atmosphere, solid reagents are always degassed using high vacuum (~0,02 mbar) and then refilling the reaction vessel with nitrogen (the procedure is repeated three times). Liquid or low-melting-point solids are degassed through a freeze-pump-thaw procedure using liquid nitrogen as a cooling agent. Reactions are monitored using Xtra SIL G UV254 silica gel plates (pore size: 60 Å, thickness 200 μm) and a double-wave UV lamp (λ: 254 and 365 nm). When cited, the composition of solvent mixtures is always indicated as a volume/volume ratio. Basic alumina (Al_2O_3) employed for the purification of dimethylacrylamide (**12c**) is purchased from Sigma-Aldrich, and it's a basic activated aluminium oxide having an activity grade Brockman I. Melting points are measured employing a Büchi M-560 apparatus. Solution Nuclear Magnetic Resonance (NMR) spectra are acquired with a Bruker Avance 400 NEO spectrometer. ^{1}H and ^{13}C NMR of known compounds are included after each synthetic procedure to provide the reader with the chemical shifts of the compound. ^{1}H NMR of new molecules are also included in chapter **4.5.3.2**. Gel permeation chromatography (GPC) analyses were carried out using a Waters chromatographic system equipped with a refractive index detector (RID). The separation was performed on Styragel HR columns (HR1–HR4, Waters), maintained at 35 °C to ensure stable and reproducible elution profiles. HPLC grade THF was used as the mobile phase at a constant flow rate of 1.0 $mL \cdot min^{-1}$. Samples were prepared by dissolving 10 mg of material in 20 mL of THF and stirring until complete solubilization was achieved. Prior to injection, the solutions were filtered through 0.45 μm PTFE syringe filters to remove any insoluble residues. An injection volume of 150 μL was used for all measurements. Calibration of the instrument was performed using monodisperse polystyrene standards covering the molecular weight range from 580 Da to

3.0×10^6 Da. Based on the calibration curve, the number-average molecular weight (Mn), weight-average molecular weight (Mw), and molar mass dispersity (Đ = Mw/Mn) were determined. Data acquisition and processing were performed using Empower software.

4.5.2 Synthetic protocols

4.5.2.1 Alkyl-oligoacrylate mixed side chain-containing 6,6'-dibromo isoindigo synthetic routes

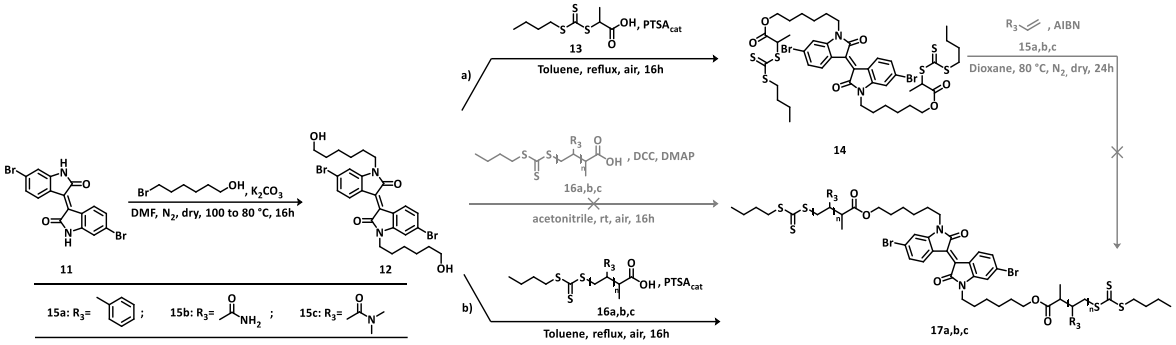

Scheme 4. *7 Two different pathways for the synthesis of target molecule 17a,b,c: pathway a) grafting from protocol via the formation of a double macroCTA (**14**); pathway b) grafting to/through protocol*

The synthesis of 6,6′-dibromoisoindigo functionalized with mixed alkyl/oligoacrylate side chains (**17**) was pursued through two distinct strategies, both beginning with the alkylation of 6,6′-dibromoisoindigo (**9**). In the first approach, a grafting-from method was employed: esterification of the alkylated isoindigo afforded a bifunctional macro-CTA (**14**), which would enable the direct growth of pendant chains from the monomer. In the second approach, a grafting-to/through strategy was applied, in which a polymeric chain synthesised via RAFT polymerisation (**16**) was subsequently grafted onto the alkylated isoindigo monomer.

*6,6'-dibromo isoindigo (Br_2IIG) synthetic route (**11**)*

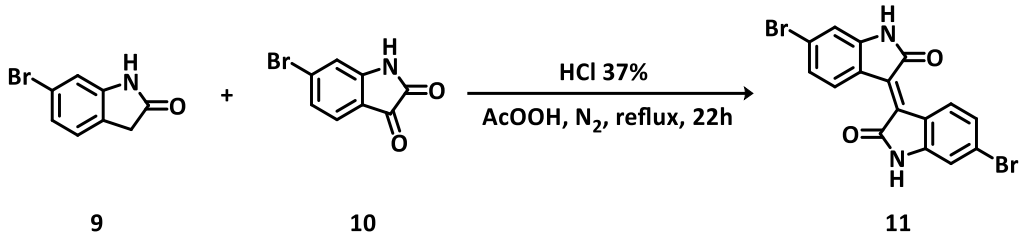

9 10 11

Scheme 4. 8 *Synthetic protocol for the obtainment of (**11**)*

5000 mg of 6-bromo-2-oxindole (**9**) (23,6 mmol, 1 eq) and 5330 mg of 6-bromoisatin (**10**) (23,6 mmol, 1 eq) are added to a 2-neck 250 mL round-bottom flask and degassed. They are then dispersed in 100 mL of glacial acetic acid and stirred for 10 minutes at room temperature. 1 mL of HCl 37% is added to the mixture, then it is stirred for 22 h at reflux temperature. The suspension is subsequently cooled down to room temperature, vacuum filtered, washing the filtrate with distilled water, EtOH, and AcOEt. The red solid is dried in the vacuum oven overnight (yield: 98%)

^{1}H NMR (400 MHz, DMSO-d6) δ(ppm) 11.09 (2H, s), 8.99 (2H, d, J=8.6), 7.19 (2H, dd, J1=8.6, J2=1.9), 7.00 (2H, d, J=1.9)

*(3E)-6-Bromo-3-[6-bromo-1,2-dihydro-1-(6-hydroxyhexyl)-2-oxo-3H-indol-3-ylidene]-1,3-dihydro-1-(6-hydroxyexyl)-2H-indol-2-one (6-hydroxyhexyl$_2$Br$_2$IIG) synthetic route (**12**)*

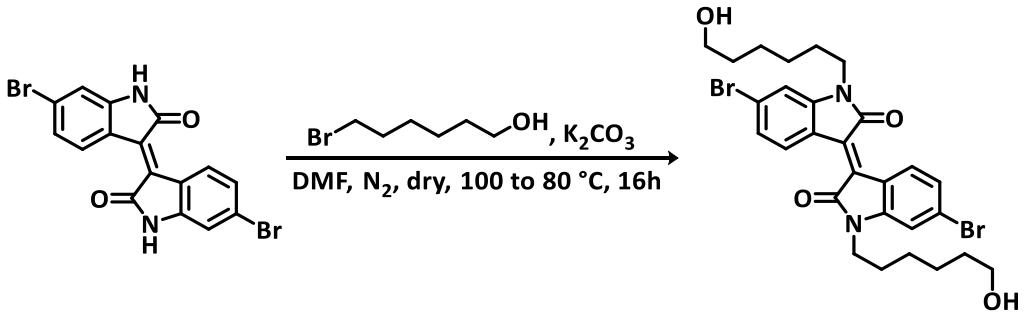

11 12

Scheme 4. 9 *Synthetic protocol for the obtainment of (**12**)*

5700 mg (13,57 mmol, 1 eq) of Br_2IIG (**11**) and 9377 mg (67,85 mmol, 5 eq) of K_2CO_3 are added to an oven-dried 2-neck 250 mL round-bottom flask. The reagents are degassed, then dissolved in 40 mL of anhydrous DMF. The reaction mixture is stirred at 100 °C for 1 h, then the temperature is lowered to 80 °C, and 3,92 mL of 6-bromo-1-hexanol are added to the solution. The reaction is stirred for 16 hours, keeping the same temperature as the addition, then it is brought back to room temperature. The DMF is then removed using a rotary evaporator, and the crude product is suspended in 300 mL of DCM and stirred for 30 minutes. The crude is washed with 3x 300 mL of brine. The organic layer is dried with Na_2SO_4 and filtered. The solvent is evaporated to afford a red solid. (yield: 97%)

^{1}H NMR (400 MHz, $CDCl_3$) δ(ppm) 9.06 (2H, d, J=8.6), 7.17 (2H, dd, J1=8.6, J2=1.8), 6.93 (2H, d, J=1.7), 3.75 (4H, t, J=7.2), 3.64 (4H, t, J=6.4), 1.78-1.65 (4H, m), 1.62-1.51 (4H, m), 1.49-1.36 (8H, m)

*6-[Br_2IIG [6-hexyl2 [[(butylthio)thioxomethyl] thio] propanoate] hexyl 2[[(butylthio)thioxomethyl]thio]propanoate (6-BTPEhexyl$_2$$Br_2$IIG) synthetic route (**14**)*

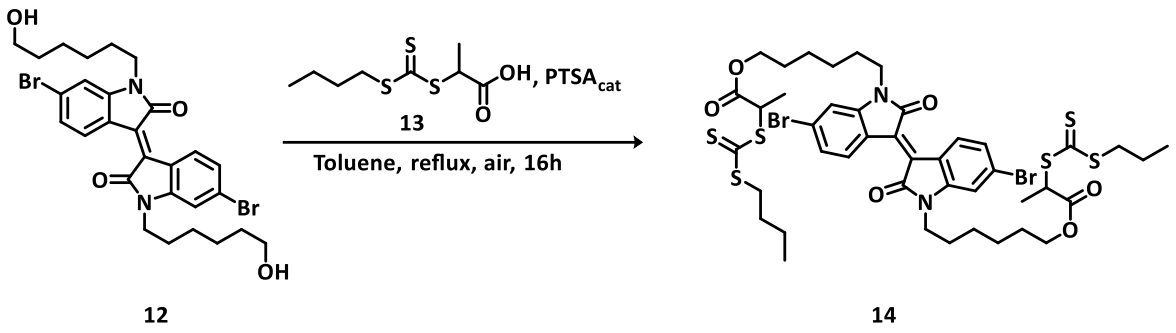

Scheme 4. 10 *Synthetic protocol for the obtainment of (14)*

200,0 mg of 6-hydroxyhexyl$_2$$Br_2$IIG (**12**) (0,32 mmol, 1 eq), 153,7 mg of 2-(butylthiocarbonothioylthio)propanoic acid (BTPA) (**13**) (0,64 mmol, 2 eq), and 20,6 mg of p-toluenesulfonic acid (PTSA) (0,09 mmol, 0,3 eq) are placed into a 50 mL two-neck round-bottom flask equipped with a condenser and a Dean-Stark apparatus. The powders are dissolved in 10 mL of toluene and stirred at reflux temperature for 16 h. The reaction mixture is then brought back to room temperature, washed with 3x15 mL of brine to remove the

PTSA. The organic layer is dried over Na_2SO_4 and filtered. The solvent is evaporated to afford a red liquid. (yield: 78%)

^{1}H NMR (400 MHz, $CDCl_3$) δ(ppm) 9.08 (2H, d, J=8.6), 7.17 (2H, dd, J1=8.6, J2=1.8), 6.93 (2H, d, J=1.8), 4.80 (2H, q, J= 7.4), 4.13 (4H, sxt, J=5.9), 3.74 (4H, t, J=7.2), 3.34 (4H, td, J1=7.2, J2=2.5), 1.72-1.61 (12H, m), 1,58 (6H, d, J=8.4), 1.47-1.37 (12H, m), 0,92 (6H, t, J=7.4)

*Synthesis of oligo-dimethylacrylamide side chains (**16c**)*

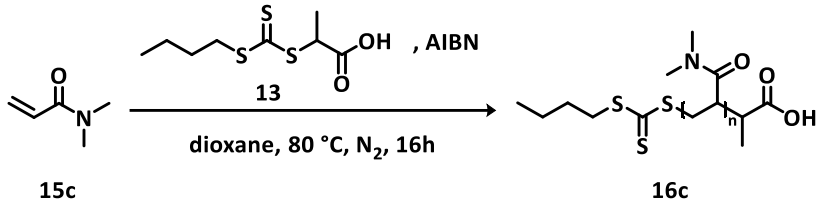

Scheme 4. 11 *Synthetic protocol for the obtainment of (**16a,b,c**)*

Stabilized dimethylacrylamide (DMA) (**15c**) is purified over a column of basic alumina to remove monomethyl ether hydroquinone and kept in the fridge to prevent its uncontrolled polymerization.

entry	*monomer*[a]	*CTA*	*m (mg)*	*Mn*[b]
1	Styrene	BTPA	199,1	655
2	Acrylamide	BTPA	200,4	520
3	DMA	BTPA	198,7	566

Table 4. 1 *a) list of the different monomers used for the synthesis of oligomeric side chains; b) Mn is obtained through room temperature GPC analysis*

710 mg of DMA (10,1 mmol, 12 eq), 198,7 mg of BTPA (**13**) (0,84 mmol, 1 eq), and 1,640 mg of azobisisobutyronitrile (AIBN) (0,01 mmol, 0,012 eq) are added to a 10 mL flask and are dissolved in 4,42 mL of dioxane. The reaction mixture is degassed for 15 minutes, then it's heated at 80 °C and stirred for 16h. The solution is brought back to room temperature, then the solvent is removed using a rotary evaporator. The unreacted monomer is removed

through sublimation at 150 °C under high vacuum (0,018 mbar) using a glass oven to afford a glassy yellow solid. (yield: 40%)
Mn = 566 Da, Đ = 1,12

^{1}H NMR (400 MHz, $CDCl_3$) δ(ppm) 5.30-5.12 (1H, br), 3.39-3.29 (2H, br), 3.25-2.82 (24H, m), 2.81-1.53 (17H, m), 1.48-1.37 (3H, m), 2.18-2.12 (2H, m), 0.98-0.88 (3H, m)

*Alkyl-oligoacrylamide mixed side chain 6,6'-dibromo isoindigo synthesis through a "grafting to" procedure (**17c**)*

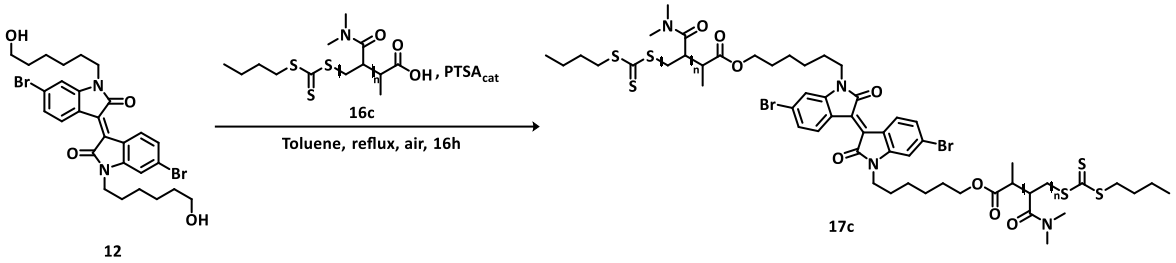

Scheme 4. 12 *Synthetic protocol for the obtainment of (17c)*

23,6 mg of 6-hydroxyhexyl$_2$Br$_2$IIG (**12**) (0,038 mmol, 1 eq) and 100 mg of oligo-dimethylacrylamide (**16c**) (0,76 mmol, 2 eq) are added together with 2,1 mg of PTSA·H_2O (0.01 mmol, 0.3 eq) to a 25 mL two-neck round-bottom flask equipped with a condenser and a Dean-Stark apparatus. 13 mL of toluene are added to the same flask, then the solution is brought to reflux temperature and stirred for 16h. The reaction mixture is brought back to room temperature, the solvent is evaporated, and the crude is suspended in brine and stirred for 10 minutes. The product is extracted three times with DCM and washed with 3x30 mL of brine. The organic layer is dried over Na_2SO_4 and filtered. The solvent is evaporated to afford a red glassy solid (yield: 99%)

^{1}H NMR (400 MHz, $CDCl_3$) δ(ppm) (*see chapter 4.5.3.2*)

Note: because of the different relaxation times of the isoindigo core and the ODMA chains, the accuracy of the integration of the 1H NMR peaks of compound 17c is reduced; for this reason, FT-IR techniques is employed to assure the completion of the reaction.

4.5.3 Material characterisation

4.5.3.1 Optical characterisation

Absorbance (ABS) analysis in the UV-vis range are performed to calculate the concentration of carboxylic functionalities concentration in a $7{,}5 \cdot 10^{-5}$ M solution of **16c**. The analysis has been propaedeutic for the calculation of the quantity of 16c for the synthesis of 17c, to have an exact 1:2 ratio of **12**:**16c**. Spectra are collected using a Jasco V-750 UV/Vis/NIR spectrophotometer equipped with a PbS detector and a dual-beam optical system. The instrument covers a spectral range from 190 to 2500 nm, using a deuterium lamp for the UV region (190–350 nm), a tungsten–halogen lamp for the visible region (350–800 nm), and a PbS photoconductive detector for the near-infrared region. The spectral resolution is set to $\Delta\lambda$ = 1 nm and the scanning speed to 400 nm·min^{-1}. All measurements are performed in two-face 1 cm path length quartz cuvettes. Background correction is performed using the spectrum of pure DCM as a reference. Baseline and absorbance of the samples are recorded in the range 300–600 nm. The sample is prepared by dissolving the analytes in DCM at concentrations of 0,3–0,1 mg·mL^{-1} ($7{,}5 \cdot 10^{-5}$ mmol·mL^{-1}), ensuring absorbance values within the linear range of the Beer–Lambert law (A < 1)

$$A = \varepsilon \cdot l \cdot c$$

where A is the absorbance, ε (M^{-1}·cm^{-1}) the molar absorption coefficient, l (cm) is the optical path, and c is the concentration (mol·L^{-1}). The calibration curve is prepared by means of the "calibration curve" function of the instrument using five different BTPA solutions whose concentrations range from $1{,}0 \cdot 10^{-4}$ to $5{,}0 \cdot 10^{-6}$. Data acquisition and preliminary processing are performed with Jasco Spectra Manager, while further analysis (λ_{max} determination) are carried out using OriginPro software.

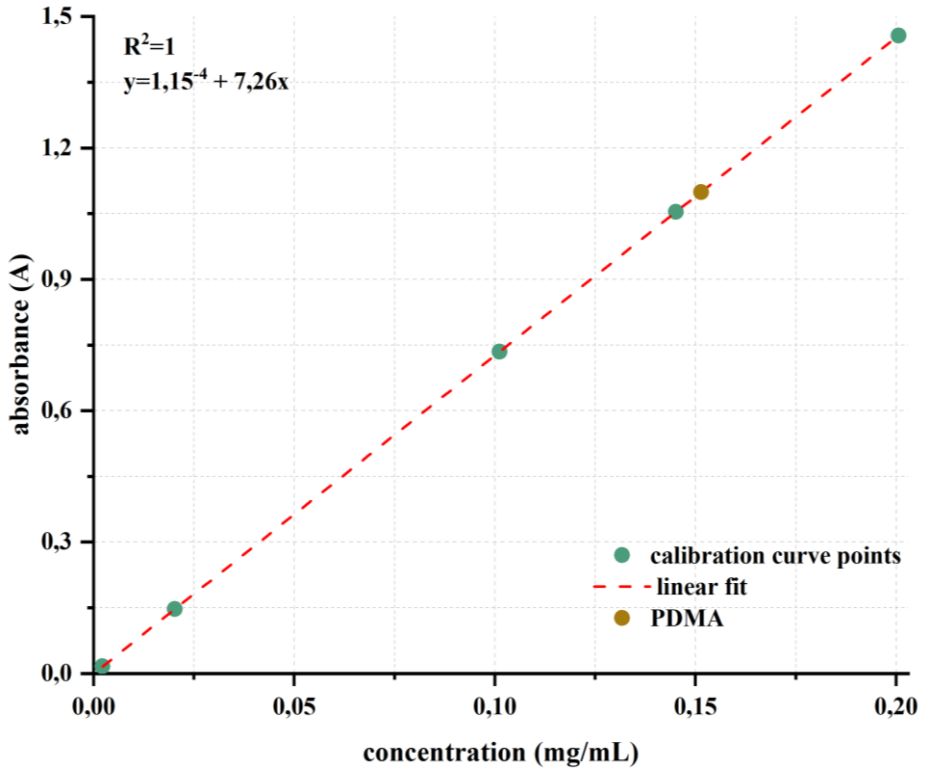

Graph 4. 2 *UV-vis calibration curve of a BTPA solution in the $1{\cdot}10^{-4}$-$5{\cdot}10^{-6}$ range for the quantification of the thiocarbonyl group absorption at λ_{max} = 308 nm of PDMA due to its p–p* allowed transition*

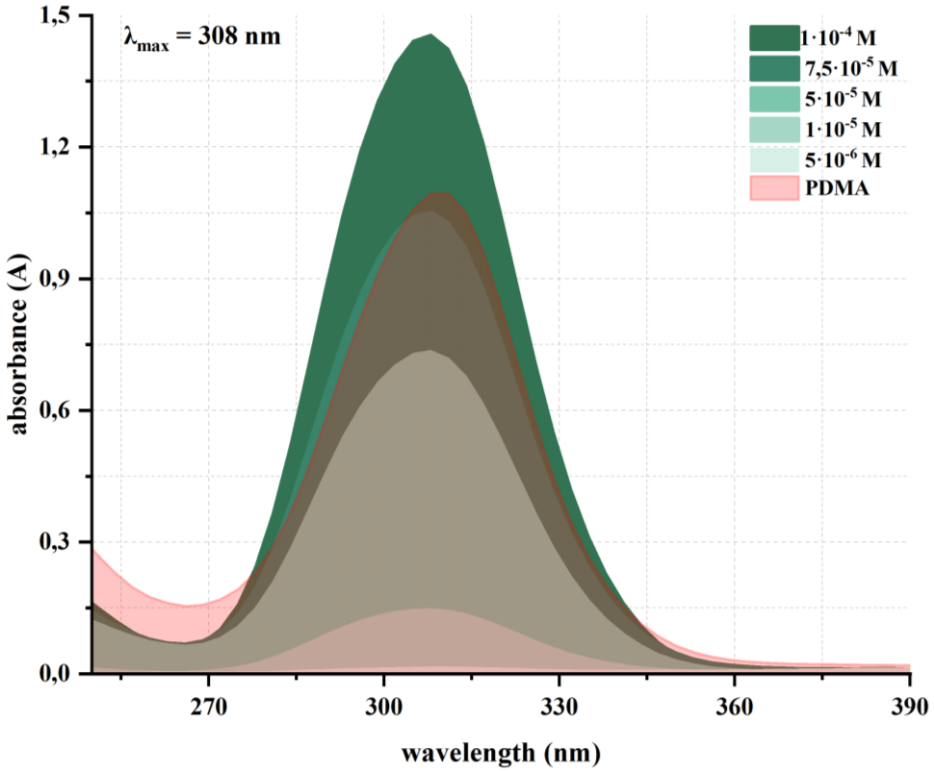

Graph 4. 3 *Absorption spectra in DCM of the five BTPA calibration standards and a PDMA solution for the quantification of the thiocarbonyl groups present in the product through its peculiar 308 nm absorption due to the p–p* allowed transition*

4.5.3.2 Spectroscopic characterisation

^{1}H NMR spectra

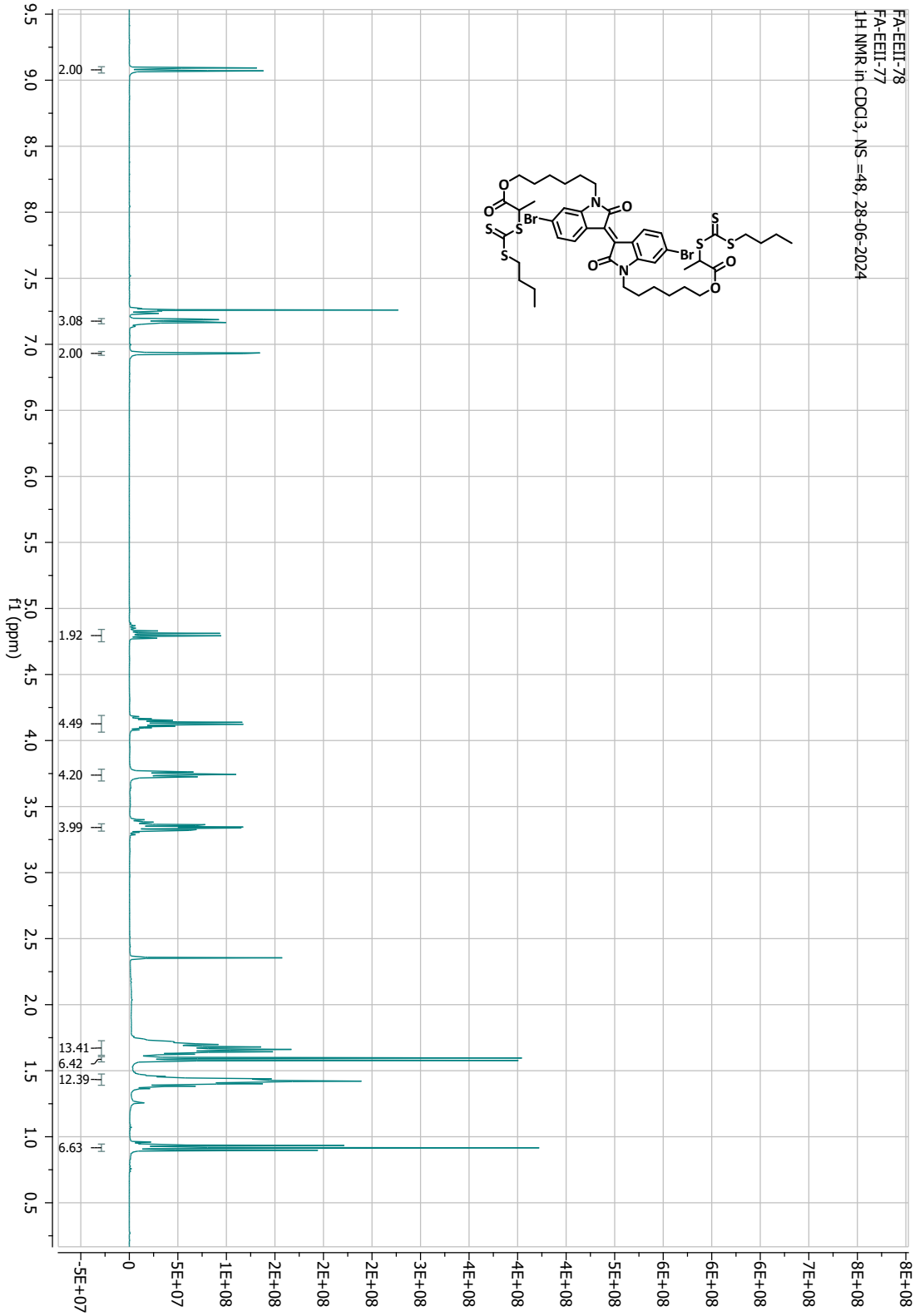

Figure 4. 14 *^{1}H NMR in $CDCl_3$ spectrum of compound* ***(14)***

Bibliography

68. He, Y., Kukhta, N. A., Marks, A. & Luscombe, C. K. The effect of side chain engineering on conjugated polymers in organic electrochemical transistors for bioelectronic applications. *J. Mater. Chem. C* **10**, 2314–2332 (2022).
69. Surgailis, J. *et al.* The Role of Side Chains and Hydration on Mixed Charge Transport in *n* -Type Polymer Films. *Adv. Mater.* **36**, 2313121 (2024).
70. Perrier, S. *50th Anniversary Perspective*: RAFT Polymerization—A User Guide. *Macromolecules* **50**, 7433–7447 (2017).
71. Siauw, M., Hawkett, B. S. & Perrier, S. Short chain amphiphilic diblock co-oligomers via RAFT polymerization. *J. Polym. Sci. Part Polym. Chem.* **50**, 187–198 (2012).
72. Yao, G. *et al.* Flexible bioelectronics for physiological signals sensing and disease treatment. *J. Materiomics* **6**, 397–413 (2020).
73. Xiao, K., Wan, C., Jiang, L., Chen, X. & Antonietti, M. Bioinspired Ionic Sensory Systems: The Successor of Electronics. *Adv. Mater.* **32**, 2000218 (2020).
74. Cherian, D. *et al.* Large-area printed organic electronic ion pumps. *Flex. Print. Electron.* **4**, 022001 (2019).
75. Simon, D. T., Gabrielsson, E. O., Tybrandt, K. & Berggren, M. Organic Bioelectronics: Bridging the Signaling Gap between Biology and Technology. *Chem. Rev.* **116**, 13009–13041 (2016).
76. Savva, A. *et al.* Balancing Ionic and Electronic Conduction for High-Performance Organic Electrochemical Transistors. *Adv. Funct. Mater.* **30**, 1907657 (2020).
77. Hazra, S., Banerjee, A. & Nandi, A. K. Organic Mixed Ion-Electron Conductivity in Polymer Hybrid Systems. *ACS Omega* **7**, 32849–32862 (2022).
78. Rivnay, J. *et al.* Organic electrochemical transistors. *Nat. Rev. Mater.* **3**, 17086 (2018).

79. Berggren, M. & Malliaras, G. G. How conducting polymer electrodes operate. *Science* **364**, 233–234 (2019).

80. Paulsen, B. D., Tybrandt, K., Stavrinidou, E. & Rivnay, J. Organic mixed ionic–electronic conductors. *Nat. Mater.* **19**, 13–26 (2020).

81. Sun, H., Gerasimov, J., Berggren, M. & Fabiano, S. n-Type organic electrochemical transistors: materials and challenges. *J. Mater. Chem. C* **6**, 11778–11784 (2018).

82. Khodagholy, D. *et al.* High transconductance organic electrochemical transistors. *Nat. Commun.* **4**, 2133 (2013).

83. Bernards, D. A. & Malliaras, G. G. Steady-State and Transient Behavior of Organic Electrochemical Transistors. *Adv. Funct. Mater.* **17**, 3538–3544 (2007).

84. Lövenich, W. PEDOT-properties and applications. *Polym. Sci. Ser. C* **56**, 135–143 (2014).

85. Proctor, C. M., Rivnay, J. & Malliaras, G. G. Understanding volumetric capacitance in conducting polymers. *J. Polym. Sci. Part B Polym. Phys.* **54**, 1433–1436 (2016).

86. Nielsen, C. B. *et al.* Molecular Design of Semiconducting Polymers for High-Performance Organic Electrochemical Transistors. *J. Am. Chem. Soc.* **138**, 10252–10259 (2016).

87. Kukhta, N. A., Marks, A. & Luscombe, C. K. Molecular Design Strategies toward Improvement of Charge Injection and Ionic Conduction in Organic Mixed Ionic–Electronic Conductors for Organic Electrochemical Transistors. *Chem. Rev.* **122**, 4325–4355 (2022).

88. Stavrinidou, E. *et al.* Engineering hydrophilic conducting composites with enhanced ion mobility. *Phys Chem Chem Phys* **16**, 2275–2279 (2014).

89. Harman, D. G. *et al.* Poly(3,4-ethylenedioxythiophene):dextran sulfate (PEDOT:DS) – A highly processable conductive organic biopolymer. *Acta Biomater.* **14**, 33–42 (2015).

90. Kim, J. H., Kim, S., Kim, G. & Yoon, M. Designing Polymeric Mixed Conductors and Their Application to Electrochemical-Transistor-Based Biosensors. *Macromol. Biosci.* **20**, 2000211 (2020).

91. Wang, S., Ha, M., Manno, M., Daniel Frisbie, C. & Leighton, C. Hopping transport and the Hall effect near the insulator–metal transition in electrochemically gated poly(3-hexylthiophene) transistors. *Nat. Commun.* **3**, 1210 (2012).

92. Paulsen, B. D. & Frisbie, C. D. Dependence of Conductivity on Charge Density and Electrochemical Potential in Polymer Semiconductors Gated with Ionic Liquids. *J. Phys. Chem. C* **116**, 3132–3141 (2012).

93. Sato, K. *et al.* Diffusion-Cooperative Model for Charge Transport by Redox-Active Nonconjugated Polymers. *J. Am. Chem. Soc.* **140**, 1049–1056 (2018).

94. Qin, S. *et al.* Organic Mixed Ionic–Electronic Conductors for Organic Electrochemical Transistors: Sidechain Structure Influences Ion Uptake and Functional Performance. *ChemPhysChem* e202500403 (2025) doi:10.1002/cphc.202500403.

95. Moser, M. *et al.* Side Chain Redistribution as a Strategy to Boost Organic Electrochemical Transistor Performance and Stability. *Adv. Mater.* **32**, 2002748 (2020).

96. Giovannitti, A. *et al.* Controlling the mode of operation of organic transistors through side-chain engineering. *Proc. Natl. Acad. Sci.* **113**, 12017–12022 (2016).

97. Wang, Y. *et al.* Designing organic mixed conductors for electrochemical transistor applications. *Nat. Rev. Mater.* **9**, 249–265 (2024).

98. Nicolini, T. *et al.* A Low-Swelling Polymeric Mixed Conductor Operating in Aqueous Electrolytes. *Adv. Mater.* **33**, 2005723 (2021).

99. Dimov, I. B., Moser, M., Malliaras, G. G. & McCulloch, I. Semiconducting Polymers for Neural Applications. *Chem. Rev.* **122**, 4356–4396 (2022).

100. Inal, S. *et al.* A High Transconductance Accumulation Mode Electrochemical Transistor. *Adv. Mater.* **26**, 7450–7455 (2014).

101. Mohn, T., Plitzko, I. & Hamburger, M. A comprehensive metabolite profiling of Isatis tinctoria leaf extracts. *Phytochemistry* **70**, 924–934 (2009).

102. Irimia-Vladu, M. *et al.* Indigo - A Natural Pigment for High Performance Ambipolar Organic Field Effect Transistors and Circuits. *Adv. Mater.* **24**, 375–380 (2012).

103. Robb, M. J., Ku, S., Brunetti, F. G. & Hawker, C. J. A renaissance of color: New structures and building blocks for organic electronics. *J. Polym. Sci. Part Polym. Chem.* **51**, 1263–1271 (2013).

104. Głowacki, E. D., Voss, G. & Sariciftci, N. S. 25th Anniversary Article: Progress in Chemistry and Applications of Functional Indigos for Organic Electronics. *Adv. Mater.* **25**, 6783–6800 (2013).

105. Hu, A. *et al.* Unravelling the influence of side-chain symmetry on device performance: insights from isoindigo-based polymers in thin-film transistors. *RSC Appl. Polym.* **1**, 292–303 (2023).

106. Mei, J., Graham, K. R., Stalder, R. & Reynolds, J. R. Synthesis of isoindigo-based oligothiophenes for molecular bulk heterojunction solar cells. *Org. Lett.* **12**, 660–663 (2010).

107. Meacham, R. F. *et al.* Contrasting interchain order and mixed ionic–electronic conduction in conjugated polymers: an isoindigo case study. *RSC Appl. Polym.* **2**, 1193–1201 (2024).

108. Wang, Y. *et al.* Hybrid Alkyl-Ethylene Glycol Side Chains Enhance Substrate Adhesion and Operational Stability in Accumulation Mode Organic Electrochemical Transistors. *Chem. Mater.* **31**, 9797–9806 (2019).

109. Zhao, Y. *et al.* Donor Engineering Tuning the Analog Switching Range and Operational Stability of Organic Synaptic Transistors for Neuromorphic Systems. *Adv. Funct. Mater.* **32**, 2205744 (2022).

110. Wang, L. *et al.* Poly(*N* , *N* -dimethyl)acrylamide-based ion-conductive gel with transparency, self-adhesion and rapid self-healing properties for human motion detection. *Soft Matter* **18**, 6115–6123 (2022).

111. Zhu, M., Guo, Y. & Liu, Y. A thriving decade: rational design, green synthesis, and cutting-edge applications of isoindigo-based conjugated polymers in organic field-effect transistors. *Sci. China Chem.* **65**, 1225–1264 (2022).

112. Fang, L. *et al.* Side-Chain Engineering of Isoindigo-Containing Conjugated Polymers Using Polystyrene for High-Performance Bulk Heterojunction Solar Cells. *Chem. Mater.* **25**, 4874–4880 (2013).

113. Charron, B. P. *et al.* Electronic properties of isoindigo-based conjugated polymers bearing urea-containing and linear alkyl side chains. *J. Mater. Chem. C* **6**, 12070–12078 (2018).

114. Moad, G., Rizzardo, E. & Thang, S. H. RAFT Polymerization and Some of its Applications. *Chem. – Asian J.* **8**, 1634–1644 (2013).

115. Konkolewicz, D., Hawkett, B. S., Gray-Weale, A. & Perrier, S. RAFT Polymerization Kinetics: Combination of Apparently Conflicting Models. *Macromolecules* **41**, 6400–6412 (2008).

116. Lee, J., Kwon, Y., Yu, C., Konkolewicz, D. & Kwon, M. S. The livingness of poly(methyl acrylate) under visible light photoiniferter-RAFT polymerization mediated by trithiocarbonates. *Polym. Chem.* **16**, 1798–1806 (2025).

117. Mei, J., Graham, K. R., Stalder, R. & Reynolds, J. R. Synthesis of Isoindigo-Based Oligothiophenes for Molecular Bulk Heterojunction Solar Cells. *Org. Lett.* **12**, 660–663 (2010).

118. Sarjadi, M. S., Tan, S. E., Wong, X. L. & Rahman, L. N-Alkylation Of 6,6'-Dibromoisoindigo via Tosylate: An Economical Pathway. (2018).

119. Skrabania, K., Miasnikova, A., Bivigou-Koumba, A. M., Zehm, D. & Laschewsky, A. Examining the UV-vis absorption of RAFT chain transfer agents and their use for polymer analysis. *Polym. Chem.* **2**, 2074 (2011).

Chapter 5

OligoSAR-containing OMIEC for OECTs

"For the things we have to learn before we can do them, we learn by doing them."

Aristotele

"Designing polymers for OECTs is like building a bridge that must be both strong and flexible: the backbone must conduct electrons efficiently, while the side chains must interact with the aqueous media. In this chapter, this molecular 'bridge' is built by grafting oligosarcosine chains onto a conjugated thiophene backbone via a bifunctional initiator. This strategy allows precise control over the polymer architecture, ensuring both electronic and ionic performance."

The work presented in this chapter was carried out during my research stay abroad at the Georgia Institute of Technology (Atlanta, USA), within the research group of Professor Antonio Facchetti in the School of Materials Science and Engineering. The experimental work was conducted in collaboration with the group of Professor Jason Azoulay in the Department of Molecular Science and Engineering of the same university. This project represented both a scientific and personal challenge, as the chemistry explored here did not belong to my primary field of research, nor to that of my hosting supervisor. However, approaching a new field and pursuing the final objective – despite the inevitable obstacles

and difficulties – proved to be an invaluable learning experience. It taught me the importance of perseverance, curiosity, and the deep understanding of the delicate interplay of factors required to achieve complex chemical transformations.

5.1 Introduction

5.1.1 Historical and mechanism background of R-NCA polymerisation

The synthesis of amino acid-derived N-carboxyanhydrides (NCAs) was first reported by Hermann Leuchs in the early 1900s.[120–122] At that time, the polymerisation of NCAs occurred largely by chance, due to the thermal instability of the monomers.

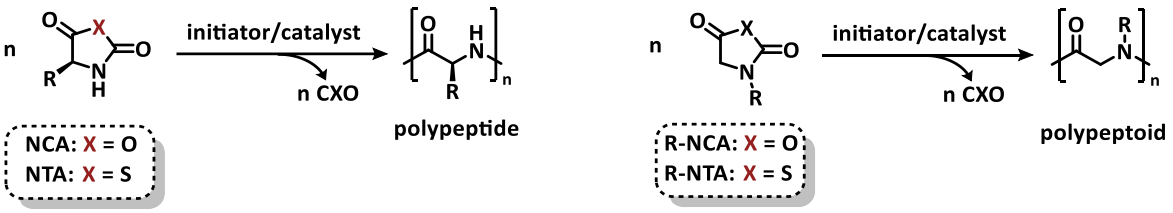

Figure 5. 1 *A general schematic representation of the ring-opening polymerisations of amino acid-derived NCAs/NTAs and N-substituted glycine-derived R-NCAs/R-NTAs, leading to the formation of polypeptides and polypeptoids, respectively*

Over the subsequent decades, a wide variety of amino acid-derived NCAs have been synthesised and systematically studied as polymerisation substrates.[123] More recently, numerous initiator and catalyst systems have been developed to mediate the ring-opening polymerisations (ROPs) of NCAs in a controlled manner, allowing the preparation of polypeptides with precise molecular weights and narrow dispersities.[124–126] Alongside conventional NCAs, N-substituted glycine-derived NCAs (R-NCAs) have emerged as particularly versatile monomers for the preparation of polypeptoids (**Figure 5.1**).[127,128] Compared to conventional NCAs, R-NCAs are more stable due to the absence of the N–H proton, and controlled ROPs of R-NCAs or their thiocarbonyl analogues (R-NTAs) have enabled the synthesis of well-defined polypeptoids with precise control over molecular weight and chain-end functionality.[129–131]

5.1.2 Synthesis of NCAs and R-NCAs

NCAs are commonly prepared via the Fuchs–Farthing method, which involves acylation and cyclisation of amino acids using phosgene or its derivatives (**Figure 5.2**, route a).

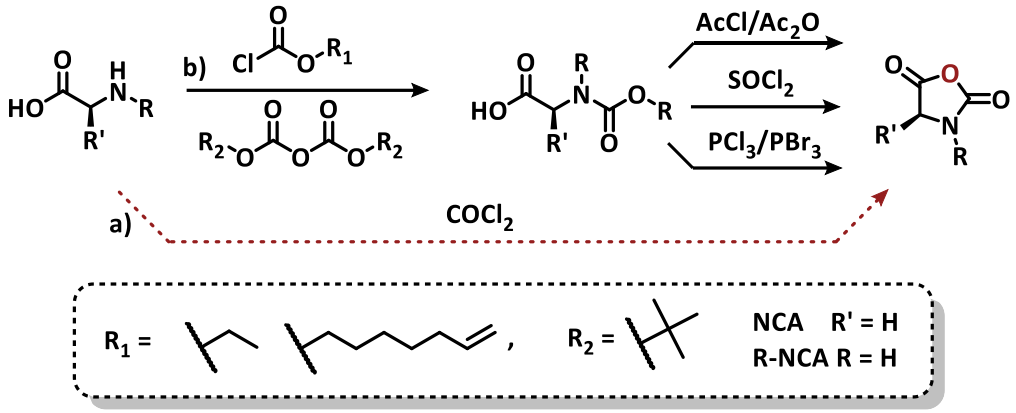

Figure 5. 2 *Obtainment of NCA and R-NCA monomers through a) Fuchs – Farthing and b) Leuchs' synthetic strategies.*

On the other hand, the Leuchs method relies on the nitrogen protection with carboxyalkyl groups, followed by cyclisation with acylating agents such as PCl_3, PBr_3, or $SOCl_3$. In the case of R-NCAs, N-substituted glycine precursors undergo cyclisation under similar conditions, often after prior protection of the nitrogen substituent.[132] Both NCAs and R-NCAs are highly sensitive to moisture; for this reason, they are typically purified under rigorously anhydrous conditions using recrystallisation, sublimation or chromatography with glovebox or Schlenk techniques.

5.1.3 Mechanistic Considerations: Normal Amine Mechanism (NAM)

The inherent electrophilicity of NCAs allows nucleophilic initiators – including primary and secondary amines, water, alcohols, and thiols – to initiate polymerisation via the normal amine mechanism (NAM). In this pathway, nucleophilic attack occurs at the C5 carbonyl of the NCA, followed by decarboxylation to generate a primary amino terminus from which chain propagation proceeds. Sterically unhindered primary amines are generally the most efficient initiators, as they enable rapid initiation relative to propagation, resulting in polymers with narrow dispersity. The synthesis of R-NCAs proceeds through a similar NAM pathway (**Figure 5.3**). Here, a primary amine initiates regioselective ring-opening at the C5

carbonyl of the R-NCA to generate a secondary amino terminus after a decarboxylation step. Such terminus is the starting point for subsequent monomer addition. Secondary amines are generally less nucleophilic than primary amines due to increased steric hindrance. This reduced nucleophilicity favours faster initiation relative to propagation, a key requirement for achieving controlled (living) polymerisation behaviour.[133]

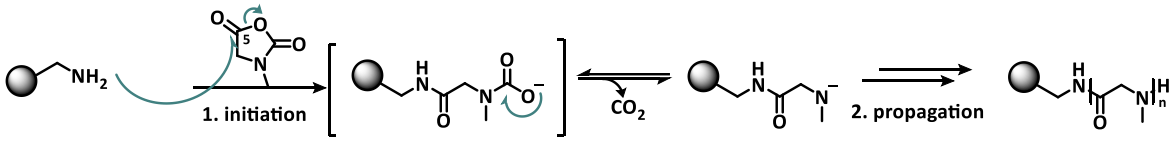

Figure 5. 3 *The normal amine mechanism for the ROPs of NCAs using primary amines as initiators*

The N-substitution in R-NCAs suppresses side reactions commonly observed in conventional NCAs, such as the formation of isocyanates or hydantoins, leading to improved control over molecular weight and polymer architecture.[134] Steric and electronic effects of the N-substituents further influence the polymerisation kinetics, with bulkier substituents slowing chain propagation due to reduced nucleophilicity of the propagating chain end. Kinetic investigations on various R-NCAs have demonstrated a first-order dependence of the polymerisation rate on both the monomer concentration and the primary amine initiator, in agreement with the NAM.[135] As the steric bulk of the N-substituent increases, a progressive decrease in the overall polymerisation rate is observed. This trend is consistent with a propagation step governed by nucleophilic attack of the secondary amine chain end, whose reactivity is attenuated by steric and electronic effects.[136]

5.1.4 The rate-determining step in ROP of NCA and R-NCA

The success of this process in achieving controlled polymerisations depends critically on the kinetics and mechanism of the elementary reaction steps involved. Among these, the rate-determining step (RDS) plays a central role in defining polymerisation rates, molecular weight control, and end-group fidelity. Over the past decade, a combination of experimental kinetics and density functional theory (DFT) studies has provided an increasingly detailed understanding of the RDS in amine-initiated ROPs. Depending on the structure of the

initiator, the substituents on the monomer, and the reaction environment, the RDS can shift between nucleophilic carbonyl addition and decarboxylation.[137]

5.1.4.1 The Classical Normal Amine Mechanism

In the NAM, the initiator attacks the electrophilic carbonyl carbon at the C5 position of the NCA ring, forming a zwitterionic tetrahedral intermediate. This step is followed by ring opening and CO_2 evolution, yielding a reactive amine terminus that can propagate the polymer chain. DFT investigations[138] established that in amine-mediated ROPs of both NCAs and N-substituted NCAs, the nucleophilic addition to the carbonyl carbon is the rate-determining step.

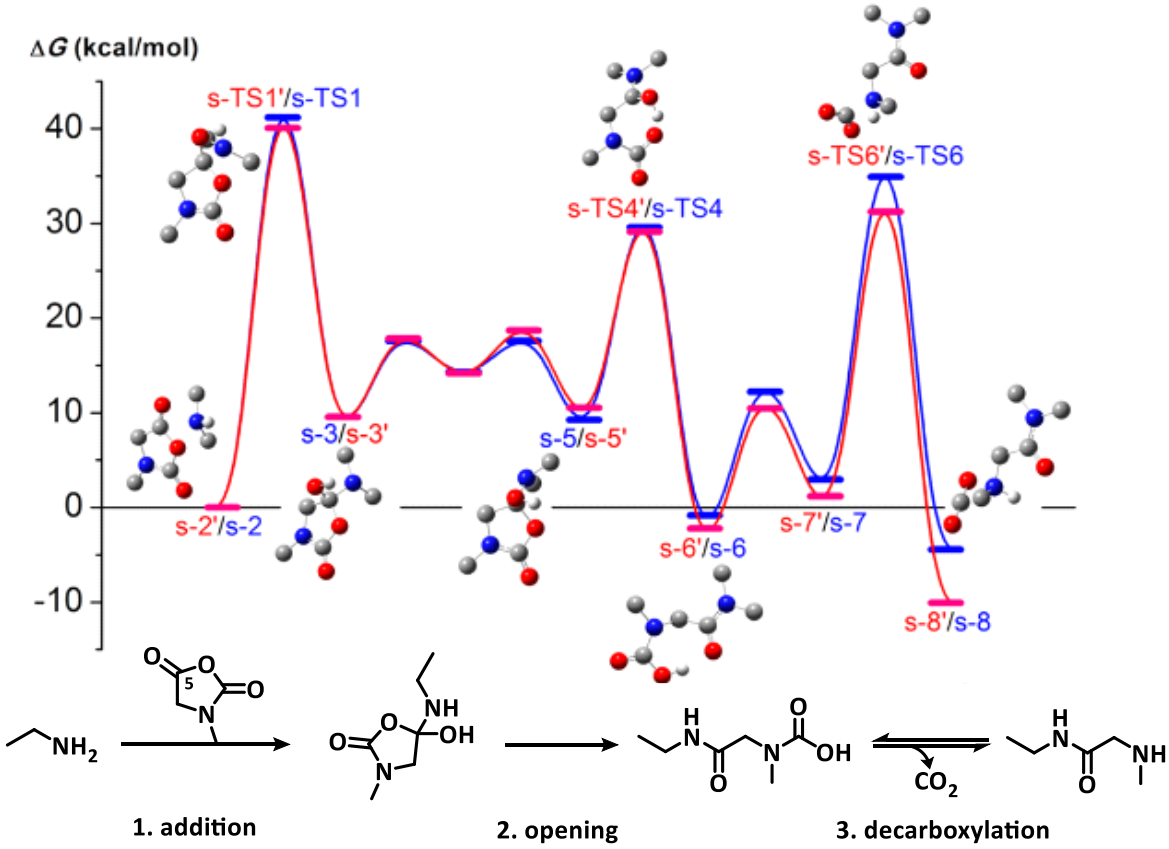

Figure 5. 4 Calculated Gibbs free energy profiles of the ring opening reaction of sarcosine-NCA with Me_2NH (blue line) and $EtNH_2$ (red line). Some crucial intermediates and TSs of the secondary amine pathway are illustrated by 3D models. Adapted from Liu & Ling[138] © American Chemical Society.

This step exhibits the highest activation barrier among the three elementary reactions-addition, ring-opening, and decarboxylation. The calculated free energy barriers were

consistent with experimentally observed polymerisation rates and explained the living character of the process under anhydrous conditions (**Figure 5.4**). Mechanistically, this pathway involves multiple proton transfer events that facilitate charge stabilisation and enable the rearrangement of intermediates. The proton transfer steps, though rapid, are crucial in maintaining the balance between initiation and propagation. Polar solvents and protic additives can significantly influence these processes by stabilising the charged transition states, thereby lowering the overall activation barrier.

5.1.4.2 Dependence of the RDS on monomer structure: the case of R-NCAs

Beyond the role of the initiator, the structure of the monomer also exerts a profound influence on the RDS. For R-NCAs, steric and electronic effects arising from the side chains can significantly affect the nucleophilic attack step and, consequently, the overall polymerisation kinetics. The propagation of a series of N-alkyl glycine N-carboxyanhydrides has been examined to elucidate how side-chain architecture impacts reactivity. For all systems studied, the carbonyl addition step remained the rate-determining event, consistent with the traditional NAM pathway. However, the source of the high activation barrier varied with the type of substitution (**Figure 5.5**).[139]

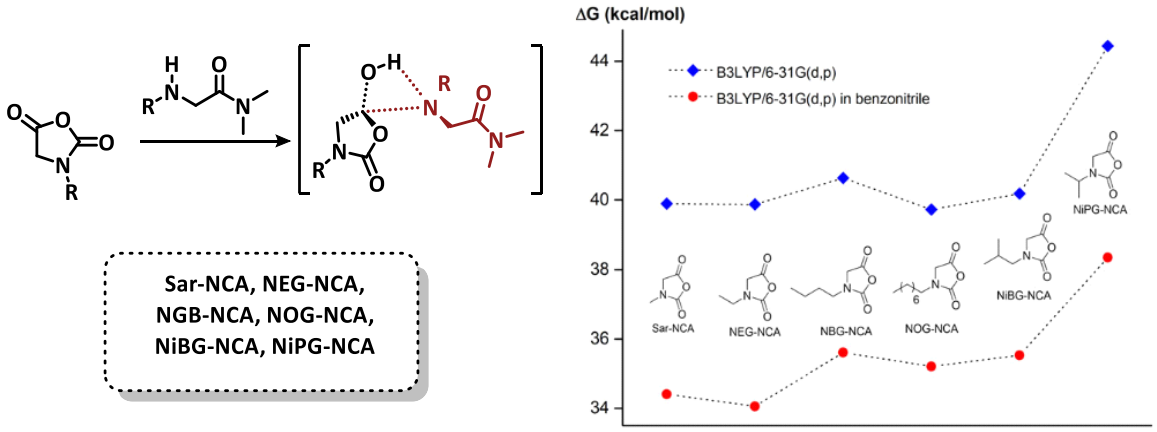

Figure 5. 5 *Schematic illustration of the carbonyl addition step of NNCA propagations on the model compound of the corresponding polymer ends (left) Calculated Gibbs free energy barrier of carbonyl addition step for various NNCAs in Scheme 1 on the basis of B3LYP/6-31G (d,p) (blue) and in benzonitrile (red) with SMD solvation model. The dash line is used as a guide (right). Adapted from Ling et al.*[139] *© American Chemical Society.*

For β-branched monomers, such as isopropyl glycine NCA, steric hindrance between β-hydrogens and the reacting carbonyl carbon increases the energy barrier, resulting in slower

polymerisation. In contrast, for linear or γ-branched monomers, the reduced polymerisation rate is not primarily due to steric congestion but rather to aggregation effects among long alkyl side chains. These noncovalent Van der Waals interactions promote chain association, decrease monomer solubility, and hinder the diffusion and effective collisions required for the carbonyl addition step. Thus, while steric factors dominate in short, branched side chains, aggregation phenomena govern the kinetics of long linear substituents. These findings emphasise that the apparent RDS observed experimentally may stem from a combination of intrinsic molecular reactivity and macroscopic solution behaviour.

5.1.5 Initiator strategies for in-solution synthesis of polypeptoids

The synthesis of linear high molecular-weight polypeptoids has been greatly advanced through solution-phase approaches, including ROP. This method provides access to polypeptoids with diverse side-chain functionalities while allowing control over chain lengths and dispersity. The ROP of R-NCAs proceeds via nucleophilic initiation; however, achieving high degrees of polymerisation, accelerating the polymerisation rate, and polymerising monomers with bulky or hydrophilic side chains remain significant challenges.

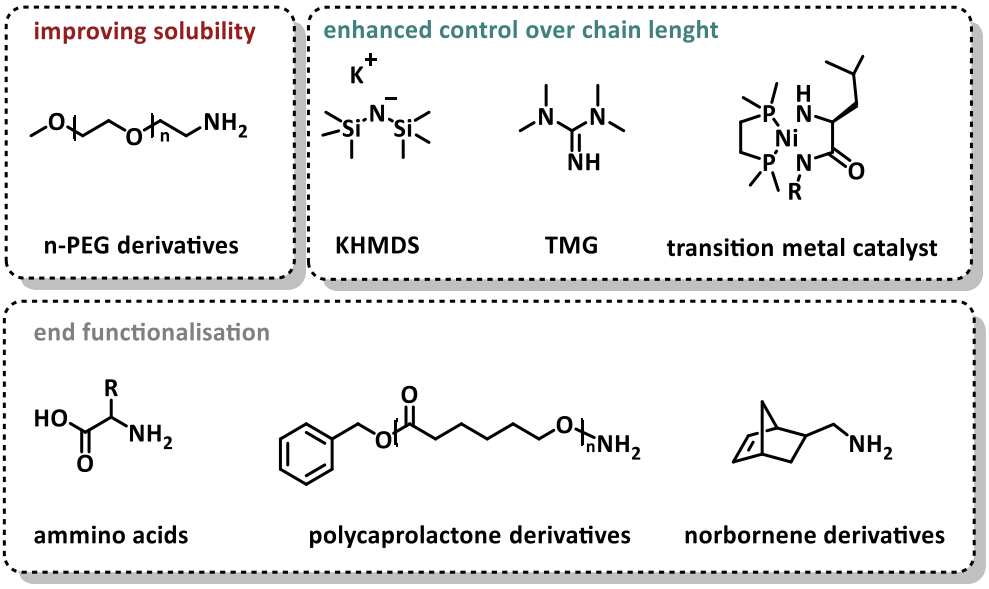

Figure 5. 6 *Accurate selection of the initiator to tune solubility, chain lengths, and potential end groups of the synthesised polypeptoids.*

Initiator selection is a key factor influencing polymerisation efficiency, solubility, molecular weight, and chain-end functionality.[140] Soluble initiators (**Figure 5.6**), such as methoxy polyethylene glycol amine (mPEG-NH_2)[141], enhance the solubility of growing polypeptoid chains, preventing premature precipitation and enabling access to higher molecular weights and improved yields. Amino acid-based initiators[142], such as L-methionine, L-tryptophan, and L-phenylalanine (**Figure 5.6**), can directly introduce functional end groups, eliminating the need for post-polymerisation modification. Through careful selection of initiators, solution-phase methods can thus produce polypeptoids with tailored molecular weights, controlled architectures, and functional chain ends (**Figure 5.6**) suitable for advanced biomedical and materials applications.

5.1.6 Activation of alcohol initiators

Recent works[143–145] have demonstrated that alcohols, despite their lower nucleophilicity compared to amines, can serve as effective initiators for the ROP of R-NCAs when properly activated (e.g., deprotonation to form alkoxides or through hydrogen-bonded complexes). In particular, benzyl alcohol, in combination with a catalytic amount of 1,1,3,3-tetramethylguanidine (TMG), has been shown to mediate the controlled polymerisation of *n*-butyl-NCA (Bu-NCA) in low-dielectric solvents such as THF or toluene, affording well-defined polypeptoids with number-average molecular weights (Mn) in the 3–21 $kg \cdot mol^{-1}$ range and narrow dispersities (Đ=1.03–1.08). In the absence of TMG, benzyl alcohol alone fails to initiate polymerisation under identical conditions, confirming the crucial role of the catalyst in activating the hydroxyl functionality.[143] Kinetic analyses revealed first-order dependence of the polymerisation rate on both the monomer and the alcohol initiator, and zero-order dependence on TMG concentration. Spectroscopic evidence (^{1}H NMR) supports the formation of a hydrogen-bonded complex (**Figure 5.7**) between TMG and the alcohol, which enhances the nucleophilicity of the latter and facilitates the nucleophilic ring-opening of the R-NCA monomer during initiation. This activation pathway enables rapid initiation relative to propagation, a prerequisite for achieving controlled (living) polymerisation behaviour. The efficiency of this activation strongly depends on the steric and electronic properties of the alcohol. Less hindered alcohols (e.g., methanol, ethanol, propanol, benzyl alcohol) exhibit efficient initiation and yield polymers whose experimental Mn values

correlate well with theoretical predictions. In contrast, bulkier alcohols such as isopropanol and tert-butanol show diminished reactivity due to steric encumbrance around the reactive centre, resulting in poor control or complete inhibition of polymerisation. Similarly, electron-withdrawing substituents (e.g., in 2,2,2-trifluoroethanol) reduce the nucleophilicity of the alcohol–TMG complex, leading to deviations from ideal living polymerisation behaviour.

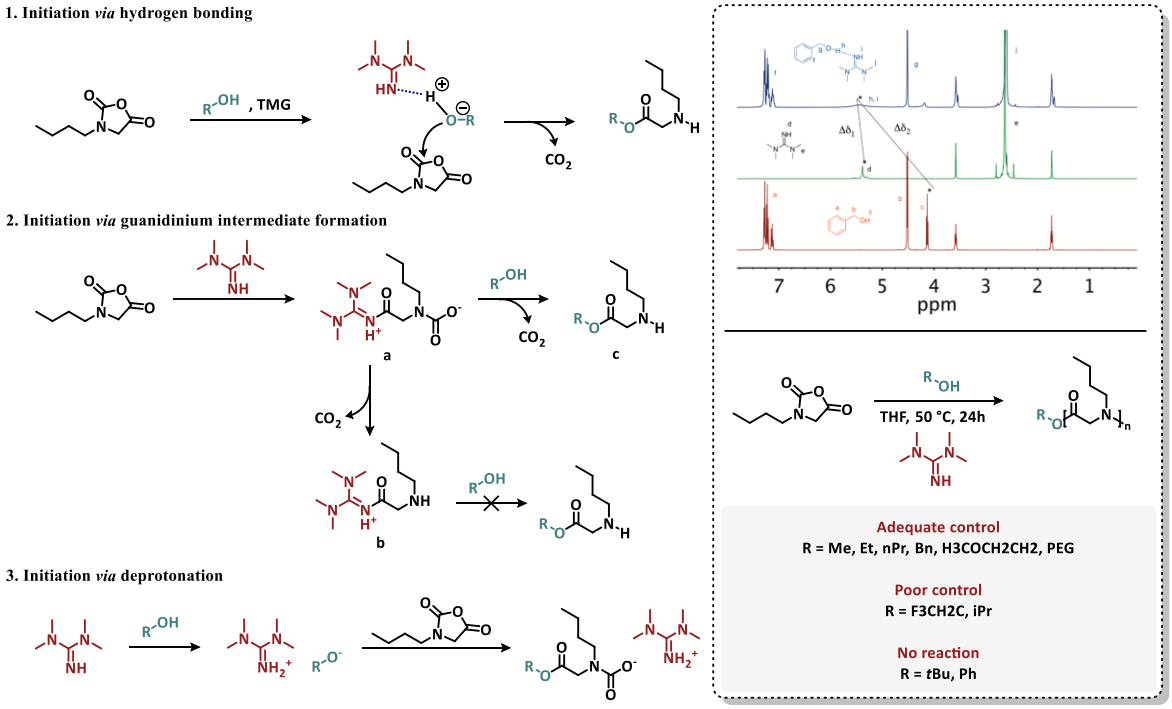

***Figure 5.** 7 Three Proposed Initiation Mechanisms of the TMG-Promoted ROP of Bu-NCA Using Alcohol Initiators. Adapted from Chan et al.[144] © American Chemical Society.*

This catalytic activation strategy has also been extended to macroinitiators bearing terminal hydroxyl groups, such as PEG. The PEG–TMG system effectively initiates ROP of Bu-NCA, yielding well-defined PEG-block-polypeptoid copolymers with predictable molecular weights and compositions. These findings underscore the importance of hydrogen-bond-mediated activation in expanding the scope of controlled ROPs of R-NCAs, enabling the incorporation of diverse functional initiators and macroinitiators into complex polymer architectures.

5.1.7 Synthesis and troublesome purification of Sarcosine-NCA

Polysarcosine(pSar), a member of the polypeptoid family, is a well-established synthetic polypeptide analogue obtained by the ROP of N-methylglycine N-carboxyanhydride (Sar-NCA).[146] It has recently attracted significant attention as a potential alternative to PEG in biomedical applications.[147] PEG has long been employed to improve the solubility, stability, and circulation time of therapeutic molecules; however, its widespread use is increasingly associated with limitations such as immunogenicity, non-biodegradability, and accumulation in tissues over time.[148] In contrast, pSar exhibits several properties that address these limitations. It is inherently biocompatible, biodegradable, and highly water-soluble, making it particularly suitable for in vivo applications.[149] Moreover, its polypeptoid structure allows for facile chemical modification, enabling the design of tailored biomaterials with controlled properties.[150,151]

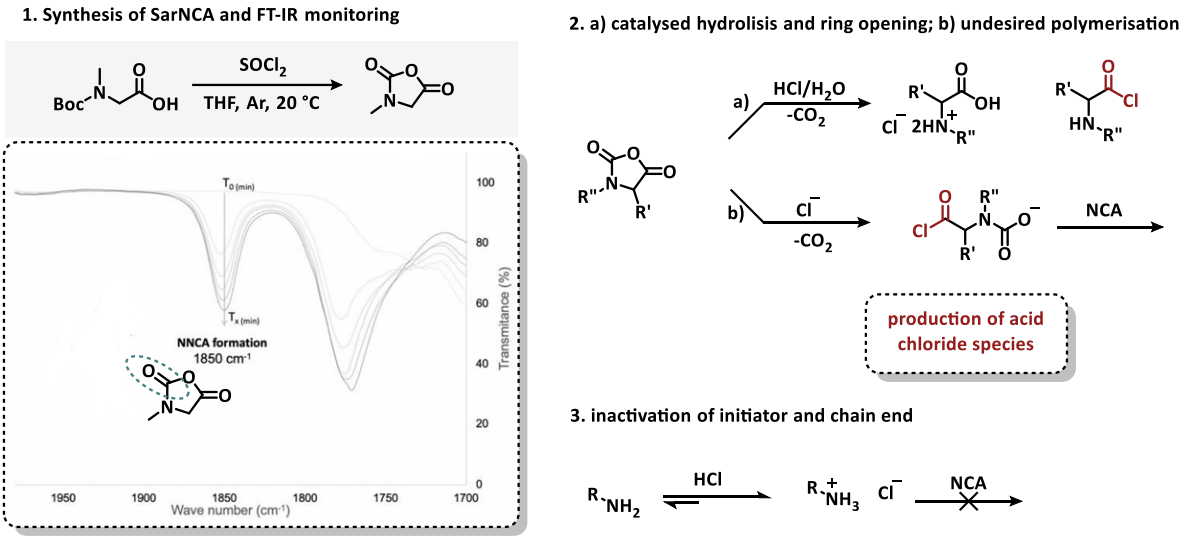

Figure 5. 8 *Monitoring of the R-NCA formation. 1) Synthesis scheme and evolution of the NCO stretching signal during the R-NCA formation monitored by FT-IR at 1850 cm−1; 2,3) Summary of hydrochloride acid- and chloride ion-induced side reactions. Adapted from Chapeloa et al.[152]and Salas-Ambrosio et al. [153]© American Chemical Society.*

Recent studies have demonstrated that pSar and its derivatives display favourable interactions with proteins and biological systems, often outperforming PEG in terms of reduced protein adsorption and immunogenicity.[154] Furthermore, comprehensive reviews have highlighted the versatility of pSar in drug delivery, surface functionalization, and polymer therapeutics, positioning it as a highly promising alternative to PEG.[146] The direct polymerisation of Sar-NCA provides a versatile route to polypeptoids with controlled chain

lengths and narrow molar mass distributions (Đ = 1.1–1.3).[155] The most common method for the synthesis of Sar-NCA is the Leuchs method, which involves cyclisation of the N-Boc-protected N-methylglycine using thionyl chloride $SOCl_2$ (**Figure 5.8** left). This reaction generates HCl and chlorinated byproducts, which can remain as trace contaminants even after recrystallisation (**Figure 5.8**, right).[152] These acidic impurities are particularly detrimental because they slow down the ROP kinetics and can reduce polymerisation efficiency. Recent studies have shown that proper purification of Sar-NCA is essential to achieve reproducible polymerisation.[153] The first-order rate constants, determined from FTIR monitoring of the carbonyl stretching band at 1850 cm^{-1}, revealed that impurities strongly decrease the ROP rate. This result confirms that removing acidic byproducts is critical for efficient polymerisation and supports the living character of Sar-NCA ROP. Sar-NCA is particularly reactive among R-NCAs, in part due to its minimal steric hindrance.

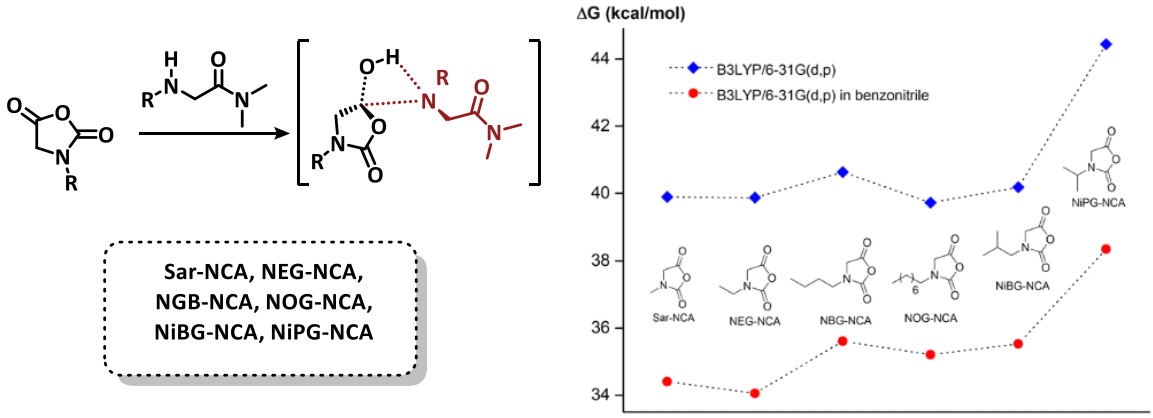

Figure 5. 9 *Schematic illustration of the carbonyl addition step of NNCA propagations on the model compound of the corresponding polymer ends (left). Calculated Gibbs free energy barrier of carbonyl addition step for various NNCAs in Scheme 1 on the basis of B3LYP/6-31G (d,p) (blue) and in benzonitrile (red) with SMD solvation model. The dashed line is used as a guide (right). Adapted from et al. [139]© American Chemical Society.*

Kinetic studies comparing different NNCAs[139] highlight that bulkier N-substituents significantly slow polymerisation, while the electronic effects of small N-alkyl groups, such as the methyl in Sar-NCA, have a negligible effect on ring-opening rates. Consequently, Sar-NCA serves as a model monomer to study the controlled polymerisation of polypeptoids and to optimise purification and polymerisation protocols (**Figure 5.9**).

5.2 Aim of the work

The aim of this work is to develop well-defined semiconducting polythiophene-based polymers functionalized with oligosarcosine side chains through the controlled ring-opening polymerisation (ROP) of sarcosine N-carboxyanhydride (Sar-NCA). The study use the DBT-MA initiator to graft chemically stable, hydrophilic, and conformationally flexible oligosarcosine segments onto a π-conjugated thiophene core. This approach is intended to combine the electronic properties of conjugated polymers with the biocompatibility and solubility advantages of polypeptoid side chains. The work focuses on designing and synthesising a bifunctional initiator capable of bridging NCA polymerisation and subsequent conjugated polymer formation, preparing and purifying highly reactive Sar-NCA under strictly anhydrous conditions, and establishing optimised polymerisation protocols. By carefully controlling the rate of monomer addition and capping the chain ends, the study aims to achieve uniform, well-defined oligosarcosine-grafted conjugates. Additionally, the role of initiator chemistry, including the exploration of alcohol-terminated analogues, is investigated to understand how hydrogen-bonding interactions influence polymerisation kinetics and selectivity. Overall, the objective is to establish a versatile synthetic platform for producing semiconducting polymers with tuneable side-chain architectures, suitable for bioelectronic applications such as organic electrochemical transistors (OECTs).

5.3 Results and discussion

5.3.1 Literature background

A particularly relevant precedent for the present work is provided by the study of Güler et al.[156], which introduced an innovative strategy for the synthesis of semiconducting polythiophenes bearing polypeptidic side chains. In that work, the 2,5-dibormo-3-thiophenemethanamine (DBT-MA) unit was employed as a macroinitiator for ROP of in situ formed NCA monomers derived from amino acids, in particular L-lysine. This approach enabled the direct growth of peptide segments from the conjugated dibromide monomer, yielding hybrid materials (**Scheme 5.1**)

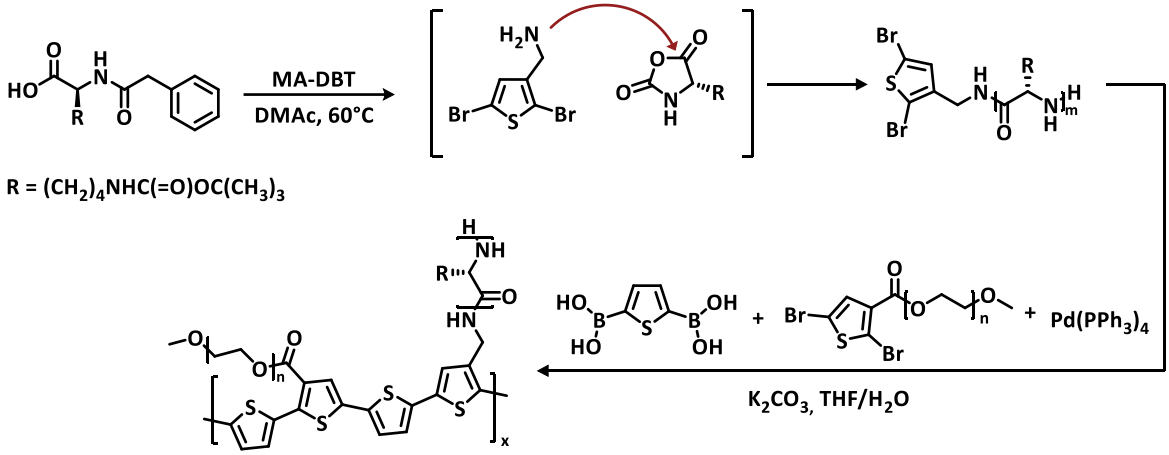

Scheme 5. 1 *Synthesis of DBT-PLL(boc) by in Situ NCA ROP and subsequent copolymerization of DBT-PLL(boc) and DBTPEG via Suzuki Coupling. Adapted from Guler et al. [156]© American Chemical Society.*

They were designed as theragnostic nanoplatforms, combining the intrinsic fluorescence of the conjugated polymer with the biocompatibility and functional versatility of polypeptides for targeted drug delivery and imaging applications. Although the aim of that work was biomedical rather than electronic, the synthetic strategy proposed by Güler and co-workers demonstrated the feasibility of using DBT-MA as an efficient macroinitiator for controlled ROP directly from a conjugated core. This approach provided a valuable foundation for developing well-defined grafted conjugated polymers with tuneable side-chain architectures. Building upon this methodology, the present study adapts the same DBT-MA-initiated ROP concept but replaces the polypeptidic side chains with oligosarcosine (polypeptoid) segments. This substitution maintains the desired hydrophilicity and conformational

flexibility while introducing enhanced chemical stability, resistance to hydrolysis, and synthetic versatility. The resulting polythiophene-oligosarcosine hybrids are therefore conceived not as theranostic systems, but as semiconducting polymers tailored for organic electrochemical transistors (OECTs), where controlled ion-electron transport and interfacial biocompatibility are critical.

5.3.2 Synthesis of the dibromide ROP initiator

The synthesis of DBT-MA (**23**) was developed to provide a bifunctional initiator capable of bridging two different polymerisation domains: the nucleophilic ROP of Sar-NCA, and the subsequent incorporation of the thiophene-based unit into a semiconducting π-conjugated polymer. The final molecule was thus designed to combine a reactive primary amine functionality, necessary for initiating the ROP of sarcosine NCA, with a dibrominated thiophene scaffold suitable for further cross-coupling polymerisation. A four-step synthetic sequence was established, following and adapting literature procedures based on the Gabriel amine synthesis, which allows the introduction of a primary amine starting from the corresponding alcohol under controlled conditions.

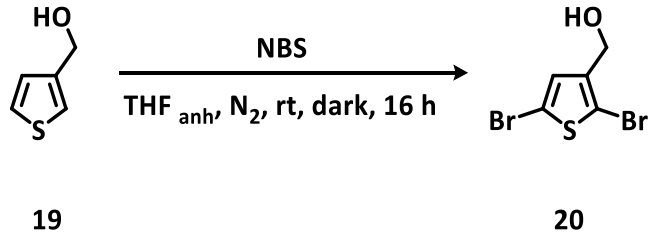

Scheme 5. 2 *Synthetic procedure for the obtainment of (**20**)*

The first step (**Scheme 5.2**) involved the selective dibromination of thiophen-3-ylmethanol (**19**) using N-bromosuccinimide (NBS) in anhydrous THF. Careful control of temperature, stoichiometry, and exclusion of light ensured preferential bromination at the 2- and 5-positions of the thiophene ring while keeping under control overbromination or other side reactions (*See Experimental Section for further information*). After a chromatography column purification, (2,5-dibromothiophen-3-yl)methanol (**20**) was afforded in good yield (68%) as a crystalline solid, whose purity was confirmed by ^{1}H NMR spectroscopy.

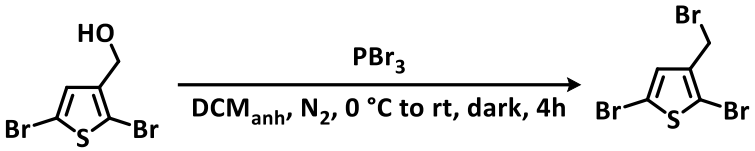

20 21

Scheme 5. 3 Synthetic procedure for the obtainment of (21)

In the second step (**Scheme 5.3**), the benzylic hydroxyl group was converted into a bromomethyl functionality using phosphorus tribromide. The transformation proceeded smoothly and with high selectivity, yielding 2,5-dibromo-3-(bromomethyl)thiophene (**21**) in 77% yield. This intermediate proved to be a key substrate for the subsequent nucleophilic substitution, as it allowed efficient introduction of the phthalimide moiety without degradation of the dibrominated aromatic ring.

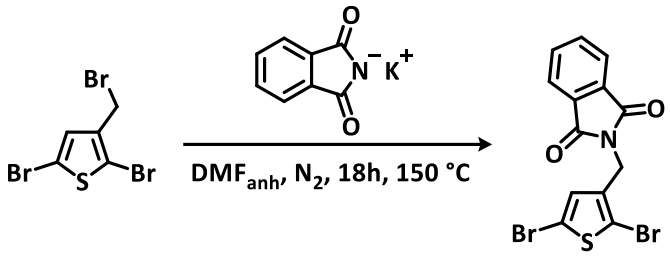

21 22

Scheme 5. 4 Synthetic procedure for the obtainment of (22)

The third step (**Scheme 5.4**) employed potassium phthalimide in anhydrous DMF, following the classical Gabriel route. The reaction required elevated temperature (150 °C) to promote complete substitution and afforded the corresponding protected amine, 2-[(2,5-dibromo-3-thienyl)methyl]-1H-isoindole-1,3(2H)-dione (**22**), in 87% yield after purification. The spectral data (^{1}H NMR) confirmed the aromatic signals characteristic of the phthalimide group, consistent with the successful substitution.

The final deprotection step was performed via hydrazinolysis under refluxing ethanol. (**Scheme 5.5**) Hydrazine hydrate efficiently cleaved the phthalimide protecting group, liberating the primary amine and yielding 2,5-dibromothiophenemethylamine as a yellow oil (81%).

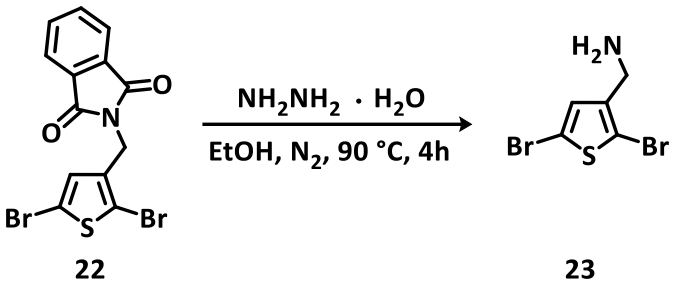

22 23

Scheme 5. 5 *Synthetic procedure for the obtainment of (23)*

The product was isolated and stored under an inert atmosphere to prevent oxidation or debromination. The formation of the free amine was confirmed by the disappearance of phthalimide resonances and the appearance of characteristic benzylic and amine-related signals in the ^{1}H NMR spectrum. The synthesised 2,5-dibromothiophenemethylamine was carefully dried under vacuum over molecular sieves for at least 24 hours prior to use as an initiator in the ROP of sarcosine N-carboxyanhydride. This precaution was crucial because the ROP mechanism is extremely sensitive to moisture, and even trace amounts of water from the synthetic work-up can lead to uncontrolled chain initiation or termination. Drying under rigorous anhydrous conditions ensured reproducible polymerisation behaviour and consistent molecular weight control.

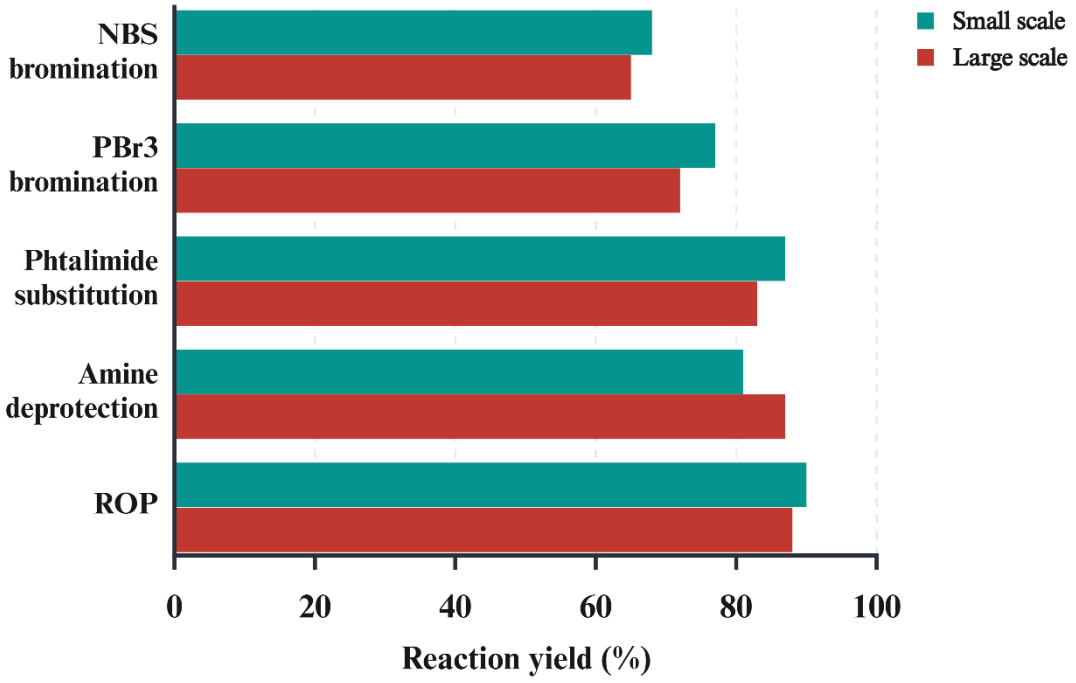

Graph 5. 1 *Comparison in between the reaction yields of each synthetic step for the obtainment of DBT-MA (23) at small scale (green) and large scale (red)*

To evaluate the robustness of the synthetic route, the reaction sequence was successfully scaled up to 88 mmol without any observable change in reaction outcome or yield. As shown in **Graph 5.1**, all steps maintained comparable yields to the small-scale synthesis, and no significant differences were detected in product purity or chromatographic behaviour. The work-up procedures remained identical across scales, except for the additional acid–base treatment described above, which was systematically applied during the final amine liberation step to prevent product loss through carbonation. On a larger scale, partial carbonation of the free amine was found to be more pronounced, likely due to slower degassing and a greater surface exposure of the reaction mixture to atmospheric CO_2 during quenching and extraction. Under these conditions, the liberated amine can readily react with dissolved carbon dioxide to form carbamate or ammonium carbonate species, which remain in the aqueous phase and reduce the apparent extraction yield. The acidification–neutralisation step efficiently reconverted these carbonated forms into the free amine, ensuring complete recovery of the product and reproducible overall yields.

From a synthetic perspective, this route demonstrated high reproducibility, operational simplicity, and good scalability. The choice of the Gabriel methodology proved advantageous in avoiding over-alkylation or quaternary ammonium formation, ensuring selective access to the primary amine. The presence of the two bromine substituents on the thiophene ring was maintained throughout the sequence without significant loss, confirming the robustness of the synthetic design. Functionally, the resulting 2,5-dibromothiophenemethylamine serves as a highly versatile intermediate. The primary amine allows for the controlled initiation of the ROP of sarcosine NCA to yield oligosarcosine chains covalently attached to the thiophene unit. At the same time, the dibrominated aromatic core preserves the potential for subsequent polymerisation of the thiophene through metal-catalysed cross-coupling reactions (e.g., Suzuki, Stille, or Yamamoto polymerisations). This dual reactivity enables the construction of hybrid systems in which the polypeptoid segment can be directly linked to π-conjugated polymeric frameworks, facilitating the development of semiconducting materials.

5.3.3 Synthesis and purification of SarNCA

The synthesis of Sarcosine N-carboxyanhydride (Sar-NCA) (**25**) represents a crucial step in the preparation of well-defined oligosarcosine side chains through ROP. Given the exceptional reactivity and instability of this monomer, its preparation required strict control of moisture, temperature, and atmosphere. In this work, the Sar-NCA was obtained following a slightly modified literature procedure starting from Boc-N-methylglycine, which was cyclized using phosphorus trichloride (PCl_3) as the carbonylating agent (**Scheme 5.6**) in place of phosgene for safety and practical reasons. The reaction was carried out in anhydrous DCM under a nitrogen atmosphere and at low temperature to limit side reactions and premature ring-opening of the cyclic anhydride. After the dropwise addition of PCl_3, the reaction mixture was maintained under stirring for three hours to ensure complete conversion, followed by filtration through a pre-dried Celite layer to remove insoluble by-products such as phosphorylated residues.

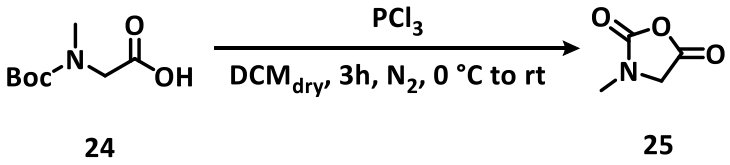

Scheme 5. 6 *Synthetic route for the obtainment of (25)*

Due to the known instability of Sar-NCA toward hydrolysis and polymerisation, all manipulations were performed under strictly anhydrous and inert conditions. The use of oven-dried glassware, freshly distilled solvent, and continuous nitrogen flow proved essential to prevent product degradation. The crude solid obtained after solvent removal exhibited a white, slightly hygroscopic appearance. Conventional recrystallisation was avoided, as exposure to even trace moisture or heat typically results in ring-opening or oligomerisation. For this reason, high-vacuum sublimation was employed as the purification method of choice. Sublimation at 57 °C and 0.018 mbar, using a −10 °C cold trap, allowed for the isolation of Sar-NCA as pure, crystalline material with a 92% yield. This approach minimises both thermal and hydrolytic decomposition, affording a monomer suitable for controlled ROP (*See experimental section for ^1H NMR of purified Sar-NCA*). The sublimation setup was transferred directly into a glovebox after cooling, ensuring that the

product was never exposed to ambient moisture. The resulting crystals were stored under argon atmosphere at −32 °C, maintaining their integrity over extended periods.

The appearance of well-defined white crystalline Sar-NCA confirmed the success of the synthesis and purification. The product was later characterised by its distinctive carbonyl stretching bands around 1850 and 1780 cm^{-1} in the IR spectrum, consistent with the anhydride functionality of NCAs. These results align with the literature reports describing the inherent lability of Sar-NCA and the necessity of sublimation for obtaining high-purity monomer. Overall, this procedure provided a reproducible and high-yielding route to pure Sar-NCA, suitable for the subsequent ROP initiated by DBT-MA. The careful optimisation of purification and handling steps proved critical to ensure the stability of the monomer and the controlled growth of oligosarcosine side chains in the later stages of polymer synthesis.

5.3.4 Controlled ROP of Sarcosine NCA Using DBT-MA as Initiator

The ROP of Sar-NCA (**Scheme 5.7**) represents the key step enabling the grafting of oligosarcosine side chains onto the conjugated DBT-MA initiator. The polymerisation and the workup were conducted under strictly anhydrous and oxygen-free conditions, entirely within the glovebox under an Ar atmosphere, to prevent premature hydrolysis or uncontrolled polymerisation of the highly reactive Sar-NCA monomer.

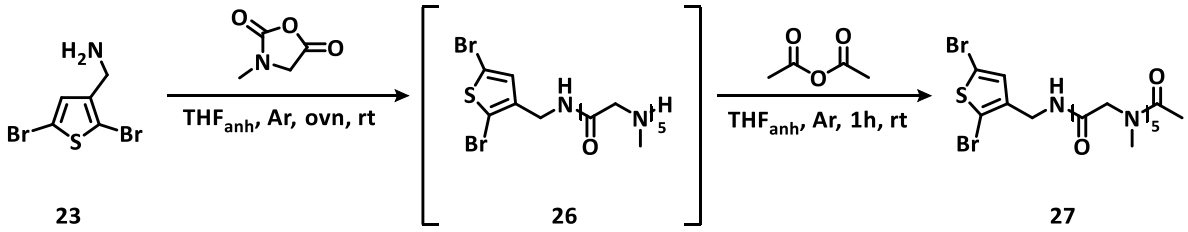

***Scheme 5.** 7 ROP protocol for the obtainment of DBT-MA Osar (**27**) using DBT-MA as initiator*

A 0.09 M solution of DBT-MA in extra-dry THF was used as the macroinitiator, while freshly sublimated Sar-NCA (5 eq) was slowly introduced via syringe pump at a controlled rate of 0.01 $mL \cdot min^{-1}$. (**Figure 5.10**) The slow and controlled dropwise addition of the monomer proved essential to maintain a homogeneous, transparent solution and to moderate the polymerisation kinetics. A clear solution throughout the entire addition indicated that the polymerisation proceeded in a controlled manner, without precipitation of short chain

species (n = 2/3), a common issue when localised monomer concentration spikes occur in NCA polymerisations. Following complete addition of the monomer, the reaction mixture was stirred for two additional hours at room temperature to ensure full conversion of the monomer. At this stage, the chain termination step became critical. To quench the reactive amine termini generated during ROP, acetic anhydride (1.1 eq), previously dried over molecular sieves, was introduced into the reaction mixture. The termination step capped the terminal secondary amines through acetylation, preventing further uncontrolled chain growth or post-polymerisation reactions upon exposure to trace moisture.

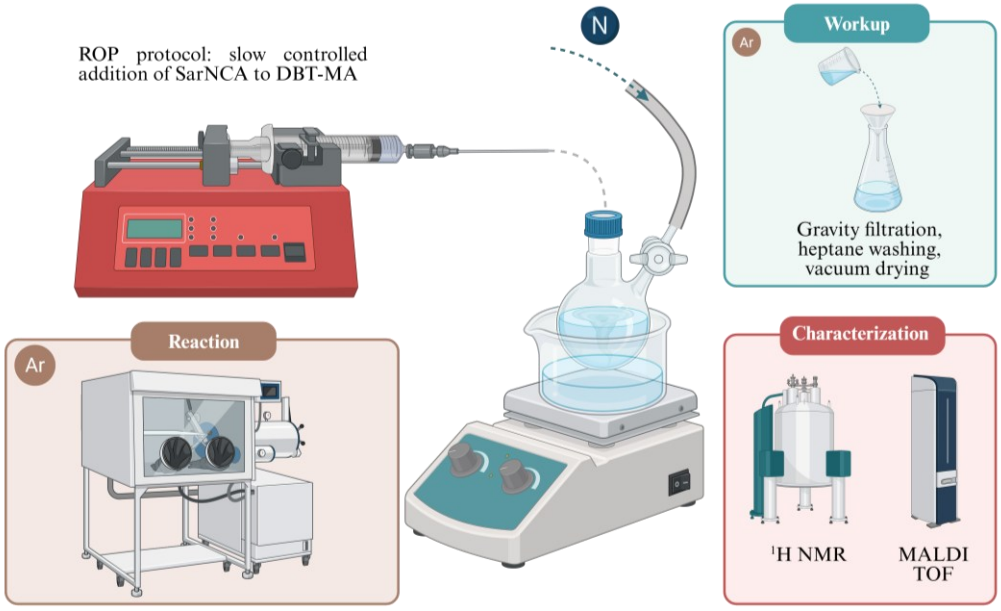

Figure 5. 10 *Cartoon representation of the set-up used for the ROP synthesis, workup and characterisation*

If this termination step is omitted, the oligosarcosine chains remain end-reactive, bearing a nucleophilic amine terminus. These reactive ends can initiate unwanted side reactions such as interchain condensation or even partial depolymerisation upon storage. From a spectroscopic perspective, the absence of proper chain termination is readily detectable in the ^{1}H NMR spectrum, where undefined broad signals appear in the 2.8–3.2 ppm region. After acetylation, these signals disappear, and a new singlet associated with the acetamide methyl group confirms successful capping of the oligomer termini.

The terminated product was isolated by precipitation in dry heptane, yielding a white powder that was filtered and dried under dynamic vacuum overnight. The clean precipitation and absence of low-molecular-weight residues indicate the effective removal of unreacted monomer and solvent. The resulting oligosarcosine-functionalized DBT-MA was stored under argon at −32 °C to ensure long-term stability.

5.3.5 Mechanistic considerations in the DBT-MA-initiated ROP of Sar-NCA

The main difference between polymerisation and oligomerisation of Sar-NCA lies in the kinetic control of the propagation step. In both cases, the mechanism follows the classical amine-initiated ROP pathway, involving nucleophilic attack of the initiator's amine on the carbonyl carbon of the NCA ring, accompanied by CO_2 release and formation of a new amide bond. However, the reaction regime - that is, the ratio of monomer to initiator, the concentration, and the rate of monomer addition - determines whether the system proceeds under controlled oligomer growth or uncontrolled chain extension.

Chain length and control

In a polymerisation regime (high monomer/initiator ratio, rapid monomer addition, or batch conditions), the monomer concentration around each active site remains high, favouring rapid and successive ring openings. This results in long chains and often incomplete initiation, particularly problematic for Sar-NCA, whose propagation rate is intrinsically fast due to the absence of steric hindrance on the amide nitrogen.[157,158] In contrast, the oligomerisation regime used in this work relies on slow, controlled addition of monomer to a diluted initiator solution. This ensures that each monomer molecule reacts promptly upon addition and minimises the probability of chain overgrowth (**Figure 5.11**). The clear, homogeneous appearance of the solution throughout the process indicates a uniform reaction and absence of precipitation or aggregation, which typically accompany uncontrolled polymerisation.

Postulated role of CO_2 pressure

During ROP, one equivalent of CO_2 is released per NCA ring-opening. In closed systems, CO_2 accumulation can shift the equilibrium backwards, slowing down the propagation. However, in the used setup, the local CO_2 pressure is negligible, so its influence on the kinetics should be minimal.

Reaction kinetics and concentration effects

The kinetics of Sar-NCA ROP are typically first order in monomer and independent of initiator concentration under controlled conditions.[132] However, for highly reactive NNCAs such as Sar-NCA, propagation is extremely fast, often diffusion-controlled, meaning that any local excess of monomer immediately produces long chains before other sites can initiate.[157] That is precisely why, in this work, the monomer was added dropwise to the initiator. The slow addition rate (0.01 mL·min^{-1}) should exhibit "pseudo-living kinetics" and uniform chain initiation.

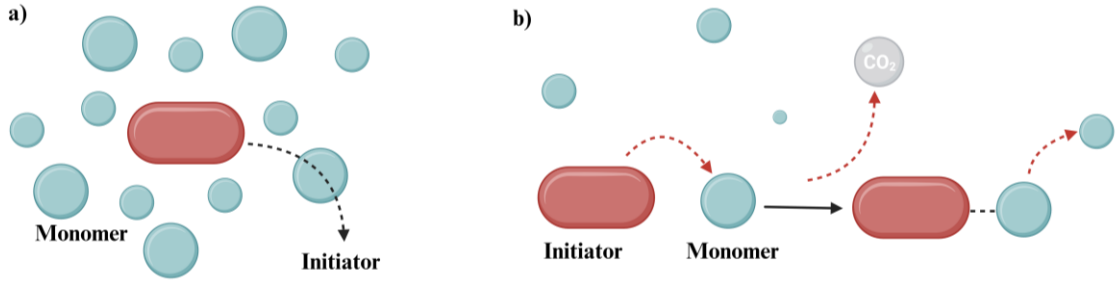

Figure 5. 11 *a) polymerisation and b) oligomerisation regime for Sar-NCA ROP, where monomer concentration and addition are crucial for a controlled "pseudo living" chain formation*

A control experiment was carried out under the same optimised conditions described above, with the only difference being the inverted order of addition: instead of adding the monomer to the initiator solution, the initiator was added to a solution of Sar-NCA in dry THF. This change in addition sequence resulted in a markedly different outcome. At the moment of addition, the monomer concentration surrounding the initiator is maximal, leading to instantaneous multiple ring-openings and therefore the formation of long, uncontrolled chains, as highlighted by the ^{1}H NMR experiment. In this case, the polymerisation proceeds

under a "rushed" regime, characterised by fast CO_2 evolution, polymer precipitation, and loss of control over chain length. The NMR spectra of the sample show broadened signals, consistent with a wide molecular weight distribution and possibly partial aggregation.

Importance of termination

Finally, because oligomeric Sarcosine chains possess an active amine terminus, they remain reactive even after complete monomer consumption. Without a proper termination step – such as acetylation with acetic anhydride – the chain ends can attack other carbonyl sites, leading to secondary polymerisation, branching, or gradual depolymerisation. Experimentally, this is observed in ^{1}H NMR as new broad resonances. The presence of a sharp singlet at ~2.05 ppm after acetylation confirms successful end-capping and stabilisation of the oligomeric product. Overall, the success of the DBT-MA-initiated ROP strongly depended on the precise control of addition rate, reaction atmosphere, and termination chemistry. The slow monomer addition allowed for uniform grafting from the initiator and prevented chain aggregation, while acetyl capping proved indispensable to stabilise the resulting oligomers. These conditions collectively afforded reproducible synthesis of DBT-MA–oligosarcosine conjugates, suitable for subsequent incorporation into semiconducting polythiophene frameworks.

5.3.6 From DBT-MA to DBT-MeOH: exploring the role of initiator chemistry in Sar-NCA ROP

The initial choice of DBT-MA as the initiator for the ROP of Sar-NCA was mainly dictated by synthetic practicality. Given the intrinsic instability and reactivity of the Sar-NCA monomer, employing a primary amine as the initiating site represented the most straightforward and reliable strategy to achieve controlled chain growth. Primary amines are well-known to readily open N-carboxyanhydrides under mild conditions, forming amide bonds with predictable kinetics and minimal side reactions. Therefore, DBT-MA provided an efficient entry point to the synthesis of polythiophene derivatives bearing oligosarcosine side chains.

Once the ROP conditions were optimised, attention shifted toward understanding whether the corresponding alcohol analogue (DBT-MeOH) could also serve as an initiator. This

modification would replace the terminal N-H group, which acts primarily as a hydrogen-bond donor, with a hydroxyl-terminated group, whose oxygen atom behaves mainly as a hydrogen-bond acceptor. Such a substitution subtly alters the balance of donor and acceptor interactions at the interface between the conjugated backbone and the oligosarcosine side chains. In the context of OMIECs, this change can influence how the material interacts with water and ions within the electrolyte, affecting hydration dynamics, ion mobility, and morphology of the active layer, and therefore may ultimately impact the ionic-electronic coupling efficiency in OECT operation.

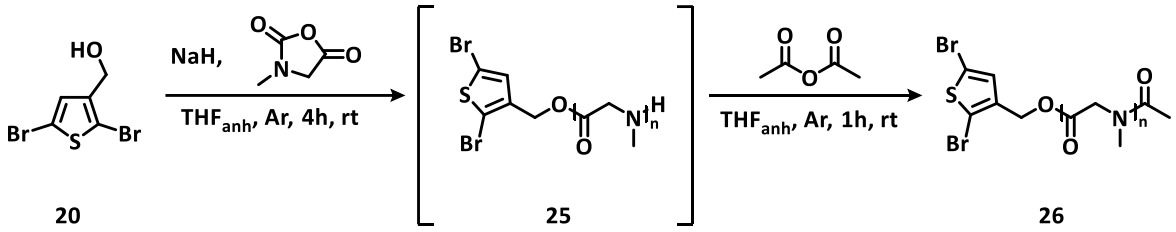

Scheme 5. 8 *ROP of Sar-NCA using DBT-MeOH as initiator and NaH as base, following the experimental conditions of Lipshutz et al*[159]

In literature, the use of alcohols as initiators for NCA polymerisation has been reported, although it typically requires activation by a strong base. For instance, Lipshutz and co-workers[159] demonstrated that NaH-activated alcohols can initiate NCA polymerisations in the development of a designer surfactant. Inspired by this methodology, an analogous experiment was conducted (**Scheme 5.8**) using NaH to deprotonate DBT-MeOH prior to Sar-NCA addition. However, in our case, the polymerisations were consistently uncontrolled, yielding undefined, high-molecular-weight products and resulting in incomplete initiation. The most plausible explanation for this outcome is the presence of NaOH impurities in the NaH reagent, which can lead to partial hydrolysis of the NCA and uncontrolled chain initiation.

To overcome these limitations, the use of TMG as a milder and more selective catalyst has been taken into consideration. This approach was inspired by previous reports[143,144] showing that TMG can promote NCA ring-opening through the formation of hydrogen bonds with the initiator's hydroxyl group, thereby enhancing its nucleophilicity without generating strongly basic conditions. To verify whether TMG can interact through hydrogen bonding with DBT-MeOH, ^{1}H NMR experiments were carried out.

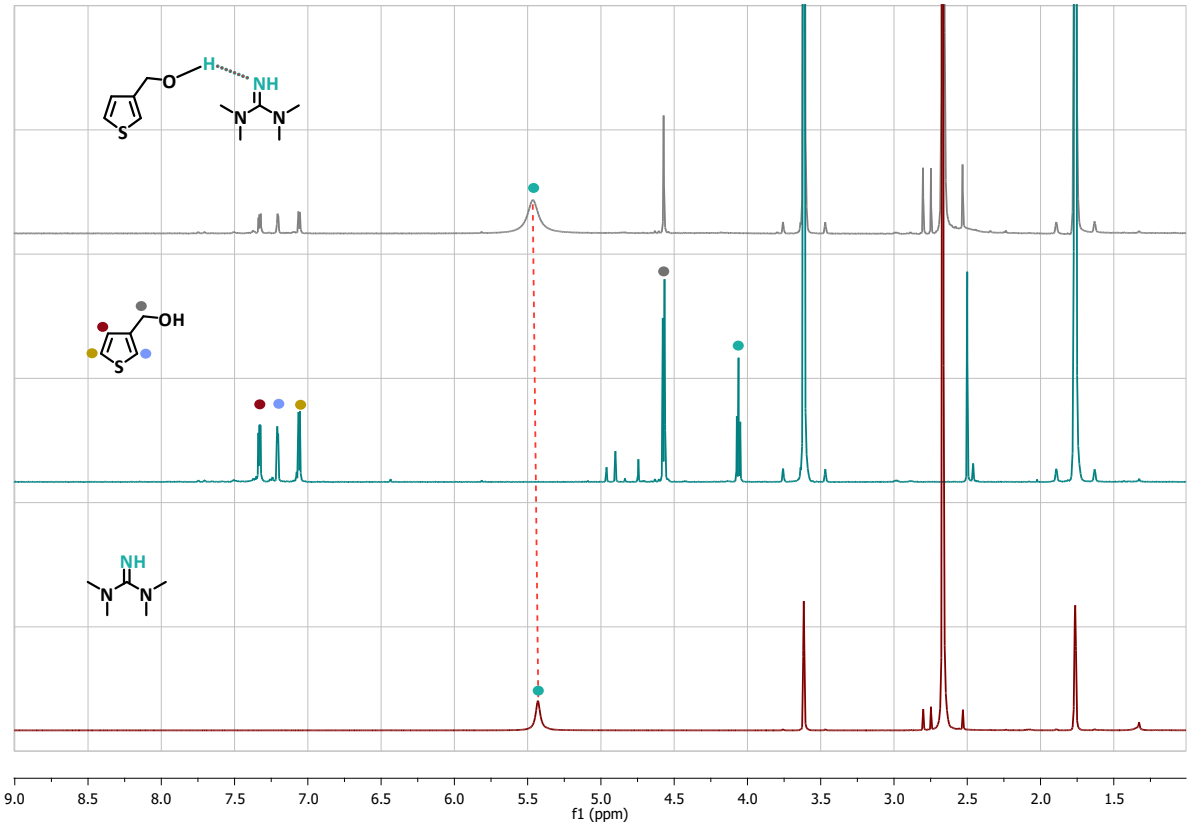

Graph 5. 2 *Stacked ^{1}H NMR spectra in THF-d8 of TMG (red), ThMeOH (blue) and a 1:1 mixture of ThMeOH and TMG (prepared in the glovebox in the absence of moisture)*

^{1}H NMR tubes were prepared in the glovebox. Firstly, a 1:1 mixture of ThMeOH and TMG was prepared and analysed. The ^{1}H NMR of such mixture showed a clear interaction between the two molecules: the triplet assigned to the OH proton of ThMeOH at 4.07 ppm disappears, and the multiplicity of the aliphatic CH2 change (singlet), furthermore the singlet associated to the TMG NH downshift compared to the OH in the absence of TMG ($\Delta\delta \sim 0.6$ ppm) and broadened, consistent with the formation of a hydrogen bond between the alcohol and the guanidine nitrogen.

The same experiment was conducted with DBT-MeOH to assess the role of the two bromides on the Th core in the process, confirming also in this case the presence of the hydrogen bond between the OH of the initiator and the guanidinium NH. The triplet assigned to the OH proton of ThMeOH at 4.38 ppm disappears, and the multiplicity of the aliphatic CH_2 changes (singlet). Furthermore, also in this case, the singlet associated to the TMG NH shift at higher fields compared to the OH in the absence of TMG ($\Delta\delta \sim 0.9$ ppm) and broadened.

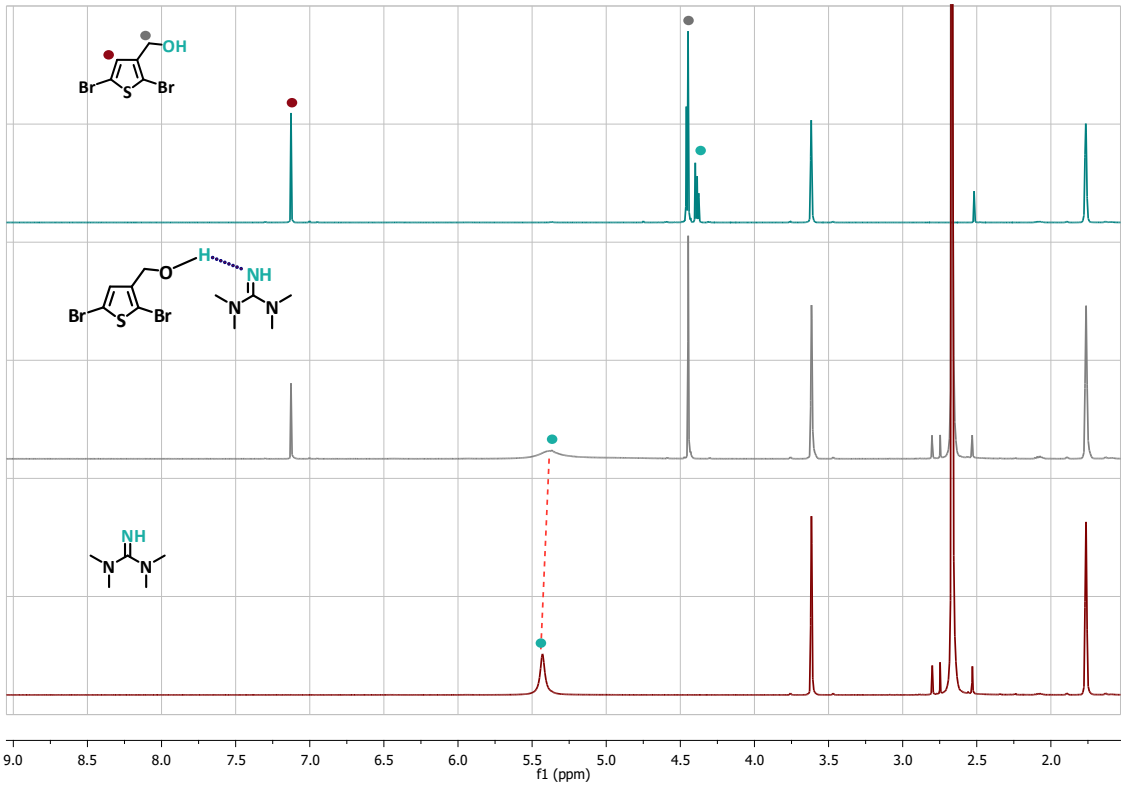

Graph 5. 3 *Stacked ^{1}H NMR spectra in THF-d8 of TMG (red), DBT-MeOH (blue) and a 1:1 mixture of DBT-MeOH and TMG (prepared in the glovebox in the absence of moisture)*

The comparative NMR analysis of ThMeOH and DBT-MeOH mixtures with TMG reveals how the electronic nature of the thiophene core influences the hydrogen-bonding interaction. In the ThMeOH-TMG mixture, the NH signal of TMG shifts slightly downfield ($\Delta\delta \approx 0.6$ ppm) and broadens moderately, consistent with the formation of a moderately strong O–H···N hydrogen bond between the alcohol and the guanidine nitrogen.

In contrast, when DBT-MeOH is used, the NH resonance of TMG shifts upfield ($\Delta\delta \approx 0.9$ ppm) and becomes broader, appearing as two partially overlapping components. These spectral behaviours suggest a different hydrogen-bonding regime compared to the non-brominated analogue. The upfield shift indicates an increased electronic shielding of the NH proton, which can arise from a weaker and more transient hydrogen bond. The presence of the two bromine atoms on the thiophene ring likely plays a key role in this behaviour. Through their inductive electron-withdrawing effect, the bromine substituents slightly decrease the electron density on the thiophene oxygen substituent, thereby reducing the overall hydrogen-bond donating ability of the hydroxyl group. Consequently, the interaction

with TMG can become less stable and more, which explains the broader and partially split resonance observed for the NH proton. Overall, these findings indicate that bromination does not prevent hydrogen bonding between DBT-MeOH and TMG but rather modulates its strength and dynamics, leading to a more labile interaction. This subtle tuning may influence the initiation behaviours during ROP, as a more dynamic H-bonding equilibrium could modify the transient activation of the hydroxyl group, thus affecting the balance between initiation and propagation in the polymerisation process.

Based on these NMR results, future studies will focus on evaluating DBT-MeOH as a potential initiator for the ring-opening polymerisation of Sar-NCA, in the presence of catalytic TMG, to assess whether such hydrogen-bond activation can enable a controlled and selective initiation process.

5.4 Conclusions

This work demonstrates the successful synthesis of the DBT-MA initiator through a robust four-step Gabriel-based procedure, yielding a bifunctional molecule capable of initiating the controlled ROP of Sar-NCA while retaining a dibrominated thiophene core suitable for further polymerisation. The Sar-NCA monomer was obtained in high purity via sublimation, a strategy that minimised hydrolytic and thermal degradation and ensured reproducible polymerisation outcomes. Controlled ROP using DBT-MA was achieved by slow, dropwise monomer addition under strictly anhydrous conditions, followed by acetylation to cap the chain ends. This approach produced oligosarcosine-grafted conjugates with uniform chain length and excellent reproducibility. Mechanistic studies highlighted the critical importance of monomer addition rate, initiator-to-monomer ratio, and proper chain termination in achieving pseudo-living polymerisation, preventing uncontrolled growth and aggregation. The investigation of DBT-MeOH as an alcohol-based initiator revealed that while NaH activation led to uncontrolled polymerisation, hydrogen-bonding interactions with TMG provided insight into potential strategies for controlled alcohol-initiated ROP. Taken together, these results establish a versatile and reproducible platform for the synthesis of semiconducting polythiophene–oligosarcosine hybrids, providing a foundation for the rational design of bifunctional polymers for OECTs and related bioelectronic devices.

5.5 Experimental

5.5.1 Materials and methods

All reagents are purchased from VWR, Sigma-Aldrich, Fluorochem, BLD pharm, TCI, Ambeed, Fisher Scientific, and ThermoFisher. Solvents – including anhydrous and NMR solvents – are purchased from Carlo Erba, Fisher Scientific, and Acros and used as received unless otherwise stated. Extra dry solvents packed under Ar and stored over molecular sieves having a >99,5% purity are always employed if a reaction requires inert and anhydrous conditions. Glassware is dried for 24 hours at 130 °C before being used when the synthetic protocol requires an anhydrous environment. If the synthetic protocol requires an inert atmosphere, solid reagents are always degassed using high vacuum (~0,02 mbar) and then refilling the reaction vessel with nitrogen (the procedure is repeated three times). Liquid or low-melting-point solids are degassed through a freeze-pump-thaw procedure using liquid nitrogen as a cooling agent. Reactions are monitored using Xtra SIL G UV254 silica gel plates (pore size: 60 Å, thickness 200 µm) and a double-wave UV lamp (λ: 254 and 365 nm). When cited, the composition of solvent mixtures is always indicated as a volume/volume ratio. Chromatographic purifications are performed using two different silica gels: flash chromatographies are performed using a 60 Å Silica gel and flash chromatographic columns are performed using a Combi Flash NextGen 300+ Chromatographer. RediSep Gold® Silica Gel Disposable Flash Columns, 20–40 micron are used as the stationary phase. The column is packed with hexane with a flow rate of 10 mL·min^{-1}; the same rate is kept during the entire process. Melting points are measured employing a Büchi M-560 apparatus. Solution Nuclear Magnetic Resonance (NMR) spectra are acquired with a Bruker Avance 400 NEO spectrometer. ^{1}H and ^{13}C NMR of known compounds are included after each synthetic procedure to provide the reader with the chemical shifts of the compound. ^{1}H and ^{13}C spectra of new molecules are also included in Chapter 5.5.3. Gas chromatography–mass spectrometry (GC–MS) analyses were carried out using an Agilent 8860 gas chromatograph coupled with an Agilent 5977 mass selective detector (MSD). Helium was employed as the carrier gas, and the separation was achieved on an Agilent HP-5MS capillary column (30 m × 0.25 mm i.d., 0.25 µm film thickness). The method was operated under the following conditions: inlet temperature 250 °C, ion source temperature 220 °C, initial oven temperature 100 °C, followed by a heating ramp of 20 °C·min^{-1} up to 300 °C, which was maintained for

5 minutes. Samples were prepared by dissolving the crude material in DCM at a concentration of 1 mg·mL^{-1}. The resulting solutions were filtered through a cotton and silica layer to remove traces of water and salts. The purified solutions were then subjected directly to GC–MS analysis.

5.5.2 Synthetic procedures

5.5.2.1 2,5-Dibromo-3-thiophenemethanamine (DBT-MA) synthetic route

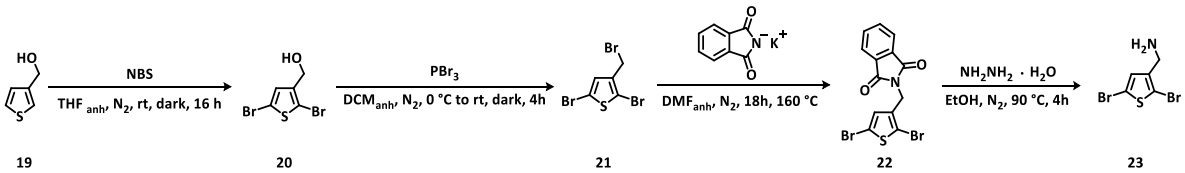

Scheme 5. 9 *Schematic representation of the synthetic pathway for the preparation of the ROP initiator DBT-MA (**23**).*

OSar initiator DBT-MA (**23**) was synthesised using the Gabriel synthesis of primary amines, starting from the corresponding alcohol (2,5-dibromothiophen-3-yl)methanol (DBT-MeOH, 20). Prior to the synthesis of the primary amine, a bromination step at the 2 and 5 positions of the thiophene ring was carried out, enabling the subsequent polymerisation of the oligopeptoid chain-functionalized monomer.

*Synthesis of (2,5-dibromothiophen-3-yl)methanol (**20**)*

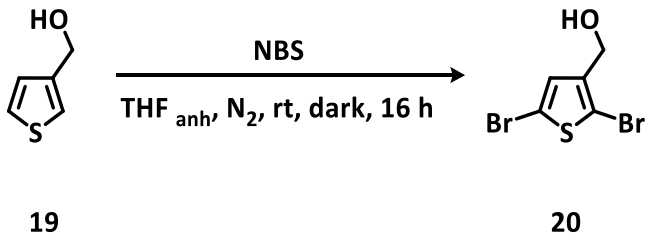

Scheme 5. 10 *Synthetic protocol for the obtainment of (**20**)*

The procedure has been adapted from an existing literature protocol[160]. 8000 mg of thiophen-3-ylmethanol (**19**) (70,0 mmol, 1 eq) are added to an oven-dried 2-neck 250 mL round-bottom flask. The reagent was degassed through freeze-pump-thaw, then it was dissolved in 63,6 mL of anhydrous THF and placed into an ice bath for 15 minutes. 25566 mg (143,6

mmol, 2,05 eq) of freshly recrystallized N-bromosuccinimide is added portion-wise to the reaction flask, keeping the flask in the dark. The reagents are left to react for 16 hours, then the solvent is removed using the rotavapor. The crude product is then suspended in hexane and filtered. The powder is washed with hexane until no more UV-active. The solvent is then evaporated, and the crude product is purified through a flash chromatography column using 1:9 AcOEt:Hexane as eluent. The third fraction is collected. The solvent is evaporated to obtain a pale-yellow liquid. The product is crystallized using cold heptane to yield a white powder, filtered, and dried overnight using the Schlenk line (yield: 68%).

^{1}H NMR (500 MHz, $CDCl_3$) δ(ppm) 7.04 (1H, s), 4.58 (2H, d, J=5.8), 1.78 (1H, t, J= 5.9)

*Synthesis of 2,5-Dibromo-3-(bromomethyl)thiophene (**21**)*

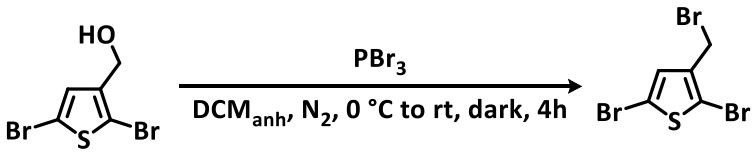

20 **21**

Scheme 5. 11 *Synthetic protocol for the obtainment of (**21**)*

A literature procedure has been followed, performing minor adjustments.[160] 10000 mg of (2,5-dibromothiophen-3-yl)methanol (**20**) (36,7 mmol, 1 eq) are added to an oven-dried 3-neck 250 mL round-bottom flask equipped with a dropping funnel. The reagent is degassed, then dissolved in 188 mL of anhydrous DCM. The colourless solution is placed in an ice bath for 15 minutes, then 3,56 mL (37,5 mmol, 1.02 eq) of PBr_3 are dropwise added to the flask over 20 minutes in the dark. The reaction mixture is stirred for 4h in total, and the temperature is slowly increased from 0 °C to rt. The reaction mixture is quenched with 200 mL of a 10% $NaHCO_3$ aqueous solution. The crude is extracted three times using DCM and washed with brine. The organic layer is dried with Na_2SO_4 and filtered. The solvent is evaporated to afford a white solid. The product is dried overnight using the Schlenk line (yield: 77%).

^{1}H NMR (500 MHz, $CDCl_3$) δ(ppm) 7.02 (1H, s), 4.39 (2H, s)

*Synthesis of 2-[(2,5-Dibromo-3-thienyl)methyl]-1H-isoindole-1,3(2H)-dione (**22**)*

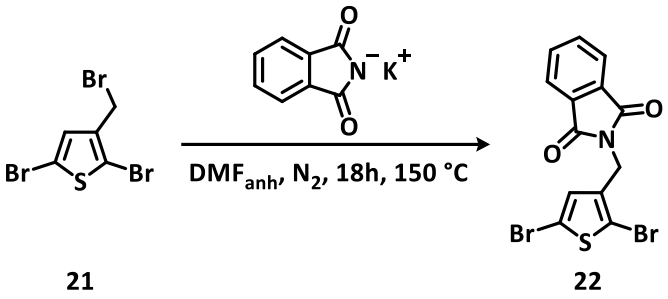

***Scheme 5. 12** Synthetic protocol for the obtainment of (22)*

The procedure has been adapted from an existing literature protocol[156]. 7380 mg of potassium phthalimide (39,8 mmol, 1,5 eq) are weighed into an oven-dried 2-neck 100 mL round-bottom flask equipped with a condenser and degassed. 8895 mg of 2,5-Dibromo-3-(bromomethyl)thiophene (**21**) (26,6 mmol, 1 eq) are dissolved in 22 mL of anhydrous mL of DMF in the glovebox. The solution is added to the reaction flask, then the mixture is stirred at 150 °C for 16h. The reaction mixture is then brought back to rt and quenched with 80 mL of distilled water to precipitate the product. The crude is filtered and washed with additional water, then dried overnight using the Schlenk line to afford a light-brown powder. The powder is then purified with a flash chromatography column using DCM as solvent. The solvent is evaporated to afford a white powder (yield 87%).

^{1}H NMR (500 MHz, CDCl3) δ(ppm) 7.90-7.75 (4H, M), 7.00 (1H, s), 4.79 (2H, s)

*Synthesis of 2,5-Dibromo-3-thiophenemethanamine (**23**)*

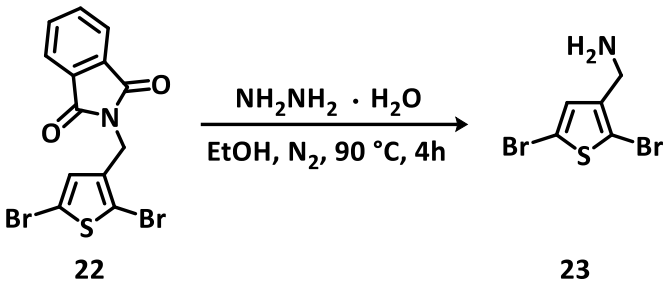

***Scheme 5. 13** Synthetic protocol for the obtainment of (23)*

The procedure has been adapted from an existing literature protocol[156]. 8895 mg of 2-[(2,5-Dibromo-3-thienyl) methyl]-1H-isoindole-1,3(2H)-dione (**22**) (21,7 mmol, 1 eq) are degassed after being placed into a 3-neck 500 mL round-bottom flask equipped with an addition funnel and a condenser. Then 216 mL of degassed absolute EtOH are added to the flask. 10,54 mL $NH_2NH_2H_2O$ solution (54-64% solution, 217 mmol, 10 eq) are dropwise added to the reaction flask. The mixture is stirred at 90 °C for 4h, then it is brought back to room temperature and quenched with 150 mL of 10% $NaHCO_3$ aqueous solution. The crude product is extracted three times with DCM, then the organic layer is washed with brine, dried with Na_2SO_4, and filtered. The solvent is evaporated to yield a yellow oil. The oil is dried overnight using the Schlenk line vacuum, then dried for at least 24h over molecular sieves before further use (yield 81%).

Large-scale additional step: The crude is dispersed in water, and HCl 37 wt% is slowly added until complete dissolution of the suspended compound. After 30 minutes of stirring, the aqueous solution pH is brought to 9.0 by slowly adding NaOH. The product is then extracted with Et_2O, dried with Na_2SO_4, and filtered. The solvent is evaporated to yield a yellow oil.

^{1}H NMR (500 MHz, CDCl3) δ(ppm) 6.97 (1H, s), 3.76 (2H, s), 1.48 (2H, br)

5.5.2.2 Oligopeptoid functionalized monomer 2,5-Dibromo-3-thiophene oligosarcosine (DBT-Osar) synthetic route

The oligopeptoid chain was grafted onto the previously synthesized initiator via a ring-opening polymerization (ROP) process. Specifically, a pentameric sarcosine segment was incorporated following the synthesis and purification of the cyclic carboxyanhydride precursor

*Synthesis of Sarcosine-N-carboxyanhydride (SarNCA) (**25**)*

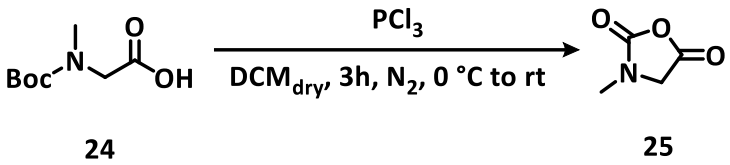

***Scheme 5. 14** Synthetic protocol for the obtainment of (**25**)*

A literature procedure has been followed, performing minor adjustments. 6000 mg of Boc-*N*-methylglycine (**24**) (37,71 mmol, 1 eq) are added to an oven-dried 3-neck 250 mL round-bottom flask equipped with a dropping funnel. The reagent is degassed, then dissolved in 40 mL of anhydrous DCM and stirred for 15 minutes in an ice bath. 2,22 mL of PCl_3 (25,37 mmol, 0,8 eq) are placed into the dropping funnel, together with 20 mL of dry DCM. The solution is dropwise added to the reagent over 20 minutes. The mixture is stirred for 3h after the end of the addition, then it is filtered under a nitrogen flux over a 48h oven-dried celite layer to remove the solid precipitate. The solvent is removed, and the resulting white powder is sublimated at 57 °C and 0,018 mbar using a -10 °C cold trap (H_2O/Ethylene glycol 60:40) to afford white crystals. The sublimator was cleaned, dried and moved into a glovebox without ever exposing the product to oxygen and moisture. The product is removed from the sublimator trap and stored under Ar at -32 °C (yield: 92%).

^{1}H NMR (500 MHz, $CDCl_3$) δ(ppm) 4.15 (2H, s), 3.08 (3H, s)

*Synthesis of 2,5-Dibromo-3-thiopheneoligosarcosine (DBT-Osar) (**27**)*

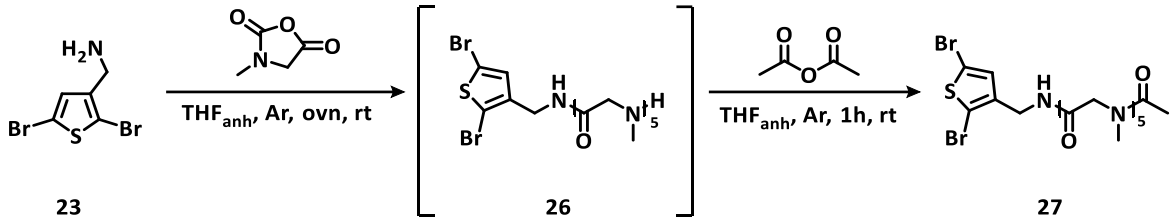

Scheme 5. 15 *Synthetic protocol for the obtainment of (27)*

A 0,09 M extra-dry THF solution of DBT-MA (**25**) (0,64 mmol, 1 eq) is added to an oven-dried MW vial equipped with a magnetic stirrer in the glovebox. 368 mg of freshly sublimated SarNCA (3,20 mmol, 5 eq) are dissolved in 7 mL of extra-dry THF. The monomer solution is dropwise added to the initiator-containing vial using a syringe pump (addition rate: 0,01 mL·min^{-1}). The addition is performed at rt, ensuring that the solution remains visibly clear during the entire procedure. After the end of the addition, the reaction mixture is stirred for an additional 2 hours, then 66,3 µL (1,1 eq) of acetic anhydride (dried for at least 24h over molecular sieves) are added to the solution to terminate the oligomeric chains. After 45 minutes, 10 mL of extra-dry heptane is added to precipitate the product. The powder is gravity-filtered inside the glove box to yield a white solid. The product is dried overnight using the Schlenk line vacuum and stored under Ar at -32 °C.

^{1}H NMR (500 MHz, $CDCl_3$) δ(ppm) 7.04-6.89 (1H, br), 4.42-3.84 (12 H, m), 3.21-2.90 (15H, m), 2.2-1.93 (3H, br)

5.5.3 Material characterization

^{1}H NMR spectra

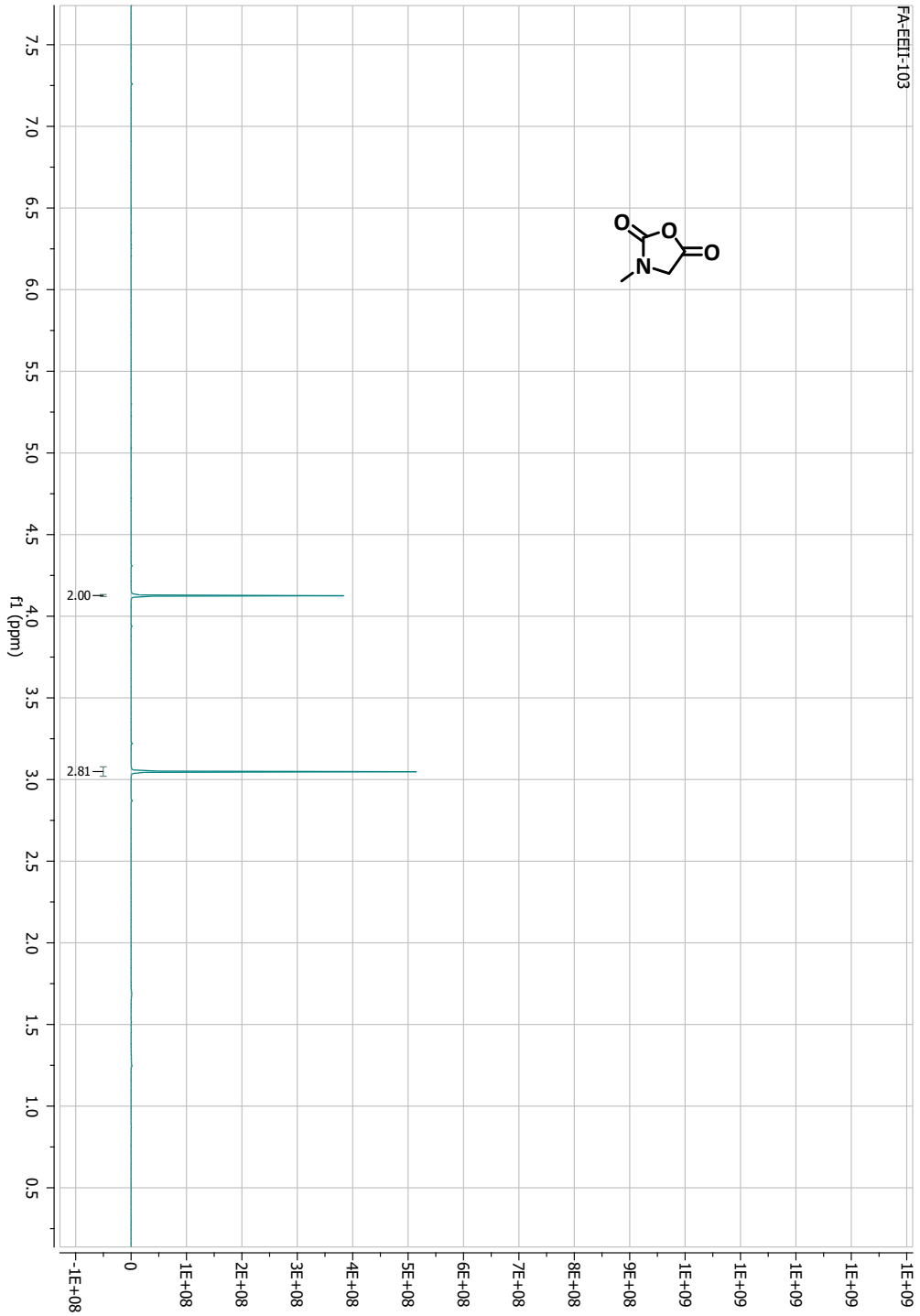

Figure 5. 12 *^{1}H NMR in $CDCl_3$ spectrum of compound (**25**) after sublimation. The NMR tube is oven-dried overnight and prepared in the glovebox using a $CDCl_3$ with a low water content*

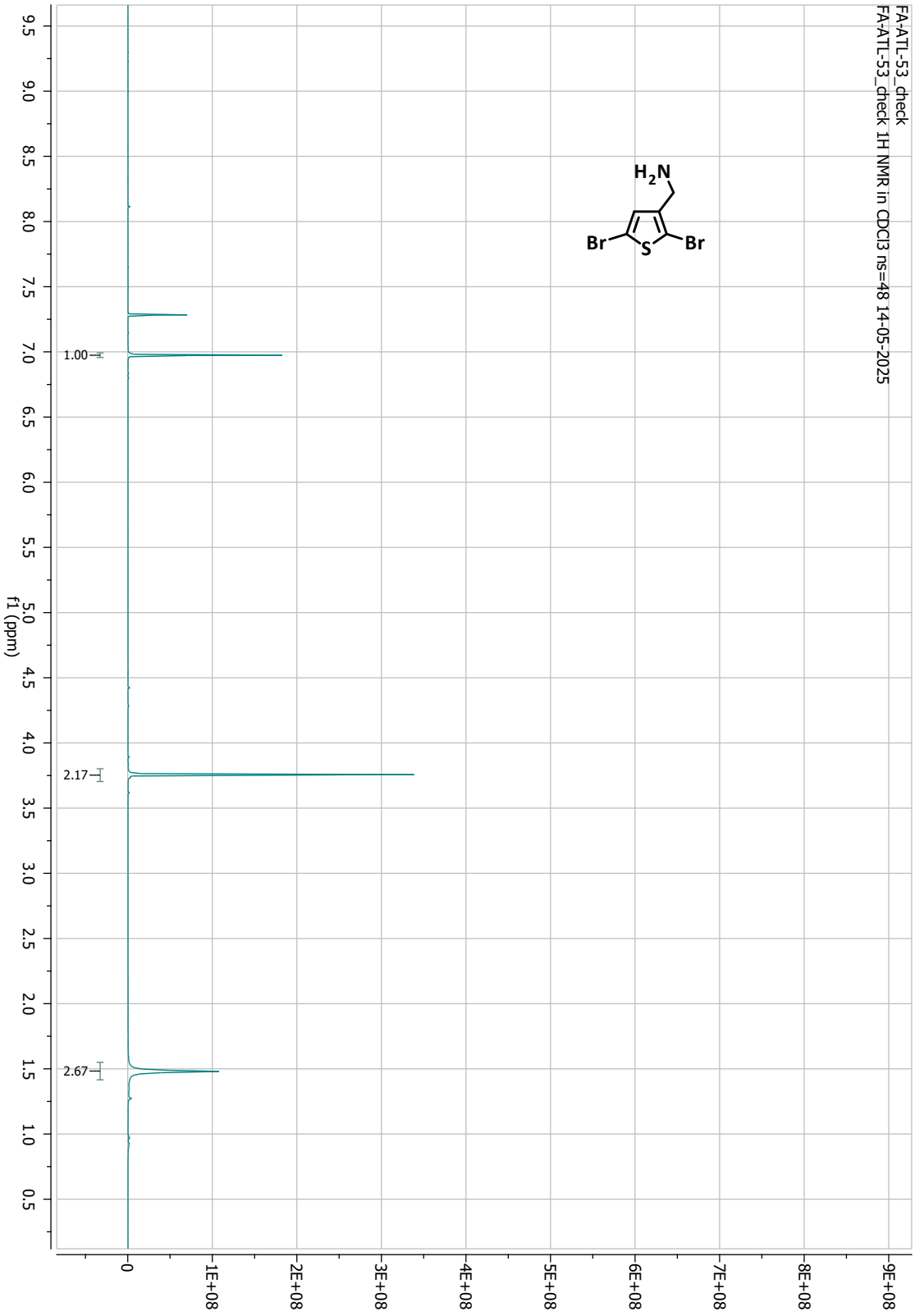

Figure 5. 13 *^{1}H NMR in $CDCl_3$ spectrum of compound* ***(23)***

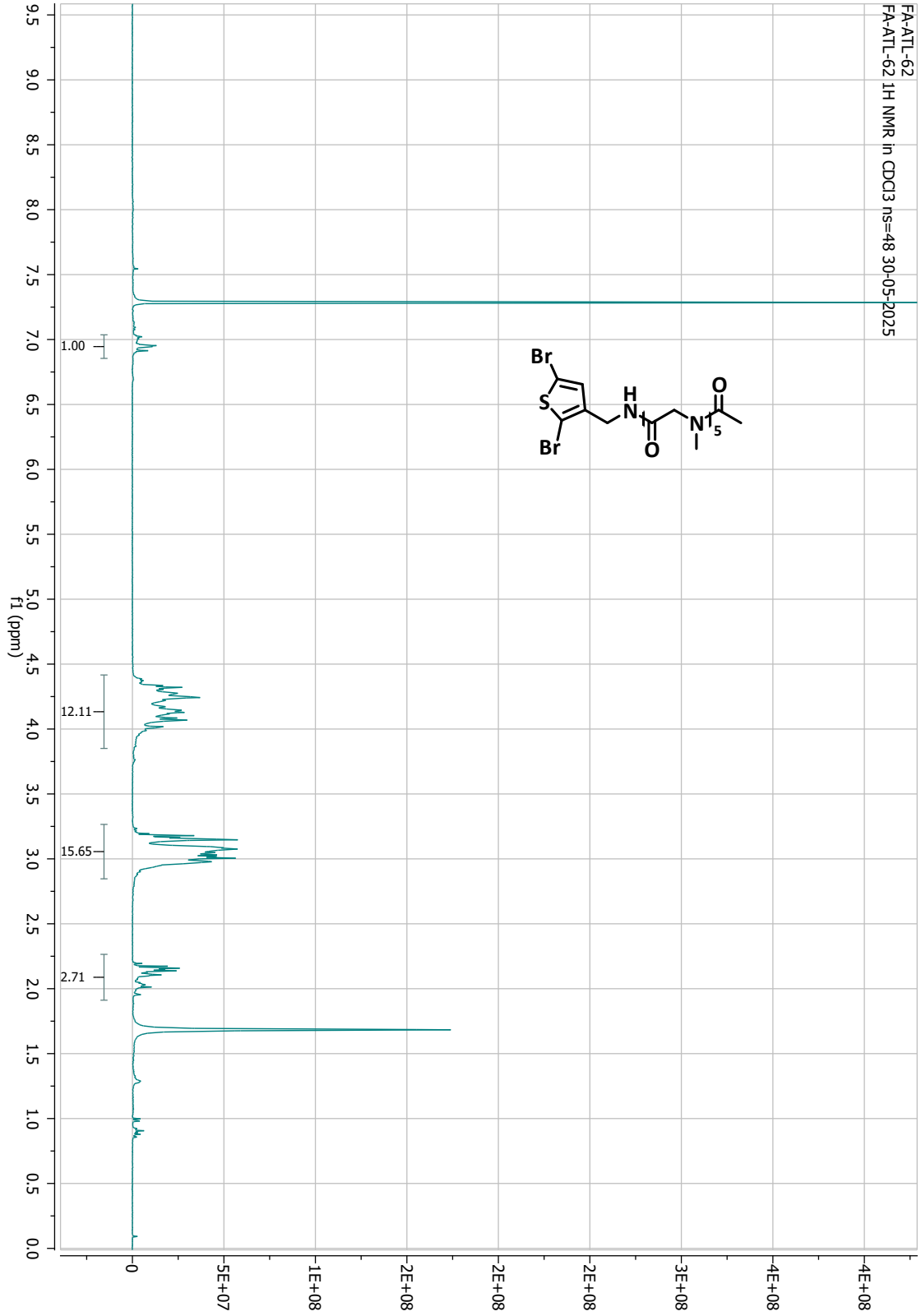

Figure 5. 14 ^{1}H *NMR in* $CDCl_3$ *spectrum of compound (27)*

5.5.4 ^{1}H NMR analysis for the investigation of hydrogen bonding

TMG was kept in the glovebox and used without further purification; ThMeOH was degassed and kept in the glovebox and used without further purifications; DBT-MeOH was synthesised according to the procedure in *Chapter 5.5.2*; THF-d8 (anhydrous, stored under Ar atmosphere) was used without further purification.

NMR Sample Preparation

All manipulations are performed in a glovebox under a nitrogen atmosphere to prevent moisture exposure. Three types of samples are prepared:

1. TMG solution in THF-d8.
2. ThMeOH or DBT-MeOH solution in THF-d8.
3. 1:1 molar mixture of ThMeOH and TMG, or DBT-MeOH and TMG, in THF-d8.

The solutions are stirred for five minutes, then they are transferred into NMR tubes directly in the glovebox.

Data acquisition

NMR spectra are recorded at 500 MHz at ambient temperature (25 °C). Chemical shift changes (δ, ppm) and signal broadening were compared between individual components and the mixtures to evaluate hydrogen-bond formation between the initiator hydroxyl group and the TMG-NH group. Changes in CH2 multiplicity adjacent to the hydroxyl and the NH chemical shifts (Δδ) were analysed as indicators of hydrogen-bonding interactions.

Data Analysis

Comparative analysis of ThMeOH and DBT-MeOH mixtures with TMG allowed assessment of the effect of bromine substituents on the thiophene core on hydrogen-bond strength and dynamics. NH signal broadening and upfield or downfield shifts were interpreted as indicators of the strength and lability of the hydrogen-bond interaction.

Bibliography

120. Leuchs, H. & Manasse, W. Über die Isomerie der Carbäthoxyl-glycyl glycinester. *Berichte Dtsch. Chem. Ges.* **40**, 3235–3249 (1907).

121. Leuchs, H. & Geiger, W. Über die Anhydride von α-Amino- *N* -carbonsäuren und die von α-Aminosäuren. *Berichte Dtsch. Chem. Ges.* **41**, 1721–1726 (1908).

122. Leuchs, H. Ueber die Glycin-carbonsäure. *Berichte Dtsch. Chem. Ges.* **39**, 857–861 (1906).

123. Kricheldorf, H. R. Polypeptides and 100 Years of Chemistry of α-Amino Acid *N* -Carboxyanhydrides. *Angew. Chem. Int. Ed.* **45**, 5752–5784 (2006).

124. Hadjichristidis, N., Iatrou, H., Pitsikalis, M. & Sakellariou, G. Synthesis of Well-Defined Polypeptide-Based Materials via the Ring-Opening Polymerization of α-Amino Acid *N* -Carboxyanhydrides. *Chem. Rev.* **109**, 5528–5578 (2009).

125. Lu, H. *et al.* Recent advances in amino acid N-carboxyanhydrides and synthetic polypeptides: chemistry, self-assembly and biological applications. *Chem Commun* **50**, 139–155 (2014).

126. Deng, C. *et al.* Functional polypeptide and hybrid materials: Precision synthesis via α-amino acid N-carboxyanhydride polymerization and emerging biomedical applications. *Prog. Polym. Sci.* **39**, 330–364 (2014).

127. Gangloff, N., Ulbricht, J., Lorson, T., Schlaad, H. & Luxenhofer, R. Peptoids and Polypeptoids at the Frontier of Supra- and Macromolecular Engineering. *Chem. Rev.* **116**, 1753–1802 (2016).

128. Zhang, D., Lahasky, S. H., Guo, L., Lee, C.-U. & Lavan, M. Polypeptoid Materials: Current Status and Future Perspectives. *Macromolecules* **45**, 5833–5841 (2012).

129. Deng, Y. *et al.* Poly(ε-caprolactone)- *block* -polysarcosine by Ring-Opening Polymerization of Sarcosine *N* -Thiocarboxyanhydride: Synthesis and Thermoresponsive Self-Assembly. *Biomacromolecules* **16**, 3265–3274 (2015).

130. Tao, X., Deng, C. & Ling, J. PEG-Amine-Initiated Polymerization of Sarcosine *N* -Thiocarboxyanhydrides Toward Novel Double-Hydrophilic PEG- *b* -Polysarcosine Diblock Copolymers. *Macromol. Rapid Commun.* **35**, 875–881 (2014).

131. Chan, B. A. *et al.* Polypeptoid polymers: Synthesis, characterization, and properties. *Biopolymers* **109**, e23070 (2018).

132. Siefker, D. & Zhang, D. Ring-opening Polymerization of N-carboxyanhydrides Using Organic Initiators or Catalysts. https://doi.org/10.1039/9781788015738-00367 (2018) doi:10.1039/9781788015738-00367.

133. Wang, S. *et al.* Precision Synthesis of Polysarcosine via Controlled Ring-Opening Polymerization of N-Carboxyanhydride: Fast Kinetics, Ultrahigh Molecular Weight, and Mechanistic Insights. *J. Am. Chem. Soc.* **146**, 5678–5692 (2024).

134. Fetsch, C. & Luxenhofer, R. Highly Defined Multiblock Copolypeptoids: Pushing the Limits of Living Nucleophilic Ring-Opening Polymerization. *Macromol. Rapid Commun.* **33**, 1708–1713 (2012).

135. Fetsch, C., Grossmann, A., Holz, L., Nawroth, J. F. & Luxenhofer, R. Polypeptoids from n-substituted glycine n-carboxyanhydrides: Hydrophilic, hydrophobic, and amphiphilic polymers with poisson distribution. *Macromolecules* **44**, 6746–6758 (2011).

136. Xuan, S. *et al.* Synthesis and Characterization of Well-Defined PEGylated Polypeptoids as Protein-Resistant Polymers. *Biomacromolecules* **18**, 951–964 (2017).

137. Wang, S. & Lu, H. Unveiling Proton Transfer as the Key Process to Understand and Promote the Ring-Opening Polymerization of N-Carboxyanhydrides. *Polym. Sci. Technol.* **1**, 76–81 (2025).

138. Liu, J. & Ling, J. DFT Study on Amine-Mediated Ring-Opening Mechanism of α-Amino Acid N-Carboxyanhydride and N-Substituted Glycine N-Carboxyanhydride: Secondary Amine versus Primary Amine. *J. Phys. Chem. A* **119**, 7070–7074 (2015).

139. Bai, T. & Ling, J. Polymerization rate difference of N-alkyl glycine NCAs: Steric hindrance or not? *Biopolymers* **110**, e23261 (2019).

140. Clapperton, A. M., Babi, J. & Tran, H. A Field Guide to Optimizing Peptoid Synthesis. *ACS Polym. Au* **2**, 417–429 (2022).

141. Fu, X., Li, Z., Wei, J., Sun, J. & Li, Z. Schiff base and reductive amination reactions of α-amino acids: a facile route toward *N* -alkylated amino acids and peptoid synthesis. *Polym. Chem.* **9**, 4617–4624 (2018).

142. Zheng, B., Xu, S., Ni, X. & Ling, J. Understanding Acid-Promoted Polymerization of the *N* -Substituted Glycine *N* -Thiocarboxyanhydride in Polar Solvents. *Biomacromolecules* **22**, 1579–1589 (2021).

143. Li, K. *et al.* Organobase 1,1,3,3-tetramethyl guanidine catalyzed rapid ring-opening polymerization of α-amino acid *N* -carboxyanhydrides adaptive to amine, alcohol and carboxyl acid initiators. *Polym. Chem.* **13**, 586–591 (2022).

144. Chan, B. A., Xuan, S., Horton, M. & Zhang, D. 1,1,3,3-Tetramethylguanidine-Promoted Ring-Opening Polymerization of *N* -Butyl *N* -Carboxyanhydride Using Alcohol Initiators. *Macromolecules* **49**, 2002–2012 (2016).

145. Xu, G., Tang, G. & Bai, H. Cyclodextrin-Initiated N-Carboxyanhydride Polymerization for the Design of Stereostructural Dobby Polypeptides with Jellyfish-

Type Architecture. *Angew. Chem. Int. Ed.* e202501058 (2025) doi:10.1002/anie.202501058.

146. Kabil, M. F., Azzazy, H. M. E. S. & Nasr, M. Recent progress on polySarcosine as an alternative to PEGylation: Synthesis and biomedical applications. *Int. J. Pharm.* **653**, (2024).

147. Huesmann, D., Sevenich, A., Weber, B. & Barz, M. A head-to-head comparison of poly(sarcosine) and poly(ethylene glycol) in peptidic, amphiphilic block copolymers. *Polymer* **67**, 240–248 (2015).

148. Maiti, D., Yokoyama, M. & Shiraishi, K. Impact of the Hydrophilicity of Poly(sarcosine) on Poly(ethylene glycol) (PEG) for the Suppression of Anti-PEG Antibody Binding. *ACS Omega* **9**, 34577–34588 (2024).

149. Wang, H. *et al.* Polysarcosine-based surfactants: syntheses and properties. *J. Biomater. Sci. Polym. Ed.* 1–12 (2025) doi:10.1080/09205063.2025.2522744.

150. Morrell, A. H., Warren, N. J. & Thornton, P. D. The Production of Polysarcosine-Containing Nanoparticles by Ring-Opening Polymerization-Induced Self-Assembly. *Macromol. Rapid Commun.* **45**, 2400103 (2024).

151. Yao, X. *et al.* Polysarcosine as PEG Alternative for Enhanced Camptothecin-Induced Cancer Immunogenic Cell Death. *ACS Appl. Mater. Interfaces* **16**, 19472–19479 (2024).

152. Capelôa, L., Miravet Martí, R., Duro-Castaño, A., Nebot, V. J. & Barz, M. Utility of Triethyloxonium Tetrafluoroborate for Chloride Removal during Sarcosine *N* -Carboxyanhydride Synthesis: Improving NCA Purity. *Chem. – Eur. J.* **30**, e202304375 (2024).

153. Salas-Ambrosio, P. *et al.* Effect of N-alkylation in N-carboxyanhydride (NCA) ring-opening polymerization kinetics. *Polym. Chem.* **13**, 6149–6161 (2022).

154. Settanni, G., Schäfer, T., Muhl, C., Barz, M. & Schmid, F. Poly-sarcosine and Poly(Ethylene-Glycol) Interactions with Proteins Investigated Using Molecular Dynamics Simulations. *Comput. Struct. Biotechnol. J.* **16**, 543–550 (2018).

155. Wang, S. *et al.* Precision Synthesis of Polysarcosine via Controlled Ring-Opening Polymerization of N-Carboxyanhydride: Fast Kinetics, Ultrahigh Molecular Weight, and Mechanistic Insights. *J. Am. Chem. Soc.* **146**, 5678–5692 (2024).

156. Guler, E. *et al.* Complex Structured Fluorescent Polythiophene Graft Copolymer as a Versatile Tool for Imaging, Targeted Delivery of Paclitaxel, and Radiotherapy. *Biomacromolecules* **17**, 2399–2408 (2016).

157. Tao, X., Zheng, B., Kricheldorf, H. R. & Ling, J. Are N-substituted glycine N-thiocarboxyanhydride monomers really hard to polymerize? *J. Polym. Sci. Part Polym. Chem.* **55**, 404–410 (2017).

158. Salas-Ambrosio, P. *et al.* Effect of N-alkylation in N-carboxyanhydride (NCA) ring-opening polymerization kinetics. *Polym. Chem.* **13**, 6149–6161 (2022).

159. Kincaid, J. R. A. *et al.* Introducing Savie: A Biodegradable Surfactant Enabling Chemo- and Biocatalysis and Related Reactions in Recyclable Water. *J. Am. Chem. Soc.* https://doi.org/10.1021/jacs.2c13444 (2022) doi:10.1021/jacs.2c13444.

160. Dong, B. X. *et al.* Complex Relationship between Side-Chain Polarity, Conductivity, and Thermal Stability in Molecularly Doped Conjugated Polymers. *Chem. Mater.* **33**, 741–753 (2021).

Chapter 6
Heterogeneous and heterogenized Pd^0 catalysts

"The support is not a spectator — it shapes the catalyst's identity."

C. Copéret,

In this chapter, metal meets polymer in a delicate balance. Tiny palladium nanoparticles find a home inside PFO, a soft and flexible polymer that keeps them apart but alive, reactive yet stable. Together, they form a material where structure and function move in harmony — a nanoscale choreography that turns simple components into something far greater than the sum of their parts.

Although this chapter does not deal directly with the synthesis of organic semiconductors, it addresses a fundamental aspect that such synthetic processes inherently depend upon. These compounds are largely obtained through polycondensation polymerisation, typically catalysed by palladium complexes. As discussed in the previous introductory sections, trace amounts of residual catalyst can reduce the performance of the material once integrated into the final device. Moreover, residual Pd nanoparticles adversely affect both edibility and overall biocompatibility of the developed materials, due to their intrinsic cytotoxic and pro-inflammatory effects.

This section of the project is embedded within the broader research framework developed by the group in which I have carried out my research during the past three years at the

University of Milano-Bicocca. Among its principal research directions, the group is particularly engaged in the development of more sustainable synthetic methodologies for monomers[161,162] and polymers[163] employed in the field of green electronics. Specifically, several protocols have been designed and are currently under investigation with the aim of minimising the use of organic solvents at every stage of synthesis. This is achieved through the implementation of heterogeneous catalysis in aqueous media and the use of benign surfactants[164,165] capable of compatibilizing scaffolds that are otherwise poorly soluble in both conventional organic solvents and water. In line with the goal of achieving a fully circular synthetic approach, particular attention is also devoted to the use and recycling of catalysts. Building upon preliminary studies performed on commercial Pd/C[166], which is widely used in cross-coupling reactions, the results presented herein can be considered as a further step toward maximising catalyst efficiency and recovery by minimising the leaching of active sites.

6.1 Introduction

6.1.1 Beyond misconception: the green approach

Environmental damages, water, land and air pollution increase, as well as a serious impact on human health, have been the price people have paid during the past decades in order to achieve industrial and chemical innovation, medical advances, and satisfy fundamental living needs.[167] Chemistry has undeniably improved people's lives, having a giant footprint on the environment. Historically, the value of synthetic products was judged by their ability to accomplish a precise function, not considering the adverse consequences their production process or the chemical itself could cause. Furthermore, safety was not included in the definition of “performance” of a chemical. Nowadays, the effects of bioaccumulation in people's bodies and global changes caused by pollution are more undeniable than ever and are pushing people toward a major sensibility for sustainability and chemists towards a radical change of traditional methodologies and processes.[168]

The green chemistry concept arose during the nineties, and its purpose is the achievement of sustainability (working at the molecular scale). In other words, it is a branch of chemistry focused on reducing the detrimental impact of chemical protocols without giving up innovation. Design procedures and chemical nature must be checked. Green Chemistry

Twelve Principles (**Figure 6.1**) are hence a powerful tool for safer and meticulous chemical synthesis planning, and they must be applied to all stages of a process life cycle. Moreover, the prevention of waste generation is another crucial point concerning sustainable chemical protocols.

Figure 6. 1 *Twelve principles of Green Chemistry*

Green chemistry tries to avoid waste formation rather than disposing of it. Thereby, the Environmental Impact Factor (*E-factor*) and the concept of *Atom Economy* (AE) cannot be overlooked in a greener approach. The former helps in the quantification of the amount of waste generated per kilogram of useful product, giving the idea of how "environmentally acceptable" a protocol is and how much it impacts.[169] The latter is the concept of maximising the incorporation of starting material atoms into the final product. An ideal reaction should be able to incorporate all the atoms of the reactants. It is a value assessing the efficiency of a reaction, as it is the ratio of the molecular weight of the product over the molecular weight of the reactants.[170] Without any doubt, the use of renewably sourced feedstocks contributes to the design of a sustainable procedure, hopefully transitioning from a linear to a circular one.[171] In this way, even low-value wastes – if generated – can be upgraded to renewable

feedstock useful in other processes. It is important to highlight that the definition of waste includes not only undesired side products but also any valueless materials, unused energy and solvents. Solvents are perhaps the majority of wasted mass during a chemical process, as they are involved both in the synthetic process and in the purification. Traditional fossil-based solvents are generally flammable and toxic. Because of their volatility and they give a non-negligible contribution to environmental pollution and contamination, as far as to the worsening of workers' health. Their recovery and recycling is desirable even if it requires massive energy involvement, distillations and cross-contamination risk is in any case possible.[9] Undoubtedly, the best solvent is no solvent and solventless systems are for sure investigated. Nevertheless, a large portion of reactions cannot be performed under neat conditions as solvents facilitate mass and heat transfer. To overcome this issue, greener and sustainable solvents have been developed over the past decades; they should be biodegradable, non-corrosive, recyclable, non-carcinogenic, and they should not harm the ozone layer. Supercritical fluids, ionic liquids, bio-solvents and water are a part of the answer to the sustainability issue.[172]

6.1.2 Emulating nature: water as a reaction medium

Water is both the most abundant molecule on the Earth's surface and the solvent in which nature has always performed its chemical reactions. It is a safe, non-toxic, cheap, and environmentally friendly alternative to petroleum-based solvents. Despite its unquestionable green features, water has, hence, a not surprisingly limited role in organic synthesis. Chemists, in fact, have avoided water for decades following the paradigm that "like dissolves like". Dissolution was actually considered crucial for the achievement of high reaction conversion; therefore, organic solvents have always been the norm. More recent studies proved it wrong. A large number of organic reactions have been demonstrated to take place in aqueous media.[173] Water shows a high dielectric constant and cohesive energy density while remaining liquid at ambient pressure. It is a non-inert medium having a unique structure and properties that are the reason behind reaction-affecting interactions such as polarity, hydrogen bonding and hydrophobic effect, which in some cases proved to enhance both rate and selectivity of different synthetic pathways, allowing also more straightforward workups.[174] The advantages of water are mainly due to the hydrophobic effect: the repulsive

interaction between water and lipophilic molecules promotes the formation of hydrophobic aggregates, thus reducing the contact surface between the two counterparts.[175] Water molecules are arranged around the non-soluble aggregates, causing an internal pressure that leads to rate enhancement.

6.1.3 Getting around the solubility issue with micelles

Because of the brand-new popularity acquired by water, surfactants came into play, and micellar catalysis emerged as an attractive alternative approach to disperse lipophilic chemicals in the aqueous medium.

6.1.3.1 The identikit of a surfactant

Sometimes referred to as amphiphiles, tensides or surface-active compounds, surfactants are defined as amphiphilic molecules having a two-part structure: a polar hydrophilic head group covalently linked to a hydrophobic tail (**Figure 6.2**).

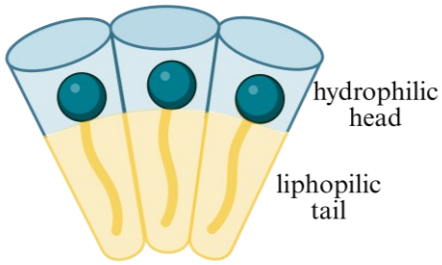

Figure 6. 2 *Structure of a generic tenside and disposition of the surfactant molecules at the interface in a biphasic system*

The former is endowed with an enhanced affinity for an aqueous environment, while the latter tends to interact with an apolar one. Due to their unique morphology, they form monolayers at biphasic systems interfaces (liquid-liquid or gas-liquid; if the disperse phase is a solid, dispersants come into play), hence lowering the surface or interfacial tension of the medium in which they are dissolved (**Figure 6.2**). All things considered, surfactants can be pictured as compatibilizing agents for immiscible fluids.[176] As far as the polar head is concerned, it can interact with water through dipole-dipole or ion-dipole interaction.

Depending on them, the nature of the polar head of the surfactant can be identified, and surfactants divided into two main classes: non-ionic and ionic ones.[177] Non-ionic amphiphiles carry no charge on their polar head; on the other hand, ionic ones possess one or more charges on their hydrophilic portion. To be more precise, cationic, anionic and zwitterionic surfactants carry respectively a positive, a negative and both charges. Furthermore, both head and tail can have a tailored structure in order to fulfil specific tasks. Low surfactant concentration aqueous solutions can be equated to electrolyte solutions. The situation drastically changes when amphiphile concentration increases. The observed behaviour is strictly related to the spontaneous formation of colloidal aggregates called micelles (**Figure 6.3**). The micelle is a theoretically spherical nanometric object composed of 50-100 amphiphiles whose existence is due to surfactant self-assembly into a three-dimensional structure. Their lipophilic tails are confined into the core of the colloid to reduce their energetically unfavourable interaction with the solvent. On the other hand, hydrophilic heads face and interact with the aqueous medium.[178] As the core of the micelle is essentially composed of hydrocarbon chains, its properties can be compared to those of liquid hydrocarbons. The micelle is a dynamic entity having a limited lifetime, whose constituting units continually exchange with free solute ones. Its formation process is connected to hydrophobic and electrostatic contributions, and it is also ruled by intricate equilibria.

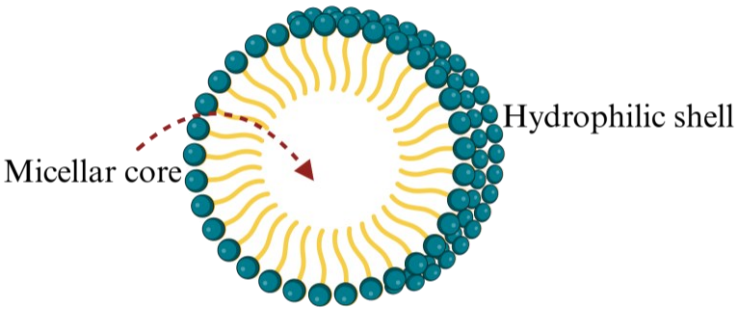

Figure 6. 3 *Theoretical representation of a micelle*

The micelle-forming concentration is named Critical Micellar Concentration (cmc).[179] It is not a universal value, as it changes according to temperature, pressure, additive presence and, of course, the nature of the surfactant itself. Despite being commonly referred to as a numerical value, the transition between single surfactant molecules and micellar aggregates occurs over a range of concentrations whose breadth is related to the nature of the tails.

Contrary to what one could believe, mixed micelles do exist: they comprise more than one type of surfactant aggregating together.

This description suggests that micelles, in reality, are far from being objects having a spherical, defined shape; they rather form a *pseudo-phase*, a not sharply distinct phase with respect to the aqueous one.[180]

6.1.3.2 From colloidal objects to nanoreactor: micellar catalysis

Now, a step forward must be done to have a more precise idea of a significant part of this thesis. Up to this point, micelles have been depicted as nanometric objects forming and interfacial tension-reducing agents. It is important to point out clearly that when low concentration (10^{-4} M) water-insoluble chemicals (both liquid and solid) are placed into a micellar aqueous medium, they do not perturb the micellar environment; surfactants and dispersants help in compatibilizing them with the surrounding medium and in shielding them from contact with water. Basically, the hydrophobic chemicals are confined in the inner part of the micelles, where the lipophilic tails of the surfactants provide a suitable medium in which such molecules can settle. The nature of the colloidal entity ensures the creation of a controlled nanometric environment able to accommodate substrates to perform organic reactions (**Figure 6.4**).

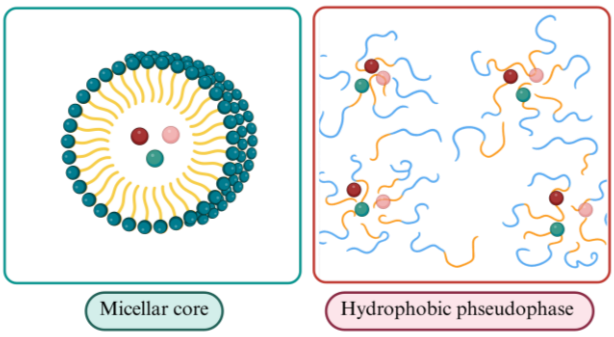

Figure 6. 4 *Reagent distribution inside a surfactant-containing dispersion below (left) and above (right) MAC value*

Under such conditions, one can speak of "micellar catalysis". Such surroundings, having a unique morphology, can impart reactions with peculiar features. For example, the compartmentalisation of reagents inside the apolar core of the colloids causes an enhanced

local concentration. As a consequence of this, reagents are closer to each other and thus generally react more easily. Furthermore, unique stereo-, regio- and chemo-selectivity can be reached[181] When reagent concentrations reach higher values, exceeding the maximum additive concentration (MAC), there are substantial deviations from the aforementioned micellar model. Multi-phase inhomogeneous systems are created, and this does not prevent surfactant-enhanced catalysis. These multiphase systems still contain micelles or other forms of bigger aggregates but suffer from a lack of reproducibility associated with the change of the experimental setup.[165]

6.1.3.3 The perks of having a co-solvent: miniemulsion

As previously said, surfactants are well-known for the stabilisation of biphasic systems. When mixed, two liquid immiscible portions form a thermodynamically unstable emulsion. Emulsions are defined as a mixture of an oil phase and a water one (**Figure 6.5a**). The disperse phase appears as spontaneously diffused droplets into the continuous one, and surfactants stabilise the colloidal droplets, lowering the interfacial tension (**Figure 6.5b**).

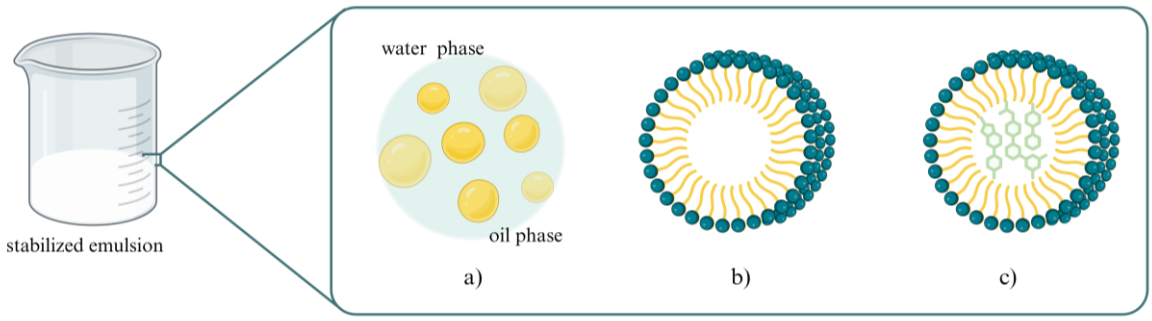

Figure 6. 5 *a) representation of a liquid-liquid biphasic system; b) confinement of the disperse phase inside the micellar core in a biphasic system; c) schematic representation of the theoretical confinement of the reagents inside the micellar core*

Stabilised emulsion can be exploited to carry out organic reactions, as micellar media are suitable for the addition of an organic water-immiscible cosolvent (**Figure 6.5c**). Depending on the surfactant concentration and the homogenization method, these droplets can range from microns to nanometres. (To be more precise, a surfactant thermodynamically stabilised emulsion with droplets around or under the micron is called *miniemulsion)*.[177] The organic solvent is usually added in the 1-10% v/v range when one or both reaction partners are water-

immiscible. The involvement of an organic solvent can improve the reaction performance: it helps in dissolving the solutes and bringing them into the micellar core. Usually, the organic solvent is located "inside" the micelle as it is compatible with the amphiphile tails. For this reason, micelles have in this case an expanded inner core and a bigger size, and they can accommodate higher volumes of both reagents and catalyst. A stable emulsion can secure, in certain cases, a more morphologically controlled reaction, preventing agglomeration. Of course, the choice of the co-solvent relies on the substrates involved into the reaction, as they must be dissolved in it.[173]

6.1.4 A glimpse into the field of catalysis

The origin of the term "catalysis" dates back to the nineteenth century and was introduced to indicate a chemical able to promote the occurrence of a reaction without being consumed during the process. It acts on the reaction mechanism, changing the reaction energy profile, thus speeding it up (**Figure 6.6**).

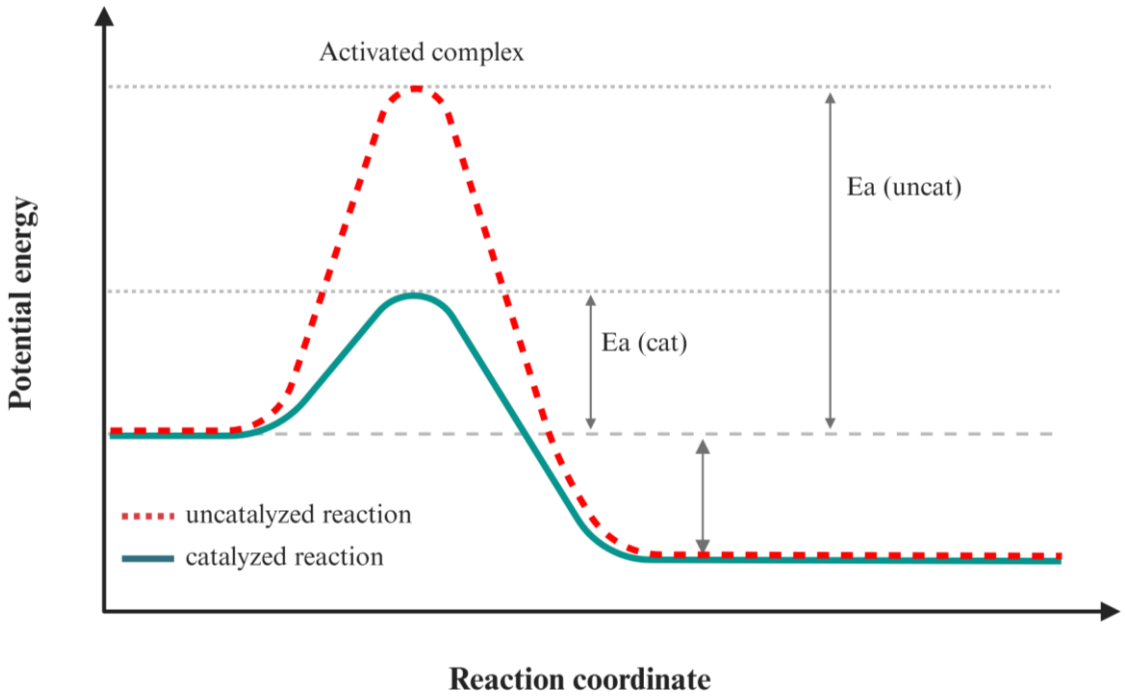

Figure 6. 6 *Energy profile of a catalysed and an uncatalyzed reaction*

Its specific role is the reduction of the activation energy – the energy barrier which must be overcome to see the formation of the product. The catalyst presence can also alter product

distribution, since it offers new reaction pathways compared with non-catalysed reactions. Altogether, the involvement of catalysts affects the kinetics of a process without touching its thermodynamic side. As a consequence of this, catalytic reactions occur under milder conditions and show an enhanced selectivity.[182] Some examples of well-known catalytic species are transition metal complexes or enzymes. Among them, nowadays metal complexes are by far the most used.

6.1.5 Homogeneous vs heterogeneous catalysis

Common catalysts can be divided into two main groups: homogeneous and heterogeneous ones. The main difference between them lies in whether they exist in the same phase as the reagents (homogeneous) or in a different one (heterogeneous). Both enable the synthesis of a large variety of pharmaceuticals, polymers, agrochemicals, fine chemical products, and other high-technology materials.[183]

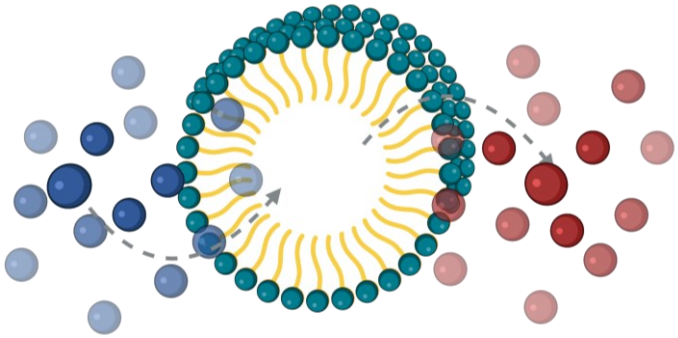

Figure 6. 7 *Schematic representation of a micellar-catalysed reaction*

High catalytic activity, low poisoning rate and high selectivity are associated with homogeneous catalysis as each catalytic entity acts as a single active site exposed to the reactants. Furthermore, the chemical mechanisms of homogeneously catalysed reactions are well known. Besides, tedious workup procedures, as well as the involvement of both toxic ligands and solvents, are driving scientists' attention towards heterogeneous catalysis.[184] Actually, homogeneous catalyst separation from the reaction mixture and its recovery still remains almost unachievable. As a consequence, reaction products usually suffer from catalyst contamination, resulting in lower purity level compounds. Reuse of the catalyst is

nowadays desired both for economic and environmental reasons, as the most used transition metals are rare, expensive, and toxic.

Apparently, heterogeneous catalysts can help in overcoming homogeneous ones' drawbacks: they have the advantage of easy recovery and reuse after completion of reactions.[185] Unfortunately, lower activity, selectivity, leaching of metal, as well as a not completely clear chemical mechanism, make traditional heterogeneous catalysts still an open challenge.

6.1.6 A quick glance at heterogeneous catalysis

The research in the field of heterogeneous catalysis is extremely wide, mainly because of its impact on industrial protocols. They are actually preferred in high-volume product synthetic processes.[186] Immobilisation of a molecular catalyst on a solid support would be one of the most straightforward methods to have a heterogeneous catalyst, keeping the advantages of both types of catalysts. Unfortunately, immobilised homogeneous catalysts are less effective than their molecular counterpart.[187] As chemical reactions mainly take place at the surface of the material, the most efficient choice is to stabilise nanosized particles (2-20 nm) of the active transition metal counterpart on a proper support. When reduced to the nanoscale, metal particles show unique physicochemical properties. The surface of the active sites affects the reaction through electronic and geometrical effects: surface metal atoms modify their local electronic structure according to the environment they face.[188]

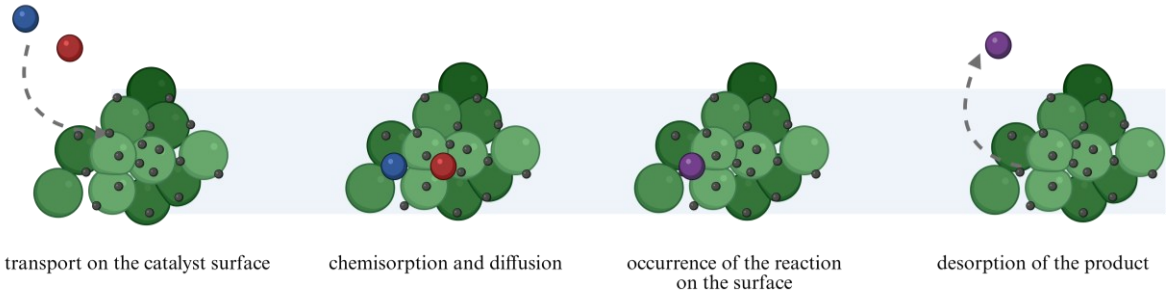

Figure 6. 8 *Schematic representation of the heterogeneous catalysis mechanism*

Geometrical effects are, on the other hand, linked to different surface geometries associated with the various ways in which a nanoparticle can interact with the support. It is clear that nanoparticle (NPs) size also has an impact on the process: the smaller the NPs, the higher the catalytic activity. This is linked to the fact that the number of surface atoms, which are

the ones that effectively play a key role in catalysis, increases as the particle size is reduced. Conversely, their direct application is, however, challenging because of their high tendency toward agglomeration when in reduced dimensions and due to Van der Waals forces.

Even if the catalytic mechanism is not completely clear, heterogeneous catalysis relies on four fundamental steps allowing the formation of the product (**Figure 6.8**): reagents transport on the catalyst surface (1), their chemisorption and diffusion (2) enabling the occurrence of the reaction (3) on the surface itself and subsequent diffusion and desorption of the product (4).[189] Given the process leading from the starting point to the very end of the reaction, is beyond doubt that the supporting material not only holds active sites throughout the process, but also defines catalyst performance.

6.1.7 The importance of having proper support

The answer to the aforementioned drawbacks of promising metal NPs is properly supporting them. During the last decades, scientists have put their efforts into finding suitable transition metal supporting materials for the promotion of green C – C bond forming reactions, as they are among the most common reactions requiring a catalysed protocol. High porosity, large surface area, small molecule comparable pore size and appropriate active sites are features the support should exhibit, and make inert microporous (i.e., having pore size < 2 nm) zeolites, silicas and activated carbon, appealing catalyst supports.[190]

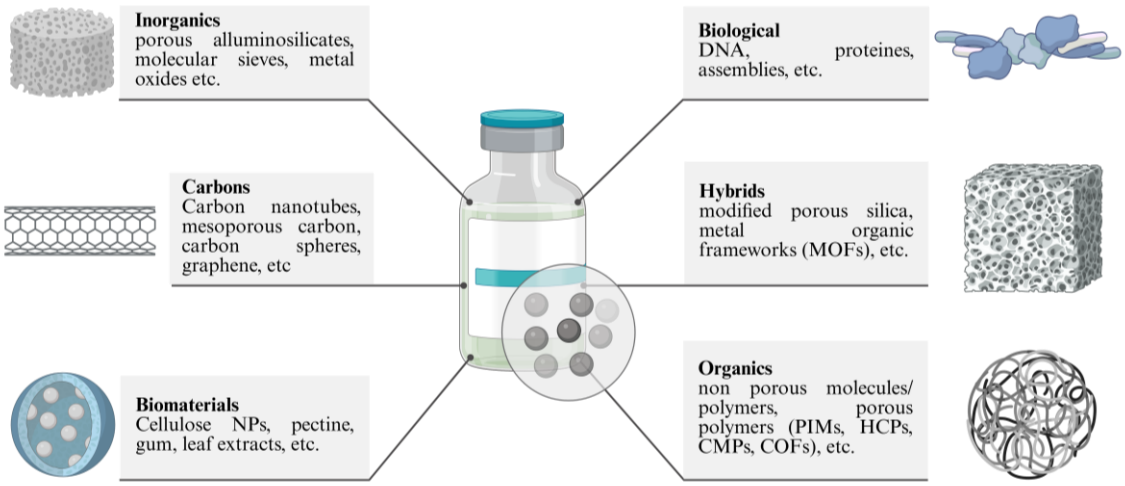

Figure 6. 9 *Classification of support materials for heterogeneous catalysts*

However, their inorganic chemical nature doesn't guarantee adequate reactant compatibility and limits their potential for chemoselective processes.[188] Nowadays, a wide and diversified playground of nanostructured transition metals supporting materials is available and it is summarised in (**Figure 6.9**).[191]

6.1.8 π-conjugated organic polymers supporting metal NPs

In this varied playground, scientists are also directing their attention towards conjugated aromatic polymers (CPs). They have recently emerged for numerous applications involving not only catalysis but also organic electronics, biomedical imaging and therapy and sensing technology.[192] Literature provides us with a plethora of examples about both linear and cross-linked polymeric materials.[193] Linear polymer chains are usually flexible, and their structure can be fine-tuned by choosing the right monomers to achieve the best immobilisation of metal nanoparticles. Different functional groups, as well as heteroatoms, the extended conjugated structure and double/triple bonds help in achieving controlled nucleation, stabilisation, and coordination of the metal guest. Van der Waals, electrostatic, hydrogen or covalent bonds are the intramolecular forces playing an active role in this process.[194] Because of the delocalized π system, conjugated polymers generally possess planar structures that also favour stacking interactions.[192] Furthermore, the unlimited number of polymeric platforms (ranging from natural to synthetic ones) and the ease of preparation via well-established protocols are additional pros linked to this family of organic supports. When crosslinkers are added, the nature of the support obviously changes, and so does its morphology and the interactions established with supported metal clusters. Among nonlinear polymeric supports, π-conjugated microporous polymers (CPMs) have emerged as an essential polymeric material platform. They are a class of crosslinked polymers combining permanent microporosity with a π-conjugated skeleton, forming a three-dimensional network. They show an enhanced chemical, mechanical and thermal stability if compared to other conventional materials such as metal-organic frameworks (MOFs) and covalent organic frameworks (COFs). As far as their design at the molecular level is concerned, they can rely on a broad diversity of building blocks (ranging from phenyl units to more complex arenes) to obtain a fine-tuned final porous architecture and an optimised conjugated skeleton, high specific area and tuneable pore size.[195] Their introduction to this field was pioneered

by Cooper et al.[196] Given their tuneable surface functionalities and structure, these porous organic materials can not only stabilise metal NPs through coordination and electrostatic interactions, but also use their porosity as a spatial confinement limiting the growth of NPs size.[191] Speaking about their synthesis, various organic reactions, such as Suzuki cross-coupling, are effective for their preparation. When the catalytic moiety is introduced into the framework, it becomes a heterogeneous catalyst.

6.1.9 Introduction of the active moiety on the support

Metal nanoparticles can be either deposited or *in situ* synthesised on a suitable support. In the second protocol, it is speculated that the support material also plays an active role in controlling NPs nucleation and growth, preventing their agglomeration, and enabling their homogeneous distributions. To achieve this goal, the most diffused technique is the reduction of oxidised metal precursors. Reduction can be achieved through different pathways, including thermal, sodium boron hydride ($NaBH_4$), or gas (H_2/CO) reduction.[197] The most universal approach is the one involving $NaBH_4$ and a metal ion precursor. The $NaBH_4$ solution is hydrophilic, while the polymer is hydrophobic.

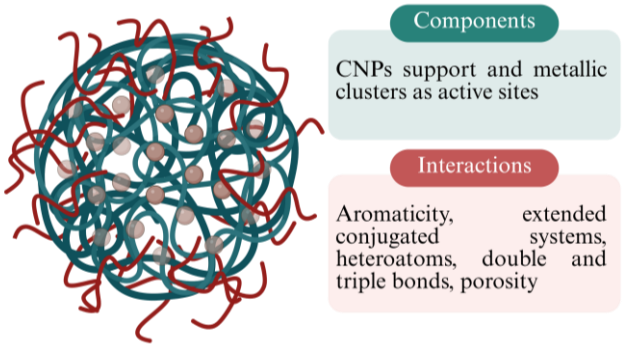

Figure 6. 10 *A CPNP embedding metal clusters and its peculiar features, making it a suitable support*

However, this procedure allows *in situ* metal ion reduction into the polymer coil, as uncoordinated metal ions tend to penetrate the water-dispersed support surface and then get reduced. The nucleation and growth are hence restrained by the porous structure, if present.[198] This reduction procedure allows a narrow nanoparticle size distribution; unfortunately, the majority of particles remain on the surface of the support rather than place

themselves more inside because of the different nature of the solid support and the reducing solution.

Because of the low solubility of conjugated polymers and their challenging processability, it can be unavoidably interesting to adapt them to nanoparticle shapes (**Figure 6.10**), hence making them easily water-dispersible.[199]

6.1.10 Synthetic routes for CPNPs: top-down approach

The state-of-the-art of conjugated polymer nanoparticles (CPNPs) production encompasses two different approaches: the top-down and the bottom-up strategy. The former is accomplished through miniemulsification or nanoprecipitation. **Figure 6.11** resumes the steps of the aforementioned methodologies.

The conjugated polymer is previously synthesised and then dissolved in a suitable water-immiscible solvent (disperse or oil phase), e.g., toluene. On the other hand, surfactants are dissolved in water (continuous phase). When the oil phase is drop-by-drop added to the water under vigorous magnetic stirring, a spontaneous emulsion (SE) is obtained. Otherwise, when the water phase is slowly added to the oil phase, an inverse phase emulsification (EPI) is performed. Refinement of particle dimensions can be obtained in various ways, i.e., by applying strong shear forces via ultrasonication to the two-phase system.

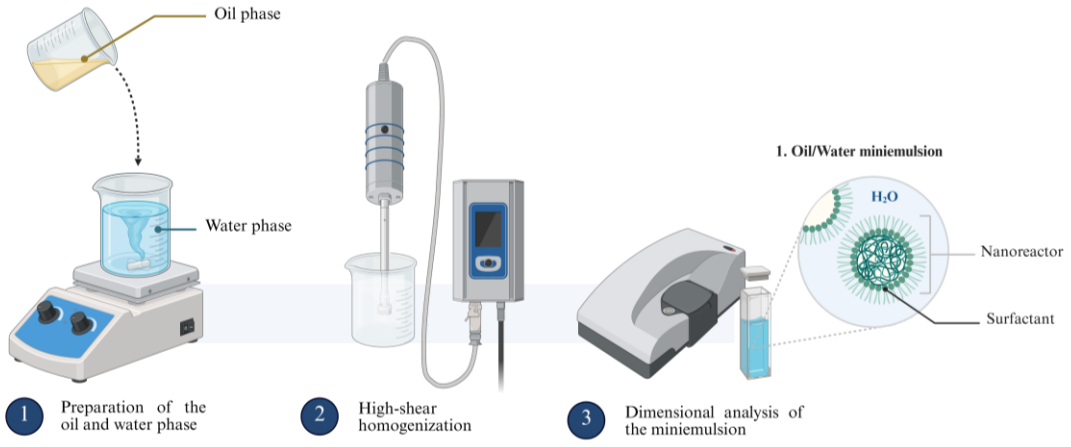

Figure 6. 11 *Top-down approach for the CPNPs formation*

These protocols lead to the formation of small droplets containing the CP. They are thermodynamically stabilised by the presence of surfactant molecules, which suppress

Ostwald ripening. The size of the nanoparticles can be adjusted by varying the polymer/surfactant ratio and typically ranges from 40 to 500 nm., The water-immiscible organic solvent is removed via an evaporation final step. On the other hand. The nanoprecipitation approach relies on the use of an organic water-miscible solvent in which the polymer is preliminary dissolved. The resulting solution is quickly injected under vigorous stirring or sonication into water. In one step, it acts as a non-solvent for the polymer, hence promoting the formation of a suspension of spherical nanoparticles (after solvent evaporation) having a diameter ranging from 20 to 500 nm.[200]

6.1.11 Synthetic routes for CPNPs: bottom-up approach

The scalability of miniemulsion can be improved by in situ synthesis of the polymer within sub-micrometric stabilised droplets in a one-pot process to directly obtain polymer nanoparticles. Furthermore, a one-pot alternative helps in saving NP formulation costs if compared to two-step methods.[201] This process is termed mini-emulsion polymerisation (**Figure 6.12**).

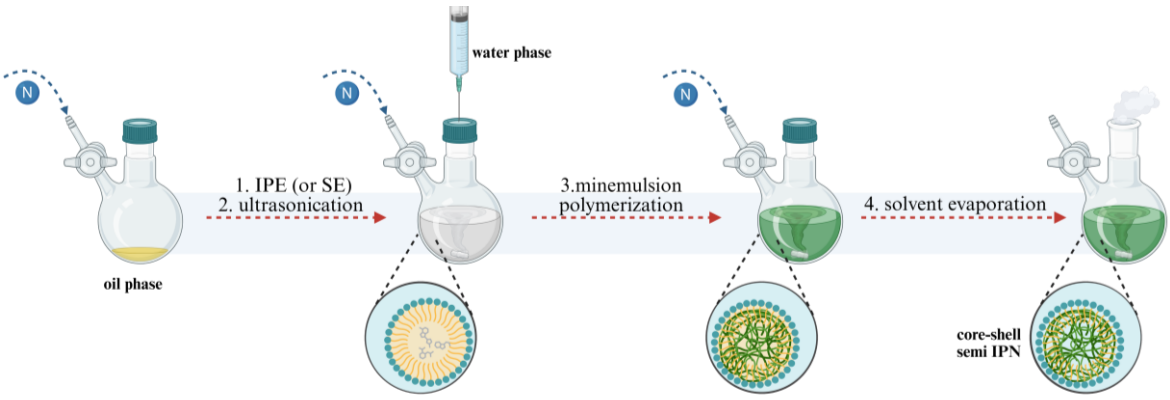

Figure 6. 12 *Bottom-up approach for CPNPs formation*

It has been optimised using different homogenization methods and carefully selecting both surfactants and hydrophobes to obtain nanoparticles of controlled size (~20–500 nm). A range of polymerisation techniques has been reported to operate in mini-emulsions, including palladium-catalysed cross-coupling reactions.[192] Miniemulsion droplets are highly stable, and they can be converted into nanoparticles upon polymerisation without showing a significant variation in size.[202]

6.1.12 Application of CMNPs in the heterogeneous catalysis field

Once synthesised (or formulated) and generally purified by surfactants, conjugated polymer colloids are ready to be applied. Notably, Pd nanoparticles and *in water* Suzuki-Miyaura cross-coupling reactions have been taken into consideration.

6.1.12.1 Suzuki-Miyaura cross-coupling reaction

Nobel Prize winner Akira Suzuki in 1979 developed one of the most crucial organic synthetic cross-coupling protocols for $C(sp^2)$ – $C(sp^2)$ bond formation. Such a reaction occurs between two aryl subunits: an aryl halide reacts with an organoboron compound (aryl boronic acid or its derivatives), expanding its carbon framework. The generally low toxicity and simplicity associated with the preparation of organoboron compounds, their relative stability to air and water, coupled with relatively mild reaction conditions and the formation of nontoxic by-products, make the Suzuki–Miyaura an important method for enlarging the carbon skeleton.[203]

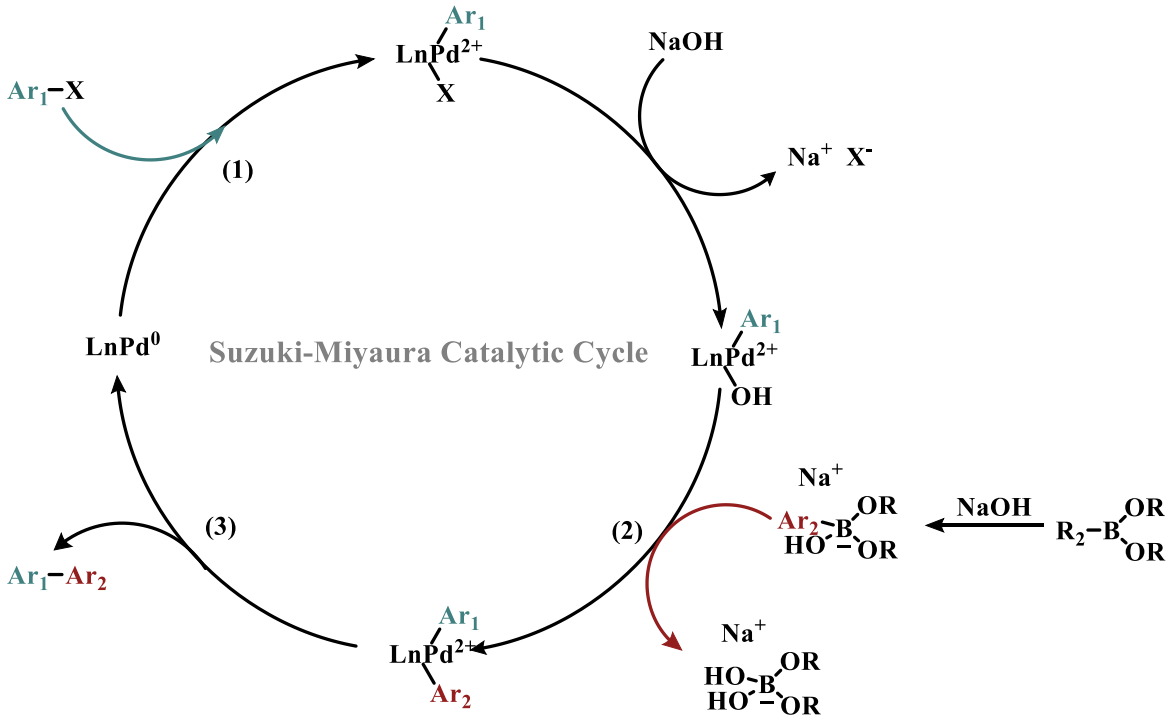

Figure 6. 13 *Schematic representation of the Suzuki-Miyaura catalytic cycle*

The catalytic cycle of this cross-coupling reaction (**Figure 6.13**) involves three main steps:

1. Oxidative addition of the aryl halide to the zero-valence Pd complex, to form a Pd(II) complex Ar_1-Pd^{2+}-X
2. Transmetalation step involving the Pd(II) complex and the arylboronic compound promoted by the base. At the end of this step, the complex Ar_1-Pd^{2+}-Ar_2 is created.
3. Reductive elimination of the new formed molecule Ar_1-Ar_2 and regeneration of the Pd(0) complex.

This reaction was originally performed in organic media, allowing for reagents and catalyst solubilization. The advent of green chemistry left its mark also on the Suzuki-Miyaura coupling. For instance, studies were focused on working at ultra-low catalyst loading,[204] avoiding the use of toxic phosphine ligands or the use of ligands at all, using neat water or aqueous solution as an environmentally friendly reaction medium and working under milder conditions (lower temperature).[205] Another important step forward was made by focusing attention on the use of Pd heterogeneous catalysts, instead of homogeneous ones. In this context, a major role is played by Pd NPs. Homogeneous Pd complexes can actually collapse with the release of atomic Pd that immediately aggregates into nanoparticles during the reaction. This process involves Pd complexes having weak bonds with the metal centre, such as triphenylphosphine. The stabilisation of the Pd NPs can hence be accomplished by compounds with the ability to be adsorbed on a conjugated organic polymer surface both during their synthesis or after their synthetic process, as said before. High activities are actually associated with catalysts supported on conductive polymers, as the expanded conjugated electronic system significantly affects the energy levels of Pd atoms in Pd NPs.[206] Two literature processes showing the application of such systems are now presented. Wang et al.[207] developed a synthetic procedure leading to high-surface solution dispersible CMP NPs by a miniemulsion Sonogashira cross-coupling reaction, obtaining a microporous support for additional Pd nanoparticles. After the synthesis, the surfactants were removed, and the obtained colloids were further capped with N-[2-(4-iodophenoxy)-ethyl]-N, N-dimethylamine and loaded with additional Pd NPs using $Pd(OAc)_2$ as a Pd source. The authors underlined the advantage of following a miniemulsion polymerisation for the control of the nanoparticle morphology and the beneficial influence of both ethynylene component and mesophorosity on the Pd NPs. Although intriguing, the main drawbacks of the process are the need for additional Pd and the removal of the ionic surfactant, followed by another

synthetic step, namely the capping one. As far as the Pd loading is concerned, there is evidence showing the possibility of using the Pd catalyst involved in the synthesis of polymeric networks itself as a source of Pd. Zhi et Al.[208] in fact, developed an in-situ one-pot synthesis of CMP-supported Pd having a well-defined porosity and monodisperse Pd clusters through a [2+2+2] homociclotrimerization.

6.2 Aim of the work

The present work has the objective of developing polyfluorene-based polymeric nanomaterials as efficient and reusable platforms for heterogeneous catalysis, achieved through the incorporation of palladium nanoparticles (Pd NPs) within the polymer matrix. Polyfluorene (PFO), a conjugated polymer known for its excellent photophysical properties, high stability, and ability to form well-defined nanostructures, was selected as a functional support capable of stabilising metal nanoparticles while maintaining accessible catalytic sites. The study aimed to establish a systematic approach for the synthesis, characterisation, and optimisation of Pd-loaded PFO hybrid nanomaterials (Pd@PFO). Specifically, it sought to (i) investigate the influence of synthetic parameters - such as solvent system, stabilizer concentration, and reducing conditions - on nanoparticle formation and dispersion within the polymeric network; (ii) examine the resulting morphology, surface characteristics, and distribution of palladium species; and (iii) evaluate their catalytic efficiency, stability, and reusability in representative model reactions.

Building upon these findings, the work further aimed to enhance the catalytic and structural properties of Pd@PFO by developing semi-interpenetrated polymer network (sIPN) architectures using dispersion and miniemulsion polymerisation techniques. These methodologies were designed to produce hybrid nanostructures with improved mechanical integrity, controlled porosity, and increased accessibility of the active Pd sites. The final goal was to create a versatile and tuneable polymer–metal composite platform that combines the advantages of conjugated polymers and metallic catalysis, providing a sustainable route toward advanced heterogeneous catalytic systems.

6.3 Results and discussion

6.3.1 Pd@Polifluorene (Pd@PFO), the starting point of the journey

The first step of the project has been a preliminary palladium placement onto a post-synthesis nanosphere-shaped π-conjugated organic polymer through *in situ* hydrogenation. This procedure allowed the obtainment of a novel catalytic powder along the line of Palladium on charcoal (Pd/C), one of the most widespread heterogeneous catalysts involved in C – C bond forming cross-coupling reactions.[209]

Poly(9,9-dioctylfluorene) (PFO) (**27a**) was selected as polymeric support: it is renowned as a blue light-emitting electroluminescent conductive polymer, whose monomer is formed by an aromatic fluorene core – $C_{13}H_6$ – bearing two aliphatic n-octyl tails on the central sp^3 carbon. The choice has been dictated by PFO extended π-conjugation all along the backbone, which can be beneficial for subsequent Pd NPs deposition, even if the polymer features no branching points, leading to a porous structure. The novel heterogeneous catalyst will be referred to as Pd@PFO. It has been considered as the proof-of-concept of this section of the project; for this reason, it seemed also reasonable to start with a polymer whose synthetic procedure was already well-established in the research group[163].

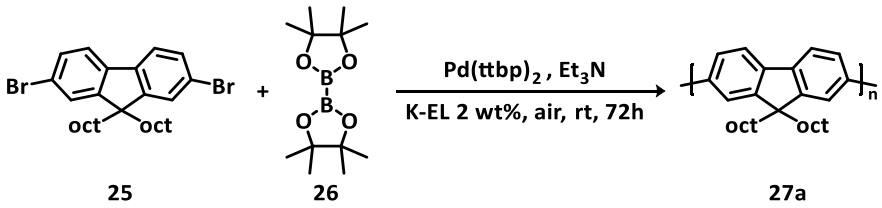

Scheme 6. 1 *Dispersion polymerisation protocol for the obtainment of (**27a**). The product is obtained through a Suzuki-Miyaura polycondensation without the involvement of an inert atmosphere or organic solvent/co-solvents.*

PFO has been obtained following a straightforward one-pot green procedure (**Scheme 6.1**) previously optimised within the research group. The protocol was based on a Suzuki-Miyaura cross-coupling reaction between 9,9-dioctyl-2,7-dibromofluorene (**25**) and bis(pinacolato)diboron (B_2pin_2) (**26**) employing bis (tri-tert-butyl phosphine) palladium (0) ($Pd(ttbp)_2$) as catalyst, and triethylamine (Et_3N) as organic base. The reaction was carried out under mild conditions at room temperature, without the need for an inert atmosphere, using a 2 wt% aqueous dispersion of Kolliphor EL (K-EL) as the reaction medium. The presence of this non-ionic surfactant promotes the formation of association colloids – here a

stable dispersion – upon mixing the reagents in water, thus creating a micro-heterogeneous aqueous environment.[210] This organization enables the accumulation of hydrophobic organic substrates within low-polarity domains, effectively increasing their local concentration and consequently enhancing the reaction rate.[211] As a result, the process can proceed under milder conditions in terms of both temperature and palladium loading. K-EL was selected not only for its ability to efficiently disperse hydrophobic reagents[212] but also for its proven stability in maintaining and protecting the hydrophobic microenvironment from oxygen, ensuring reaction robustness under ambient conditions.[213,214] To the best of our knowledge, no literature examples reporting such an experimental procedure have been published to date.

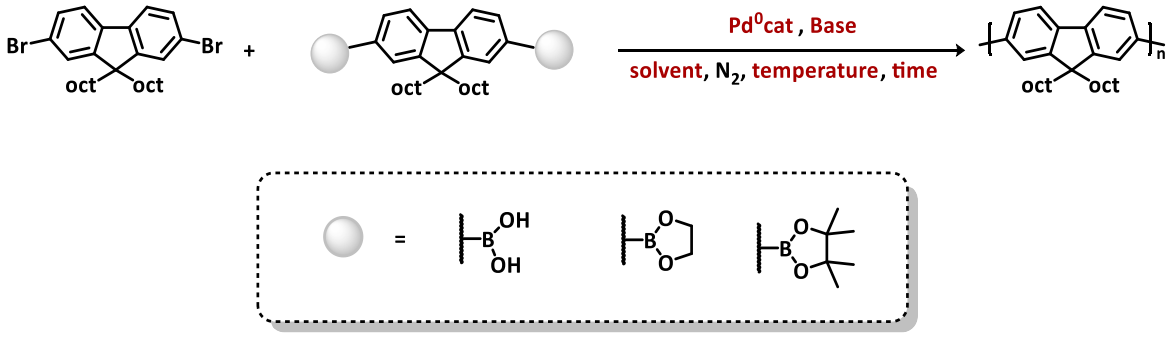

Entry	Catalyst/ligands	Base	Solvent	Temperature	Time	Yield
1[215]	$Pd(PPh_3)_4$	K_2CO_3	Toluene	80 °C	8	75%
2[216]	$Pd(PPh_3)_4$	K_2CO_3 + TBAB cat	Toluene	80 °C	48	66%
3[217]	$P(t\text{-}Bu)_3$ Pd G2	K_3PO_4	THF	60 °C	1	90%
4[218]	$Pd(PPh_3)_4$	TEAB	Toluene/H_2O	100 °C	6	92%

Table 6. 1 *Comparison of the most common reaction conditions for the homopolymerization of 9,9-dioctylfluorene via Suzuki polycondensation. All reaction involves organic solvents, work with homogeneous catalysts, an inert atmosphere, and high temperatures.*

PFO is mainly synthesised through Suzuki cross-coupling between the dibromide and diboronic acid (or diboronic esters) derivatives of 9,9-dioctyl fluorene, either under homogeneous conditions or by using biphasic organic solvent/water mixtures. However, in

2009, Reynolds et al. [219] demonstrated the beneficial role of fluoride-ion-activated B_2pin_2 in the homopolymerization of different fluorene derivatives. Although most reported one-pot borylation/Suzuki reactions concern small molecule coupling,[220,221] a similar approach has also been applied to the synthesis of a semiconductive polymer.[222] Nonetheless, to date, no procedure enabling the reaction to proceed entirely in the absence of an organic solvent has been reported. **Table 6.1** summarizes and compares the most common literature conditions for the homopolymerization of dioctyl fluorene via Suzuki polycondensation. Notably, all the conventional strategies must be carried out under an inert atmosphere and at elevated temperature, as the beneficial role of surfactants, present in the protocol shown in **Scheme 6.1**, is absent.

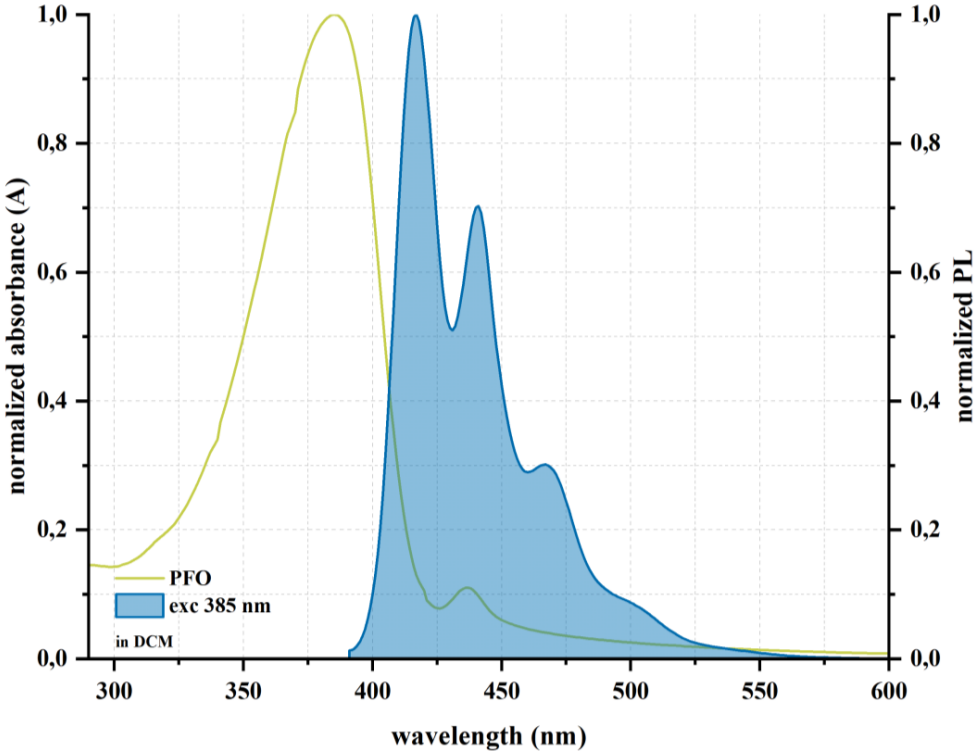

Graph 6. 1 *comparison between normalised ABS (yellow line) and PL (blue areas) spectra (using DCM as solvent) of compound* ***27a****. Excitation wavelength is set at 385 nm*

Despite the sustainability of the reaction, the protocol only reached a 70–75% conversion, and the resulting polymeric chains notably exhibited a broader molecular weight distribution compared to those obtained via standard protocols. These differences can be attributed to the microheterogeneous nature of surfactant-promoted reactions in water. During the synthesis described in **Scheme 6.1**, precipitation occurs from the original dispersion, forming a sticky lump around the stirring bar. In micellar-catalysed reactions, the success generally depends

on the ability of the reagents to reach the active catalytic site within the lipophilic pocket. If mass transfer between the aqueous suspension and the associated colloids is hindered—as is the case with the phase separation observed during the polymerisation-controlled chemical reaction cannot occur. Similar effects can be observed for poorly soluble products.[223] The crude product has thus been purified with Methanol (MeOH) precipitation and filtration, followed by a Soxhlet extraction with Ethanol (EtOH), petroleum ether (PE), and Acetone to both remove residual surfactants and short-length polymer chains. The recovered powder has then been characterised by ^{1}H NMR, optical spectroscopy (ABS and PL), and thermogravimetric analysis (*See Chapter 6.5.5*). The solution absorption spectra (**Graph 6.1**) exhibited a band at 373–395 nm assigned to the $S_0 \rightarrow S_1$ 0-0 transition of PFO, while the small low-energy shoulder at 435 nm is characteristic of β-phase PFO. The PL spectrum exhibited a characteristic vibronic progression with peaks located at 418, 441 and 467 nm due to $S_0 \rightarrow S_1$ 0-0 singlet exciton transition of solution PFO with 0-1, 0-2 and 0-3 vibronic replicas.[224] The support synthesis step has been followed by the introduction of the active moiety on the polymer. A standard literature hydrogenation procedure, originally allowing for *in-situ* reduction of a Pd^{2+} precursor ($PdCl_2$) on activated charcoal, has been followed and schematized in **Figure 6.14**

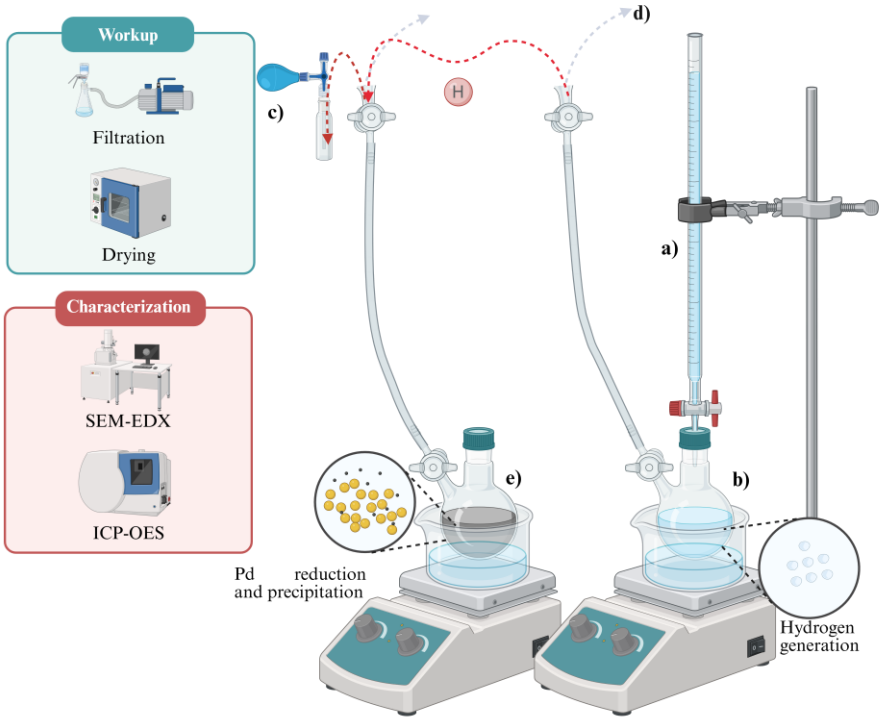

Figure 6. 14 *Visual representation of the laboratory hydrogenation setup used for the reduction of Pd^{2+} by in situ generated H_2 using $NaBH_4$/NaOH and AcOOH. The flask where H_2 is generated and the flask where the Pd is reduced are both connected to a Schlenk line, allowing the gas to fill the entire sealed system.*

Following a series of optimisation attempts, the procedure was refined to maximise Pd NPs deposition on the polymer substrate. The protocol employs water as the reaction medium; consequently, a crucial aspect was the development of an effective strategy to disperse the highly hydrophobic support in the aqueous environment. To facilitate this phenomenon, the formation of polymeric micro- and nanoparticles enhances the surface area exposed to the solution, thereby increasing the number of sites available for Pd deposition. A miniemulsification strategy proved ineffective in this case: the polymer's low solubility in most water-immiscible solvents limited its concentration inside the droplets (maximum value obtained was 0.71 mg/mL; see Experimental Section). As a result, the polymer was directly dispersed in the aqueous phase with the aid of an appropriate dispersant. The commercially available and inexpensive Jeffsperse® was selected, as its effectiveness had been demonstrated in previous studies by our research group.[225] After achieving a proper dispersion of the support, a Pd^{2+}-containing solution was added to the same flask and stirred for 30 minutes. Pd^{2+} was reduced through in-situ hydrogen generation. A 1 M $NaBH_4$/NaOH solution was added dropwise to a two-neck round-bottom flask containing acetic acid (AcOOH). When the alkaline solution encountered the acidic environment, H_2 gas was generated. The hydrogenation setup was designed to direct the produced H_2 toward the flask containing both the Pd and the polymer support. Here, H_2 immediately reacted with Pd^{2+}, reducing it to Pd^0. The reduced Pd then precipitated as nanoparticles on the surface of the dispersed polymer. The hydrogenation proceeded rapidly, as evidenced by the swift darkening of the dispersion from yellow to grey. Upon completion of the hydrogenation, the dispersion was filtered, and the resulting powder was washed with water to yield a green product. The same hydrogenation procedure was applied to activated charcoal to produce a non-commercial Pd/C reference material, which was subsequently used to evaluate the catalytic performance of Pd@PFO in cross-coupling reactions (see chapter **6.3.5**).

Inductively coupled plasma mass spectrometry (ICP-MS), optical spectroscopy (ABS, PL), as well as scanning electron microscopy-energy dispersive spectroscopy (SEM-EDS) were performed to check, respectively the eventual influence of NPs deposition on the absorption and emission spectra, the Pd content, and the morphology of the powder as well as the distribution of the metal centres on the support. ICP-MS analysis has been performed on two

different batches of Pd/PFO (batch 1 and batch 2), as the hydrogenation procedure has been conducted more than once to optimise the protocol. The results not only confirmed the effectiveness of the protocol but also revealed the beneficial influence of an optimal PFO dispersion. The mass percentage of Pd supported by the polymeric material is around goes from 1,9% (1st batch, poorly dispersed PFO) to 4,6% (2nd batch, properly dispersed PFO). The percentage does not differ much from the one obtained for Pd/C (1,82% ad 5%).

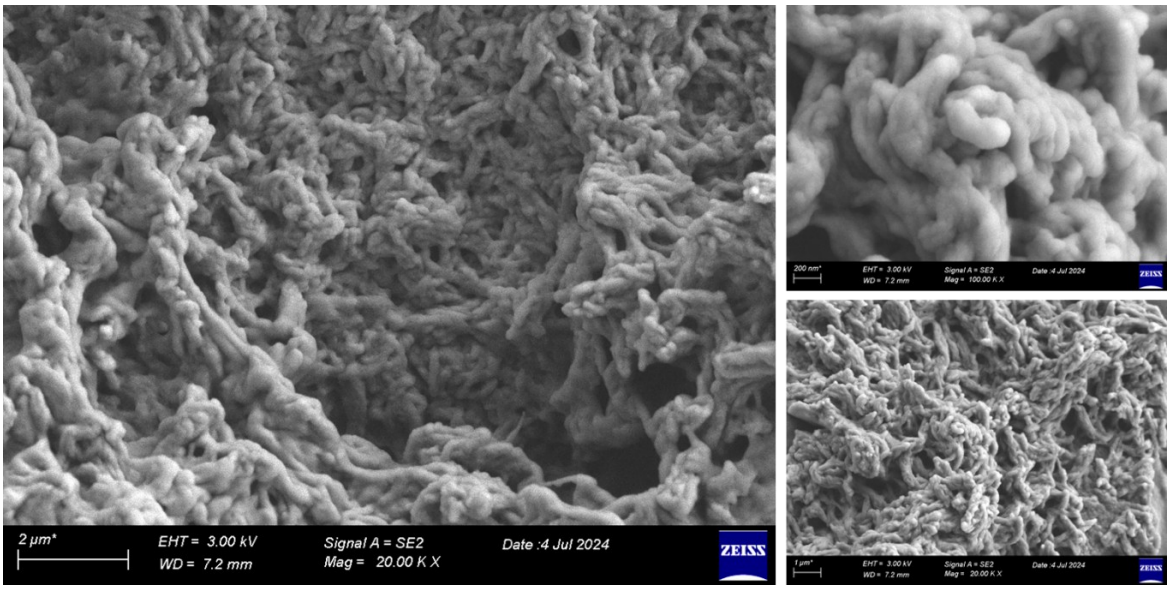

Figure 6. 15 *SEM image of PFO after Soxhlet purification at three different magnifications, showing a road-like morphology*

If optical and spectroscopical properties are not affected by Pd NPs deposition, the morphology of the material drastically changes after the post-synthesis deposition. **Figure 6.15** shows the PFO morphology after its synthesis and purification. The polymer forms irregularly shaped aggregates: the surface of the polymer particles appeared rough, showing limited porosity, which is consistent with the semi-crystalline and hydrophobic nature of PFO.

After palladium deposition, a remarkable morphological transformation was observed. The previously irregular aggregates evolved into well-defined spherical particles, suggesting that the reduction and metal nucleation processes most likely promoted a partial reorganization of the polymer surface. The spheres appeared smooth and homogeneous (**Figure 6.16 a**). No distinct Pd-related spots could be detected in the SEM micrographs, likely due to the small

size and uniform dispersion of the Pd nanoparticles, which are below the detection limit of conventional SEM imaging.

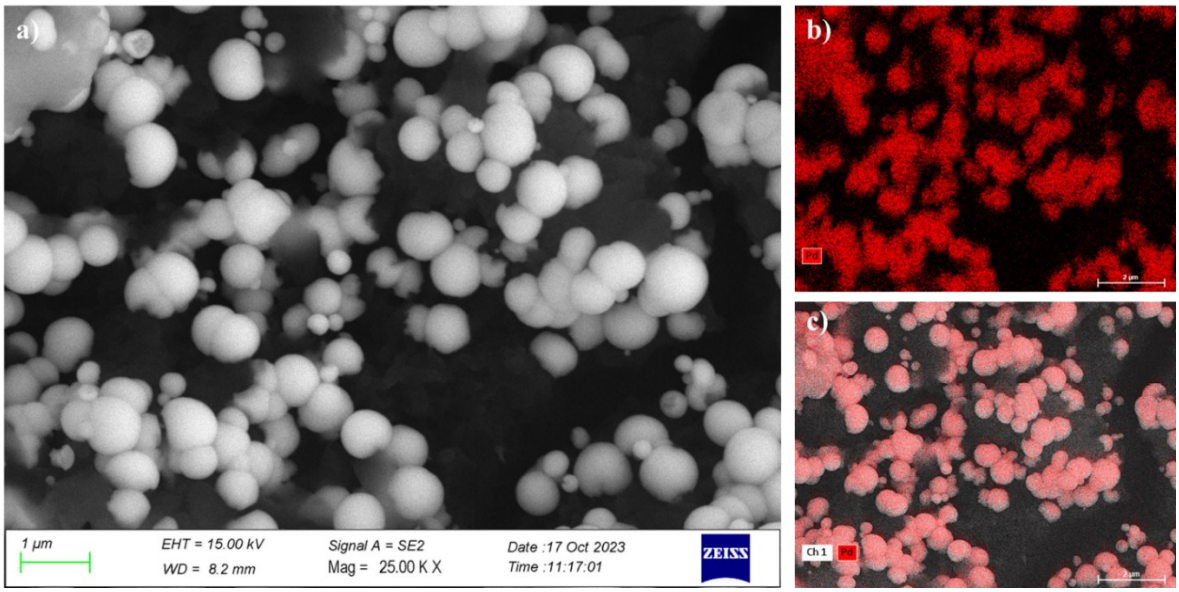

Figure 6. 16 *SEM image of Pd@PFO: a) spherical nanometric morphology of the powder; b)Pd distribution on the nano-shaped support obtained through EDS analysis; c) superimposition of SEM image and EDS elemental mapping.*

EDS elemental mapping, however, clearly confirmed the presence of palladium homogeneously distributed over the surface of the polymer spheres (**Figure 6.16 b,c)**. The EDS spectrum (Energy vs. cps/eV) of the Pd@PFO sample displays characteristic peaks corresponding to carbon from the polymeric matrix, as well as distinct signals associated with palladium (lines at approximately 2.84 and 3.02 keV) (**Figure 6.17**).

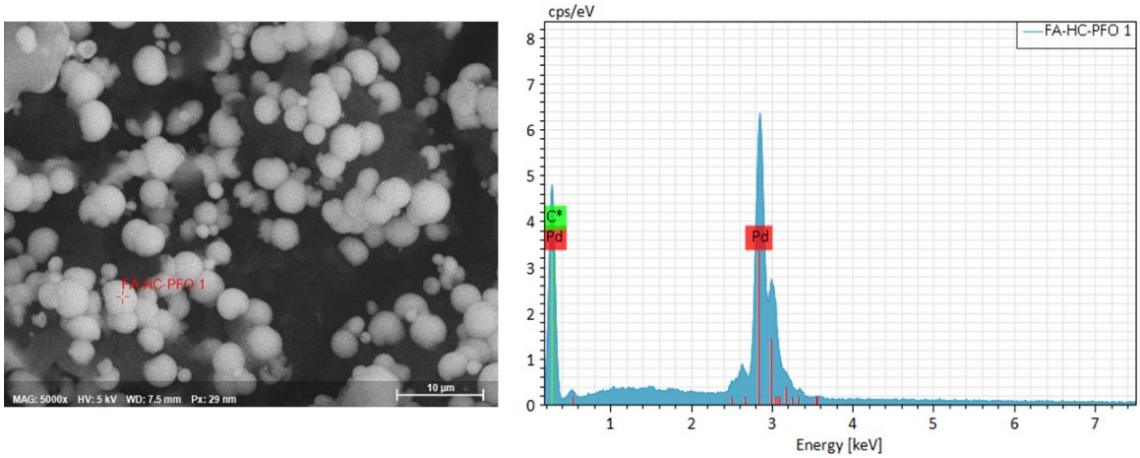

Figure 6. 17 *Punctual analysis of Pd@PFO showing the characteristic peaks associated with the presence of Pd*

The intensity and uniform distribution of Pd peaks across multiple acquisition points confirm the successful and homogeneous deposition of palladium on the polymer surface. No additional peaks related to impurities were detected, indicating the high purity of the synthesised material. All these findings indicate that the adopted procedure allowed for a uniform metal deposition, without significant aggregation or preferential localisation of the Pd NPs. It is also plausible that the use of Jeffsperse® as dispersant contributed to the formation of these well-defined spherical aggregates by reducing interfacial tension of the polymer surface during dispersion, which may have facilitated a more even metal nucleation across the surface.

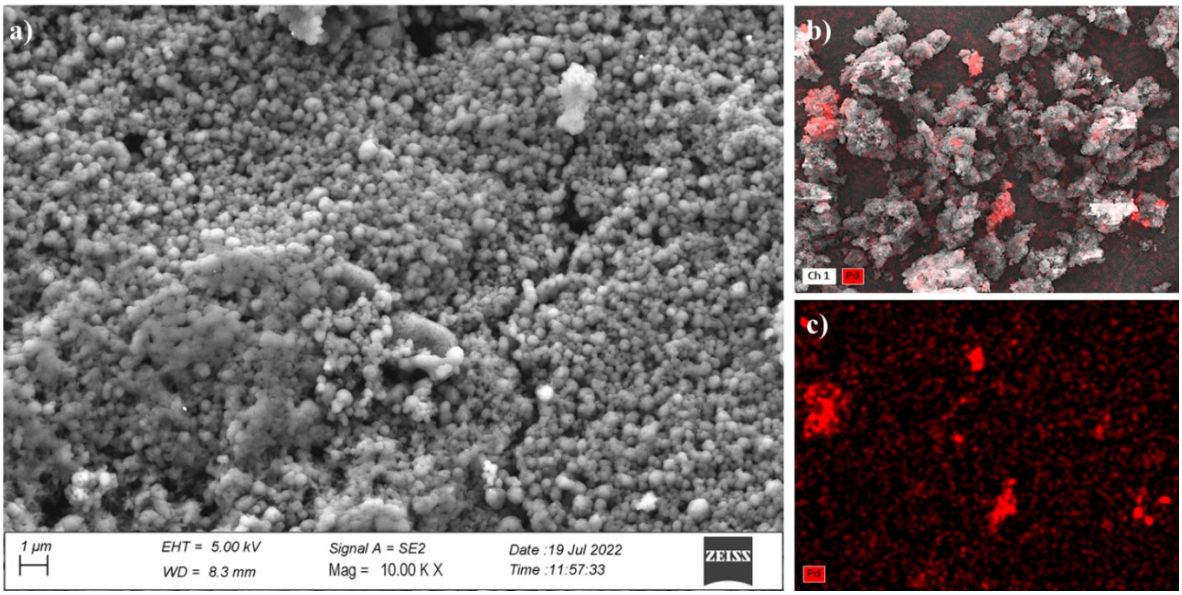

Figure 6. 18 *SEM image of Pd@PFO obtained from a poorly dispersed PFO during the hydrogenation procedure: a) more irregular morphology of the powder; b) superimposition of the SEM image and EDS elemental mapping; c)Pd distribution on the support obtained through EDS analysis*

In contrast, when PFO dispersion was not optimal, the morphology of the polymer particles appeared less spherical and more irregular (**Figure 6.18 a**). In this sample, SEM-EDS images showed the presence of larger Pd clusters unevenly distributed across the polymer surface. These observations confirm that an efficient dispersion of the hydrophobic PFO in water is crucial to ensure homogeneous metal deposition and to prevent the formation of aggregated palladium domains. These results confirm that Pd NPs can be effectively deposited onto PFO, yielding a well-dispersed metallic phase across the polymer surface. The study further highlights that the final particle morphology is sensitive to the polymer dispersion quality,

underscoring the importance of controlled processing conditions for achieving uniform Pd deposition.

6.3.2 From powder to dispersion: bottom-up approach for sIPN colloidal structures

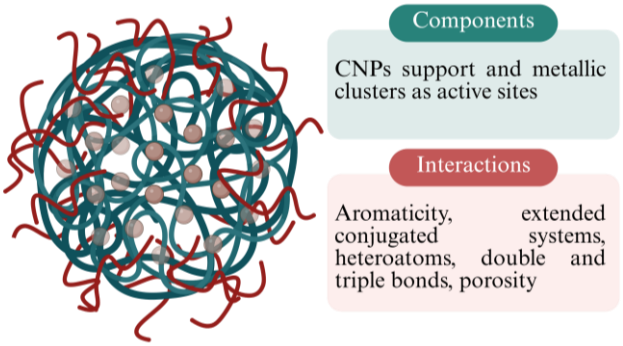

Figure 6. 19 *Cartoon of a sIPN. The green lines represent the polymeric core, while the red lines represent the entangled branched surfactants. The brown spheres represent the Pd NPS confined in the colloidal core-shell structure*

Although promising, Pd@PFO represents only the first step toward the synthesis of the final heterogenized catalyst. The PFO-based catalyst has been further improved by optimising a bottom-up, one-pot procedure for the formation of palladium-containing PFO nanoparticles (NPs) (**Figure 6.19**). This approach reduces the number of synthetic steps, as well as the consumption of organic solvents and energy. Two different strategies have been investigated: dispersion and miniemulsion polymerisation.

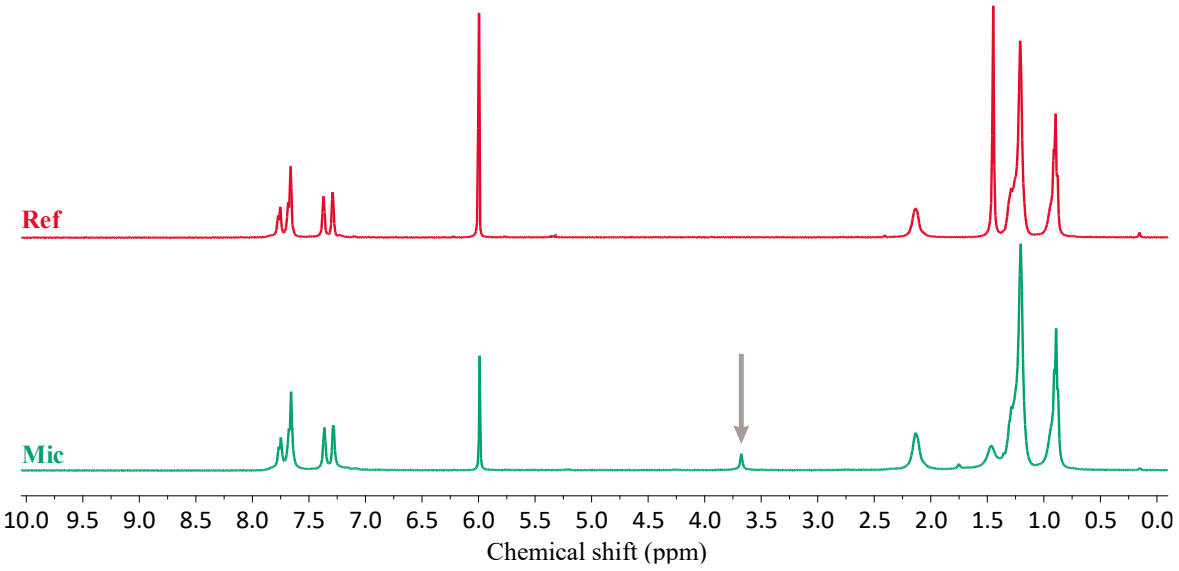

Figure 6. 20 *^{1}H NMR spectra of: Ref) F8T2 synthesised using an organic solvent; Mic) F8T2 synthesized using a micellar protocol after its purification. The surfactant peak is clearly distinguishable, highlighting its entanglement.*

In both approaches, the aim is to generate polymer NPs via a Suzuki or Suzuki-Miyaura cross-coupling reaction, exploiting the presence of surfactants and their tendency – particularly when branched – to become entangled within coiled polymeric networks during micellar synthesis, thereby forming a semi-interpenetrated network (sIPN) (**Figure 6.19**). This phenomenon has previously been demonstrated within the research group during the synthesis of semiconductive polymers, such as poly(9,9-dioctylfluorene-alt-bithiophene) F8T2, as evidenced by ^{1}H NMR spectra (**Figure 6.20**), where K-EL surfactant (employed for the synthesis) peaks remain clearly distinguishable even after extensive purification and washing steps.

The desired material thus comprises two components – a linear polymeric chain and a branched surfactant – mechanically entangled to form a core-shell structure (polymer core and surfactant shell) without requiring covalent linkages. Direct polymer growth in the micellar medium is expected to favour this arrangement. Additionally, when used as a catalyst, the core-shell architecture enhances the dispersibility of the nano-object, as far as compatibility with water-immiscible reactants. Surfactants, therefore, serve a dual function:

1. Promoting nanoparticle formation,
2. Maintaining consistent dispersibility of the PFO NPs.

Their presence in the final material eliminates the need for organic solvents and time-consuming purification steps. Importantly, unlike the previous approach (Pd@PFO), in this case, the synthesis of the polymeric NPs and the incorporation of Pd into the support occur

simultaneously: the Pd source not only catalyses the polymerisation but is also trapped within the surfactant-stabilised polymeric colloids in the form of a Pd^0 cluster, acting as the active phase of the heterogenized catalyst.

6.3.3 Dispersion polymerisation

Initially, the dispersion protocol was selected as a bottom-up strategy to maintain consistency with the formulative approach that had proven effective in the top-down process. Dispersion polymerisation represents a green synthetic route, as it eliminates the need for organic solvents and relies on amphiphilic molecules to generate a confined nano-environment suitable for polymer growth. **Scheme 6.2** provides a schematic representation of the coupling partners, also highlighting the inclusion of 5 mol% of the cross-linking unit 2,2′,7,7′-tetrabromo-9,9′-spirobifluorene. At the outset, T-80 (*See Experimental Section 6.5.3*) was selected as the surfactant due to its distinctive molecular architecture. This non-toxic, inexpensive, and commercially available branched molecule was expected to favour physical entanglement within the polymer matrix during its growth, thereby promoting the formation of a sIPN network structure.

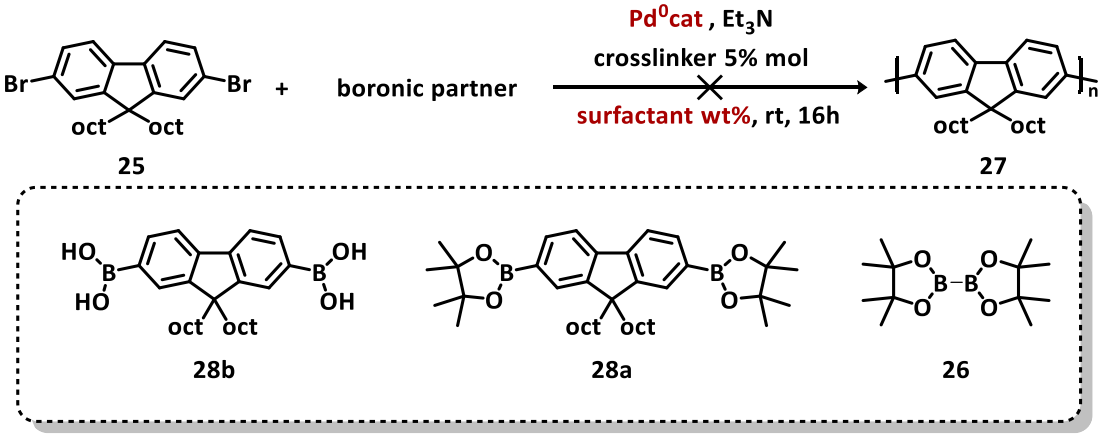

Scheme 6. 2 *Dispersion polymerisation protocol for PFO nanodispersion (ND) synthesis*

The reaction was performed at low surfactant and reactant concentrations in water (scale: 40 mL) to stay under the aforementioned MAC value and thus consider the classical micellar model with hydrophobic species located inside the micellar core (0,2 wt% T-80 and 2,4 mg/mL of reagents or 2,8 mM with respect to limiting bromide). These quantities have been

optimised to have around $7 \cdot 10^{17}$ micelles, considering T-80 aggregation number ($a.n._{T\text{-}80}$ = 59) (*note: the aggregation number is the average number of surfactant molecules creating a micelle*). Each micelle thus ideally contains 100 molecules of (**27**) (see *experimental part, for further details about calculation and precise quantities*). The dispersion appeared opalescent, and the morphology of the aggregates was monitored through dynamic light scattering (DLS). The analysis revealed the presence of aggregates having a ~40 nm diameter (PdI: 0,2, *see experimental part for further information about data fitting*). Triethylamine (Et_3N) is a renowned organic base for micellar Suzuki-Miyaura reactions. It was selected as its addition does not significantly affect the morphology of the colloids (~50 nm, PdI: 0,3). A Pd^0 catalyst, bis(tri-tert-butylphosphine)palladium(0) ($Pd(ttbp)_2$) has been initially selected to directly have the Pd in its reduced active form.

entry	Boronic partner	Catalyst	Surfactants	mM (25)	27[f]
1	26	$Pd(ttbp)_2$	T-80 0,2 wt%	2,8	n.d.
2	26	$Pd(ttbp)_2$	T-80 0,5 wt%	2,8	n.d
3[c]	26	$Pd(ttbp)_2$	T-80 0,5 wt%	2,8	n.d
4[b,c,d]	28b	$Pd(ttbp)_2$	T-80 0,5 wt%	2,5	n.d.
5[a,e]	228a	$Pd(PPh_3)_4$	K-EL 2 wt%	170	present

Table 6. 2 *Reaction conditions for dispersion polymerisation approach a) no 2,2′,7,7′-tetrabromo-9,9′-spirobifluorene; b)addition of 1,2 propanediol as inhibitor of reactants detrimental crystallisation out of micelles core; c) inert atmosphere; d)reaction prolongation to 48 h and e) 72 h; f)evidence from 1H NMR and ABS spectrum.*

Table 6.2 summarises the experiments carried out following this strategy, none of which led to complete polymerisation of the starting materials, despite variations in several reaction parameters (boronic partner, catalyst, and surfactant concentration).

After these attempts, it became evident that the issue was neither related to the borylation step nor to an insufficient dispersion quality, but rather to the limited "interaction" between the coupling partners caused by the low reagent concentration (bromide concentration = 2.8 mM). This hypothesis was supported by the partial polymerisation observed only when both the reagent concentration and the surfactant amount were significantly increased (**Table 6.2**, entry **5**).

^{1}H NMR analysis revealed the presence of unreacted monomers together with broad signals in the characteristic PFO region (7.85-7.67 ppm). These peaks are indicative of the formation

of both oligomeric and polymeric species, as the slower relaxation of larger macromolecules broadens the corresponding resonances. This observation confirms the positive effect of increasing reagent molarity on polymer growth. ABS and PL spectra (**Graph 6.2**) also supported partial conversion of the monomers. The characteristic PFO absorption maximum appeared blue-shifted (λ_{max} = 371 nm) compared to that of PFO synthesised via dispersion polymerisation (λ_{max} = 385 nm), suggesting the formation of shorter and more polydisperse PFO chains. As the degree of conjugation, and thus polymer chain length, increases, the HOMO-LUMO band gap decreases, leading to a red shift in the absorption profile. Consistently, the PL spectra displayed identical emission features, while the absence of monomer-related fluorescence can be ascribed to energy transfer processes, where excited electrons migrate through reabsorption toward the lower-energy LUMOs associated with the longest polymer chains.

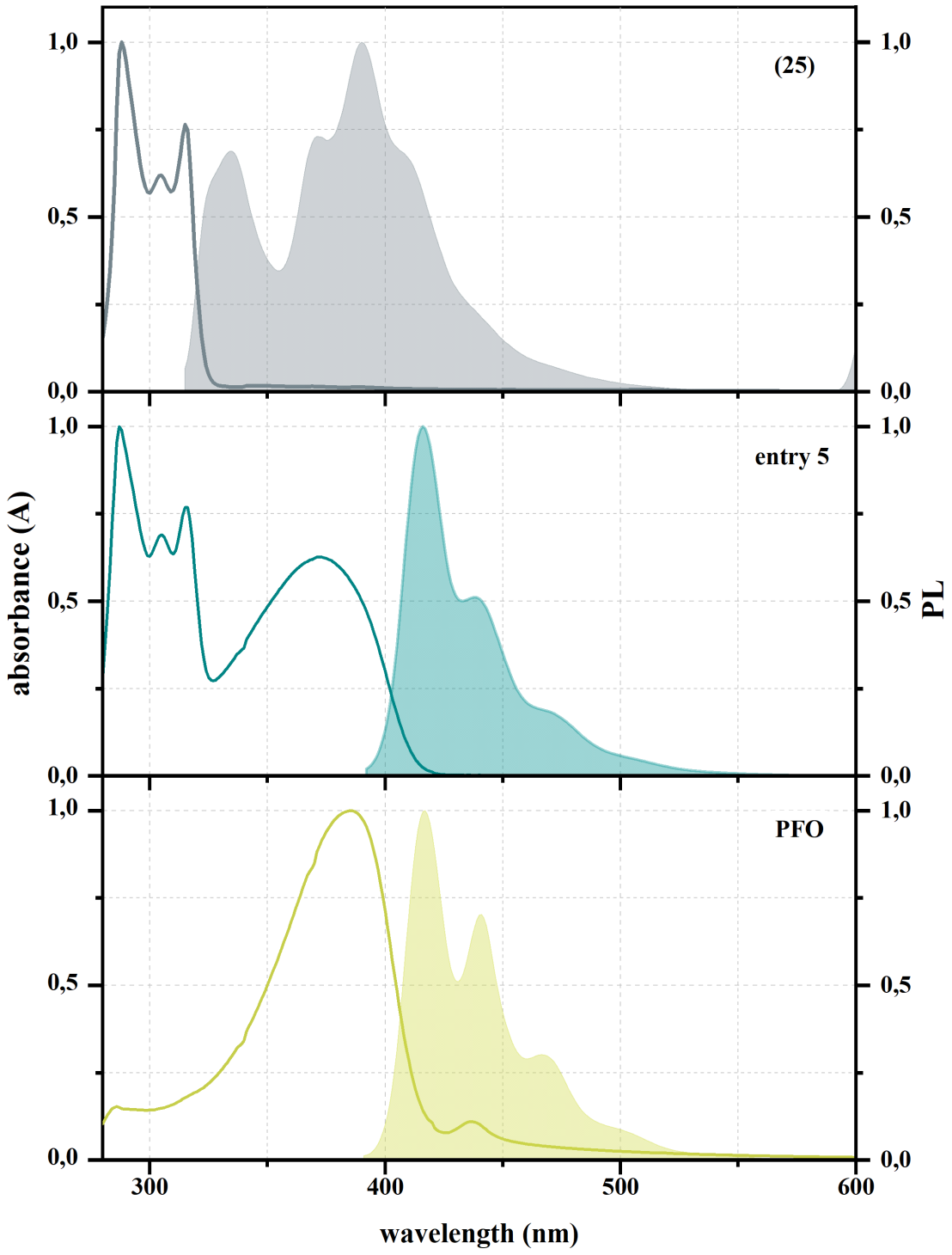

Graph 6. 2 *Comparison between normalised ABS (curves) and PL (filled area curves) spectra (using toluene as solvent) of 9,9-Dioctyl-2,7-dibromofluorene (grey), PFO (yellow) and entry 5 (cyan), showing both reagent peaks between 276 and 327nm and a blue-shifted PFO peak (371 nm), excitation wavelength = 385 nm.*

Despite these improvements on the synthetic side, the formulation of the reaction mixture was negatively affected by the increased concentrations. The resulting dispersion was

inhomogeneous, the morphology of the colloidal aggregates could not be controlled (DLS measurements could not be performed), and both reagents and polymer partially precipitated, forming a paste-like material.

6.3.4 Miniemulsion polymerisation

Although environmentally friendly, the first approach exhibited both formulation and reactivity limitations. To address these issues, attention was directed toward exploiting the presence of a cosolvent system (toluene/water 1:20), thus operating within the miniemulsion polymerisation regime. This strategy aimed to enhance the probability of coupling-partner encounters and to improve control over the reaction formulation.

6.3.4.1 Literature background

The literature approach, as fine-tuned by Turner *et al.*[193] (**Scheme 6.3**), involves the bottom-up synthesis of PFO nanoparticles starting from 9,9-dioctyl-2,7-dibromofluorene (**25**) and 9,9-dioctyl-9H-fluorene-2,7-diboronic acid bis(pinacol) ester (**28a**), using tetrakis(triphenylphosphine)palladium ($Pd(PPh_3)_4$) as the Pd^0 source, sodium hydroxide (NaOH) as the inorganic base, and an inert nitrogen atmosphere to prevent Pd^0 oxidation. The miniemulsion is prepared using toluene as the dispersed phase and sodium dodecyl sulphate (SDS, 0.25 wt%), a linear ionic surfactant, as the stabiliser.

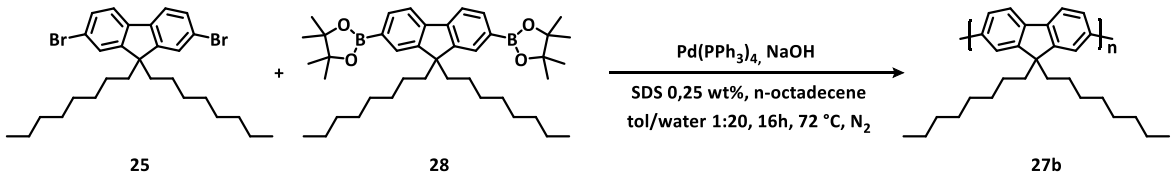

Scheme 6. 3 *Turner et al.*[193] *reaction conditions for PFO NPs miniemulsion synthesis.*

These literature conditions were first reproduced to characterise the features of the nanoparticles obtained through the miniemulsion strategy. DLS analysis revealed dispersed aggregates with an average diameter of approximately 160 nm (PDI = 0.13). ^{1}H NMR and ABS spectra (**Graph 3.2**) confirmed the formation of short PFO chains together with

residual monomers. Although partially effective, this nanoparticle synthetic route was also not suitable for the intended application. The use of a linear ionic surfactant such as SDS hinders the formation of the desired semi-interpenetrated network (sIPN) structure. Nevertheless, these conditions served as the foundation for the development of a more appropriate protocol for the synthesis of the targeted colloidal catalytic systems.

6.3.4.2 Formulative Optimization

Since maintaining a stable formulation throughout the entire process plays a pivotal role in obtaining suitable PFO ND, the first step consisted of optimising the morphology of the miniemulsion itself. To this aim, different solvents, surfactants, and miniemulsification methods were investigated to identify the conditions leading to a stable system.

Initially, the emulsion conditions were finely tuned in the absence of both catalyst and monomers to define the most suitable reaction medium. Toluene was selected as the organic, water-immiscible solvent due to its compatibility with both PFO and typical aryl monomers. Four inexpensive commercial surfactants – Tween 80 (T-80), K-EL, Triton X-100 (TX-100), and Span 80 (S-80) – were combined and tested as stabilisers for the organic phase droplets.

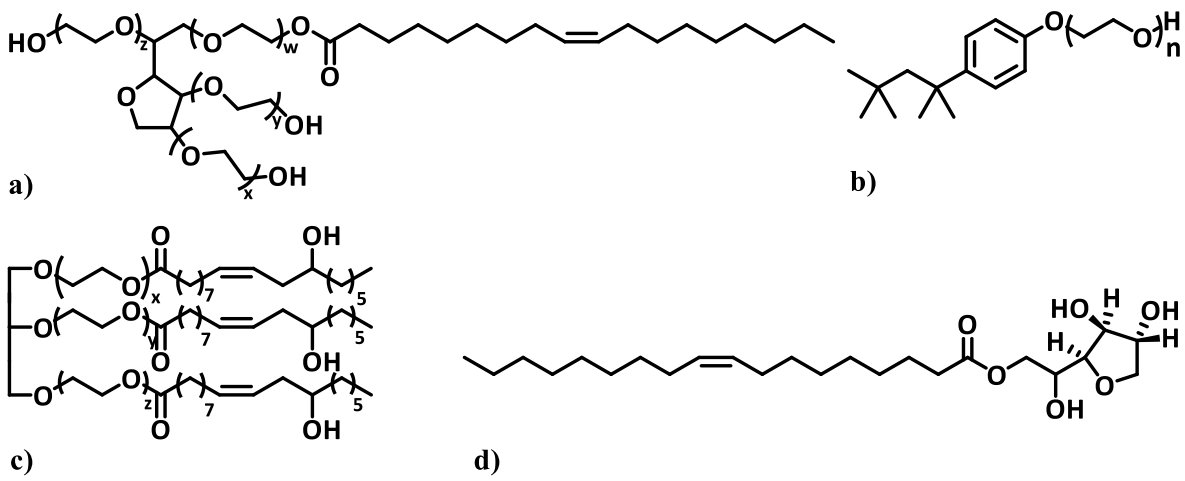

Figure 6. 21 *molecular structure of surfactants used for the obtainment of miniemulsion*

T-80 (**Figure 6.21a**) was chosen for its branched molecular structure, which favours physical entanglement within the polymer network. K-EL (**Figure 6.21c**) was selected not only for its branched architecture but also for its ability to shield the reaction medium from oxygen.[214]

Although linear, TX-100 (**Figure 6.21b**) was included because its aromatic lipophilic fragment is structurally compatible with both the reagents and the PFO backbone. Finally, S-80 (**Figure 6.21d**) was employed in some tests to reduce the overall hydrophilic-lipophilic balance (HLB) of the surfactant mixture, replacing TX-100. **Table 6.3** summarizes all the experiments carried out to optimize the reaction environment for subsequent polymerization reactions.

entry	surfactants	wt %	method	d (nm)	PdI
1	T-80	0,5%	SE[a]	-	-
2	T-80	1%	SE[a]	-	-
3	T-80	1%	EPI	222,0	0,2
4	T-80,K-EL 1:1	1%	SE[a]	-	-
5	T-80,K-EL,T X-100 1:1:1	2%	SE	105,5	0,5
6	T-80,K-EL,T X-100 1:1:1	2%	SE[a]	88,5	0,5
7	T-80,K-EL,T X-100 1:1:1	2%	EPI	68,4	0,5
8	T-80,K-EL,T X-100 1:1:1	2%	SE[b]	99,4	0,3
9	T-80,K-EL,T X-100 1:1:1	2%	SE[c]	182,9	0,6
10	T-80,K-EL,T X-100 1:1:1	1%	SE[b]	204,2	0,3
11	T-80,K-EL,T X-100 1:1:1	3%	SE[b]	159,4	0,4
12	T-80,K-EL,T X-100 1:1:1	1%	EPI	165,1	0,2
13	T-80,K-EL,S-80 1:1:1	1%	EPI	194,5	0,2

Table 6. 3 *DLS droplets dimensions and dispersity data referred to miniemulsions obtained with different surfactant mixtures dissolved in the oil phase. All ratios are indicated as w/w. The symbol "-" is used when de-mixing occurs; a) no drop-by-drop addition; b) refinement of droplet dimensions via 1,5 minutes ultrasonication; c) refinement of droplet dimensions via 3 minutes homogenization using a turbo-emulsifier.*

Both SE (**Table 6.3**, entries **1**, **2**, **4**, **5**, **6**, **8**, **9**, **10**, **11**) and EPI (**Table 6.3**, entries **3**, **7**, **12**, **13**) approaches were employed. The best results were achieved when the oil phase (in SE) or the aqueous phase (in EPI) was added dropwise to the complementary phase. In both methodologies, the surfactants were dissolved in the oil phase prior to emulsification. In some experiments, the nanoparticle size distribution was further refined by applying high shear forces through ultrasonication or high-shear homogenization. All the prepared miniemulsions appeared milky in appearance (Figure **6.x**). The droplet diameters were determined by dynamic light scattering (DLS) using the cumulant fitting method (*see*

experimental section for further details). The most satisfactory results were obtained with surfactant concentrations of 1 or 2 wt% relative to the aqueous phase. In particular, formulations **7**, **11**, **12**, and **13** exhibited the best performance in terms of emulsion stability, droplet size, and polydispersity index (PDI). Consequently, these optimised miniemulsion conditions were selected for subsequent polymerisation experiments. In all these cases, the amount of base required for the reaction did not significantly alter the formulation or compromise the emulsion stability.

6.3.4.3 Optimisation and control of reaction parameters leading to the formation of CPNPs

The optimisation process aimed at obtaining a stable miniemulsion capable of producing water-dispersible PFO nanoparticles required several steps and iterative adjustments. However, presenting all experimental attempts in detail would detract from the linear understanding of this section. Therefore, only the most relevant experiments – those that effectively contributed to the development of the final material – are presented below, while unsuccessful trials, although informative, have been omitted to ensure clarity and readability. It should be noted that not all the experiments reported here were fully successful; nevertheless, they are included as they help to illustrate the logical process that ultimately led to the identification of the optimal parameters.

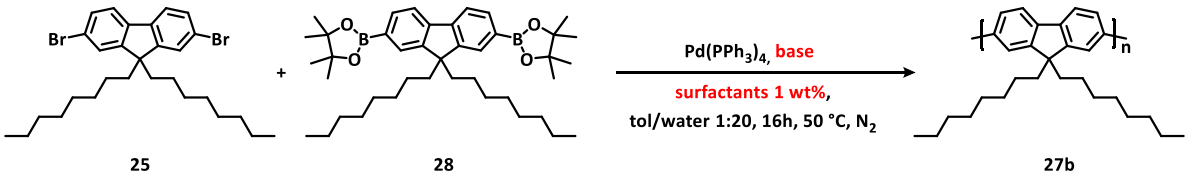

Scheme 6. 4 *Synthetic protocol for the obtainment of Pd@PFO ND; the synthesis only shows the chemical structure of the support of the catalyst; however, the final material must be intended as a core-shell structure whose core is formed by PFO and shell by surfactants, forming a semi-IPN. Pd NPs are trapped inside these nanostructured spheres.*

After the preliminary optimisation steps, both the reagents and the catalyst were added to the organic phase. **Scheme 6.4** summarises the general reaction protocol employed for the bottom-up synthesis of Pd@PFO NDs (Figure 6.23). Once again, compound (**25**) was used as the bromide partner, while (**6**) was selected as the boronic ester. $Pd(PPh_3)_4$ served as the Pd^0 source, and both NaOH and Et_3N were investigated as bases. The following library of

reactions was performed under a strictly inert atmosphere to avoid catalyst oxidation. The use of a cosolvent enabled the employment of higher reaction temperatures compared to the dispersion polymerisation approach. Miniemulsifications were consistently carried out at 50 °C, and both SE and EPI methods yielded stable emulsions when the reagents were introduced into the oil phase. DLS measurements were systematically performed before and after base addition to verify the stability of the reaction medium.

Entry	Base	Surfactants	Phase-transfer agent	27b
1	NaOH[a]	T80, K-EL, T X-100 1:1:1, 1 wt%	-	-
2	Et_3N[b]	T80, K-EL, T X-100 1:1:1, 1 wt%	Aliquat HTA-1[c]	-
3	NaOH[a]	T80, K-EL, T X-100 1:1:1, 1 wt%	Aliquat HTA-1[c]	present[f]
4[e]	NaOH[a]	T80, K-EL, T X-100 1:1:1, 1 wt%	Aliquat-HTA-1[c]	present[f]
5[d,e]	NaOH[a]	T80, K-EL, T X-100 1:1:1, 1 wt%	Aliquat-HTA-1[c]	present[f]

Table 6. 4 *Different bases and formulation conditions used for the optimization of the synthesis of Pd@PFO ND; a) NaOH is degassed and dissolved in 1mL of degassed water, then added as a 1M solution to the reaction vessel; b) Et3N is degassed through freeze pump thaw and added without the addition of any solvent to the reaction vessel; c) when present, Aliquat HTA-1 is added to the reaction vessel right before the addition of the water phase; d) 5,4 mol% of catalyst; e)sonicated before base addition; f) evidence from ^{1}H NMR and ABS spectrum.*

The first attempt consisted of adapting the literature procedure developed by Turner *et al.*[193] to the optimised miniemulsion system, employing a 1 wt% 1:1:1 mixture of three different surfactants (**Table 6.4**, entry **1**). Despite the several similarities with the reported method, no polymerisation occurred. The situation drastically changed upon the addition of Aliquat HTA-1 to the reaction mixture (**Table 6.4**, entry **3**). This compound is a water-soluble quaternary ammonium salt specifically designed for phase-transfer-catalysed reactions, enabling interactions between species located in immiscible phases by transferring active water-soluble ions into the organic portion of the system. In this way, the reactants can effectively interact, allowing the coupling reaction to proceed. The simultaneous presence of both an inorganic base (NaOH) and the phase transfer agent proved to be crucial for the

polymerisation to take place. As expected, the Aliquat HTA-1 promoted the transfer of hydroxide ions (OH^-) from the aqueous phase into the stabilised organic droplets, thereby facilitating the transmetalation step of the catalytic cycle and enabling polymer chain growth.

Figure 6. 22 *Table 6.4 entry 3 a) before base addition and b) 24h after base addition; Table 6.4 entry 4 after 24h a) before and b) after toluene evaporation*

To further confirm the synergistic effect of NaOH and Aliquat HTA-1, a control experiment was performed using Et_3N as the base (**Table 6.4**, entry **2**), but no polymer formation was detected. Polymer formation was initially evidenced by the colour change of the miniemulsion from white to yellow (**Figure 6.22**) and subsequently confirmed by ^1H NMR and UV–Vis absorption analyses.

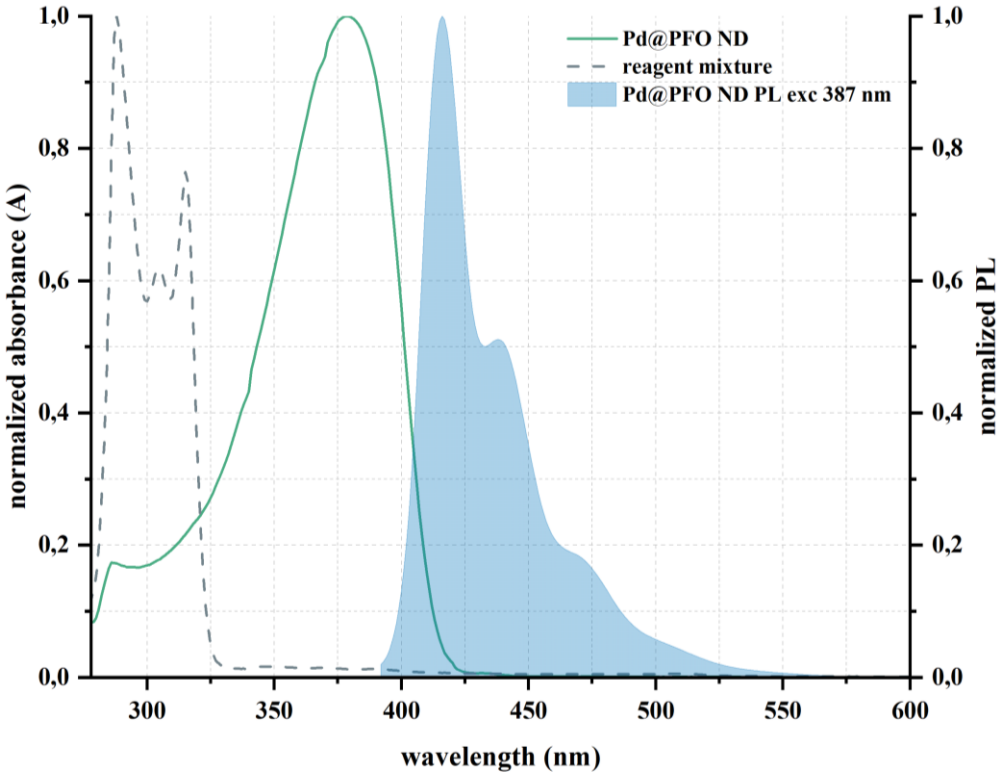

Graph 6. 3 *comparison between normalised ABS (dotted grey line) of regent mixture and ABS (green line) and PL (blue area) spectra (using toluene as solvent) of the dispersions (entry 3), highlighting the presence of the polymer. The excitation wavelength used is 387 nm*

The ^{1}H NMR spectrum showed the characteristic broad peaks of PFO, with no detectable signals from the monomers. This evidence was corroborated by both ABS and PL spectra (**Graph 6.3**), which exhibited the typical PFO optical features. The miniemulsion morphology was characterised by DLS both before and after the evaporation of the organic solvent to monitor the transition from miniemulsion to nano dispersion. The analyses revealed the coexistence of several particle populations, with sizes ranging from 80 nm to 1.2 μm, showing no significant differences before and after solvent removal (**Graph 6.4**).

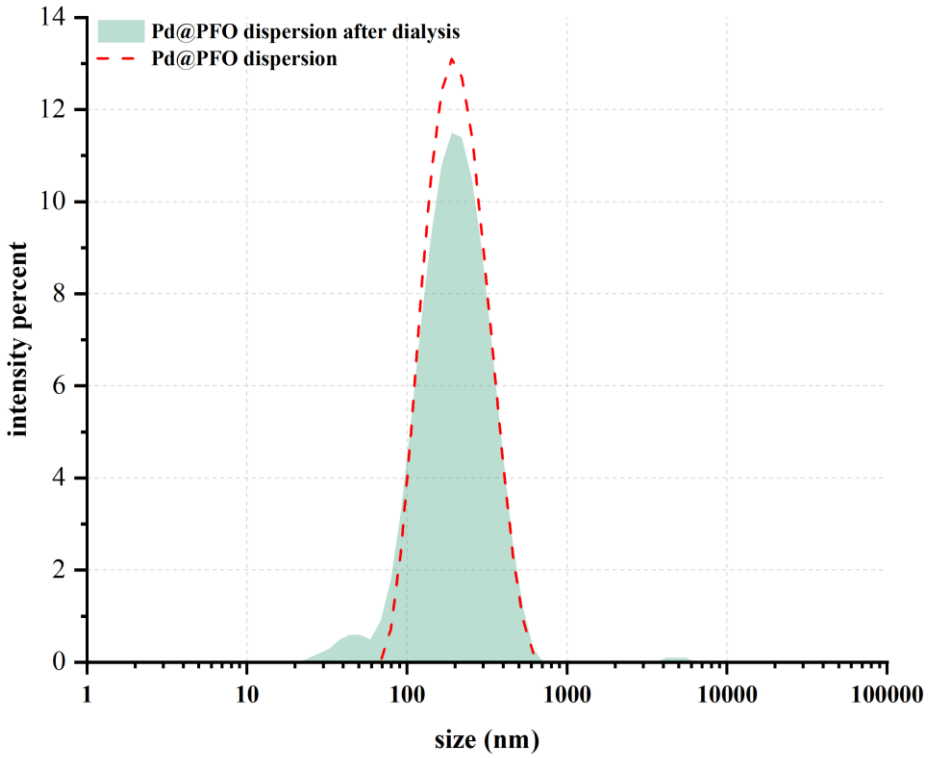

Graph 6. 4 *Representative DLS measurements of colloidal object of the abovementioned reaction; post evaporation of the solvent (dotted red line) and post dialysis (green area)*

Despite the successful polymer formation, the EPI protocol carried out at 50 °C was not sufficient to ensure controlled colloidal dimensions. This issue was overcome by introducing a 30-minute ultrasonic treatment prior to base addition, which enabled a more uniform droplet distribution without altering the reaction composition (**Table 6.4**, entry **4**).

Interestingly, temperature conditions (50 °C during both EPI and the following 16-hour reaction) were equally effective, as the appropriate phase exchange was already guaranteed under these optimised conditions (**Figure 6.23**). DLS spectra revealed the presence of a single family of colloidal objects. The average dimension of the aggregates is 190 nm (PdI 0,13). As expected, after toluene evaporation, this value slightly decreases (180 nm), whereas the polydispersity increases (PdI 0,2) (**Graph 6.4**).

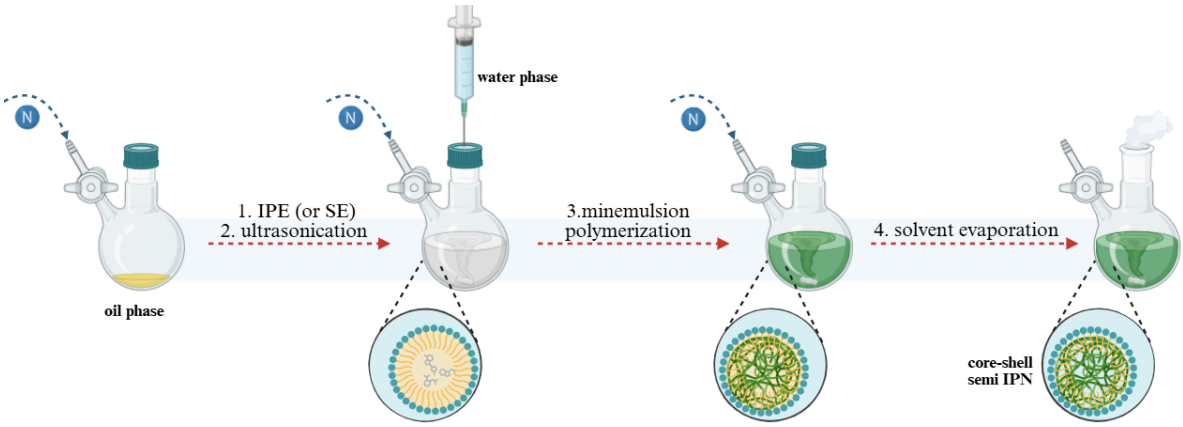

Figure 6. 23 *schematic representation of the final miniemulsion protocol involving an EPI miniemulsion formation and ultrasonication of the obtained biphasic system prior to the addition of the base to yield a stable PFO ND after the removal of the organic solvent*

The dispersion was then dialysed by ultracentrifugation to remove the salts from the reaction mixture, and then the recovered paste was redispersed in the same amount of neat water and sonicated with an ultrasound bath for 30 minutes. The discarded water didn't show any absorption peak attributable to Pd species (*see experimental session for further details about characteristic Pd species absorption features in water*). After this straightforward purification step, the quality of the dispersion is pretty much maintained (170 nm – PdI 0,2), probably because of entangled surfactant contributes. Post-dialysis ^{1}H NMR analysis confirmed the presence of surfactants inside the dispersion, supporting the idea of sIPN generation (**Graph 6.5**). The last test (**Table 6.4**, **entry 5**) aimed at increasing the catalyst loading directly during the synthesis of the nanometric support, with the goal of improving the catalytic performance of the resulting dispersion when employed as a heterogeneous catalyst. For this purpose, the amount of the catalyst was doubled, reaching 5.4 mol%, while remaining within a low-catalyst regime.

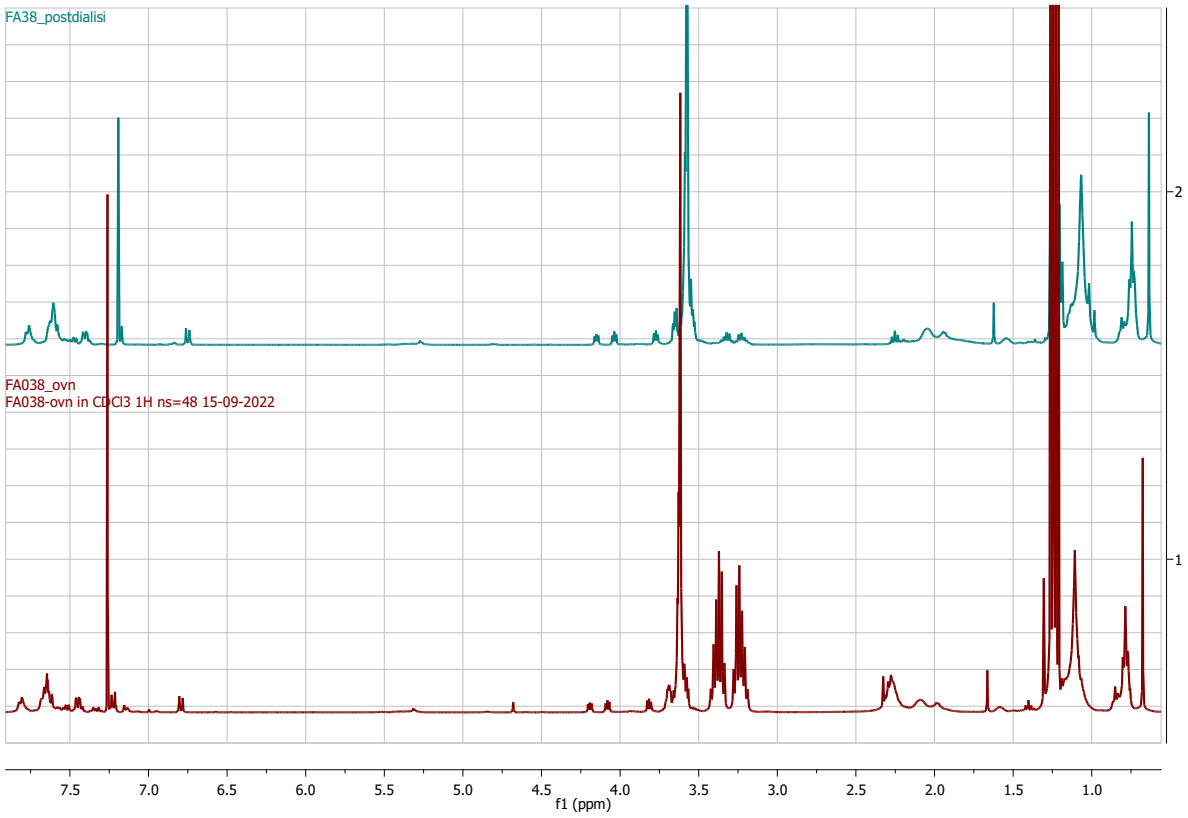

Graph 6. 5 *^{1}H NMR of Pd@PFO ND before dialysis step (red spectra)and after dialysis step. Surfactant peaks are always detected, thus confirming their entanglement into the polymeric colloidal structure*

The same optimised synthetic and purification procedures were followed as described previously. Given the promising outcomes, the dispersion obtained in **entry** 5 was further characterised by transmission electron microscopy (TEM) and SEM analysis. The TEM samples were prepared by drop-casting a small aliquot of the aqueous dispersion onto a TEM grid and subsequently drying them under ambient conditions prior to imaging. SEM samples are prepared by drop-casting a small aliquot of the aqueous dispersion onto a SEM stub, dried under ambient temperature, and pretreated with graphite prior to the analysis.

SEM images (**Figure 6.24**) confirmed the formation of the expected spherical nanometric objects. The surfactant-stabilised droplets effectively acted as templates, promoting the generation of spherical polymeric entities consistent with a semi-interpenetrated network (sIPN) structure. In addition to the dominant nanospheres, a few larger aggregates were also observed (visible as lower-contrast regions beneath the deposited surface). Their presence is most likely attributed to solvent evaporation during sample preparation, which can induce the coalescence of multiple colloidal particles. The diameters of representative particles were measured directly from SEM micrographs (**Figure 6.24 a**), and the results were in good

agreement with DLS data: the nanoparticle sizes ranged between 80 nm and 200 nm, depending on the degree of hierarchical aggregation.

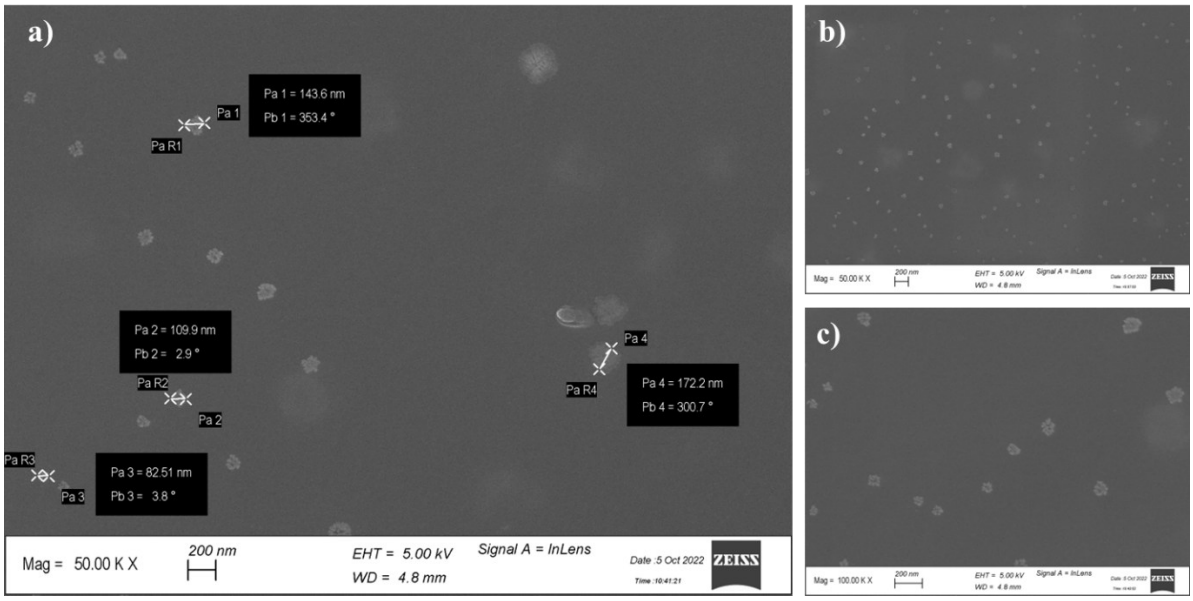

Figure 6. 24 *SEM image of Pd@PFO ND at different magnifications showing the hierarchical spherical morphology of the colloidal objects and a) highlighting the diameter of some colloidal entities*

Following SEM characterisation, TEM analysis was carried out to confirm the observed morphology and to further investigate the internal structure and Pd distribution within the nanospheres. TEM analysis further confirmed the spherical morphology of the obtained nanostructures (**Figure 6.25**).

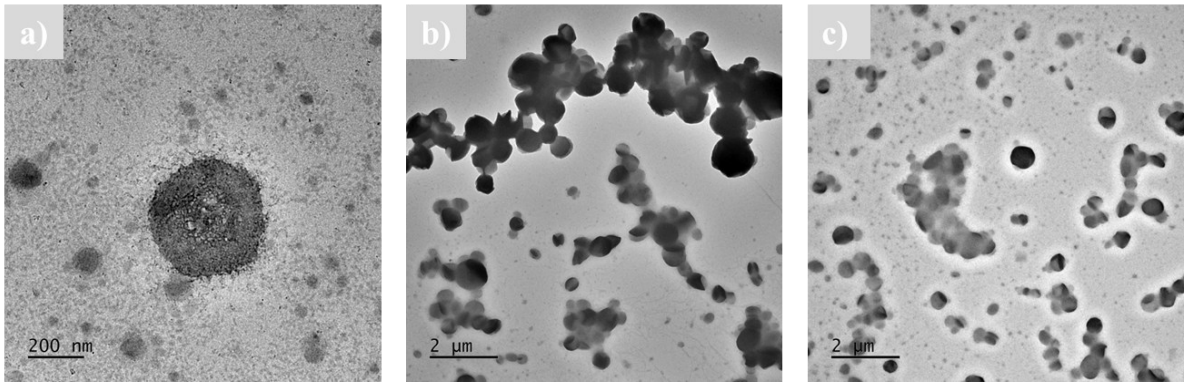

Figure 6. 25 *TEM image of Pd@PFO ND at different magnifications, confirming the spherical morphology of the colloidal objects*

At higher magnification (**Figure 6.25 a**), individual nanoparticles appear as well-defined spheres with a dense inner structure, suggesting the presence of palladium domains

homogeneously embedded within the polymer matrix, in agreement with the expected semi-interpenetrated network (sIPN) organisation. Lower magnification images (**Figure 6.25 b**,**c**) show a large population of spherical objects, mostly isolated but occasionally forming small aggregates, most likely due to solvent evaporation during sample preparation. The particles display an average diameter between 100 and 200 nm, consistent with the DLS and SEM data, confirming the good morphological control and homogeneity of the Pd@PFO ND.

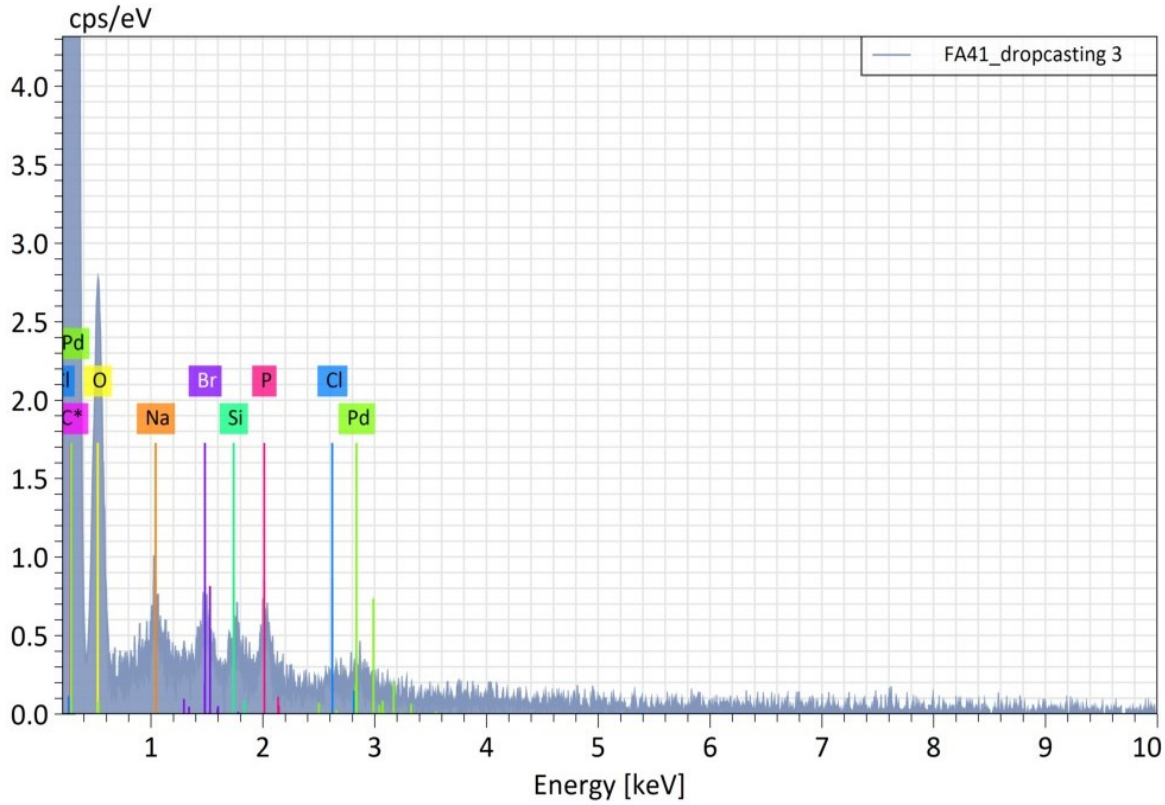

Figure 6. 26 *EDS spectrum of a specific area of Pd@PFO ND paste recovered after dialysis step, highlighting the presence of both Pd and P (linked to the use of $Pd(PPh_3)_4$)*

SEM-EDS spectrum on a selected area of a more concentrated sample (**Figure 6.26**) was performed, confirming the presence of Pd, even though in very low amounts. Conversely, under TEM-EDS analysis, the palladium signal could not be detected, most likely due to the extremely low Pd loading and the high dispersion of the metal within the polymeric matrix, which is below the sensitivity threshold of the technique. Phosphorus is also detected, and its presence is most likely linked to the use of $Pd(PPh_3)_4$) as a catalyst. It is postulated that, when exposed to air, the triphenylphosphine ligands undergo oxidation.

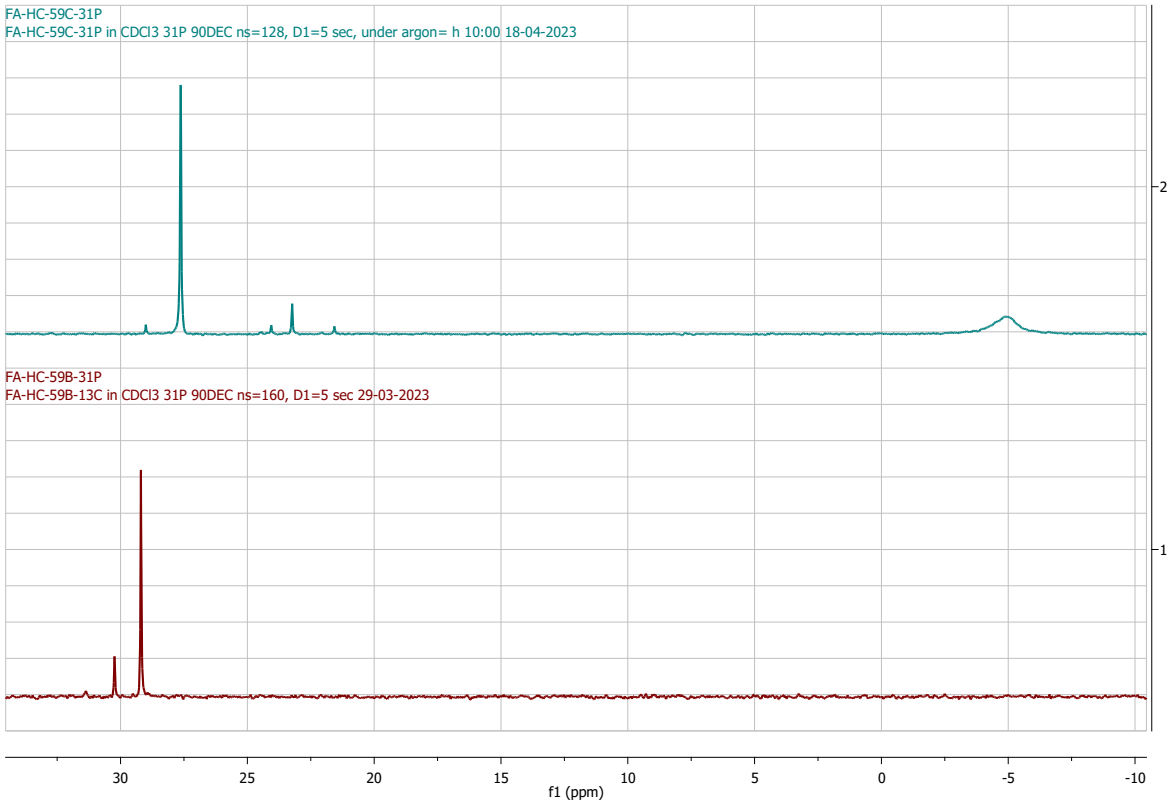

Figure 6. 27 *^{31}P NMR of Pd@PFO ND after its purification (red line) and $Pd(PPh_3)_4$) prepared under argon (green line). Both spectra are collected in $CDCl_3$*

To further confirm this hypothesis, ^{31}P NMR spectroscopy was carried out on the nano dispersion (**Figure 6.27**). The spectrum showed only one resonance corresponding to triphenylphosphine oxide ($OPPh_3$) (29.0 ppm), while no signal attributable to free or coordinated triphenylphosphine was detected (-4.86 ppm and 27.6 ppm). This indicates that all phosphine ligands were oxidised, likely remaining weakly associated with the polymeric matrix or the nanoparticle surface in their inactive oxidised form.

6.3.4.4 Exploring miniemulsion polymerization generality: fine-tuning the structure of the nano-disperse support

As mentioned in the previous paragraph, a straightforward procedure to obtain a heterogeneous nano-dispersed catalyst composed of a core-shell structure, whose core is able to support the active sites and shell enable its dispersion in the aqueous medium. In the Pd@PFO system, Pd NPs are stabilized within the polymeric matrix primarily through physio-chemical interactions, without forming direct covalent bonds with the polymer. The

aromatic segments of PFO can partially coordinate with the d-orbitals of Pd⁰ through π–metal interactions, anchoring the nanoparticles and limiting their migration or sintering. Additional stabilization arises from Van der Waals interactions and physical confinement. In semi-IPNs, branched surfactants surround the nanoparticles, creating a sterically and electrostatically stabilizing environment.

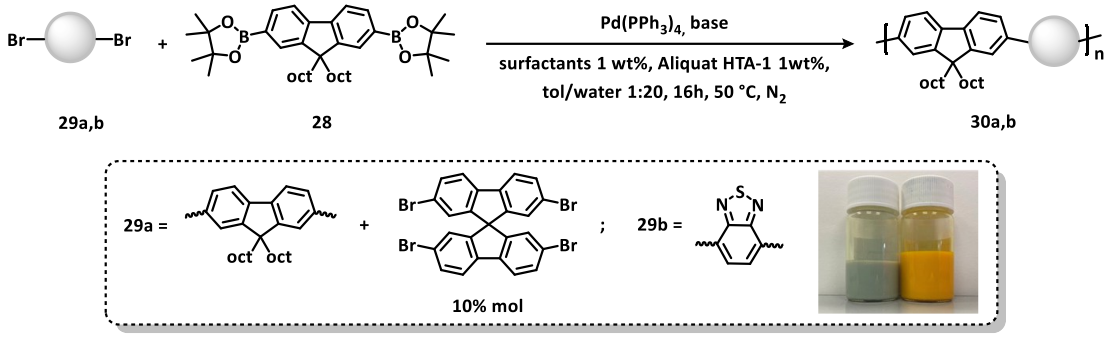

Scheme 6. 5 *General reaction scheme for the synthesis of Pd@polymer ND 30a (green dispersion) and 30b(yellow dispersion) using miniemulsion polymerisation optimised protocol.*

The next step was developing a support with a porous or semi-porous structure or containing heteroatoms that can further enhance the interaction between the active sites and the support. Porosity increases the available surface area, promoting a more uniform dispersion of nanoparticles and limiting aggregation. The pores can act as physical "traps" that confine the particles, reducing their leaching during catalytic reactions. The presence of heteroatoms (O, N, S) can provide additional coordination sites that interact with the metal, electronically stabilizing the nanoparticles and enhancing their affinity for the support. Overall, these features improve the stability of Pd nanoparticles, increase the availability of active sites, and optimize catalytic performance and material reusability. 2,2′,7,7′-Tetrabromo-9,9′-spirobifluorene (TBSBF) was selected as the crosslinking unit due to its structural compatibility with PFO monomer units. Poly(9,9-dioctylfluorene-alt-benzothiadiazole) (F8BT) was chosen as a heteroatom-containing alternative because its ability to stabilise and retain Pd nanoparticles after its synthesis has already been demonstrated.[226] The generality of the EPI miniemulsion protocol developed in the previous paragraph was thus extended to other both linear and partially crosslinked polymeric supports, showing great adaptability and not showing reduced performances when new bromides are used instead of (**25**).

Scheme 6.5 summarises the general reaction protocol employed for the bottom-up synthesis of Pd@PFO ND crosslinked (30a) and Pd@F8BT ND (30b). Once again, compound (**6**) was used as the boronic ester, while (**29a**) and (**29b**) were selected as the bromide partner. $Pd(PPh_3)_4$ served as the Pd^0 source, and NaOH was used as the base. As in the synthesis of Pd@PFO ND, the reaction was performed under a strictly inert atmosphere to avoid catalyst oxidation. Miniemulsifications were carried out at 50-60 °C, to allow for reagent solubilization in the organic phase otherwise difficult at room temperature. For this reason, only EPI methods yielded stable emulsions. A 30-minute sonication prior to base addition was again crucial for formulation refinement, thus consequential controlled final morphology of the ND.

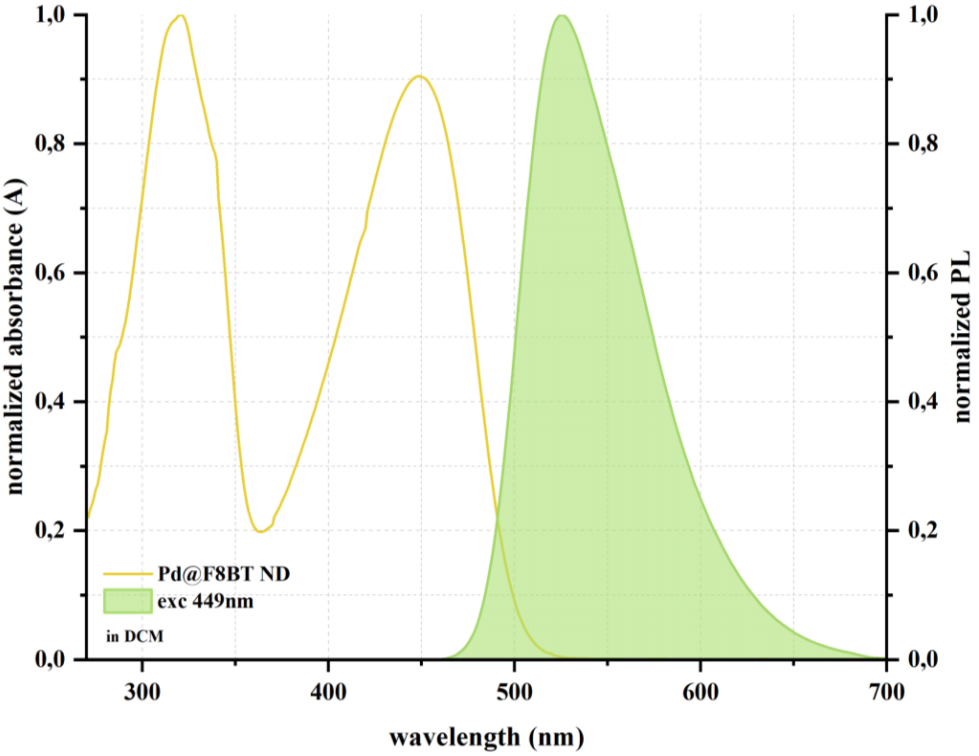

Graph 6. 6 *comparison between normalised ABS (yellow line) and PL (green area) spectra (using DCM as solvent) of compound* ***30b****. Excitation wavelength is set at 449 nm*

DLS spectra revealed in both cases the presence of a single family of colloidal objects. The average dimension of the aggregates is ~190 (30a) 180 (30b) nm (PdI 0,2). The dispersions were purified using the same protocol of Pd@PFO ND, and in both cases, after the purification step, the quality of the dispersion is pretty much maintained, further confirming the contribution of entangled surfactants.

As in the previous case, the success of the polymerisation was evaluated using ^{1}H NMR and optical spectroscopy (ABS and PL). The ^{1}H NMR spectra displayed signals characteristic of the polymeric species, while the absorption and photoluminescence spectra confirmed the corresponding absorption and emission of the two synthesised macromolecules. While the F8BT absorption (ABS) and photoluminescence (PL) spectra showed no substantial differences compared to literature-reported[226] optical spectra of the same polymer synthesised in organic solvents (**Graph 6.6**), the partially crosslinked PFO exhibited noticeable differences in both absorption and emission profiles.

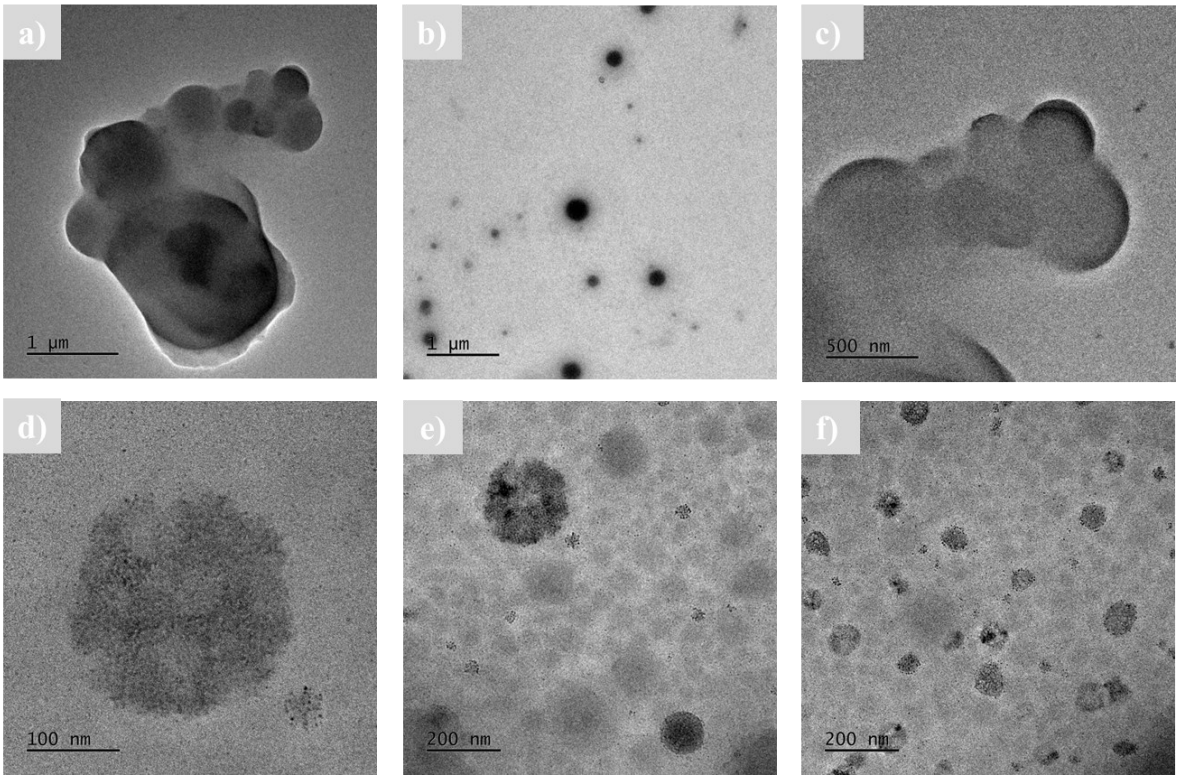

Figure 6. 28 *TEM image of Pd@F8BT ND (a, b, c) and Pd@PFO ND crosslinked (d, e, f) at different magnifications, confirming the spherical morphology of the colloidal objects*

Specifically, the incorporation of spirobifluorene units led to a blue shift of the main absorption peak, narrower spectral features, and the appearance of minor absorption bands corresponding to the spirobifluorene segments. These changes reflect a reduction in effective conjugation length, increased chain rigidity, and limited π–π aggregation compared to the linear PFO. **30a** and **30b** were then characterised by TEM analysis. The samples were prepared by drop-casting a small aliquot of the aqueous dispersion onto a TEM grid and

subsequently drying them under ambient conditions before imaging. Pd@F8BT ND samples (**Figure 6.28**, first row), the polymeric spheres are well defined and uniformly decorated with finely dispersed Pd nanoparticles, even if some aggregates are present due to the evaporation of the solvent. The metal looks evenly distributed across the polymer surface. In the Pd@PFO ND crosslinked (**Figure 6.28**, second row), the polymer spheres exhibit a denser texture and a finer, more uniform distribution of Pd nanoparticles. The crosslinked structure provides a rigid and confined environment that effectively limits nanoparticle migration and growth. Remarkably, in this sample, not only do the Pd nanoparticles remain well dispersed, but the polymeric spheres themselves do not show aggregation, maintaining a stable and well-separated morphology. This behaviour confirms that the structural rigidity introduced by the spirobifluorene crosslinker enhances both NPs stabilisation and the colloidal stability of the polymeric phase

Overall, the TEM observations clearly demonstrate that the introduction of heteroatoms (in F8BT) or crosslinking units (in PFO-spiro) improves the distribution and stabilisation of Pd nanoparticles on the polymer spheres.

6.3.5 Exploring Pd@PFO catalytic efficiency

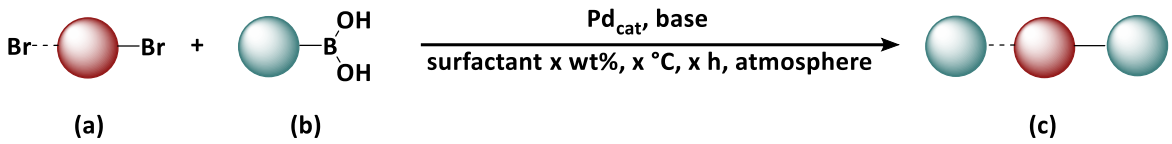

Scheme 6. 6 *Schematic representation of the reaction conditions used to perform the Suzuki cross-coupling reaction to test the catalytic activity of the different Pd-supporting catalysts. Each reaction involves a bromide (or di-bromide) (a), a boronic acid (b), a base (both organic or inorganic), water as reaction medium and a surfactant as compatibilizer and is performed at different temperature, depending on the specific test.*

Following the promising outcomes obtained from the two synthetic routes for the preparation of palladium-supported PFO, the catalytic performance of both the powder material (Pd@PFO) and the nano dispersion (Pd@PFO ND) was systematically evaluated. The study was directed towards the Suzuki cross-coupling reactions previously investigated within the research group, to assess the influence of the support morphology and preparation method on the catalytic activity and stability of the Pd-based systems (**Scheme 6.6**).

6.3.5.1 Pd@PFO generality: proof-of-concept of Pd@PFO efficiency

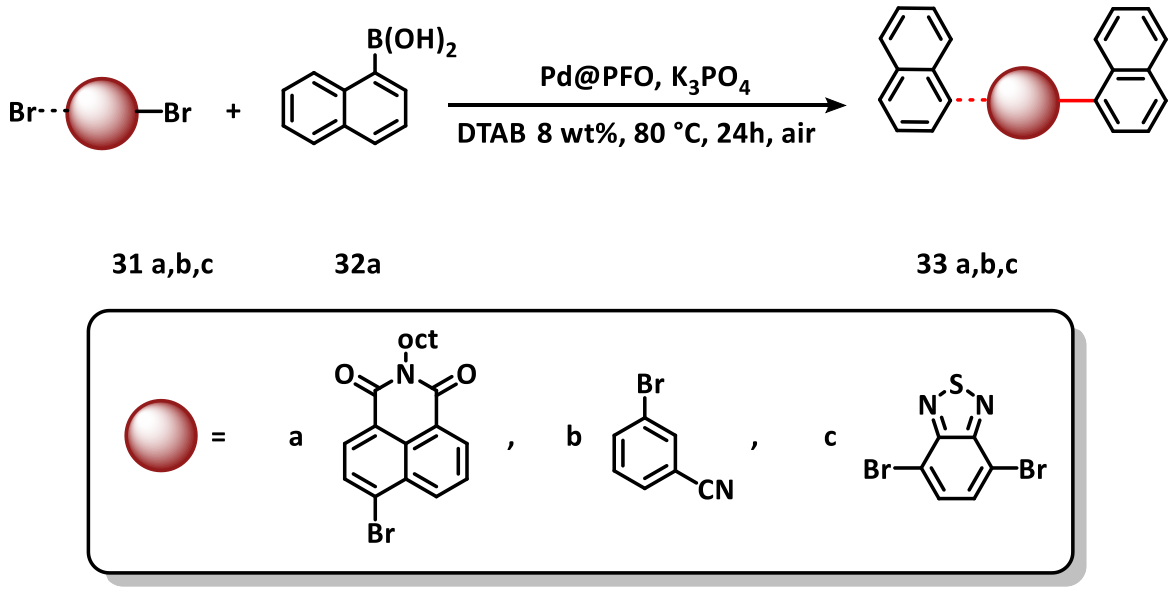

Scheme 6. 7 *First test reaction explored to prove the catalytic efficiency of Pd@PFO*

The cross-coupling between three different (di)bromides and 1-napthaleneboronic acid (**32**) was used as a test reaction (**Scheme 6.7**). The reported conditions had been previously

optimised by the research group to perform such reaction using Pd/C as a heterogeneous catalyst. Given the assonances between the two catalysts, the reaction has been simultaneously pursued using a homemade Pd/C, whose metal deposition and Pd content were comparable with that of Pd@PFO by ICP-MS analysis, following the same experimental procedure and using 14000 ppm of Pd in both cases. The comparison allowed the relative estimation of the catalytic performance of the novel catalyst. The reaction was performed by mixing together the reagents, then adding the dodecyl trimethylammonium bromide (DTAB) 8 wt% aqueous solution, the catalytic powder and the base at the end, always under vigorous stirring (see *experimental part for further details*). DTAB is a common, simple cationic surfactant, introduced in the optimisation of reaction conditions for Pd/C. The system was heated up to 80 °C for 24 hours in air. After that time, the reaction was stopped and cooled down. When N-octyl-4-bromonaphthalene-1,8-dicarbimide (**31a**) was used as bromide (**Table 6.5**, **entry 1**), the reaction vessel content appeared non-homogeneous: a turbid brownish liquid containing a green paste aggregated all around the magnetic stirrer (**Figure 6.15a,b**). The two parts were separated, and the solid one was taken up with water to remove both surfactant and salts.

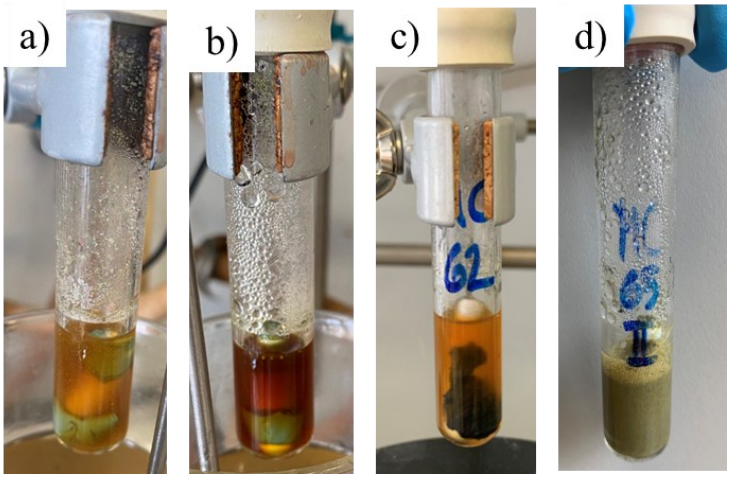

Figure 6. 29 *Reaction vessel of Pd/PFO a) two hours and b) 24 hours after the start of the reaction at 80 °C; reaction vessel of Pd/C c) after two hours at 80 °C and d) after 24 hours cooled down at RT*

The reaction output was monitored through ^{1}H NMR of the washed recovered solid. ^{1}H NMR (solvent: $CDCl_3$) relative conversion was evaluated using the ratio of the integrated areas between a reference product (**33a**) peak (8.7 ppm, doublet, 2H) and a reference reagent (**31a**) one (8.6 ppm, doublet of doublet, 2H). The comparison showed a higher conversion when Pd@PFO was used as catalyst with respect to Pd/C. The former reported a conversion of

approximately 85%, despite the low homogeneity of the reaction environment. On the other hand, the Pd/C catalysed reaction conversion settled down to around 52%, and a consistent percentage of homocoupling by-product was also detected (15%), whereas only a negligible amount of such by-product was detected when Pd/PFO was used as a catalyst (<5%). It is well known in literature that, generally, homocoupling by-product is favoured by the presence of Pd(II) species. It follows that either PFO helped in increasing the reduction conversion of Pd(II) to Pd(0), slowed down the re-oxidation of the metallic species, or it only favoured the involvement of the effectively reduced Pd(0) NPs in the reaction. Given the same reaction conditions and Pd content, the result highlights the influence of the support on the improved reaction output. The polymeric support allows an enhanced homogenization, having a major affinity with both coupling partners. Once the successful outcome of the reaction had been confirmed, an optimized workup procedure was developed to efficiently remove the catalyst from the reaction mixture and enable the recovery of both the product and Pd@PFO, thus allowing catalyst recycling. This step is a crucial element of the protocol, as it significantly contributes to its overall sustainability by preventing catalyst waste. The key factor enabling an effective separation between PFO, reagents, and the reaction product lies in their markedly different solubility in several organic solvents at room temperature, such as AcOEt. The reaction mixture was therefore extracted with this solvent, and the catalytic material was recovered through a simple filtration step.

entry	-Br	Conversion	Crude composition	Analysis
1	31a	85%	85% 33a	1H NMR
2	31b	>99%	96% 33b, 4% homocoupling	GC-MS
3	31c	41%	6% 33c, 41% mono, 23% homocoupling, 13% naphthalene	GC-MS
4[a]	31c	>99%	93% product, 7% homocoupling	GC-MS

Table 6. 5 *Summary of the reactions performed on three different EW aryl bromide to prove the efficiency of the newly synthesised heterogeneous catalyst; a) phenylboronic acid is used instead of naphtalenboronic one.*

^{1}H NMR analysis of the purified fractions confirmed the isolation of an uncontaminated catalytic powder, as well as the successful separation of the product (**33a**) from the reagent (**31a**), the former being isolated after a recrystallisation step in EtOH. Conversely, applying the same straightforward procedure proved unfeasible for the reaction catalysed by Pd/C,

mainly due to the high percentage of unreacted bromide and the presence of impurities, both of which hinder the crystallisation of the desired product.

Such reaction was performed multiple times to assess the reproducibility of the protocol. It is well known that complex multiphase systems, characterised by high reagent loading and high surfactant content, tend to be non-homogeneous and may suffer from poor repeatability. The relative ^{1}H NMR conversion was always consistent (80-90%). Ultimately, reaction reproducibility was confirmed: although conversion values exhibited some fluctuations, they remained within the same order of magnitude.

The second bromide tested was 3-bromobenzonitrile (**31b**) which, is also an electron-withdrawing (EW) aromatic core (**Table 6.5**, **entry 2**). The reaction conditions and the catalyst loading were kept identical to those employed in the previous experiment, and in this case a complete conversion of the starting material into the coupled product was achieved. The crude reaction mixture was analysed by GC-MS, and conversion was determined through the relative integration of the chromatogram peaks. Under these conditions, the chromatogram displayed only two signals, corresponding to the desired product and the homocoupling by-product, accounting for 96% and 4% of the crude, respectively.

The third bromide examined was instead an electron-poor dibromide, namely dibromo benzothiadiazole (**31c**). Here again, the same reaction conditions, catalyst loading, and analytical method for crude-mixture composition were applied. The resulting distribution was as follows (**Table 6.5**, **entry 3**): 47% overall conversion, consisting of 6% desired product and 41% mono-coupled intermediate. The reaction crude also contained 23% homocoupling by-product, 13% deboronation product, and the remaining portion corresponding to unreacted reagent and products. Usually, halides bearing electron-withdrawing groups (EWG) undergo oxidative addition more rapidly than those with electron-donating (ED) ones.[227] This refers specifically to the elementary oxidative-addition step (OA): EWGs lower the aryl halide LUMO and stabilise charge build-up in the OA transition state, which accelerates palladium insertion.[228] However, overall catalytic efficiency (observed conversion and product distribution) is governed by the entire catalytic sequence and by substrate-specific phenomena. The markedly lower efficiency observed for this substrate can be rationalised by its strong electron-deficient character and by widely reported practical difficulties of heteroaryl bromides (notably benzothiadiazole derivatives)

under standard Suzuki–Miyaura conditions, which often require careful optimisation of catalyst/ligand/base/solvent to reach high degrees of mono- or bis-arylation.[162,229] While coordination of heteroatoms (N, S) to palladium is a plausible mechanistic explanation for catalyst deactivation in some systems, direct experimental evidence proving such Pd-substrate complexes for benzothiadiazole bromides is currently lacking in the literature; therefore coordination remains a reasonable hypothesis rather than a proven mechanism in this case.

In heteroaromatic and polyhalogenated substrates (such as dibromo benzothiadiazole **31c**), the presence of heteroatoms and an electron-poor framework can stabilise off-cycle Pd^{2+} species,[230] promote side pathways (homocoupling, protodeboronation), or make subsequent steps (transmetalation, reductive elimination, or a second oxidative addition) slow or unproductive. Thus, an EWG can accelerate a single oxidative-addition event while the overall reaction yield remains low because of catalyst trapping, competing reactions, or impeded downstream steps. To further investigate the low conversions observed with **31c**, the boronic acid partner was changed to benzothiadiazole boronic acid in order to assess whether the steric hindrance of the dibromo substrate was responsible for the reduced efficiency. When this boronic acid was employed, a complete conversion of the starting material was observed, with 93% of the desired disubstituted product and only 7% of the monosubstituted intermediate. This result indicates that the steric hindrance of the dibromo benzothiadiazole plays a significant role in limiting the overall conversion in the standard cross-coupling reaction. Pd@PFO is capable of efficiently catalysing the coupling on this substrate when the steric constraints are reduced, confirming that the low yields observed with **31c** are also linked to substrate-specific steric effects.

6.3.5.2 Lowering the amount of Pd: a sustainability constraint

In the development of heterogeneous palladium catalysts, reducing the Pd loading (usually expressed in parts per million, ppm) is a critical aspect for both economic and environmental reasons. Pd is a precious metal with high cost, so minimizing its amount directly reduces the material expense of catalytic processes. Contributing to the sustainability of the protocol by decreasing the potential environmental impact associated with metal contamination in the final products.

From a synthetic and industrial perspective, high palladium residues in reaction products can pose significant challenges, especially in the pharmaceutical and fine chemical sectors, where strict regulatory limits on residual metals exist.[231] Therefore, achieving high catalytic efficiency at very low Pd loading demonstrates not only the effectiveness of the catalyst but also its practical applicability and compliance with green chemistry principles. Finally, studying reactions at reduced palladium concentrations provides insight into the intrinsic activity of the supported metal nanoparticles and the role of the polymeric support in enhancing Pd utilization. This allows the identification of conditions under which the catalyst performs optimally while minimizing precious metal consumption.

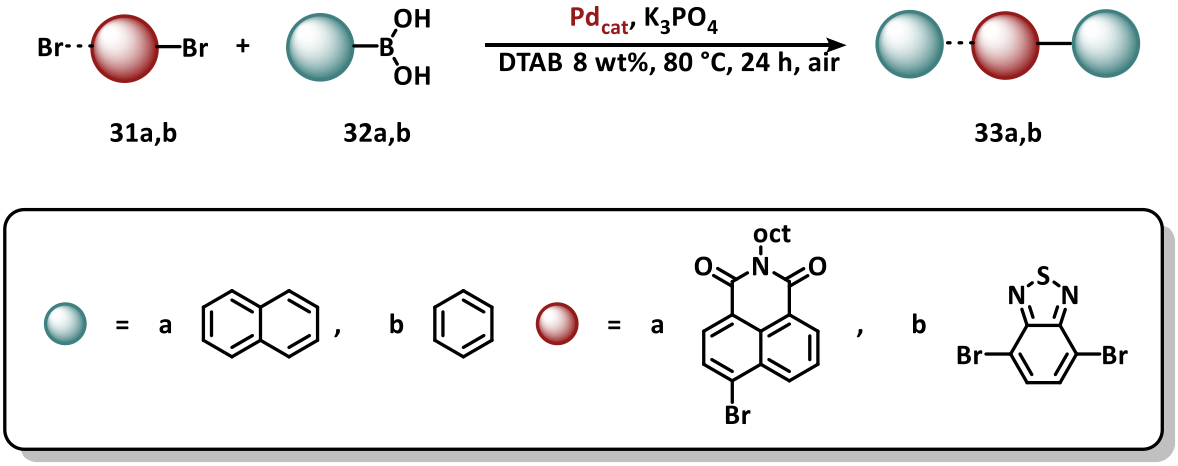

Scheme 6. 8 *Reagents and condition involved into the experiments targeting the reduction of Pd loading in the reaction mixture. Four different Pd loading are tested: 14000, 7000, 3500 and 1000 ppm*

To evaluate the intrinsic activity of Pd@PFO under more sustainable conditions, the Suzuki–Miyaura coupling previously optimised at 14000 ppm of palladium was repeated at progressively lower metal loadings (**Scheme 6.8**). Among the four benchmark reactions, two were selected for this study, starting with the cross-coupling between dibromo benzothiadiazole (**31c**) and phenylboronic acid (**32b**). Reducing the Pd loading from 14000 to 7000 ppm (**Table 6.6**, **entry 1**) did not affect the reaction outcome: the product distribution remained essentially unchanged, with 97% of the bis-substituted product and 7% of the monosubstituted intermediate. Encouraged by this result, the metal loading was further halved to 3 500 ppm (**Table 6.6**, **entry 2**). Under these conditions, the overall conversion dropped significantly to 56%, yielding 23% of the desired bis-coupled product and 33% of the monosubstituted species, while the remainder corresponded to unreacted starting

material. Notably, no homocoupling by-product was detected. A similar trend was observed when the palladium amount was decreased to 1000 ppm: the total conversion settled at 51%, composed of 25% bis-substituted product and 26% mono-substituted compound, again with no detectable homocoupling (**Table 6.6**, **entry 3**).

entry	-Br	-B(OH)$_2$	Conversion	Crude composition	Pd (ppm)
1	31b	32b	>99%	97% 33b, 3% mono	7000
2	31b	32b	56%	23% 33b, 33% mono	3500
3	31b	32b	51%	25% 33b, 25% mono	1000
4	31a	32a	17%	17% 333a	3500
5[a]	31b	32b	49%	20% 33b, 29% mono, 15% homocoupling	14000

Table 6. 6 *Summary of the reactions performed at different Pd loading with the two boronic and bromide partners; a) toluene is used as a co-solvent*

The progressive reduction in Pd loading naturally leads to a decrease in overall conversion because the number of catalytically active Pd sites available in the reaction mixture becomes limiting. At higher loadings, the concentration of Pd^0 nanoparticles is sufficiently high to sustain efficient turnover of both oxidative addition events required for bis-arylation of **31c**. Under these conditions, the reaction benefits from a large reservoir of active centres capable of compensating for any catalyst deactivation. However, when the palladium amount is decreased to 3500 ppm and below, the catalytic system enters a regime in which the availability of active Pd(0) species becomes the rate-limiting factor. At lower Pd loadings, the reduced density of active catalytic sites limits the probability that both oxidative addition steps required for full bis-arylation of dibromo benzothiadiazole occur efficiently on the same nanoparticle, favouring accumulation of the monosubstituted intermediate. In addition, any degree of Pd(0) deactivation, whether through aggregation or surface oxidation, becomes significantly more detrimental when the overall amount of palladium is low, as the system can no longer compensate for the loss of active species. The decrease in nanoparticle surface area at low loadings also slows down key catalytic steps such as transmetalation and reductive elimination. The consistent absence of homocoupling at low Pd loadings contrasted with the behaviour previously observed when using 1-naphthylboronic acid

(**32b**), where homocoupling was always considerable. To understand this divergence, an additional experiment was designed in which toluene was introduced as a co-solvent (**Table 6.6**, **entry 5**). Pd@PFO (1400 ppm) was first suspended in toluene, where its solubility is poor, and allowed to swell in the presence of DTAB (8 wt%) for 15 minutes. This pre-swelling step was expected to modify the microenvironment of the polymeric support. Subsequently, the reagents (**31c** and **32a**) and base were added, keeping all other parameters identical to those of the standard procedure. Under these modified conditions, the crude composition differed markedly from that obtained in purely aqueous medium. The fraction of the bis-substituted product decreased to 20%, while the monosubstituted intermediate increased to 29%. Most importantly, a substantial amount of homocoupling by-product (15%) was observed, an outcome never detected in the corresponding aqueous reactions. These results suggest that the reactivity of Pd@PFO is strongly influenced by the microenvironment surrounding the palladium nanoparticles. The introduction of toluene modifies the structure and swelling behaviour of PFO, likely altering nanoparticle accessibility, diffusion of reagents within the polymer matrix, and the relative stability of Pd oxidation states. The appearance of homocoupling in the presence of toluene indicates that the co-solvent facilitates the formation or persistence of Pd^{2+} species capable of undergoing reductive elimination to generate the homocoupled product. In order to further probe the influence of palladium loading on catalytic efficiency, substrate **31a** was also evaluated under analogous conditions (**Table 6.6**, **entry 4**). In this case, a Pd loading of 3500 ppm was selected. The reaction still delivered markedly low conversion (17%), highlighting that insufficient palladium availability is not the sole limiting factor in the coupling efficiency of this substrate. The low yield can be attributed to a combination of factors, including the limited stability of the naphthyl boronic acid under the reaction conditions. These results, together with those obtained for substrate 31b, clearly illustrate that Pd loading exerts a strong but substrate-dependent influence on catalytic performance.

6.3.5.3 Experimental evaluation of Pd leaching from Pd@PFO and Pd/C

A key distinction between Pd/PFO and Pd/C lies in the nature and strength of the interactions that the supporting material establishes with the metallic active centres. In Pd/C, it is generally accepted that Pd nanoparticles interact with the high surface-area activated

charcoal through non-specific and predominantly dispersive forces. The carbon matrix provides spatial confinement but lacks functional groups capable of stabilising Pd through directional or coordinative interactions.[232] Consequently, Pd leaching is widely recognised as inherent to this class of heterogeneous catalysts, and the mechanistic details of Pd/C-catalysed reactions remain a subject of active debate. Previous studies conducted within the research group have shown that Pd leaching from activated charcoal is strongly influenced by both cationic surfactants and temperature (**Figure 6.30**). The release of Pd into solution was monitored by UV–Vis spectroscopy, exploiting the characteristic absorption features of tetracoordinated Pd^{2+} species.

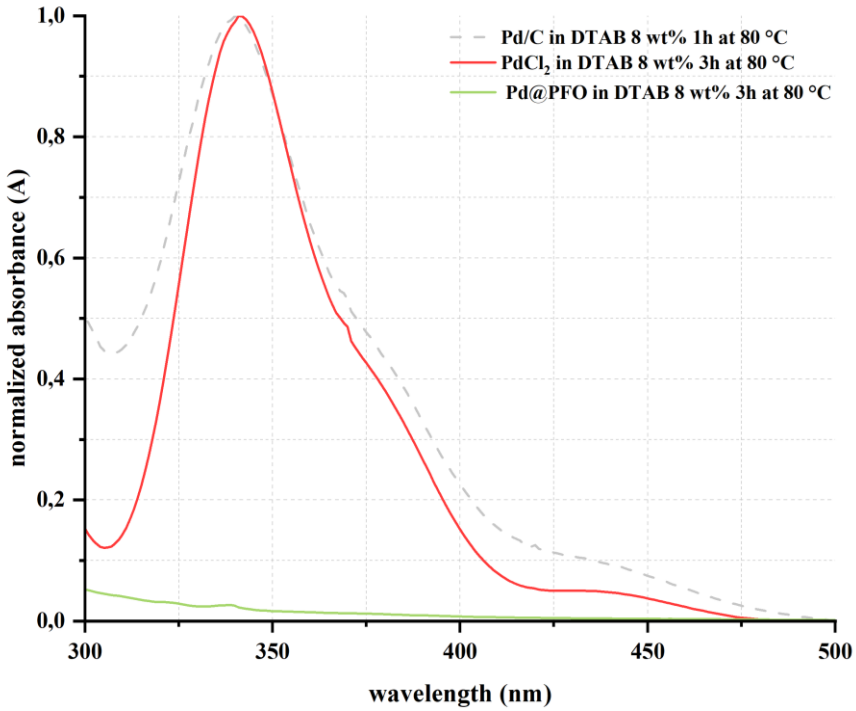

Graph 6. 7 *ABS spectra of Pd/C (dotted grey line), $PdCl_2$ (red line) and Pd@PFO (green line) residual water in DTAB 8 wt% after 3h at 80 °C. The spectra were registered using water as the solvent.*

$PdCl_2$ used as a reference source of Pd^{2+}, displayed a distinctive absorption band at 341 nm when dissolved in an 8 wt% DTAB aqueous solution (*See experimental part for further information*). The same band appeared in samples collected during Pd/C pre-treatments performed under various surfactant and temperature conditions, and its intensity increased over time, indicating a progressive and continuous extraction of Pd^{2+} promoted by the amphiphile. The same protocol was applied to Pd@PFO in order to investigate the effect of the cationic surfactant (DTAB) and the typical reaction temperature (80 °C) on Pd leaching

from the polymeric support. In this system, the nature of the metal–support interactions differs substantially: the extended π-conjugated aromatic backbone of PFO is expected to engage in π-stacking or related non-covalent interactions with the surface of the Pd nanoparticles, contributing to their stabilisation and immobilisation.

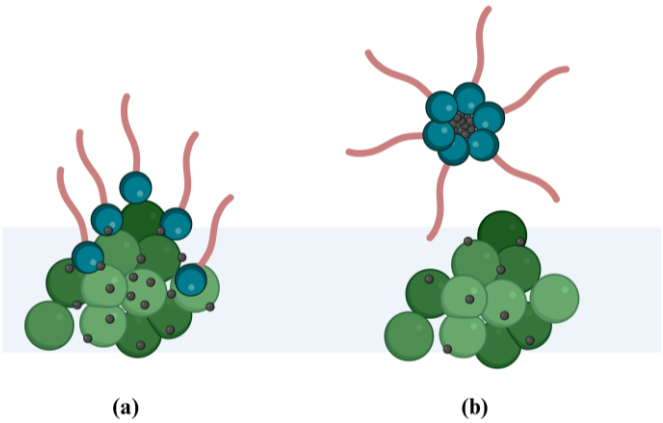

Figure 6. 30 *Cartoon representation of Pd cluster removal from the support surface promoted by surfactants*

A dispersion of Pd@PFO in an 8 wt% DTAB aqueous solution was stirred at 80 °C for 3 h, after which the UV-Vis spectrum of the supernatant was recorded. In contrast to Pd/C, no absorption band at 341 nm was detected (**Graph 6.7**). This observation indicates that, under these conditions, neither the cationic surfactant nor the elevated temperature promoted the release of Pd from the polymeric support. The results support the hypothesis that the π-stacking interactions between Pd and the PFO backbone are sufficiently strong and specific to prevent the detachment processes that readily occur with activated carbon. Further investigations involving Pd@PFO ND systems are planned to assess whether the nanodispersed architecture influences Pd retention and to clarify the role of polymer–surfactant interpenetration in mitigating metal leaching.

6.3.5.4 Evaluating catalyst stability under reaction conditions: leaching and reuse of Pd@PFO

The insights gained from the leaching studies provide a foundation for evaluating the long-term stability of Pd@PFO based catalytic systems. Demonstrating that Pd@PFO does not release Pd species under the combined action of surfactant and temperature indicates that the π-conjugated polymeric support offers a markedly stronger interaction with Pd NPs

compared to traditional carbon-based materials. However, while resistance to leaching under model conditions is necessary, it is not sufficient to guarantee catalytic robustness during real cross-coupling transformations, where reactive substrates, bases, and intermediates may impose more complex chemical stresses on the support.

For this reason, the next step of the investigation focused on assessing the recoverability and reusability of Pd@PFO under operative Suzuki conditions. Recyclability represents one of the most valuable attributes of heterogeneous catalysts, directly impacting sustainability, cost-efficiency, and practical applicability.

To verify whether this concept could be effectively applied to the Pd@PFO system, the powder sample was subjected to a recyclability study. The absence of Pd leaching under surfactant- and temperature-induced stress, combined with the straightforward physical separation of the solid after catalysis, encouraged its reuse.

The catalyst recovered after a first cross-coupling cycle was therefore employed in a second catalytic test under the same conditions used in **Scheme 6.6**. The recycled material (starting Pd content 1.9%) was introduced into the reaction following the standard procedure, and the conversion of the crude mixture was again evaluated by ^{1}H NMR spectroscopy. In this second run, the substrate reached only 40% conversion. This reduced performance was consistent with the effective Pd content of the recovered powder, quantified by ICP-OES as 0.6 wt%. Thus, despite the absence of leaching during the pre-treatment experiment, a significant loss of Pd occurred during catalysis.

This behaviour can be rationalised by considering the role of the reagents during the reaction. The π-conjugated nature of the PFO backbone enhances the diffusion of substrates into the pseudo-colloidal polymeric domains, promoting swelling of the support. This facilitates the interaction between the encapsulated Pd nanoparticles and the reacting species, an effect that favours the oxidative addition step but simultaneously weakens the non-covalent forces responsible for metal retention. As a result, Pd species can detach from the polymer surface and participate in the reaction medium as dissolved catalytic entities, ultimately failing to redeposit onto the support in their original form. This observation highlights the need for stronger and more specific interactions between metal centres and the polymeric matrix to prevent undesirable Pd release. Incorporating heteroatoms directly into the polymer backbone may reinforce electrostatic and donor-acceptor interactions with Pd. Alternatively, enhancing the spatial confinement of the nanoparticles through the formation of a porous,

crosslinked polymeric network, achieved by integrating a crosslinking agent during the bottom-up synthesis, represents a promising strategy to improve catalyst stability across multiple cycles.

6.3.5.5 From Pd@PFO to Pd@PFO ND as a strategy to increase the catalytic activity

The following stage of the study focused on evaluating the performance of Pd@PFO ND, the heterogenized catalyst synthesized through the miniemulsion polymerization of PFO (**Scheme 6.9**). In this system, the polymerization takes place inside the surfactant-stabilized nanodroplets, leading to the formation of semi-interpenetrated polymer-surfactant networks that remain structurally intact and do not collapse or precipitate. As a consequence, the catalyst is obtained as a liquid material, in which the active palladium nanoparticles are physically embedded within the polymeric matrix.

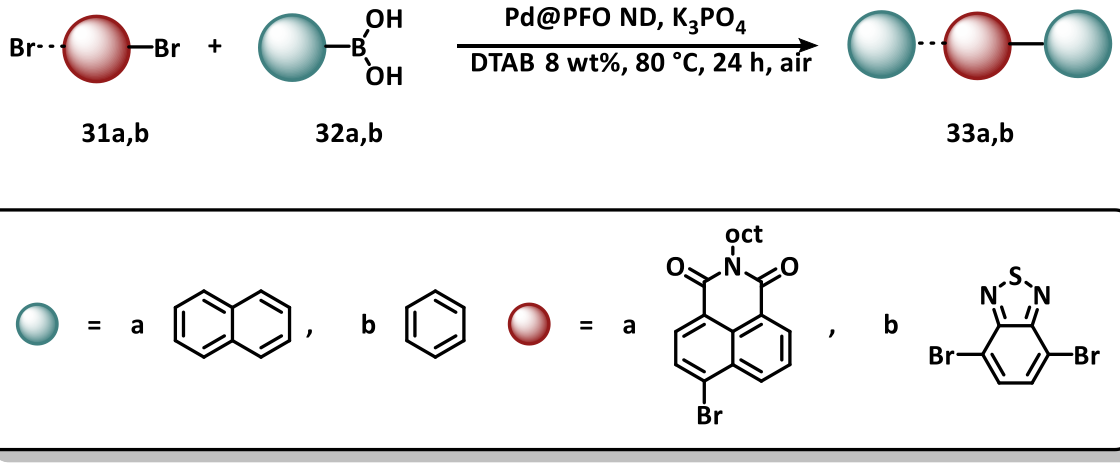

Scheme 6. 9 *Schematic representation of the reaction conditions and reagents used to test the generality of Pd@PFO ND*

Importantly, these Pd nanoparticles are not post-synthetically deposited onto the polymer; rather, they are the same metallic species initially present during the polymer growth, where they participate in the reduction and propagate the formation of the polymeric network. This synthetic strategy ensures that the metal particles become stably confined within the soft polymer domains, theoretically preventing aggregation and allowing the formation of a truly heterogenized catalytic phase. The Pd@PFO ND system thus represents an evolution of the

previous catalytic dispersions, as it combines the advantages of effective nanoparticle immobilization with the handling convenience of a liquid catalyst.

The catalytic performance of Pd@PFO-ND was evaluated using the same model Suzuki coupling previously adopted for benchmarking the heterogeneous catalyst. Reaction conditions were intentionally kept identical same substrates, base, solvent composition, and nominal Pd loading, in order to allow a direct comparison between the different catalytic systems. Upon addition of Pd@PFO-ND to the reaction mixture, the system appeared macroscopically homogeneous, a consequence of the intrinsic fluidity of the catalyst and the efficient swelling of the polymer-surfactant network under the biphasic reaction conditions (**Figure 6.31**). Throughout the reaction, no visible phase separation or precipitation of the soft polymer domains and did not undergo aggregation or leaching to a detectable extent. After 24 h, the reaction was quenched and subjected to the same work-up procedure previously established for the dispersed catalysts: removal of the polymeric phase by filtration, followed by extraction with water to eliminate residual surfactant and inorganic salts.

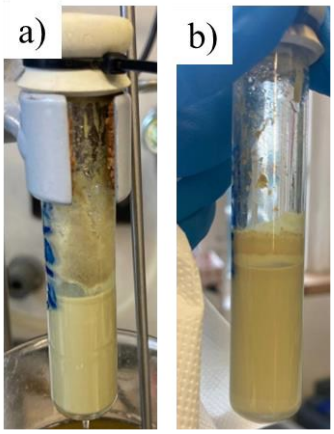

Figure 6. 31 *Reaction vessel involving Pd@PFO ND as catalyst after 24 hours a) at 80 °C and b) at RT*

^{1}H NMR analysis of the crude mixture revealed full conversion, with the desired biaryl product as the only detectable organic species and no traces of starting material or homocoupling by-products. This excellent result demonstrates that Pd@PFO ND is fully competent in promoting Suzuki cross-coupling under the selected conditions and performs comparably, or even superior, to the best-performing dispersions described in the previous section. The high efficiency of the catalyst can be attributed to the combination of factors intrinsic to its preparation. First, the confinement of palladium nanoparticles within the semi-

interpenetrated polymer-surfactant network prevents their sintering or deactivation, maintaining a high density of accessible active sites. Second, the liquid nature of the catalyst ensures intimate contact with the reacting substrates, bridging the typical gap between homogeneous and heterogeneous catalysis. Finally, the fact that Pd is embedded in the polymer from the earliest stages of its synthesis should guarantee a strong metal-matrix interaction, which stabilizes the nanoparticles and preserves their catalytic integrity throughout the reaction.

The robustness of Pd@PFO ND was further confirmed by extending the study to the coupling between **31b** and phenylboronic acid (**32b**). The reaction was conducted using Pd@PFO ND at 14 000 ppm of Pd, mirroring the benchmark conditions previously applied to the colloidal dispersions, and the catalytic performance remained remarkable. GC-MS analysis of the reaction mixture revealed a conversion higher than 99%, and the crude product consisted exclusively of the bis-coupled derivative, with no detectable monosubstituted intermediate. This result is particularly significant considering that, in many catalytic systems, dibrominated heteroarenes tend to stall after the first coupling step due to the reduced reactivity of the intermediate and competitive coordination of heteroatoms to palladium. The complete suppression of the monosubstituted species strongly suggests that Pd@PFO-ND provides a sufficiently high local concentration of active Pd sites and maintains them in a highly accessible and stable state throughout the catalytic cycle.

6.3.5.6 Influence of support morphology and crosslinking on the Pd-catalysed coupling of alkylated fluorene derivatives: a case study

A specific case study was then examined in greater detail: the Suzuki–Miyaura cross-coupling between (**25**) and (**32a**), performed using three different catalytic systems—heterogeneous Pd@PFO, Pd@PFO-ND, and the crosslinked Pd@PFO-ND analogue. The initial motivation for testing this reaction with the heterogeneous catalyst stemmed from the structural similarity between the fluorene-based substrate and the PFO support. It was hypothesised that this strong affinity could facilitate substrate-polymer interactions, promoting substrate enrichment around the catalytic sites and therefore enhancing the overall coupling efficiency. For this reason, the reaction was first conducted under the standard

conditions already established in the previous test reactions, using 14000 ppm of palladium and Pd@PFO as the catalyst (**Table 6.7**, **entry 1**).

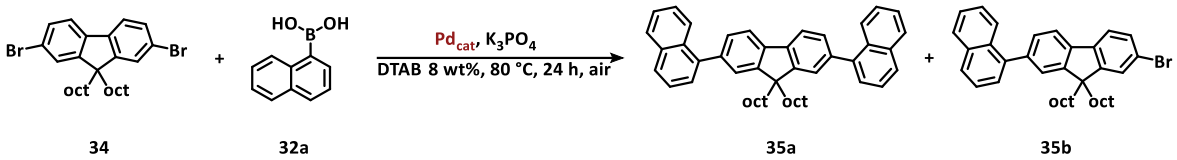

Scheme 6. 10 *Suzuki cross-coupling between 9,9-dioctyl-2,7-dibromofluorene (25) and naphtalenboronic acid (32a) performed with three different Pd supported catalysts, keeping the same reaction conditions of the previous test reactions. Product 35a is the main product of the reaction, while molecule 35b is the detected by-product.*

Contrary to expectations, the outcome obtained with the heterogeneous material deviated substantially from the anticipated high performance. ^{1}H NMR analysis revealed a conversion of only 39%, distributed as 21% of bis-arylated product (**35a**) and 18% of the monosubstituted intermediate (**35b**). Moreover, the reaction mixture showed clear evidence of palladium clusters detaching from the polymer matrix at the end of the process. This behaviour indicates that the structural similarity between the substrate and the PFO support, initially considered an advantage, actually had a detrimental effect on the catalyst's function. Since (**25**) is chemically identical to the polymeric backbone of the Pd NPs support and is present in large excess compared to the amount of polymer, the substrate effectively competes with the support for interactions with soluble Pd species. During Suzuki cross-coupling, it is well established that palladium transiently dissolves and redeposits onto the support (**Figure 6.32**).

entry	Catalyst	Conversion	Crude composition
1	Pd@PFO	38%	21% 35a, 18% 35b
2[a]	Pd@PFO	15%	8% 35a, 7% 35b
3	Pd@PFO ND	41%	6% 33c, 41% mono, 23%
4	Pd@PFO ND$_{crosslinked}$	>99%	>99%

Table 6. *7 Summary of the reaction performed on (25) as test substrate using different Pd-supported catalysts; a) Pd@PFO used for this reaction is recovered from entry (1)*

In this system, however, the overwhelming excess of fluorene-based substrate likely stabilises the dissolved Pd species in solution, preventing their redeposition onto the PFO matrix. As a result, the palladium nanoparticles are unable to return to the support after

undergoing the catalytic cycle and instead aggregate in the reaction medium, leading to the formation of detached Pd clusters. This loss of controlled redeposition directly reduces the number of accessible active sites and explains both the modest conversion and the accumulation of the monocoupled intermediate. To further investigate this phenomenon, the reaction was repeated using the catalytic material recovered from the first experiment (**Table 6.7**, **entry 2**). The conversion dropped to 15%, giving 8% of the bis-coupled product and 7% of the monosubstituted derivative. This severe decline confirms that the Pd@PFO support was irreversibly compromised: once Pd nanoparticles detached and aggregated in solution, the support could no longer stabilise or recycle the active metal species. The recycled material therefore behaved as a partially deactivated, Pd-depleted catalyst, consistent with the dramatic loss of activity observed.

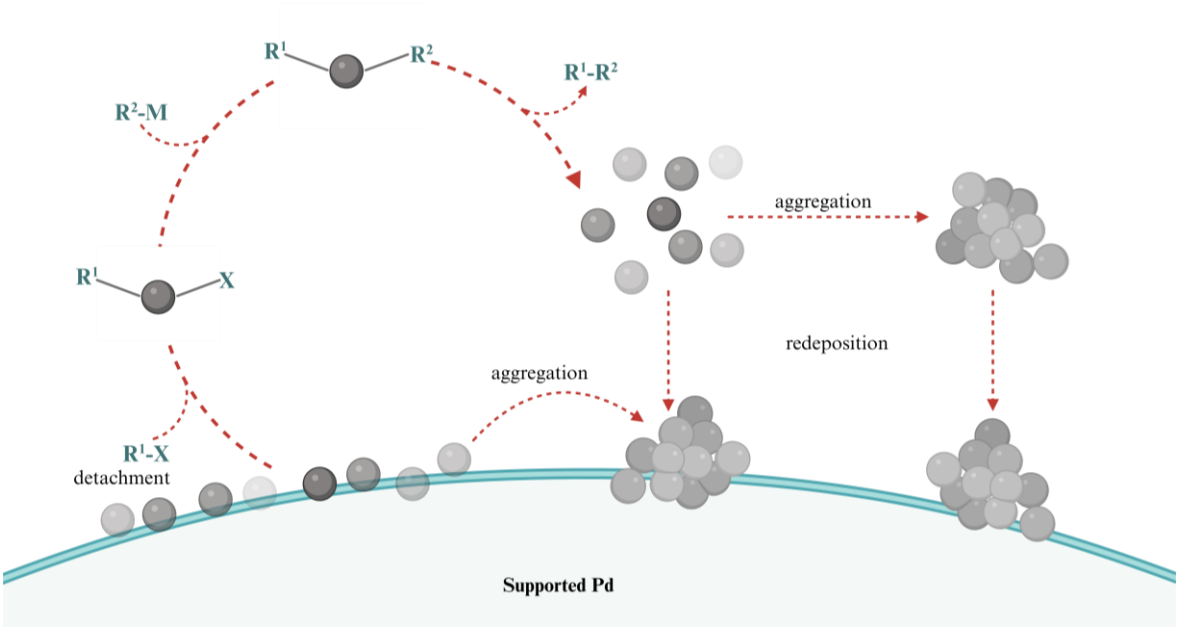

Figure 6. 32 *The "Cocktail" type nature and evolution of the catalytic species in C–C bond formation reactions catalysed by supported Pd catalysts.*

When the reaction was performed using the Pd@PFO-ND catalyst (**Table 6.7**, **entry 3**), the behaviour of the system changed markedly. The appearance of the mixture during the reaction (**Figure 6.33**) already suggested a different interaction between the catalytic material and the reaction medium: the nanodispersed catalyst led to a finer, more homogeneous system in which the catalytic phase remained well-distributed throughout the reaction time. Under these conditions, the conversion increased to 62%, and, importantly,

the crude contained **o**nly the bis-coupled product, with no detectable monosubstituted intermediate. This result indicates that the nanodispersion architecture overcomes the limitations observed for the heterogeneous Pd@PFO material. In Pd@PFO ND, the palladium nanoparticles are embedded within soft, swollen polymer–surfactant nanodomains that remain colloidally stable during catalysis. This morphology reduces the likelihood of Pd detachment and aggregation and ensures a more uniform accessibility of the active sites. Moreover, the fluidity and large interfacial area of the nanodispersion facilitate efficient substrate diffusion and catalytic turnover, preventing the accumulation of the monoarylated species that plagued the heterogeneous system. Nevertheless, the conversion does not reach full completion. A dramatic improvement was obtained with the crosslinked Pd@PFO ND system (**Table 6.7**, **entry 3**).

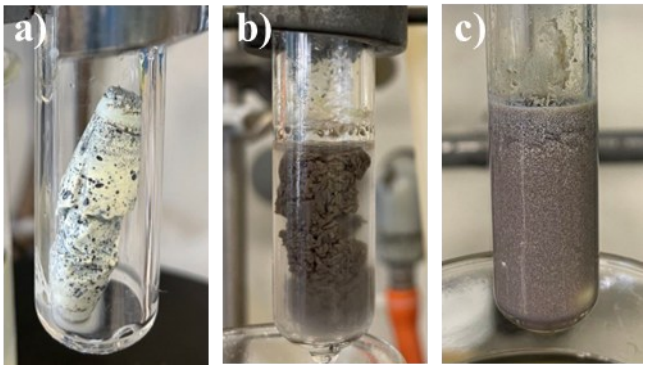

Figure 6. 33 *Formulation of the three reaction mixtures involving substrate (**25**) and the three different catalysts a)PD@PFO; b) Pd@PFO ND; c) Pd@PFO ND crosslinked*

Introducing a spirobifluorene-based crosslinker into the polymeric matrix during the nanodispersion synthesis partially rigidified the polymer network, strengthening its ability to retain palladium during the dissolution-redeposition processes characteristic of Suzuki catalysis. When used under the same reaction conditions, the crosslinked nanodispersion delivered >99% conversion (**Table 6.7**, **entry 4**), with exclusive formation of the bis-coupled product and complete suppression of the monosubstituted intermediate. This outstanding performance demonstrates that the introduction of controlled crosslinking is crucial to preserve the integrity of the catalytic environment. The crosslinked network acts as a more robust physical trap for palladium species, preventing their loss into the reaction medium and maintaining a stable population of active sites throughout the catalytic cycle. In contrast

to the heterogeneous Pd@PFO system, where Pd detachment was clearly observed, and even to the non-crosslinked nanodispersion, the crosslinked material provides a highly stabilising support that enables continuous redeposition of Pd(0) after each catalytic turnover. As a consequence, catalytic activity remains high, deactivation pathways are minimised, and the reaction proceeds to completion with excellent selectivity.

6.4 Conclusion

During this work, two straightforward procedures for the obtainment of π-conjugated organic polymer-supported Pd NPs were investigated, focusing on their catalytic activity in model Suzuki coupling reactions.

The first heterogeneous catalytic system was prepared by introducing Pd active sites onto a previously synthesised and characterised polymeric support through a hydrogenation protocol that enabled the in-situ reduction of a Pd(II) precursor. The dispersion and morphological control of the polymeric phase during this procedure proved to be crucial for the efficient embedding of Pd NPs on its surface, as confirmed by SEM-EDS and ICP-OES analyses.

The second system was developed following a greener and more efficient synthetic route, based on a miniemulsion polymerisation approach. In this one-pot bottom-up strategy, the polymeric support (PFO) was directly synthesised within surfactant-stabilised nanometric droplets, exploiting the amphiphilic molecules both as stabilisers and as functional agents during the synthesis and catalytic application. This methodology offered several appealing advantages compared to the top-down procedure: (i) the elimination of a separate Pd deposition step, (ii) an enhanced degree of dispersion, and (iii) a more controlled and uniform morphology of the resulting CNPs.

In this system, the Pd catalyst used during polymer synthesis became confined within the polymeric core of the colloidal objects, likely due to strong interactions with the aromatic structure of the conjugated polymer. The formation of a sIPN, resulting from the entanglement of branched surfactants within the polymeric coils, contributed to the structural stability and spatial confinement of Pd NPs. Furthermore, SEM-EDS analysis confirmed that ultracentrifugation, dialysis, and redispersion in water (followed by a 30-minute sonication step) did not perturb the morphology of the system, with spherical nanoparticles of approximately 200 nm still observed.

The catalytic performance of both Pd@PFO, Pd@PFO ND and Pd@PFO ND crosslinked systems was evaluated in Suzuki test reactions and compared with a commercial Pd/C catalyst. Recyclability tests were also carried out to evaluate Pd retention and catalyst

reusability. Two additional catalysts, Pd@F8BT ND and crosslinked Pd@PFO ND, were synthesised, showing promising morphological and structural features that are expected to further stabilise Pd nanoparticles within the polymer matrix. Their investigation will contribute to expanding the applicability of these systems, as well as to the optimisation of reaction and recovery conditions for sustainable and reusable polymer-supported nanocatalysts.

6.5 Experimental

6.5.1 Materials and methods

All reagents are purchased from VWR, Sigma-Aldrich, Fluorochem, BLD pharm, TCI, Ambeed, Fisher Scientific, and ThermoFisher. Solvents – including anhydrous and NMR solvents – are purchased from Carlo Erba, Fisher Scientific, and Acros and used as received unless otherwise stated. Solvents packed under Ar and stored over molecular sieves having a >99,5% purity are always employed if a reaction requires inert conditions. If the synthetic protocol requires an inert atmosphere, solid reagents are always degassed using high vacuum (~0,02 mbar) and then refilling the reaction vessel with nitrogen (the procedure is repeated three times). Liquid or low-melting-point solids are degassed through a freeze-pump-thaw procedure using liquid nitrogen as a cooling agent. If degassed water is needed, distilled water is degassed at 100°C for 4h prior to use. Reactions are monitored using Xtra SIL G UV254 silica gel plates (pore size: 60 Å, thickness 200 μm) and a double-wave UV lamp (λ: 254 and 365 nm). When cited, the composition of solvent mixtures is always indicated as a volume/volume ratio. Melting points are measured employing a Büchi M-560 apparatus.

6.5.2 Characterization instruments and sample preparation

Solution Nuclear Magnetic Resonance (***NMR***) spectra are acquired with a Bruker Avance 400 NEO spectrometer and are used together with other characterization techniques (UV-vis and PL spectroscopy) to ensure the polymerization completion. ^{1}H and of known compounds are included after each synthetic procedure to provide the reader with its chemical shifts. ^{1}H and ^{13}C spectra of new materials are also included in *Chapter 6.5.5.3*

Gas chromatography–mass spectrometry (***GC–MS***) analyses are carried out using an Agilent 8860 gas chromatograph coupled with an Agilent 5977 mass selective detector (MSD). Helium is employed as the carrier gas, and the separation was achieved on an Agilent HP-5MS capillary column (30 m × 0.25 mm). The method is operated under the following conditions: inlet temperature 250 °C, ion source temperature 220 °C, initial oven temperature 100 °C, followed by a heating ramp of 20 °C·min^{-1} up to 300 °C, which is maintained for 5 minutes. Samples are prepared by dissolving the crude material in AcOEt at a concentration

of 1 mg·mL^{-1}. The resulting solutions are filtered through a cotton and silica layer to remove traces of water, catalysts, and inorganic salts. The purified solutions are then subjected to GC–MS analysis.

Absorbance (***ABS***) analysis in the UV-vis range are collected using a Jasco V-750 UV/Vis/NIR spectrophotometer equipped with a PbS detector and a dual-beam optical system. The instrument covers a spectral range from 190 to 2500 nm, using a deuterium lamp for the UV region (190–350 nm), a tungsten–halogen lamp for the visible region (350–800 nm), and a PbS photoconductive detector for the near-infrared region. The spectral resolution is set to $\Delta\lambda$ = 1 nm and the scanning speed to 400 nm·min^{-1}. All measurements are performed in two-face 1 cm path length quartz cuvettes. Background correction is performed using the spectrum of pure toluene as a reference. Baseline and absorbance of the samples are recorded in the range 200–800 nm. The sample is prepared by dissolving the analytes in toluene at concentrations of 0,3–0,1 mg·mL^{-1}, ensuring absorbance values within the linear range of the Beer–Lambert law (A < 1)

$$A = \varepsilon \cdot l \cdot c$$

where A is the absorbance, ε (M^{-1}·cm^{-1}) the molar absorption coefficient, l (cm) is the optical path, and c is the concentration (mol·L^{-1}). Data acquisition and preliminary processing are performed with Jasco Spectra Manager, while further analyses (λ_{max} determination) are carried out using OriginPro software.

Photoluminescence (***PL***) spectra of all samples are measured on a Jasco FP-6200 fluorescence spectrofluorimeter in a 90° geometry. The samples are excited with 385 nm output of the continuous xenon lamp (Xe900). The excitation slit width is set at 5 nm, the detection slit width is set at 5 nm, and the spectral resolution to $\Delta\lambda$ = 1 nm. The PL spectra are collected over a 395-600 nm spectral range with a scanning speed of 250 nm·min^{-1}. All measurements are performed in four-face 1 cm path length quartz cuvettes. The sample is prepared by dissolving the analytes in toluene at concentrations of 0,3–0,1 mg·mL^{-1}. Data acquisition and preliminary processing are performed with Jasco Spectra Manager, while further analyses (λ_{max} determination) are carried out using OriginPro software.

Both ABS and PL graphs are normalized between 0 and 1.

Thermogravimetric analyses (**TGA**) are carried out using a TGA/DSC 1 STARe System (Mettler Toledo) equipped with alumina crucibles. Approximately 5–10 mg of each sample are heated from 30 °C to 600/700 °C at a constant heating rate of 10 °C·min^{-1}, under a continuous gas flow of 50 mL·min^{-1}. Measurements are performed under a nitrogen atmosphere (to evaluate intrinsic thermal stability). Further analysis, e.g., thermogravimetric derivative (TGD) calculation and weight loss steps determination, are performed using OriginPro software.

Dynamic light scattering (***DLS***) analysis is performed on miniemulsions using Malvern instrument Nano-S, equipped with a laser (633 nm). The material selected for proper refractive index is polystyrene latex (1,59), and water is set as dispersant (refractive index = 1,33 at RT). Measurements are collected at three different temperatures: 25 °C (equilibration time: 30 seconds), 50 °C (equilibration time: 90 seconds), and 80 °C (equilibration time: 90 seconds), positioning the laser focus on the cuvette border to reduce the internal scattering effect. Analyses are performed on 1 mL of miniemulsion using four-face quartz cuvettes. Three consecutive measurements are performed on each sample (each measurement has 10 runs). When data meet quality criteria, such measurements are averaged to obtain the final intensity distribution. When only one population is observed, the cumulant fit value is used; the distribution fit is taken into consideration when more than one population are observed. Data acquisition and preliminary processing are performed with Zetasizer software, while further analysis are carried out using OriginPro software.

Scanning electron microscopy – energy dispersive X-ray spectroscopy (***SEM-EDS***) analysis are performed using Zeiss Gemini SEM 500. A 5 kV and 10 kV electron high tension (EHT) are respectively used for imaging and elemental analysis. Samples are prepared by placing the powder on a stub equipped with a graphite tape.

Transmission electron microscopy (***TEM***) is performed on a JEOL JEM-2100 Plus operated at an accelerating voltage of **200 kV**. The sample is prepared by drop-casting a droplet (~5–

10 µL) of the dispersion onto a carbon-coated copper TEM grid (300 mesh) and allowed to dry in air.

Inductively-coupled plasma – optical emission spectroscopy (ICP-OES) OPTIMA 7000 DV Perkin Elmer is used to detect Pd content on both Pd@C and Pd@PFO. Each sample is digested in Multiwave 5000 (Anton Paar) by adding nitric acid (HNO_3 65%) and hydrogen peroxide (H_2O_2 30%) 8:2 v/v. This process is performed in a closed system to reduce the contamination risk. The system is programmed to reach a power of 1000 W and a temperature of 220 °C. The vessel is kept at 220 °C for 30 minutes. Digested samples are diluted with 10 mL of MQ water. After centrifuging and diluting (1:2), the samples are ready to be analysed by ICP-OES. A certified standard reference material of Pd 1000 mg/L (Perkin Elmer) is used for calibration and quality control. The operating parameters of ICP-OES instrument are set up using the emission line at 340,458 nm in Axial View, and the sample solutions are measured in triplicate. The detection limit (DL) for Pd is 0,01 $mg \cdot L^{-1}$.

6.5.3 Surfactant library

Surfactants main characteristics are listed on the following pages to have a clearer picture of the main amphiphilic molecules involved in the project protocols. Non-ionic surfactants have been used for dispersion polymerizations.

Kolliphor EL (Cremophor EL)

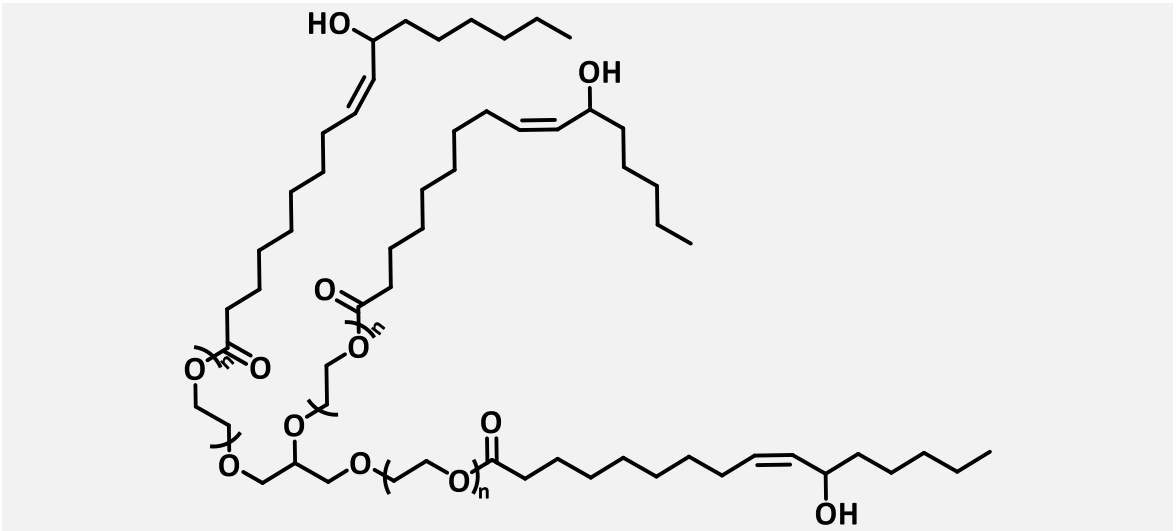

Average MW	~ 136,15 g·mol^{-1}
Composition	triricinoleate esters of ethoxylated glycerol and polyethylene glycol ricinoleate
CMC	~ 0,002 mM
Density	1,04 – 1,06 g·mL^{-1} (at ~37 °C)
Cloud point	65 °C
Aggregation number	-
HLB value	12 – 14

Span 80 (sorbitan monooleate)

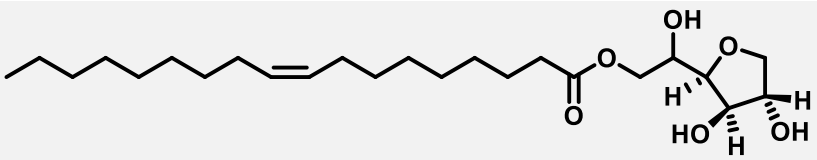

Average MW	~ 429 g·mol^{-1}
Composition	Sorbitan and oleic acid forming esters
CMC	~ 0,012 mM
Density	0,986 g·mL^{-1} (at 25 °C)
Cloud point	65 °C
Aggregation number	-
HLB value	~ 4,3

Triton X-100 (octylphenol ethoxylate)

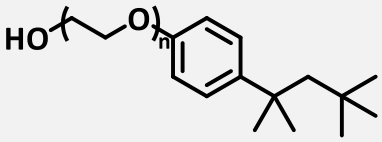

Average MW	~ 625 g·mol^{-1}
Composition	Alkylphenol ethoxylate
CMC	~ 0,22 – 0,24 mM
Density	1,07 g·mL^{-1} (at ~20 °C)
Cloud point	63 – 69 °C
Aggregation number	~ 140
HLB value	13,5

Tween-80 (polysorbate 80)

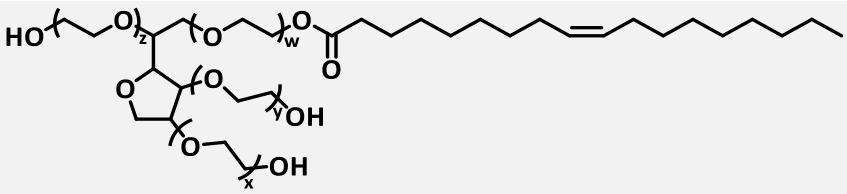

Average MW	~1310 g·mol-1
Composition	Oleic acid > 58.0% (balance primarily linoleic acid, palmitic, and stearic)
CMC	~ 0,01 – 0,02 mM
Density	~ 1,064 g·mL^{-1} (at ~20 °C)
Cloud point	65 °C
Aggregation number	50
HLB value	~ 15,0

DTAB (Dodecyltrimethylammonium bromide)

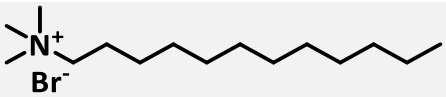

Average MW	308,41 g·mol^{-1}
Composition	Quaternary ammonium surfactant, single C12 tail
CMC	8,1mM
Density	1,0 g·mL^{-1}
Cloud point	-
Aggregation number	~ 50
HLB value	24,2

CTAB (Cetyltrimethylammonium bromide)

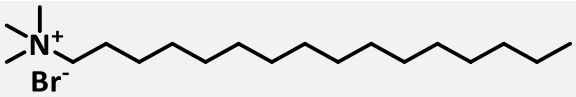

Average MW	346,45 g·mol^{-1}
Composition	Quaternary ammonium surfactant, 16-carbon tail
CMC	0,9 – 1,0 mM
Density	1,0 g·mL^{-1}
Cloud point	-
Aggregation number	~ 75 -120
HLB value	21,4

SDS (Sodium dodecyl sulphate)

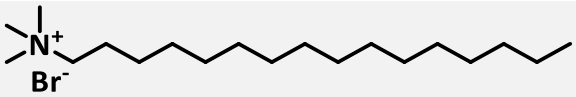

Average MW	288,38 g·mol^{-1}
Composition	Anionic surfactant, C12 tail, sulphate head
CMC	8,0 8,2 mM (at 25 °C)
Density	1,0 g·mL^{-1} at 25°C
Cloud point	-
Aggregation number	~ 72
HLB value	40

6.5.4 Synthetic procedures

6.5.4.1 Pd@PFO synthesis

*Dispersion synthesis of poly(9,9-dioctylfluorene) (**27a**)*

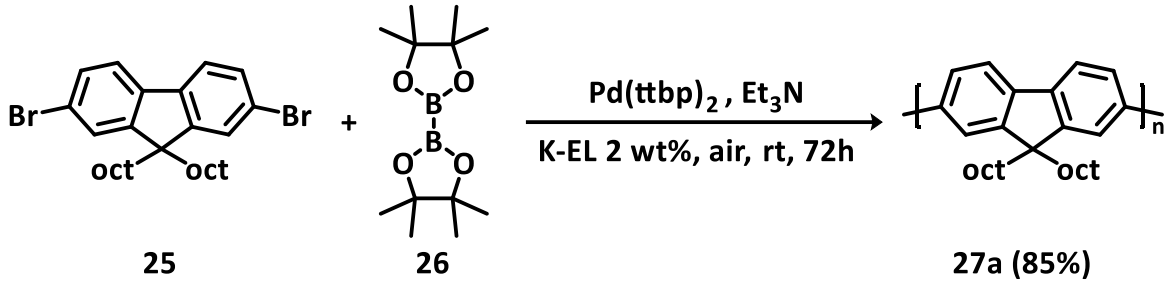

Scheme 6. 11 *Synthetic procedure for the obtainment of (**27a**)*

1096 mg of 9,9-dioctyl-2,7-dibromofluorene (**25**) (2 mmol, 1eq), 507 mg of bis(pinacolato)diboron (**26**) (2 mmol, 1 eq), and 20,4 mg of $Pd(ttbp)_2$ (0,04 mmol, 0,02 eq) are transferred into a screw cap tube and dissolved in 2 mL of K-EL 2 wt% aqueous solution, under magnetic stirring. After 10 minutes, 1,7 mL of Et_3N (12 mmol, 6 eq) are added to the reaction mixture, then the reaction vessel is sealed, and the reaction mixture is stirred for 72h at room temperature. The resulting yellow dispersion is filtered and washed with methanol (MeOH). The recovered powder is dried in a vacuum oven, then it is purified through Soxhlet extraction using 150 mL of EtOH, 150 mL of acetone, 150 mL of petroleum ether (PE), and 150 mL of DCM for the extraction of the longest chains. The solvent is removed under reduced pressure, and the final yellow powder is further dried to remove every solvent trace.

^{1}H NMR (400 MHz, $CDCl_3$) δ(ppm) 7.85 – 7.81 (m , 2H), 7.74 – 7.65 (m , 4H), 2.20 – 2.02 (br, 4H), 1.25 – 1.06 (m, 24H), 0.82 (t, J = 7.1, 6H)

*Hydrogenation procedure for Pd reduction on dispersed PFO (**Pd@PFO**)*

0,18 mL of hydrochloric acid are added to 2,1 mL of deionized water. The acidic solution is drop-by-drop added to 180 mg of $PdCl_2$ under magnetic stirring, then heated up for two hours to allow powder dissolution. The solution is cooled down, and 380 µL are transferred into a second two-neck 100 mL round-bottom flask containing 500 mg of sodium acetate

(NaOAc) dissolved in 7 mL of deionized water, 350 mg of Jeffsperse (5 wt%), and 350 mg of PFO. After the addition of the catalyst solution, the flask is placed in a water bath and stirred for 30 min at rt, then connected to a hydrogen/vacuum Schlenk line. The hydrogenation setup is composed by the following parts.

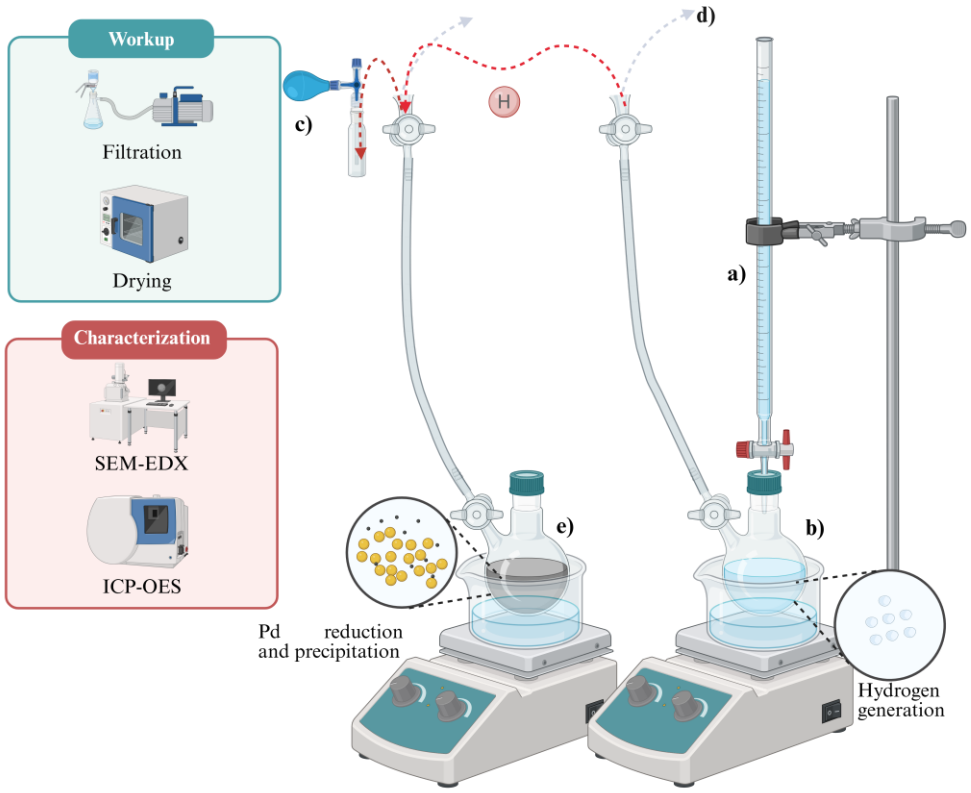

Figure 6. 34 *Visual representation of the laboratory hydrogenation setup used for the reduction of Pd^{2+} by in situ generated H_2 using $NaBH_4$/NaOH and AcOOH. The flask where H_2 is generated and the flask where the Pd is reduced are both connected to a Schlenk line, allowing the gas to fill the entire sealed system.*

a) a dropping funnel containing a 1M NaOH/$NaHB_4$ solution, prepared by dissolving 40 mg of NaOH in 200 mL of water, and then slowly adding 37,8 mg of $NaBH_4$ at 0 °C.

b) a two-neck round-bottom flask containing acetic acid (AcOOH) placed in a water bath

c) a balloon to be filled with H_2 for pressure balance, coupled with a release valve connected to the Schlenk line

d) a membrane pump to allow the evacuation of the environment

e) the Pd/PFO containing round-bottom flask

The system is evacuated and refilled with nitrogen in situ generated by slowly letting the While slowly letting the $NaOH/NaHB_4$ solution drop into the AcOOH-containing flask. The procedure is repeated three times, then the alkaline solution is drop-by-drop added to the AcOOH-containing flask until no drops are visible anymore. The reduction/precipitation process is immediate and highlighted by a change in colour (from yellow to grey). After two hours the dispersion is filtered and washed four times with water. The recovered green powder is dried in a vacuum dry oven and then characterized by SEM-EDS and ICP-OES analysis to investigate both the support morphology and Pd^0 content.

Pd leaching test

$Pd2^+$ species dispersion after Pd/PFO thermal treatment has been checked through ABS analysis in the UV-vis range, using 2mL of deionized water as baseline and $PdCl_2$ as reference standard.

a) Preparation of the $PdCl_2$ reference standard

6 mL of an aqueous DTAB 8 wt% solution is added to a vial containing 20 mg of $PdCl_2$. The mixture is stirred at 600 RPM at 50 °C until Pd complex complete dissolution. 0,1 mL of such solution is diluted with 2 mL of DTAB 8 wt% aqueous solution, and the ABS spectrum is registered and reported in the figure below. (**Graph 6.8**).

b) Sample preparation

Pd@PFO: 2 ml of an aqueous solution of DTAB 8 wt% is added to a vial containing 30 mg of Pd@PFO. The aqueous dispersion is stirred for 3 hours at 80 °C, then it is cooled down and filtered using a 0.45 μm filter to remove the powder. 0.1 mL of such aqueous dispersion is diluted with 2 mL of DTAB 8%wt aqueous solution, and the ABS spectrum is registered and reported in the figure below (**Graph 6.8**).

Pd/C: 2 ml of an aqueous solution of DTAB 8 wt% is added to a vial containing 30 mg of commercial Pd/C. The aqueous dispersion is stirred for 3 hours at 80 °C, then it is cooled down and filtered using a 0.45 μm filter to remove the powder. 0.1 mL of such aqueous

dispersion is diluted with 2 mL of DTAB 8%wt aqueous solution, and the ABS spectrum is registered and reported in the figure below (**Graph 6.8**).

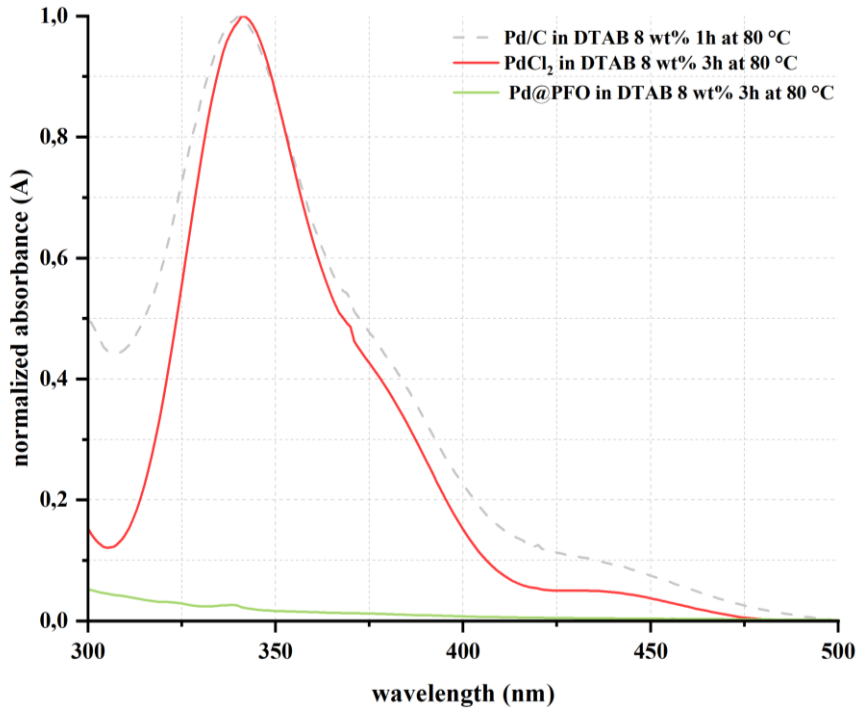

Graph 6. 8 *ABS spectra of $PdCl_2$ (grey dotted line) and Pd@PFO (green line) and commercial Pd/C dispersed using DTAB 8 wt% and stirred 3h at 80 °C; the spectra are registered using water as solvent*

6.5.4.2 Pd@PFO ND synthesis

Miniemulsion fine-tuning

Optimization of the miniemulsion morphology is achieved through a fine-tuning process. The surfactants are always dissolved in the oil phase; neither catalyst nor reagents are involved in these protocols. Toluene is selected as an organic water-immiscible solvent for its compatibility with both PFO and common aryl reactants. Tween 80, Kolliphor EL, Triton X-100 and Span 80 are combined and used as stabilizers of the organic phase droplets. Their weight is calculated using the *Equation 6.1*

$$(6.1) \quad wt\%_{\,surfactant} \times V_{water}\,(L) = m_{\,surfactant}\,(mg)$$

Two miniemulsification methods are used: SE and EPI; droplets dimension refinement was achieved using an ultrasound bath or ultrasound homogenization

entry	surfactants	wt %	method	d (nm)	PdI
1	T-80	0,5%	SEa	-	-
2	T-80	1%	SEa	-	-
3	T-80	1%	EPI	222,0	0,2
4	T-80,K-EL 1:1	1%	SEa	-	-
5	T-80,K-EL,T X-100 1:1:1	2%	SE	105,5	0,5
6	T-80,K-EL,T X-100 1:1:1	2%	SEa	88,5	0,5
7	T-80,K-EL,T X-100 1:1:1	2%	EPI	68,4	0,5
8	T-80,K-EL,T X-100 1:1:1	2%	SEb	99,4	0,3
9	T-80,K-EL,T X-100 1:1:1	2%	SEc	182,9	0,6
10	T-80,K-EL,T X-100 1:1:1	1%	SE[b]	204,2	0,3
11	T-80,K-EL,T X-100 1:1:1	3%	SE[b]	159,4	0,4
12	T-80,K-EL,T X-100 1:1:1	1%	EPI	165,1	0,2
13	T-80,K-EL,S-80 1:1:1	1%	EPI	194,5	0,2

Table 6. 8 *DLS droplets dimensions and dispersity data referred to miniemulsions obtained with different surfactant mixtures dissolved in the oil phase. All ratios are indicated as w/w. The symbol "-" is used when de-mixing occurs; a) no drop-by-drop addition; b) refinement of droplet dimensions via 1,5 minutes ultrasonication; c) refinement of droplet dimensions via 3 minutes homogenization using a turbo-emulsifier.*

Spontaneous Emulsification protocol 1: surfactants are dissolved in 1 mL of toluene, then the oil phase is drop-by-drop added to 19 mL of neat water under vigorous magnetic stirring (1100 rpm). Droplet dimensions are refined with a 30-minute ultrasonic bath step and controlled using DLS.

Spontaneous Emulsification protocol 2: surfactants are dissolved in 1 mL of toluene, then the oil phase is drop-by-drop added to 19 mL of neat water while immersion ultrasonicating using Hielscher UP200St ultrasound homogenizer for 3 min and controlled using DLS.

Inverse Phase emulsification protocol: surfactants are dissolved in 1 mL of toluene, then 19 mL of neat water are added to the oil phase under vigorous magnetic stirring (1100 rpm).

Droplet dimensions are refined with a 30-minute ultrasonic bath step and controlled using DLS.

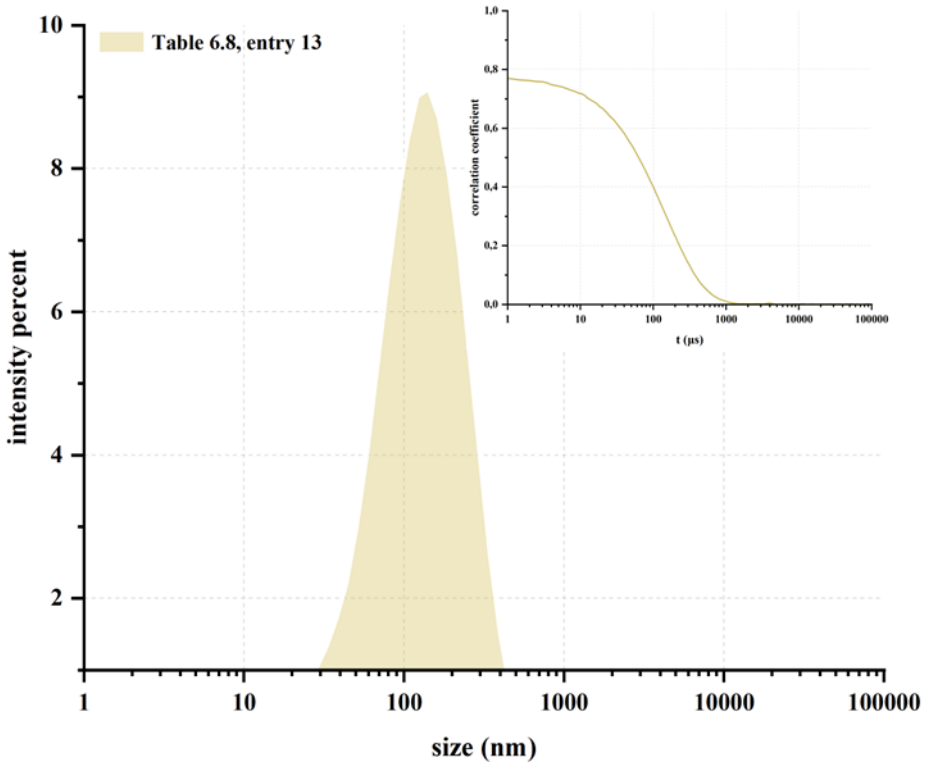

Graph 6. 9 *Representative DLS measurement and correlograms of nano-emulsion obtained using T-80,K-EL,T X-100 1:1:1 1 wt% surfactant mixture. Data are related to test 13*

General procedure for one-pot miniemulsion polymerization and synthesis of Pd@PFO ND ***(27b)***

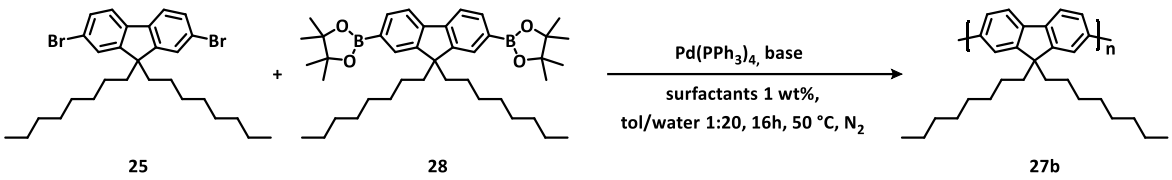

Scheme 6. 12 *Synthetic protocol for the obtainment of Pd@PFO ND; the synthesis only shows the chemical structure of the support of the catalyst; however, the final material must be intended as a core-shell structure whose core is formed by PFO and shell by surfactants, forming a semi-IPN. Pd NP are trapped inside these nanostructured spheres.*

Here, the general procedure for the synthesis of Pd@PFO ND is reported. The various attempts differ for the use of an organic or inorganic base and the synergic role of the phase

transfer agent Aliquat HTA-1. The details regarding each procedure are contained in ***Table 6.9****.*

Entry	Base	Surfactants	Phase-transfer agent
1	NaOH[a]	T80, K-EL, T X-100 1:1:1, 1 wt%	-
2	Et_3N[b]	T80, K-EL, T X-100 1:1:1, 1 wt%	Aliquat HTA-1[c]
3	NaOH[a]	T80, K-EL, T X-100 1:1:1, 1 wt%	Aliquat-HTA-1[c]

Table 6. 9 *Different bases and formulation conditions used for the optimization of the synthesis of Pd@PFO ND; a) NaOH is degassed and dissolved in 1mL of degassed water, then added as a solution to the reaction vessel; b) Et3N is degassed through freeze pump thaw and added without the addition of any solvent to the reaction vessel; c) when present, Aliquat HTA-1 is added to the reaction vessel right before the addition of the water phase.*

120,6 mg 9,9-dioctyl-2,7-dibromofluorene (**25**) (0,22 mmol, 1 eq) and 141,36 mg of 9,9-dioctyl-9H-fluorene-2,7-diboronic acid bis(pinacol) ester (**26**) (0,22 mmol, 1 eq) are dissolved together with 200 mg (in total) of surfactants (**Table 6.9**, **entry 1, 2, 3**) using the minimum THF quantity in a 100 mL two-neck round-bottom flask. The solvent is removed by evaporation using a rotavapor. The reagents and surfactants slurry-containing flask is connected to the Schlenk line, evacuated, and refilled with N_2 three times. The base is degassed in a second 25 mL two-neck round-bottom flask. One mL of a $Pd(PPh_3)_4$ toluene solution (0,012 mmol, 0,054 eq), prepared in a glovebox, is added to the flask containing both reagents and surfactants. 19 mL of deionised water is drop-by-drop added to the oil phase under vigorous magnetic stirring (1100 RPM) (**EPI**), keeping the temperature of both phases at 50 °C. After the addition, a 30-minute ultrasonication bath step allows for colloidal dimension refinement. Finally, the base (0,9 mmol, 4 eq) (**Table 6.9**, **entries a, b, c**) is added. The reaction mixture is kept under magnetic stirring for 24 hours at 50 °C, then it is cooled down to room temperature and characterised through ABS, PL, DLS, and ^{1}H NMR. If the polymer synthesis is successful, the reaction vessel septum is removed, and the reaction mixture is stirred for 5 hours to remove toluene. The colloidal dimensions are further checked through DLS at the end of the evaporation process. The dispersion is then dialysed through ultracentrifugation (4500 rpm, RT), using a Sigma 3- 16PK laboratory centrifuge, to remove the salts from the reaction mixture, washed with deionised water, then redispersed in the same amount of neat water and sonicated with an ultrasound bath for 30 minutes. The purified dispersion is characterised through DLS and SEM analysis.

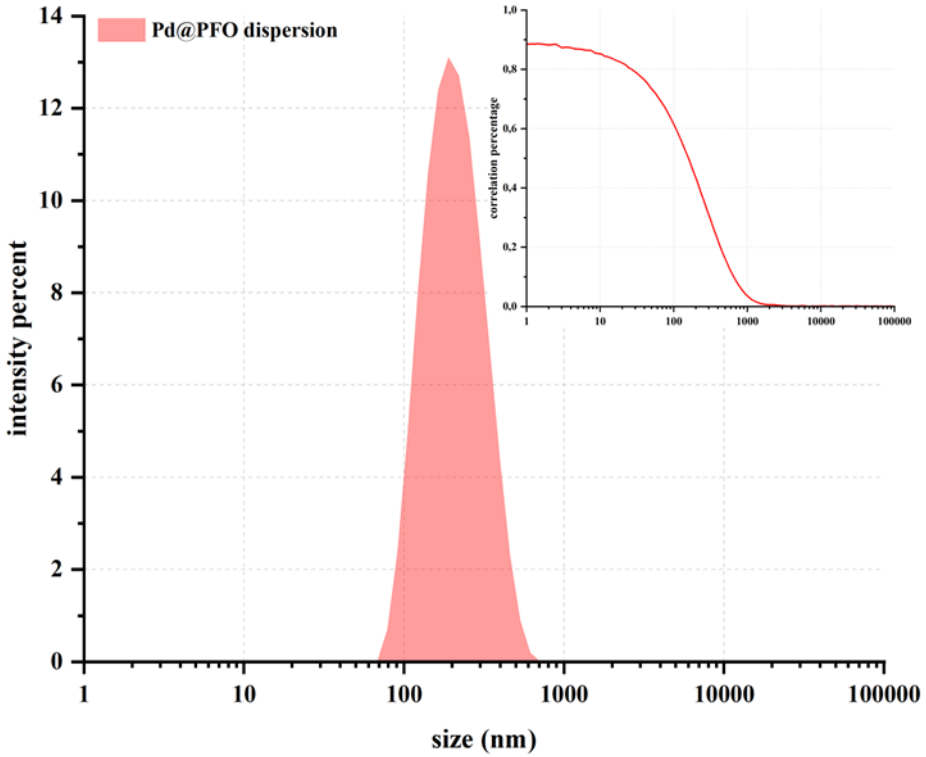

Graph 6. 10 *Representative DLS measurement and correlogram of Pd@PFO post evaporation of the solvent*

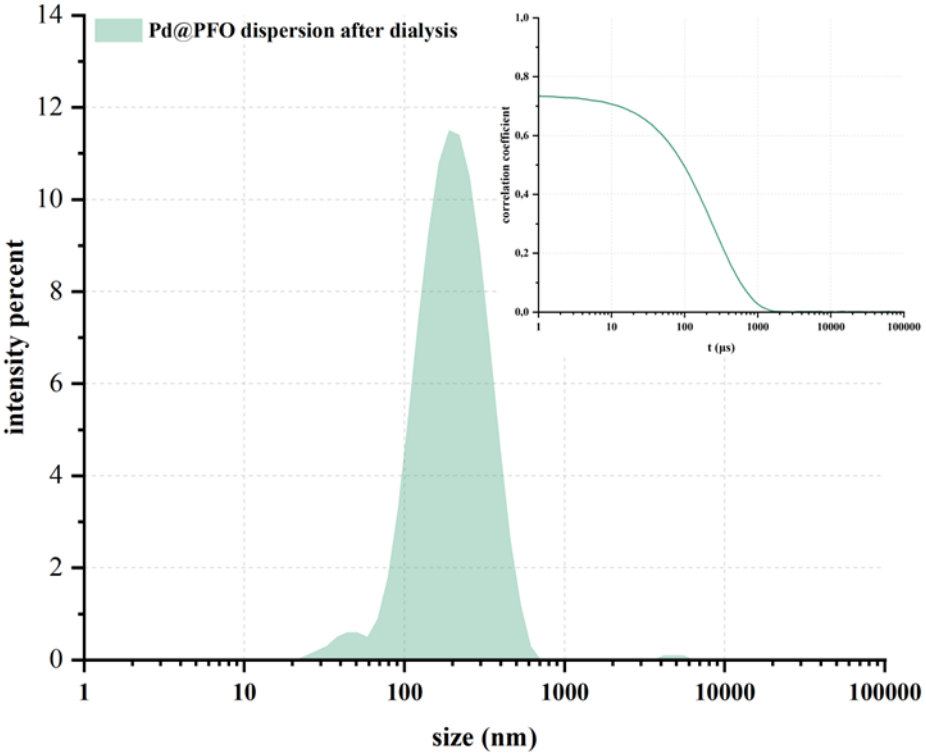

Graph 6. 11 *Representative DLS measurement and correlogram of Pd@PFO post dialysis*

6.5.4.3 Generality of the ND synthetic procedure

The synthetic protocol for the synthesis of the polymeric nano dispersions is applied to different polymer syntheses to test the generality of the protocol. F8BT and crosslinked PFO ND synthesis are herein described.

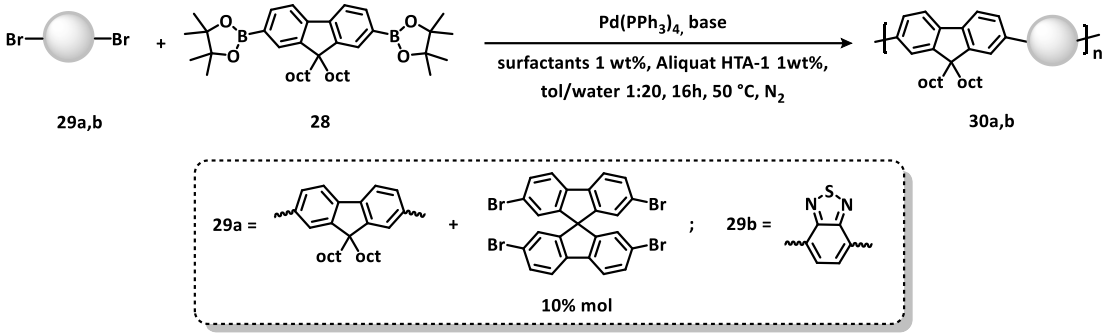

Scheme 6. 13 *General reaction scheme for the synthesis of Pd@polymer ND (30a,b) using miniemulsion polymerization optimized protocol*

General miniemulsion polymerization protocol

Aryldibromide (**29a,b**) (1 eq) and 9,9-dioctyl-9H-fluorene-2,7-diboronic acid bis(pinacol) ester (**26**) (1 eq) are dissolved together with 200 mg of surfactants using the minimum THF quantity in a 100 mL two-neck round-bottom flask. The solvent is removed by evaporation using a rotavapor. The reagents and surfactants slurry-containing flask is connected to the Schlenk line, evacuated, and refilled with N_2 three times. NaOH is degassed in a second 25 mL two-neck round-bottom flask. 1 mL of a $Pd(PPh_3)_4$ toluene solution (0,054 eq), prepared in a glovebox, is added to the flask containing both reagents and surfactants. 19 mL of deionized water is drop-by-drop added to the oil phase under vigorous magnetic stirring (1100 RPM) (**EPI**), keeping the temperature of both phases at 50 °C. After the addition, a 30-minute ultrasonication bath step allows for colloidal dimension refinement. Finally, the base (4 eq) is added. The reaction mixture is kept under magnetic stirring for 24 hours at 50 °C, then it is cooled down to room temperature. The reaction mixture is stirred for 5 hours to remove toluene. The dispersion is then dialysed through ultracentrifugation (4500 rpm, RT), washed with deionised water, then redispersed in the same amount of neat water and sonicated with an ultrasound bath for 30 minutes.

Analytical data

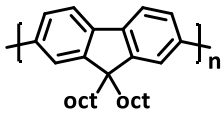

30a

Poly(9,9-dioctyl-9H-fluorene) crosslinked with 10% mol spirobifluorene (**30a**): polymer **30a** is obtained following the general procedure, on a 0,22 mmol scale with the following modifications: 0,1 eq of 2,2,7,7-tetrabromospirobifluorene are added together with the dibromide and the diboronic ester partner in the oil phase.

^{1}H NMR (400 MHz, $CDCl_3$) δ(ppm) 7.85 – 7.81 (m , aromatic protons of fluorene units), 7.74 – 7.65 (m , aromatic protons of fluorene units), 2.20 – 2.02 (br, CH_2 adjacent to fluorene core), 1.25 – 1.06 (m, CH_2 of alkyl side chains), 0.82 (t, J = 7.1, CH_3, terminal methyl groups)

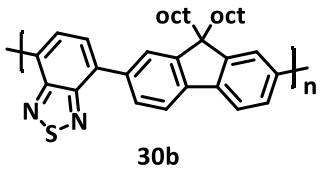

30b

Poly(9,9-dioctylfluorene-alt-benzothiadiazole) (**30b**): polymer **30b** is obtained following the general procedure, on a 0,22 mmol scale with the following modifications: the oil phase is stirred at 60 °C for 15 minutes to allow reagent solubilization before adding the water.

^{1}H NMR (400 MHz, $CDCl_3$) δ(ppm) 8.15–7.90 (m, aromatic protons of benzothiadiazole), 7.85–7.60 (m, aromatic protons of fluorene units), 2.05–1.90 (m, CH_2 adjacent to fluorene core), 1.30–1.10 (m, CH_2 of alkyl side chains), 0.85 (t, CH_3, terminal methyl groups).

6.5.5 Material characterization

6.5.5.1 Optical characterizations

Herein are reported the absorbance and photoluminescence spectra of compounds **27a**, **27b**, **30a**, and **30b**.

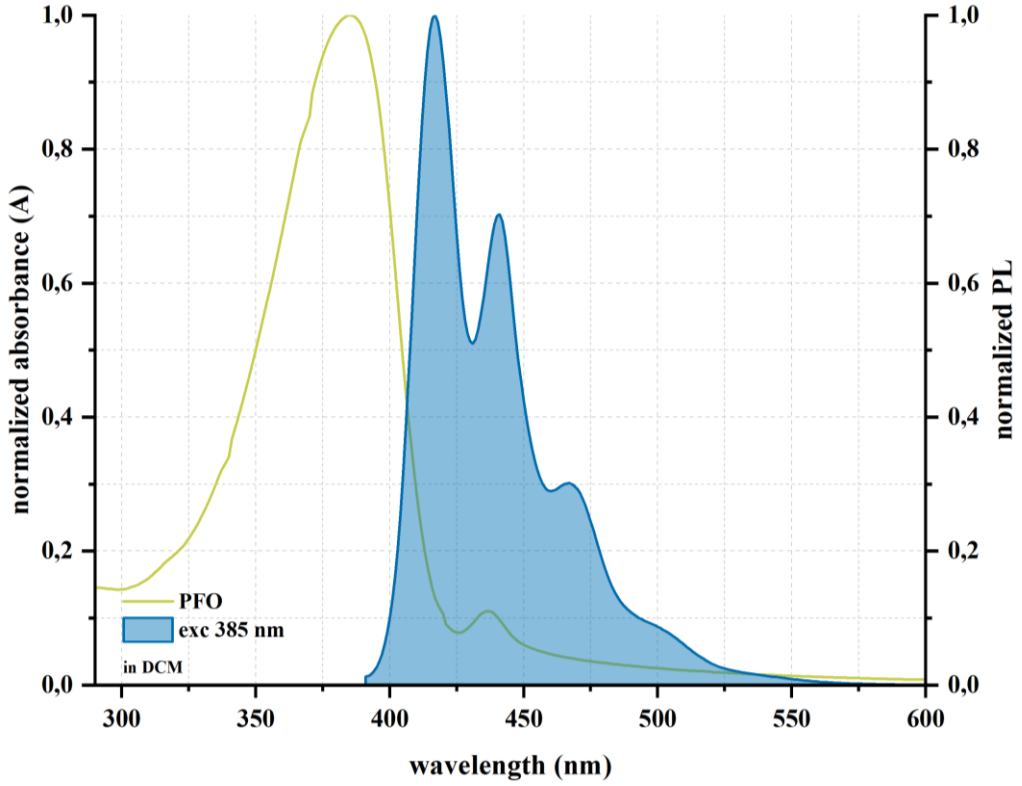

Graph 6. 12 *Comparison between normalized ABS (yellow line) and PL (blue areas) spectra (using DCM as solvent) of compound 27a. Excitation wavelength is set at 385 nm*

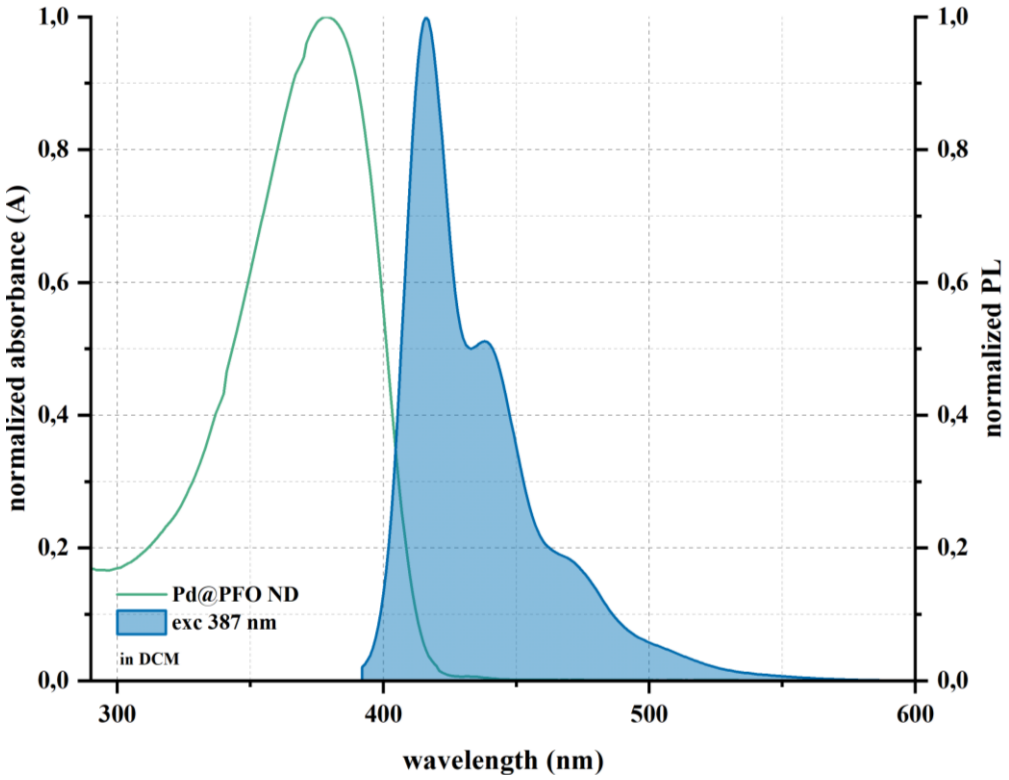

Graph 6. 13 *Comparison between normalized ABS (green line) and PL (blue area) spectra (using DCM as solvent) of compound* ***27b****. Excitation wavelength is set at 387 nm*

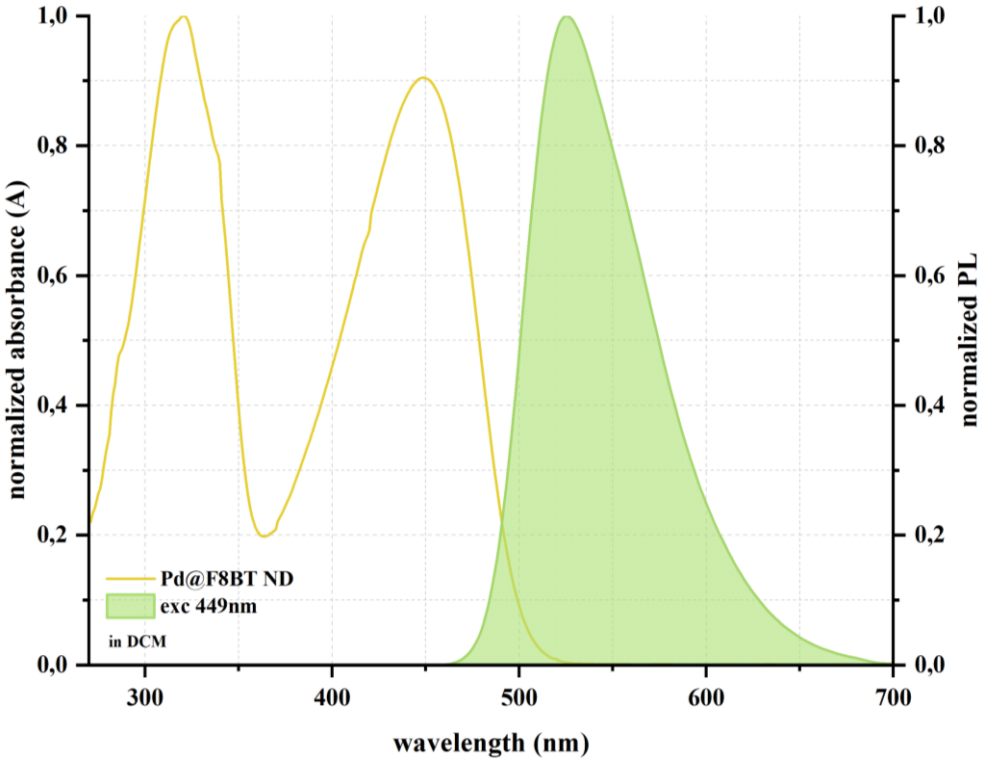

Graph 6. 14 *Comparison between normalized ABS (yellow line) and PL (green area) spectra (using DCM as solvent) of compound* ***30b****. Excitation wavelength is set at 449 nm*

6.5.5.2 Thermogravimetric analysis (TGA)

Herein are reported the TGA curves (continuous lines) and the thermogravimetric derivatives (TGD) (dotted lines) of PFO (**27a**), Pd@PFO, Pd@PFO ND (**27b**), Pd@PFO ND crosslinked (**30a**), F8BT (previously synthesized in the research group with a dispersion polymerization technique), and Pd@F8BT (**30b**) to investigate the effect of the different polymerization techniques as well as the presence of Pd^0 NPs influence on the material thermal degradation path.

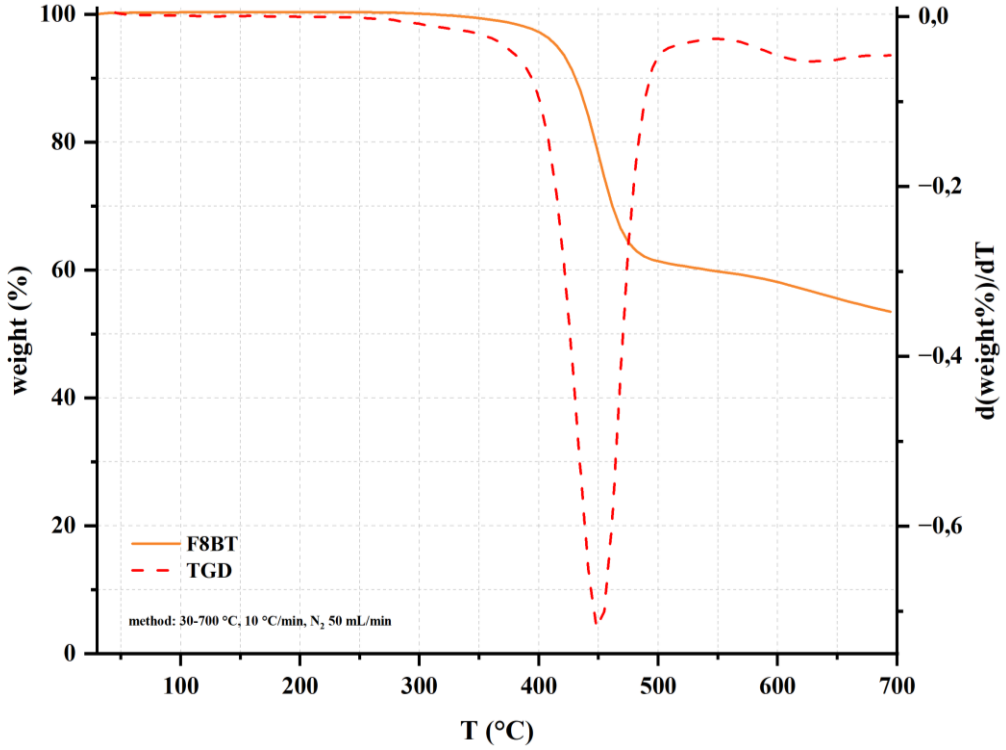

Graph 6. 15 *TGA curve and TGD of F8BT performed under nitrogen*

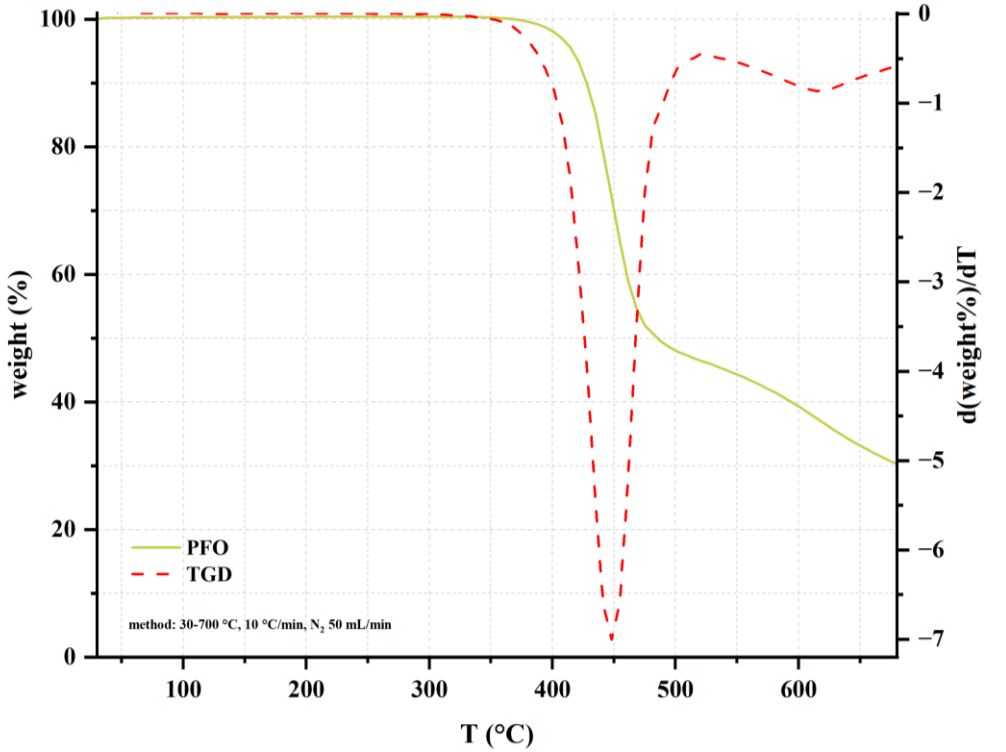

Graph 6. 16 *TGA curve and TGD of PFO (**27a**) performed under nitrogen*

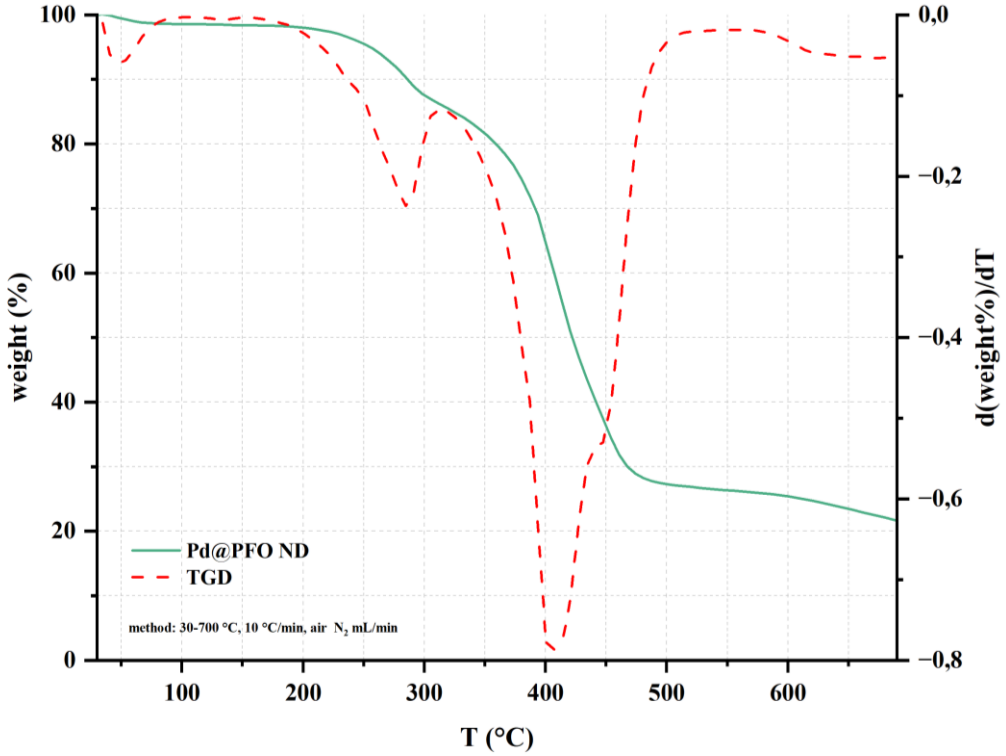

Graph 6. 17 *TGA curve and TGD of Pd@PFO ND (**27b**) performed under nitrogen*

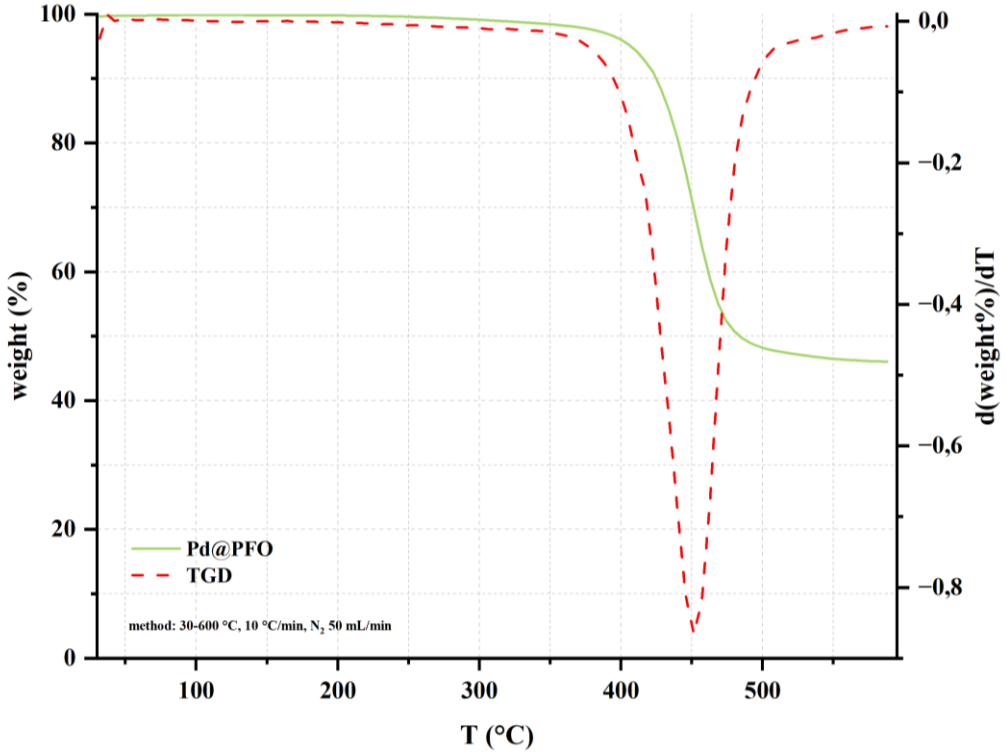

Graph 6. 18 *TGA curve and TGD of Pd@PFO performed under nitrogen*

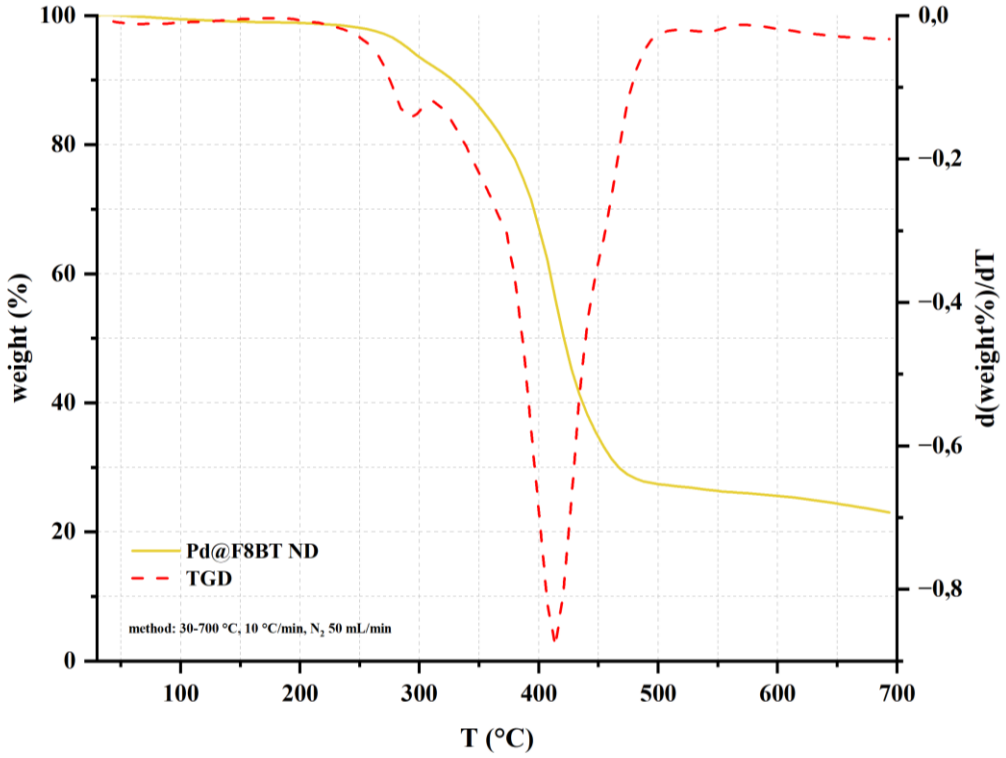

Graph 6. 19 *TGA curve and TGD of Pd@F8BT ND (**30b**) performed under nitrogen*

6.5.5.3 ^{1}H NMR spectra

The ^{1}H NMR spectra of compounds **27a**, **27b**, **30a**, **F8BT ,** and **30b** are reported below. The purpose of this section is not to present the spectra of newly synthesized compounds, but rather to highlight the differences between the NMR spectra of polymers synthesized via dispersion polymerization and those obtained through miniemulsion polymerization (conducted at concentrations below the MAC to control the material morphology during synthesis).

Due to their heterogeneity, nano dispersion spectra are not subject to pick peaking or integration; however, the signals corresponding to the surfactant hydrogens as well as the ones associated to the alkyl chains of the polymeric structures, are represented as green lines, whereas the peaks associated with the aromatic portion of the polymers are highlighted in red**.**

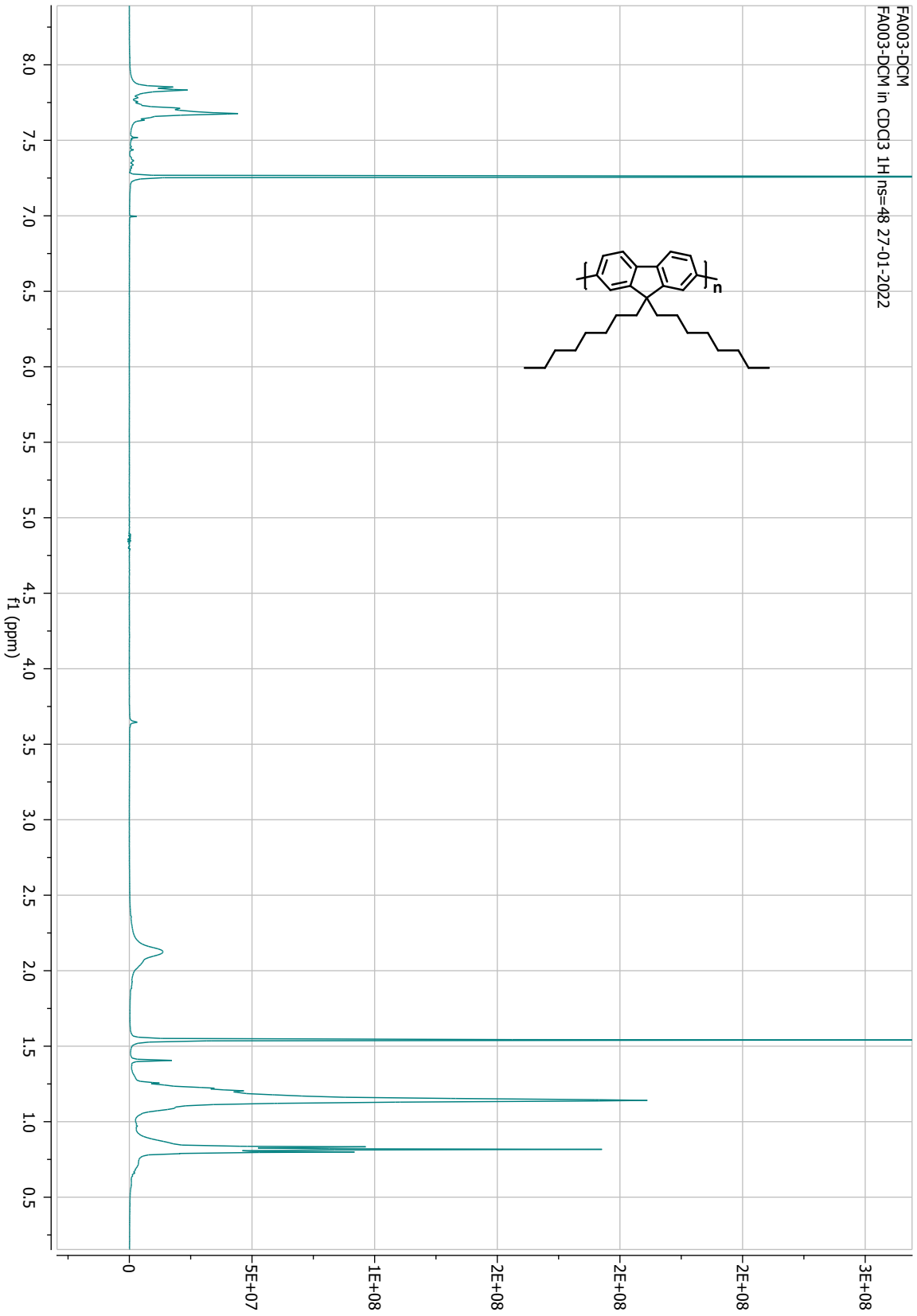

Figure 6. 35 *^{1}H NMR spectrum in $CDCl_3$ of compound (**27a**)*

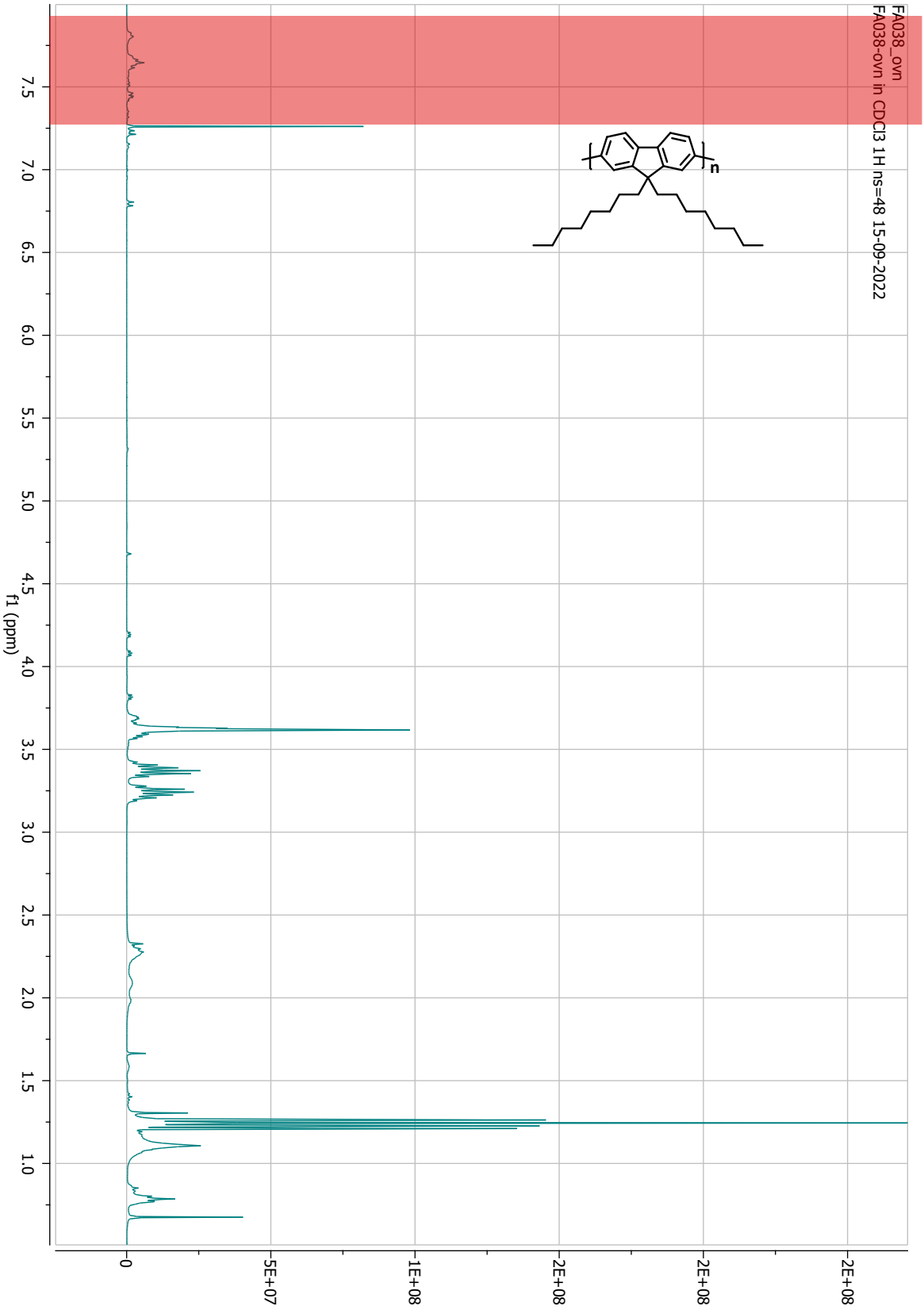

Figure 6. 36 *^{1}H NMR spectrum in $CDCl_3$ of compound (**27b**)*

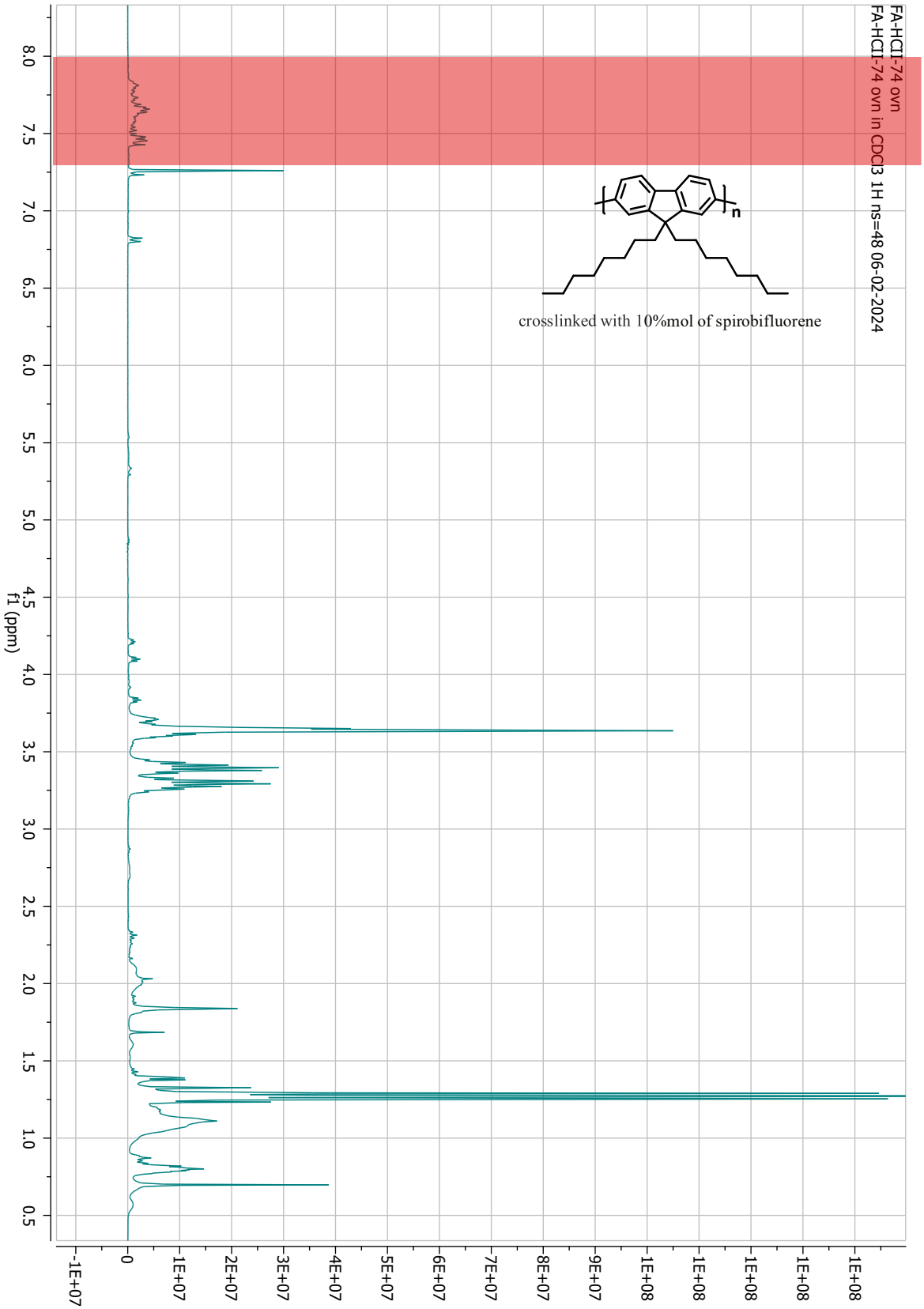

Figure 6. 37 *^{1}H NMR spectrum in $CDCl_3$ of compound (**30a**)*

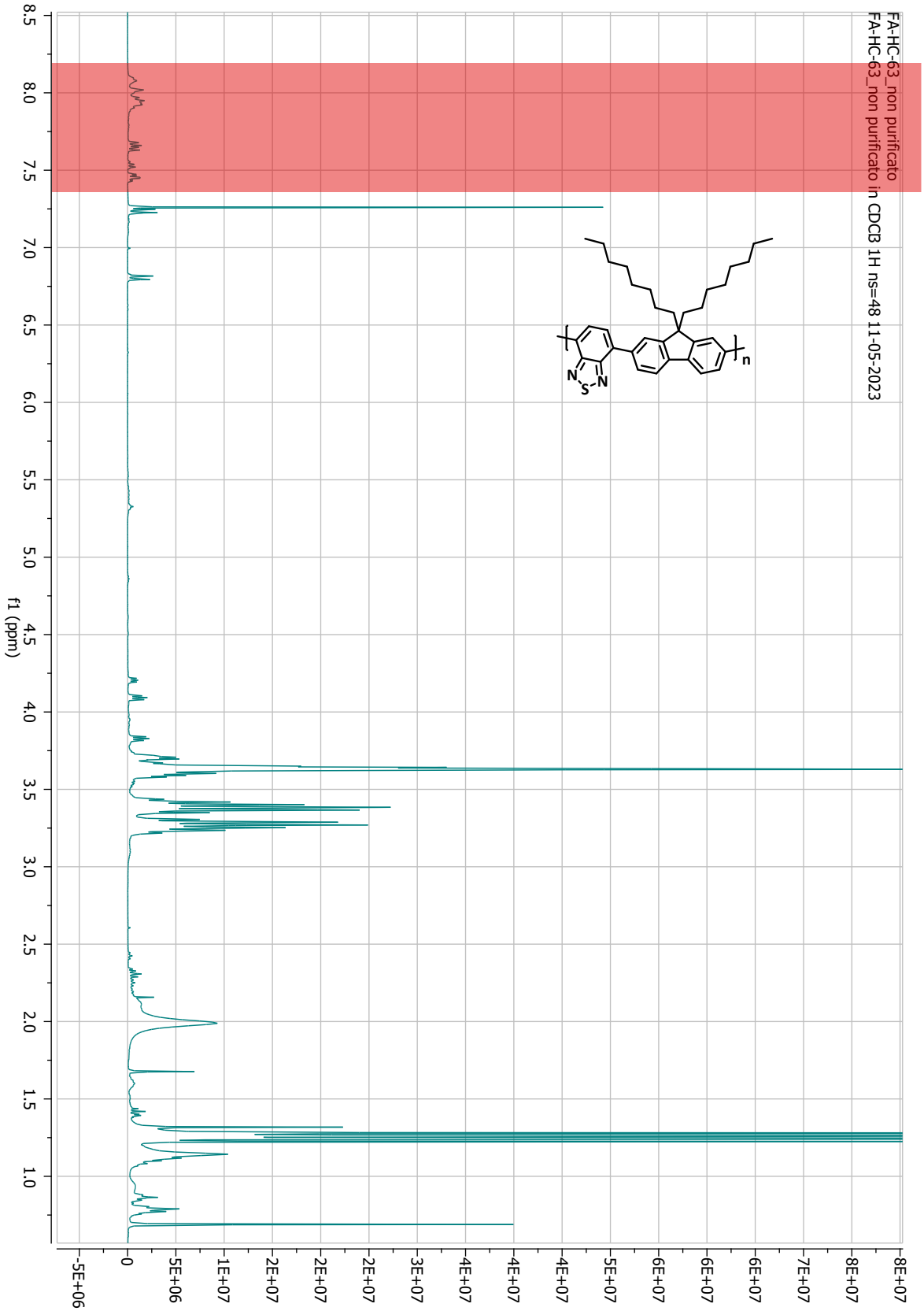

Figure 6. 38 *^{1}H NMR spectrum in $CDCl_3$ of compound (**30b**)*

6.5.6 Generality of the catalyst

6.5.6.1 Experimental procedure

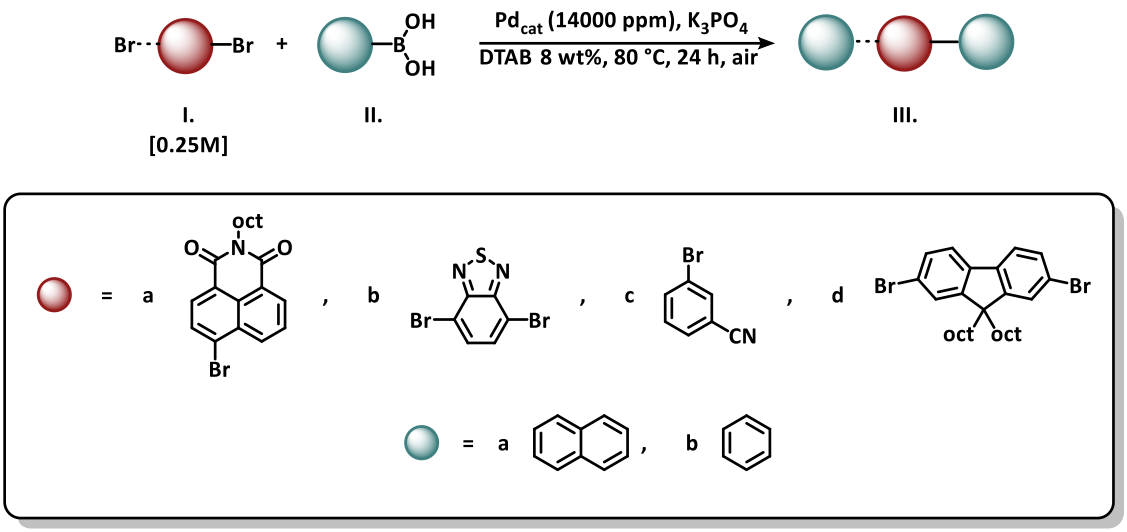

Scheme 6. 14 *general procedure for a Suzuki cross- coupling reaction*

Reagents having one -Br atom (1)

In a general procedure 1 eq of bromide (I.a,c) and 1.5 eq of boronic acid (II.a) are weighted in a microwave (MW) reaction vial and dispersed in a DTAB 8% aqueous solution. The reaction mixture is stirred for 10 minutes at 500 RPM in order to allow proper dispersion. Pd@PFO is added to the reaction mixture under stirring. After 10 minutes, 1,75 eq of K_3PO_4 are transferred into the vial, then the vessel is sealed and kept under vigorous stirring for 24 hours at 80 °C. The reaction evolution is monitored through TLC. The crude reaction product was analysed through ^{1}H NMR or GC-MS, then it was purified following an optimized procedure. The liquid was separated from the solid paste through a filtration step. The solid paste was then taken up with neat water to remove surfactants. After a second filtration step the powder is taken up with AcOEt and filtered to remove the insoluble catalyst. If possible and if present, product was separated from unreacted bromide after a recrystallization step using EtOH.

Reagents having two -Br atom (2)

In a general procedure 1 eq of bromide (I.b,d) and 3 eq of boronic acid (II.a,b) are weighted in a microwave (MW) reaction vial and dispersed in a DTAB 8% aqueous solution. The

reaction mixture is stirred for 10 minutes at 500 RPM in order to allow proper dispersion. Pd@PFO is added to the reaction mixture under stirring. After 10 minutes, 3,5 eq of K_3PO_4 are transferred into the vial, then the vessel is sealed and kept under vigorous stirring for 24 hours at 80 °C. The reaction evolution is monitored through TLC. The crude reaction product was analysed through ^{1}H NMR or GC-MS, then it was purified following an optimized procedure. The liquid was separated from the solid paste through a filtration step. The solid paste was then taken up with neat water to remove surfactants. After a second filtration step the powder is taken up with AcOEt and filtered to remove the insoluble catalyst. If possible and if present, product was separated from unreacted bromide after a recrystallization step using EtOH.

Note: if a dispersion is used, the catalyst isolation is achieved through crude dispersion in AcOEt and a centrifugation step (11000 RPM, 10 minutes, 5 °C). The supernatant is further purified and the precipitate is dried and re-dispersed in clean distilled water.

6.5.6.2 Analytical data

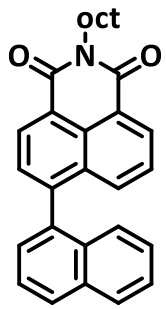

N-octyl-4-(naphthalen-1-yl)naphthalene-1,8-dicarboximide was synthetised according to general procedure (**1**) on a 0,5 mmol scale. The crude product is recrystalised from EtOH to yield a yellow powder (97%)

^{1}H NMR (400 MHz, CDCl3) δ (ppm): 8.72 (d, J = 7.4, 1H), 8.62 (dd, J2 = 1.2, J1 = 7.3, 1H), 7.99 (q, J = 8.3, 2H), 7.77 – 7.75 (m, 2H), 7.63 (dd, J2 = 7.1, J1 = 8.25, 1H), 7.56 (m , 1H), 7.54 – 7.47 (m, 2H), 7.36 – 7.29 (m, 2H), 4.23 (t, J = 7.6, 2H), 1.82 – 1.73 (m, 2H), 1.50 – 1.24 (m, 10 H), 0.89 (t, J = 7.0, 3H)

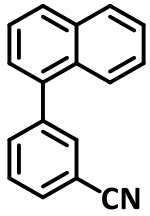

3-(1-Naphthalenyl)benzonitrile was synthetised according to general procedure (**1**) on a 0,5 mmol scale. The crude product is recrystalised from MeOH to yield a white powder (98%)

^{1}H NMR (400 MHz, $CDCl_3$) δ (ppm): 7-95-7.91 (t, J = 7.7, 2H), 7.80 (t, J = 1.6, 1H), 7.76-7.72 (m, 3H), 7.63-7.59 (t, J = 7.7, 1H), 7.57-7.51 (m, 2H), 7-50-7.46 (td, J = 7.6, J2=1.5, 1H), 7.40-7.38 (dd, J1 = 7.1, J2=1.1, 1H).

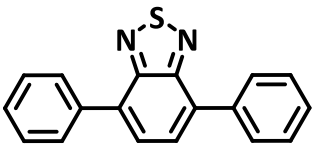

4,7-Diphenyl-2,1,3-benzothiadiazole was synthesized according to the general procedure (**2**) on a 0,5 mmol scale. The crude product is recrystalised from EtOH to yield a yellow powder (98%)

^{1}H NMR (400 MHz, $CDCl_3$) δ (ppm): 7.47 (t, J = 7.2, 2H), 7.56 (t, J = 7.2, 4H), 7.80 (s, 2H), 7.97 (d, J = 7.2, 4H).

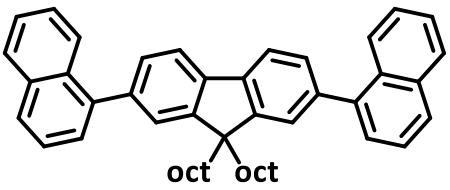

9*H*-Fluorene, 2,7-di-1-naphthalenyl-9,9-dioctyl was synthesized according to the general procedure (**2**) on a 0,5 mmol scale (98%)

^{1}H NMR (400 MHz, $CDCl_3$) δ (ppm): 7.98 (d, J=8,6, 2H), 7.95 (d, J=8,0, 2H), 7.92-7.86 (m, 4H), 7.60-7.50 (m, 10H), 7.48-7-43 (m, 2H), 2.06-1.99 (m, 4H), 1.25-1.02 (m, 24H), 0.86-0.78 (t, J=7.1, 6H).

Bibliography

161. Ceriani, C. *et al.* Micellar catalysis beyond the hydrophobic effect: Efficient palladium catalyzed Suzuki-Miyaura coupling of water and organic solvent insoluble pigments with food grade surfactants. *J. Organomet. Chem.* **962**, 122267 (2022).

162. Sanzone, A. *et al.* Suzuki–Miyaura Micellar One-Pot Synthesis of Symmetrical and Unsymmetrical 4,7-Diaryl-5,6-difluoro-2,1,3-benzothiadiazole Luminescent Derivatives in Water and under Air. *J. Org. Chem.* **83**, 15029–15042 (2018).

163. Sanzone, A. *et al.* Synthesis of Conjugated Polymers by Sustainable Suzuki Polycondensation in Water and under Aerobic Conditions. *ACS Macro Lett.* **9**, 1167–1171 (2020).

164. Sanzone, A. *et al.* Efficient synthesis of organic semiconductors by Suzuki–Miyaura coupling in an aromatic micellar medium. *Green Chem.* **21**, 4400–4405 (2019).

165. Ceriani, C., Ghiglietti, E., Sassi, M., Mattiello, S. & Beverina, L. Taming troublesome suzuki-miyaura reactions in water solution of surfactants by the use of lecithin: A step beyond the micellar model. *Org. Process Res. Dev.* **24**, 2604–2610 (2020).

166. Mattiello, S. *et al.* Sustainable access to π-conjugated molecular building blocks via phosphine-free, ppm palladium level Suzuki-Miyaura reaction in water. *Catal. Today* **442**, 114893 (2024).

167. Li, C. J. & Trost, B. M. Green chemistry for chemical synthesis. *Proc. Natl. Acad. Sci. U. S. A.* **105**, 13197–13202 (2008).

168. Zimmerman, J. B., Anastas, P. T., Erythropel, H. C. & Leitner, W. Designing for a green chemistry future. *Science* **367**, 13197–13202 (2008).

169. Sheldon, R. A. The E Factor: fifteen years on. *Green Chem.* **9**, 1273–1283 (2007).

170. Trost, B. M. On Inventing Reactions for Atom Economy. *Acc. Chem. Res.* **35**, 695–705 (2002).

171. Tuck, C. O., Pérez, E., Horváth, I. T., Sheldon, R. A. & Poliakoff, M. Valorization of Biomass: Deriving More Value from Waste. *Science* **337**, 695–699 (2012).

172. Nanda, B., Sailaja, M., Mohapatra, P., Pradhan, R. K. & Nanda, B. B. Green solvents: A suitable alternative for sustainable chemistry. in *Materials Today: Proceedings* vol. 47 1234–1240 (Elsevier Ltd, 2021).

173. Cortes-Clerget, M. *et al.* Water as the reaction medium in organic chemistry: From our worst enemy to our best friend. *Chem. Sci.* **12**, 4237–4266 (2021).

174. Simon, M. O. & Li, C. J. Green chemistry oriented organic synthesis in water. *Chem. Soc. Rev.* **41**, 1415–1427 (2012).

175. Tanford, C., Breslow, R. & Symp ; Rideout, D. The Hydrophobic Effect. *Adv. Enzymol. Relat. Areas Mol. Biol.* **110**, 22 (1980).

176. Romsted, L. S. *Surfactant Science and Technology: Retrospects and Prospets*. (CRC Press, 2014).

177. Schramm, L. L., Stasiuk, E. N. & Marangoni, D. G. Surfactants and their applications. *Annu. Rep. Prog. Chem. - Sect. C* **99**, 3–48 (2003).

178. Hiemenz, P. C. & Rajagopalan, R. *Principles of Colloid and Surface Chemistry, Revised and Expanded*. (CRC Press, 2016). doi:10.1201/9781315274287.

179. *Water A Comprehensive Treatise*. vol. 4 (Springer US, Boston, MA, 1975).

180. Khan, M. N. *Micellar Catalysis*. (CRC Press, 2006). doi:10.1201/9781420015843.

181. La Sorella, G., Strukul, G. & Scarso, A. Recent advances in catalysis in micellar media. *Green Chem.* **17**, 644–683 (2015).

182. Fanetti, E., Di Monte, R. & Kaspar, J. *Homogeneous and Heterogeneous Catalysis. Inorganic and Bio-Inorganic Chemistry,*. vol. 2 (Eloss Publishers Co. Ltd, 2009).

183. Kostas, I. D. *Suzuki-Miyaura Cross-Coupling Reaction and Potential Applications.* (MDPI AG-Multidisciplinary Digital Publishing Institute., 2017).

184. Yin & Liebscher, J. Carbon−Carbon Coupling Reactions Catalyzed by Heterogeneous Palladium Catalysts. *Chem. Rev.* **107**, 133–173 (2007).

185. Pagliaro, M., Pandarus, V., Ciriminna, R., Béland, F. & Demma Carà, P. Heterogeneous versus Homogeneous Palladium Catalysts for Cross-Coupling Reactions. *ChemCatChem* **4**, 432–445 (2012).

186. Poovan, F., Chandrashekhar, V. G., Natte, K. & Jagadeesh, R. V. Synergy between homogeneous and heterogeneous catalysis. *Catal. Sci. Technol.* https://doi.org/10.1039/d2cy00232a (2022) doi:10.1039/d2cy00232a.

187. Yang, Q. & Li, C. Catalysis in Porous-Material-Based Nanoreactors: A Bridge between Homogeneous and Heterogeneous Catalysis. in *Bridging Heterogeneous and Homogeneous Catalysis: Concepts, Strategies, and Applications* 351–396 (Wiley Blackwell, 2014). doi:10.1002/9783527675906.ch10.

188. Nørskov, J. K., Studt, Felix., Abild-Pedersen, Frank. & Bligaard, Thomas. *Fundamental Concepts in Heterogeneous Catalysis.* (Wiley, 2014).

189. Thomas, J. M. & Thomas, W. *Principles and Practice of Heterogeneous Catalysis.* (John Wiley & Sons., 2014).

190. Budroni, G., Corma, A., García, H. & Primo, A. Pd nanoparticles embedded in sponge-like porous silica as a Suzuki-Miyaura catalyst: Similarities and differences with homogeneous catalysts. *J. Catal.* **251**, 345–353 (2007).

191. Tao, R. *et al.* Porous organic polymer material supported palladium nanoparticles. *J. Mater. Chem. A* **8**, 17360–17391 (2020).

192. MacFarlane, L. R. *et al.* Functional nanoparticles through π-conjugated polymer self-assembly. *Nat. Rev. Mater.* **6**, 7–26 (2021).

193. Behrendt, J. M. *et al.* Scalable synthesis of multicolour conjugated polymer nanoparticles via Suzuki-Miyaura polymerisation in a miniemulsion and application in bioimaging. *React. Funct. Polym.* **107**, 69–77 (2016).

194. Sih, B. C. & Wolf, M. O. Metal nanoparticle - Conjugated polymer nanocomposites. *Chem. Commun.* 3375–3384 (2005) doi:10.1039/b501448d.

195. Zhou, Y. B. & Zhan, Z. P. Conjugated Microporous Polymers for Heterogeneous Catalysis. *Chem. - Asian J.* **13**, 9–19 (2018).

196. Jiang, J. X. *et al.* Conjugated microporous poly(aryleneethynylene) networks. *Angew. Chem. - Int. Ed.* **46**, 8574–8578 (2007).

197. Zecchina, A., Bordiga, S. & Groppo, E. *Selective Nanocatalysts and Nanoscience: Concepts for Heterogeneous and Homogeneous Catalysis*. (John Wiley & Sons, 2011).

198. Fan, M. *et al.* Palladium clusters confined in triazinyl-functionalized COFs with enhanced catalytic activity. *Appl. Catal. B Environ.* **257**, 117942 (2019).

199. Bandyopadhyay, S., Pallavi, P., Anil, A. G. & Patra, A. Fabrication of porous organic polymers in the form of powder, soluble in organic solvents and nanoparticles: A unique platform for gas adsorption and efficient chemosensing. *Polym. Chem.* **6**, 3775–3780 (2015).

200. Braeken, Y., Cheruku, S., Ethirajan, A. & Maes, W. Conjugated Polymer Nanoparticles for Bioimaging. *Materials* **10**, 1420 (2017).

201. He, Z. *et al.* Miniemulsion polymerization-formulated poly(fluorene-alt-6-(2-ethylhexyl)-[1,2,5]thiadiazole[3,4-f]benzotriazole) for cancer cell imaging. *React. Funct. Polym.* **170**, 105130 (2022).

202. Crespy, D. & Landfester, K. Making dry fertile: a practical tour of non-aqueous emulsions and miniemulsions, their preparation and some applications. *Soft Matter* **7**, 11054 (2011).

203. Paul, S., Islam, M. M. & Islam, S. M. Suzuki-Miyaura reaction by heterogeneously supported Pd in water: Recent studies. *RSC Adv.* **5**, 42193–42221 (2015).

204. Shen, T. *et al.* Recent advances on micellar catalysis in water. *Adv. Colloid Interface Sci.* **287**, (2021).

205. Lipshutz, B. H. & Ghorai, S. Transitioning organic synthesis from organic solvents to water. What's your E Factor? *Green Chem* **16**, 3660–3679 (2014).

206. Beletskaya, I. P., Alonso, F. & Tyurin, V. The Suzuki-Miyaura reaction after the Nobel prize. *Coord. Chem. Rev.* **385**, 137–173 (2019).

207. Zhang, P., Weng, Z., Guo, J. & Wang, C. Solution-dispersible, colloidal, conjugated porous polymer networks with entrapped palladium nanocrystals for heterogeneous catalysis of the Suzuki-Miyaura coupling reaction. *Chem. Mater.* **23**, 5243–5249 (2011).

208. Song, Q., Jia, Y., Luo, B., He, H. & Zhi, L. Covalently stabilized Pd clusters in microporous polyphenylene: An efficient catalyst for Suzuki reactions under aerobic conditions. *Small* **9**, 2460–2465 (2013).

209. Liu, X. & Astruc, D. Development of the Applications of Palladium on Charcoal in Organic Synthesis. *Adv. Synth. Catal.* **360**, 3426–3569 (2018).

210. Wincenciuk, A., Cmoch, P., Giedyk, M., Andersson, M. P. & Gryko, D. Aqueous Micellar Environment Impacts the Co-Catalyzed Phototransformation: A Case Study. *J. Am. Chem. Soc.* **146**, 19828–19838 (2024).

211. Blayo, C., Jones, B. E., Bennison, M. J. & Evans, R. C. Size and shape matter for micellar catalysis using light-responsive azobenzene surfactants. *Org. Biomol. Chem.* **23**, 138–144 (2025).

212. Ranaudo, A. *et al.* Partition of the Reactive Species of the Suzuki–Miyaura Reaction between Aqueous and Micellar Environments. *J. Phys. Chem. B* **126**, 9408–9416 (2022).

213. Mattiello, S. *et al.* Suzuki–Miyaura Micellar Cross-Coupling in Water, at Room Temperature, and under Aerobic Atmosphere. *Org. Lett.* **19**, 654–657 (2017).

214. Mattiello, S. *et al.* Self-Assembled Dual Dye-Doped Nanosized Micelles for High-Contrast Up-Conversion Bioimaging. *Adv. Funct. Mater.* **26**, 8447–8454 (2016).

215. Boota, M. *et al.* Interaction of Polar and Nonpolar Polyfluorenes with Layers of Two-Dimensional Titanium Carbide (MXene): Intercalation and Pseudocapacitance. *Chem. Mater.* **29**, 2731–2738 (2017).

216. Men, X. *et al.* Anisotropic assembly and fluorescence enhancement of conjugated polymer nanostructures. *VIEW* **3**, 20220020 (2022).

217. Zhang, H.-H., Xing, C.-H., Tsemo, G. B. & Hu, Q.-S. *t* -Bu_3 P-Coordinated 2-Phenylaniline-Based Palladacycle Complex as a Precatalyst for the Suzuki Cross-Coupling Polymerization of Aryl Dibromides with Aryldiboronic Acids. *ACS Macro Lett.* **2**, 10–13 (2013).

218. Zhang, X. *et al.* Biomass Nanomicelles Assist Conjugated Polymers/Pt Cocatalysts To Achieve High Photocatalytic Hydrogen Evolution. *ACS Sustain. Chem. Eng.* **7**, 4128–4135 (2019).

219. Walczak, R. M., Brookins, R. N., Savage, A. M., Van Der Aa, E. M. & Reynolds, J. R. Convenient Synthesis of Functional Polyfluorenes via a Modified One-Pot Suzuki−Miyaura Condensation Reaction. *Macromolecules* **42**, 1445–1447 (2009).

220. Hooper, A., Zambon, A. & Springer, C. J. A novel protocol for the one-pot borylation/Suzuki reaction provides easy access to hinge-binding groups for kinase inhibitors. *Org. Biomol. Chem.* **14**, 963–969 (2016).

221. Bahyoune, N., Eddahmi, M., Diamantopoulou, P., Kostas, I. D. & Bouissane, L. Recent Advances in Borylation and Suzuki-Type Cross-Coupling—One-Pot Miyaura-Type C–X and C–H Borylation–Suzuki Coupling Sequence. *Catalysts* **15**, 738 (2025).

222. Zhou, D. *et al.* High-quality conjugated polymers via one-pot Suzuki–Miyaura homopolymerization. *RSC Adv.* **7**, 27762–27769 (2017).

223. Gabriel, C. M. *et al.* Effects of Co-solvents on Reactions Run under Micellar Catalysis Conditions. *Org. Lett.* **19**, 194–197 (2017).

224. Palacios, R., Formentin, P., Martinez-Ferrero, E., Pallarès, J. & Marsal, L. β-Phase Morphology in Ordered Poly(9,9-dioctylfluorene) Nanopillars by Template Wetting Method. *Nanoscale Res. Lett.* **6**, 35 (2010).

225. Ceriani, C., Ghiglietti, E., Sassi, M., Mattiello, S. & Beverina, L. Taming Troublesome Suzuki–Miyaura Reactions in Water Solution of Surfactants by the Use of Lecithin: A Step beyond the Micellar Model. *Org. Process Res. Dev.* **24**, 2604–2610 (2020).

226. Griggs, S. *et al.* The effect of residual palladium on the performance of organic electrochemical transistors. *Nat. Commun.* **13**, 7964 (2022).

227. D'Alterio, M. C. *et al.* Mechanistic Aspects of the Palladium-Catalyzed Suzuki-Miyaura Cross-Coupling Reaction. *Chem. – Eur. J.* **27**, 13481–13493 (2021).

228. Audran, G., Brémond, P., Marque, S. R. A., Siri, D. & Santelli, M. Calculated linear free energy relationships in the course of the Suzuki–Miyaura coupling reaction. *Tetrahedron* **70**, 2272–2279 (2014).

229. Almond-Thynne, J., Blakemore, D. C., Pryde, D. C. & Spivey, A. C. Site-selective Suzuki–Miyaura coupling of heteroaryl halides – understanding the trends for pharmaceutically important classes. *Chem. Sci.* **8**, 40–62 (2017).

230. Elsayed, M. S. A., Chang, S. & Cushman, M. Ligand-free, palladacycle-facilitated Suzuki coupling of hindered 2-arylbenzothiazole derivatives yields potent and selective COX-2 inhibitors. *Org. Biomol. Chem.* **16**, 108–118 (2018).

231. Leso, V. & Iavicoli, I. Palladium Nanoparticles: Toxicological Effects and Potential Implications for Occupational Risk Assessment. *Int. J. Mol. Sci.* **19**, 503 (2018).

232. Felpin, F.-X. Ten Years of Adventures with Pd/C Catalysts: From Reductive Processes to Coupling Reactions. *Synlett* **25**, 1055–1067 (2014).